

Assessment and optimisation of guide fins for corner separation control in a compressor cascade

Gabriel Mondin

▶ **To cite this version:**

Gabriel Mondin. Assessment and optimisation of guide fins for corner separation control in a compressor cascade. Other. Ecole Centrale de Lyon, 2022. English. ⟨NNT : 2022ECDL0010⟩. ⟨tel-03977164⟩

HAL Id: tel-03977164

https://theses.hal.science/tel-03977164v1

Submitted on 7 Feb 2023

HAL is a multi-disciplinary open access archive for the deposit and dissemination of scientific research documents, whether they are published or not. The documents may come from teaching and research institutions in France or abroad, or from public or private research centers.

L'archive ouverte pluridisciplinaire **HAL**, est destinée au dépôt et à la diffusion de documents scientifiques de niveau recherche, publiés ou non, émanant des établissements d'enseignement et de recherche français ou étrangers, des laboratoires publics ou privés.



HAL Authorization

Numéro d'ordre : 2022ECDL0010

THÈSE de DOCTORAT DE L'UNIVERSITÉ DE LYON

opérée au sein de

l'École Centrale de Lyon

École Doctorale 162 : Mécanique, Énergétique, Génie Civil et Acoustique

Spécialité : Mécanique des fluides et Énergétique

Soutenu publiquement le 26/10/22, par :

Gabriel Mondin

Assessment and optimisation of guide fins for corner separation control in a compressor cascade

Devant le jury composé de :

Anestis Kalfas	Professor, Aristotle University of Thessaloniki, LFMT	*Rapporteur*
Antoine Dazin	Professeur, ENSAM Lille, LMFL	*Rapporteur*
Ingrid Lepot	Docteure ingénieur, Cenaero	*Président*
Xavier Ottavy	Directeur de Recherche CNRS, ECL, LMFA	*Directeur de Thèse*
Pierre Duquesne	Maître de Conférences, ECL, LMFA	*Co-encadrant de Thèse*
William Riéra	Docteur ingénieur, Safran Tech	*Co-encadrant industriel*

Remerciements

Cette thèse représente environ 3 ans et 10 mois de travail à la croisée du monde industriel et du monde académique, mais également du monde de la modélisation numérique et de celui des essais expérimentaux. Ce positionnement si particulier m'a amené à interagir avec de nombreuses personnes, que je souhaite aujourd'hui remercier.

Je souhaite tout d'abord remercier les membres du jury, pour leur examen du manuscrit, leurs remarques pertinentes et la discussion très intéressante qui en a découlée lors de la soutenance. Je remercie ensuite énormément mes encadrants, Xavier Ottavy, William Riéra et Pierre Duquesne, pour leurs conseils, leur patience, et leur confiance. Grâce à vous, cette thèse a pu prendre forme, et nous avons pu éclaircir quelques-unes des grandes questions de recherche apportées par ce sujet. Pour cela, de nombreuses questions pratiques ont dû être abordées, comme « Quels seraient les paramètres essentiels pour dessiner une sorte d'aube de compresseur exotique ?» ou « Quand puis-je dire que mon métamodèle est suffisamment raffiné ? » en passant par « A quel nombre de Mach faut-il calibrer ma sonde ? ». Si ces questions ont trouvé leur réponse au fil du temps, c'est grâce à la contribution de nombreuses personnes que je souhaite aujourd'hui profondément remercier.

Du coté de Safran Tech, merci à William évidemment, pour ton accueil dans l'entreprise et dans le monde des compresseurs. Je trouve que tu as encadré cette thèse avec un juste équilibre entre les besoins de R&D de Safran et les intérêts de la recherche académique, et je t'en remercie profondément. Merci à Etienne Tang et Emma Croner, pour leur soutien à mes débuts, notamment sur les notions de paramétrisation et de maillage hybride. Merci infiniment à Sébastien Da Veiga de m'avoir accompagné sur le chemin ardu des statistiques/optimisation/métamodélisation. Ton accompagnement et ton enthousiasme m'ont permis de découvrir un vif intérêt pour ces notions, que j'espère retrouver dans mes futurs métiers. Merci également au reste de l'équipe à Safran Tech pour vos discussions variées et votre accueil en mon début de thèse. Je pense notamment à Benoit Rodriguez, Simon Martin, Ye-Bonne Maldonado, Quentin Holka, Gaëtan Crouzy, Carlos Garcia Guillamon. Merci également à Philippe Biagi, du côté de Safran Engineering Services, pour le partage de sa connaissance sur ANSA, ce mailleur aussi puissant que complexe à prendre en main.

L'équipe turbomachine du LMFA m'a accueillie pour la plus grande partie de mes travaux, et je veux y remercier un grand nombre de personne. Tout d'abord, merci Xavier. C'était un grand plaisir de travailler avec une personne aussi humaine et pertinente que toi, et si l'équipe turbomachine tourne aussi bien (au sens propre et figuré), c'est en grande partie grâce à toi. Merci de ta confiance au quotidien, de ta flexibilité et de ton accompagnement. Merci énormément à Pierre (Duquesne) également. Tu as beaucoup contribué à me responsabiliser, comme tu aimes le faire avec les étudiants ;). Merci pour ces discussions précises et chaleureuses, et d'avoir joué le rôle du filet qui ne laisse rien passer lors des relectures et réunions en tout genre ;).

Plus généralement, un grand merci à l'équipe des techniciens / expérimentateurs, sans qui la partie expérimentale de cette thèse n'aurait pas existée ! Je sais maintenant que mesurer une variable physique est un long chemin de croix, où la rigueur, le questionnement systématique de ce l'on observe, et la patience sont les maitres mots. J'ai désormais conscience du travail nécessaire pour obtenir ces fameux points que l'on essaie d'approcher en CFD, et qu'il faut parfois savoir s'en méfier ! Pour ceci, merci infiniment à Benoit Paoletti, Pierre Laucher, Lionel Pierrard, Sébastien Goguey, Gilbert Halter, Cédric Desbois, Christoph Brandstetter et Xavier.

Je remercie également bien sûr tous les numériciens de l'équipe turbomachine, au travers de qui j'ai beaucoup appris sur la physique du décollement de coin, mais aussi sur la notion de modélisation en mécanique des fluides en général. Grâce à vous j'ai progressivement été sensibilisé aux notions de calculs sur clusters, de modélisations de la turbulence, de niveaux de fidélité, de « potards », d'optimisation, de validation expérimentale... ainsi qu'à beaucoup d'autres. Je vous remercie pour la richesse de ces discussions, qui déviaient parfois sur d'autres physiques, et que j'ai trouvées passionnantes. Pour cette partie, je remercie notamment Stéphane Aubert, Jérôme Boudet et Alexis Giauque, mais également tous mes collègues doctorant avec qui j'ai eu de nombreuses discussions de ce type.

Sur cette belle transition je vous remercie spécialement, vous les collègues doctorants. La bonne humeur qui règne au LMFA est exceptionnelle, et c'est grâce à vous, merci. Merci au noyau dur de ma génération, celles et ceux avec qui j'ai grandi : Anne-Lise Fiquet, Florent Kravtsoff, Nicolas Poujol, Martin Rodrigues, Martin Buisson, Christophe Montsarrat (mention spéciale à mon co-bureau), Aurélien Vadrot, Ivo Dawkins (mention spéciale à mon mentor sur la grille linéaire), Valdo Pages, Joffrey Chaneac et Jean Al Am. Vous comprenez mieux que quiconque l'intensité de ces années passées en thèse chez les turbos, merci de cette aventure. Merci aux plus anciens, source d'inspiration pour la thèse (Gherardo Zambonini) et pour la suite (Thomas Bontemps), ainsi qu'à ceux que j'ai pu croiser au labo ou en dehors (Julissa Grondin, Jeff Monier). Merci également à la génération des nouveaux, Alexandra Schneider et Valentin Caries, que j'ai quand même bien côtoyés ;). Bon courage pour la suite, je vous souhaite de vous éclater. Bon courage également à Malo pour son post-doc sur la grille, et aux tous nouveaux doctorants qui arrivent au moment où j'écris ces remerciements.

A côté de cet univers professionnel, la période passée au LMFA correspond pour moi à la découverte de Lyon et de ses alentours. Et, là encore, la vie m'a accueillie avec une belle équipe de choc. Merci Bastien, Cécile, Clara Cuzin, Elodie, Hubert, Hugo, Johann,Magalie , Mathieu, Clara Gomez, Morgane, Thomas, Salambô, Jean-Lynce... Merci pour ces moments bières, ces soirées déguisées que tout le monde adore, ces concerts, ces week-end montagne, ces discussions sur la vie, pour tous ces bons moments et ces beaux souvenirs. Un grand merci également à mes colocataires avec qui j'ai partagé de nombreux moments de vie. Merci Tiphaine, merci Juliette, merci Alma.

Avant de conclure ces remerciements, je voudrais spécialement remercier quelques amis avec qui j'ai particulièrement été en phase pendant ces années, tant du point de vue de la situation (tous en thèse !) que du caractère. Un merci tout particulier donc à Salambô, Jean-Lynce, Aurel, Thibault et Carlos. Vous avez chacun vos traits de caractères particuliers qui m'inspirent, m'aident à me remettre en question, et me font bien marrer.

Enfin, merci à ma famille, un peu dispatchée entre Bordeaux, Lyon et Hambourg, pour leur intérêt et curiosité envers mon travail pourtant bien éloigné de leur quotidien. Merci à mes grands-parents, et notamment mon grand-père maternel, pour m'avoir transmis le goût de la curiosité et avoir été un exemple de grand calme et de pragmatisme, du début jusqu'à la fin de ma longue scolarité.

Gabriel

Abstract

Corner separation is one of the major phenomena limiting the operability of aeronautical compressors. In this thesis, a new approach on passive technological effects for corner separation control is undertaken with the concept of guide fins, defined as "profiled devices of a priori non-conventional shapes fixed to the hub". The underlying idea is to investigate shapes typical of existing technological effects, as well as potentially interesting intermediate shapes, with a limited a priori on the physical mechanisms to implement. Through the concept of guide fins, the objectives of this thesis are a) to establish basic design rules for passive corner separation means of control, and b) to identify the physical mechanisms yielding a corner separation reduction.

This work is based on a simple configuration (subsonic compressor cascade, M=0.11, Re=3.2×10^5, modern stator blades) where the aerodynamic conditions are thoroughly controlled. In a first step, a numerical chain enabling the evaluation by Reynolds-Averaged Navier-Stokes (RANS) computations of various guide fin shapes is set up. A parametrisation integrating aerodynamic constraints is developed (15 parameters). Given the complexity of the shapes involved, a hybrid mesh approach (structured-unstructured) is used. The limitations of RANS modelling are clearly identified, and the Quadrative Constitutive Relation (QCR) correction is used to improve this modelling. This numerical chain is then used within an optimisation process that aims at reducing the endwall losses at design and near-stall operating conditions. Due to the relatively high numerical cost of RANS simulations, an optimisation strategy based on the iterative refinement of Kriging surrogate models is performed. Using this strategy, two design spaces are explored. A RANS database containing about 500 guide fins is generated for each space, as well as low-fidelity Kriging surrogate models predicting the effect of guide fin design parameters on endwall losses. The analysis of the optimisation results reveals the existence of three guide fin families: a) Short Fence: short and straight guide fins, located rather upstream within the channel b) Long Fence: long and straight guide fins, covering the whole channel c) 3D: long guide fins with a pyramidal aspect, located rather downstream within the channel. These families are mainly sensitive to 6 design parameters, and notably to their axial position, height and hub chord. A representative guide fin of each family is tested experimentally. All representative guide fins strongly reduce the endwall losses on a large range of incidence, with an absolute variation compared to the reference configuration of -0.13% to +0.08% at design incidence, and of -2.44% to -2.94% at near-stall incidence. The associated RANS computations are validated experimentally. Numerical investigations of each guide fin reveal several beneficial mechanisms for reducing corner separation, and notably the mechanisms of i) tip vortex (energises the endwall boundary layer) ii) local fence (divides the passage flow in two parts) iii) local pressure drop (reduces the adverse and transverse pressure gradients).

This work proves the potential of guide fins in an academic configuration. To go further, it is necessary to evaluate their relevance in realistic flow conditions, notably in terms of inlet boundary layer profiles and Mach numbers. Basic preliminary results are proposed on these two aspects, and are encouraging as to the adaptability of this technology in a realistic context.

Keywords : Corner separation, control, optimisation, guide fin, compressor cascade, RANS, Kriging surrogate, experimental validation, physical mechanisms.

Résumé

Le décollement de coin est un des phénomènes majeurs limitant l'opérabilité des compresseurs aéronautiques. Dans cette thèse, une nouvelle approche des effets technologiques de contrôle du décollement de coin est entreprise avec le concept d'ailette, définie comme "un dispositif profilé de forme a priori non conventionnelle fixé au moyeu". L'idée sous-jacente est d'étudier des formes typiques d'effets technologiques existants en même temps que des formes intermédiaires potentiellement intéressantes, avec peu d'a priori sur les mécanismes physiques à mettre en place. Au travers du concept d'ailettes, les objectifs de cette thèse sont a) d'établir des bases de règles de conception de moyens de contrôle passif du décollement de coin, et b) d'identifier les mécanismes physiques participant à réduire le décollement de coin.

Ce travail repose sur une configuration simple (cascade de compresseurs subsonique, M=0.11, Re=3.2×10^5, aubes de stator modernes) où les conditions aérodynamiques sont minutieusement contrôlées. Dans un premier temps, une chaine numérique permettant l'évaluation par calculs Reynolds-Averaged Navier-Stokes (RANS) de formes d'ailettes variées est mise en place. Une paramétrisation intégrant des contraintes aérodynamiques est développée (15 paramètres). Compte tenu de la complexité des formes en jeu, une approche de maillage hybride (structuré-non structuré) est utilisée. Les limites de la modélisation RANS sont clairement identifiées, et la correction Quadrative Constitutive Relation (QCR) est utilisée pour améliorer cette modélisation. Cette chaine numérique est ensuite utilisée au sein d'un processus d'optimisation visant à réduire le décollement de coin dans des conditions nominale et proche instabilité. Compte tenu du coût numérique relativement élevé des simulations RANS, une méthode de raffinement itératif de métamodèle de Krigeage est effectuée. Grâce à cette méthode, deux espaces de conception sont explorés. Une base de données RANS d'environ 500 ailettes est générée pour chacun, ainsi que des métamodèles (basse fidélité) de Krigeage prédisant l'influence des paramètres de dessin des ailettes sur les pertes de coin. L'analyse des résultats d'optimisation révèle l'existence de trois familles d'ailettes : a) Short Fence : ailette courte, raide, placée en amont du canal b) Long Fence : ailette longue, raide, couvrant une grande partie du canal c) 3D : ailette longue, de forme pyramidale, placée en aval du canal. Ces familles sont principalement sensibles à 6 paramètres de dessin, et notamment à leur position axiale, hauteur et corde en pied. Une ailette représentative de chaque famille est testée expérimentalement. Chacune de ces ailettes réduit fortement les pertes de coin sur une large gamme d'incidence, avec une variation absolue par rapport au cas de référence de -0,13% à +0,08% à incidence de dessin, et de -2,44% à -2,94% à incidence proche décrochage. Les calculs RANS associés sont validés expérimentalement. L'investigation de ces calculs révèlent plusieurs mécanismes bénéfiques pour réduire les pertes de coin, et notamment les mécanismes de i) vortex de bout de pale (énergise la couche limite de moyeu) ii) barrière locale (coupe l'écoulement du passage en deux parties) iii) dépression locale (atténue les gradients de pression adverse et transverse).

Ce travail prouve le potentiel des ailettes dans une configuration académique. Pour aller plus loin, il est nécessaire d'évaluer leur pertinence dans des conditions d'écoulement réalistes, notamment en termes de profil de couche limite incidente et de nombre de Mach. De simples résultats préliminaires sont proposés sur ces deux aspects, et sont encourageants quant à l'adaptabilité de cette technologie en contexte réaliste.

Mots clés : Décollement de coin, contrôle, optimisation, ailette, gille linéaire de compresseur, RANS, Kriegeage, validation expérimentale, mécanismes physiques.

Contents

Remerciements **iv**

Abstract **viii**

Résumé **x**

Contents **i**

List of Figures **v**

List of Tables **xiii**

Nomenclature **xv**

Introduction **1**

1 Corner separation in aeronautical compressors **3**
1.1 Physics of compressors 3
1.1.1 Turbomachinery context 3
1.1.2 Axial compressors performance and operating range limits 4
1.2 Physics of corner separation 6
1.2.1 Elements on boundary layer separation 6
1.2.2 Cause of corner separation in axial compressors 8
1.2.3 Topological description of corner separation 10
1.2.4 Impact of corner separation in axial compressors 15
1.3 Prediction of corner separation 17
1.3.1 Corner separation prediction with criteria 17
1.3.2 Corner separation prediction with CFD methods 20
1.4 Control of corner separation 22
1.4.1 Sensitivity to inflow conditions 23
1.4.2 Sensitivity to blade details 25
1.4.3 Control with blade design 26
1.4.4 Control with technological effects 28
1.5 Summary 35

2 Elements on Kriging-based optimisation **36**
2.1 Kriging surrogate modelling . . . 36
2.1.1 Concept of Kriging surrogate models . . . 36
2.1.2 Design of experiment . . . 39
2.2 Optimisation based on iterative refinement of surrogate models . . . 40
2.2.1 Basics of optimisation . . . 40
2.2.2 Iterative refinement of surrogate models . . . 42
2.3 Pearson correlation . . . 45

3 Configuration of reference **48**
3.1 Overview of the rig . . . 48
3.2 Performance of the cascade . . . 50
3.2.1 Aerodynamic load at midspan . . . 50
3.2.2 Total pressure losses . . . 50
3.2.3 Blockage . . . 53
3.2.4 Flow angles . . . 54
3.2.5 Secondary streamlines . . . 56
3.2.6 Skin friction patterns . . . 57
3.3 Numerical illustration . . . 58

4 Experimental methodology **59**
4.1 Controlling the rig . . . 59
4.1.1 Overview of the control system . . . 59
4.1.2 Detailed settings . . . 60
4.2 Measurement techniques . . . 62
4.2.1 Pneumatic five-hole probe . . . 63
4.2.2 Uncertainty quantification . . . 66
4.3 Guide fin insertion system . . . 67

5 Numerical methodology **70**
5.1 Guide fin parametrisation . . . 71
5.1.1 Parametrisation of an aerodynamic shape . . . 72
5.1.2 Parametrisation with embedded constraints . . . 73
5.2 Hybrid meshing methodology . . . 76
5.2.1 Generation of the structured part . . . 77
5.2.2 Generation of the unstructured part . . . 78
5.2.3 Unstructured mesh refinement . . . 79
5.3 RANS computations . . . 80
5.3.1 Numerical set up . . . 81
5.3.2 The topological switch . . . 82
5.3.3 Numerical convergence . . . 83
5.3.4 The choice of turbulent closure modelling . . . 84
5.3.5 Validation of the hybrid methodology . . . 87
5.4 Conclusion . . . 88

6 Optimisation methodology **89**
6.1 Definition of the objective functions . . . 90
6.2 Optimisation in the entire input space (15p) . . . 91
6.2.1 Definition of the input space . . . 91

6.2.2 Settings of the iterative process . . . 93
6.2.3 Convergence . . . 94
6.2.4 Predictability in the Pareto front region . . . 96
6.2.5 Definition of a reduced input space of interest . . . 98
6.3 Optimisation in a reduced input space (6p) . . . 100
6.3.1 Definition of the input space . . . 100
6.3.2 Settings of the iterative process . . . 100
6.3.3 Convergence . . . 102
6.3.4 Predictability in the Pareto front region . . . 103
6.4 Summary . . . 104

7 Characteristic shapes of efficient guide fins 107
7.1 Analysis of the 15-parameter space results . . . 107
7.1.1 Investigation of the RANS database (15p) . . . 108
7.1.2 Characterisation of the Short Fence (SF) and 3D families . . . 111
7.1.2.1 Geometrical specificities . . . 111
7.1.2.2 Definition of main parameters . . . 113
7.1.2.3 Analysis of main parameters effect on the losses at high incidence 114
7.1.3 Investigation of the Long Fence (LF) family . . . 118
7.1.4 Summary . . . 120
7.2 Analysis of the 6-parameter space results . . . 121
7.2.1 Investigation of the RANS database (6p) . . . 122
7.2.2 Investigation of the Short Fence (SF) family . . . 125
7.2.3 Investigation of the 3D family . . . 126
7.2.4 Investigation of the Long Fence (LF) family . . . 127
7.2.5 Complementary analysis of the SF and LF Pareto fronts . . . 129
7.3 Selection of representative guide fins of the three guide fin families . . . 129

8 Investigation of physical mechanisms reducing the corner separation 132
8.1 Investigation of the SF guide fin . . . 132
8.1.1 Validation of RANS predictions . . . 133
8.1.2 Physical mechanisms . . . 135
8.1.3 Effect on downstream profiles . . . 140
8.1.4 Summary . . . 141
8.2 Investigation of the LF guide fin . . . 141
8.2.1 Validation of RANS predictions . . . 141
8.2.2 Physical mechanisms . . . 143
8.2.3 Effect on downstream profiles . . . 148
8.2.4 Summary . . . 149
8.3 Investigation of the 3D guide fin . . . 149
8.3.1 Validation of RANS predictions . . . 150
8.3.2 Physical mechanisms . . . 151
8.3.3 Effect on downstream profiles . . . 154
8.3.4 Summary . . . 155
8.4 Influence of the inlet boundary layer . . . 155
8.5 Summary . . . 156
8.5.1 Relevance of RANS in the guide fin design process . . . 156
8.5.2 Beneficial mechanisms reducing corner separation . . . 159

9 Conclusion and Perspectives **161**
9.1 Conclusion . . . 161
9.2 Perspectives . . . 162

References **165**

A Axial compressors : basics of thermo-aerodynamics **I**
A.1 Orders of magnitude . . . I
A.2 Total and static quantities in compressible flows . . . I
A.3 Euler equation . . . III
A.4 Design coefficients . . . IV
A.5 Relation between entropic losses and total pressure losses in an adiabatic stator row . . . VI

B Elements on Kriging modelling **VIII**
B.1 Notion of Gaussian process . . . VIII
B.2 Parameters of Kriging modelling . . . X

C Characteristic shapes of efficient guide fins : complementary results **XIII**
C.1 Distribution of parameters with respect to $\Delta\omega_0$ and $\Delta\omega_{4.9}$ (15p analysis). . . . XIII
C.2 Relation between relative stagger angle, twist and $\Delta\beta_{1,H}$ . . . XVI
C.3 Efficient 6-parameter guide fins : evolution of $\Delta\omega_0$ and $\Delta\omega_{4.9}$ with all parameters. XVII
C.4 Comparison of 15p and 6p families . . . XIX
C.5 Investigation of the SF and LF Pareto front (6p analysis) . . . XIX
C.6 Surrogate predictions of SF-03, LF-01, 3D-01 . . . XXIII

D Investigation of physical mechanisms : complementary results **XXVI**
D.1 Axial evolution of total pressure losses : effect of mixing . . . XXVI
D.2 Cartographies . . . XXVIII

List of Figures

1.1 Typical modern turbofan architecture and specifications (left). Simplified Brayton cycle (left) for isentropic (solid lines) and real (dashed line) transformations. 4
1.2 Enthalpy gain and compression across an axial compressor stage. From Zambonini (2016). 5
1.3 Performance characteristic map for an axial compressor. 100% Nn : rotating velocity of the cruise regime. From Zambonini (2016). 6
1.4 Schematic of a boundary layer, from Encyclopedia2 (2022). 8
1.5 Illustration of boundary layer separations. 8
1.6 Overturning of the endwall boundary layer in the presence of the cross-passage transverse pressure gradient. From Dawkins (2021). 9
1.7 Effect of passage flow on corner separation. 10
1.8 Classification of critical points and surrounding skin friction field in the eigen vector plane [p-q], from Délery (2013) 12
1.9 Three-dimensional flow in the vicinity of a Node or a Focus. From Délery (2013). 13
1.10 Three-dimensional flow in the vicinity of a Saddle point. Adapted from Délery (2013). 13
1.11 Evolution of the number of nodes and of the boundary layer thickness when increasing the flow incidence. From (Gbadebo et al., 2005). 14
1.12 Experimental investigation of the corner separation in a compressor cascade. PIV (experimental) measurements near the endwall (i : inflow incidence). From (Dawkins et al., 2021). 14
1.13 Illustration of the single sided and double sided topology (RANS). 15
1.14 Losses and blockage induced by corner separation. 16
1.15 Lei criterion. From (Lei et al., 2008). 19
1.16 Definition of the corner shape factor. From Taylor and Miller (2017). 19
1.17 Total pressure losses measured downstream of the NACA65 compressor cascade. Full cartography : Experimental (a) vs Wall resolved LES (b). Pitchwise mass-averaged total pressure loss coefficient (c). From Gao et al. (2015). 20
1.18 Total pressure losses measured downstream of the NACA65 compressor cascade. Full cartography : Experimental (a) vs LES-LBM wall modelled (b) vs Navier-Stokes wall resolved LES (c). From Boudet et al. (2022). 21
1.19 Evolution of integrated total pressure losses downstream of the compressor cascade studied in this work. Experimental results (Datum) vs RANS predictions with three commonly used turbulence models. 21
1.20 Overview of existing corner separation control strategies. 23

1.21 Effect of boundary layer thickness on total pressure losses downstream of the NACA65 compressor cascade (Boudet et al., 2022): (a) with the reference inlet boundary layer, (b) with a 3 to 5 times thinner inlet boundary layer. LES-LBM results. . . . 24
1.22 Effect of inlet boundary layer profile details on corner separation (Auchoybur and Miller, 2018). . . . 24
1.23 Effect of small geometry changes on hub losses (Goodhand and Miller, 2012). . . . 26
1.24 Illustration of three-dimensional blading (Gallimore et al., 2002). . . . 27
1.25 Effect of lean angle on pressure surface and downstream losses (Taylor and Miller, 2017). . . . 27
1.26 Schematic illustrations of secondary flows interaction in the presence of hub clearance. From Beselt et al. (2014) 28
1.27 Illustration of a slotted configuration (Sun et al., 2021). . . . 28
1.28 Illustration of the concept of vortex generator. . . . 30
1.29 Effect of VG on separated region (oil visualisation) at design incidence ($Mach = 0.66$). . . . 30
1.30 Evaluation of various vortex generator arrangements in a compressor cascade ($Mach = 0.66$) (Hergt et al., 2013). . . . 31
1.31 32
1.32 Illustration of endwall fences concept and its influence of loss variation with the incidence (Hergt et al., 2011). . . . 32
1.33 Schematic of an axisymmetric (2D) endwall contouring, from (Denton and Xu, 1998). . . . 33
1.34 Illustrations from Hergt et al. (2009) 34
1.35 From Reutter et al. (2017). Left : optimised 3D endwall. Right : Evolution of losses with the incidence. Non optimised blade (black dots), optimised 2D blades (red squares), optimised 2D blades + optimised 3D endwall (red triangles). 34

2.1 Illustration of the construction of a surrogate model. Adapted from Da Veiga (2019). . . . 37
2.2 Principle of Kriging modelling. Adapted from Helbert (2020). . . . 38
2.3 Predicted vs true value. Each dot corresponds to an observation point. The red line is represents the region of perfect predictability (True value = Predicted value). . . . 39
2.4 Examples of DOEs on a two-parameter space. Triangles : observation set. . . . 39
2.5 Illustration of a bi-objective, bi-parameter optimisation problem. The red line on the right hand side figure corresponds to the optimal region, or Pareto front. 41
2.6 Illustration of the principle of dominance in the Pareto sense. . . . 41
2.7 Illustration of surrogate refinement process. Arrows indicate the previous and next refinement points. The yellow frame indicates a region of minima well predicted by the surrogate model. Adapted from (Da Veiga, 2019). . . . 43
2.8 EHVI in a bi-objective context : (a) hypervolume on a given set of Pareto solutions, (b) improvement of the hypervolume by the deterministic inclusion $[f_1(x_c),\ f_2(x_c)]$ of a new candidate x_c, and (c) EHVI by the uncertain inclusion $[\hat{f}_1(x_c),\ \hat{f}_2(x_c)]$ of a new candidate x_c in the front. f_i : Kriging average prediction of objective function i. $\hat{f}_i$: Probabilistic values of objective function i (Kriging uncertainty). Adapted from (Martínez-Frutos and Herrero-Pérez, 2016). . . . 44

2.9 Values of Pearson correlation coefficient computed on samples of various shapes. From *https://en.wikipedia.org/wiki/Pearson_correlation_coefficient*. 46
2.10 Illustration of Pearson correlation coefficient significance. The p-value is the probability that the inferred linear correlation on the sample originates from pure randomness (case B). 47

3.1 Side view of the rig. 49
3.2 50
3.3 Pressure coefficient distribution ($C_{p,s}$) along the blade at midspan. Experimental data. c_{ax} : axial stator chord. 50
3.4 Cartographies of total pressure losses ω 0.2c downstream of the cascade. BL : Boundary Layer. 52
3.5 Spanwise evolution of total pressure losses ω as the incidence increases. 52
3.6 Evolution of endwall losses ω_{EW} with the incidence. Experimental data. 53
3.7 Cartographies of dimensionless velocity $\widetilde{V_x}$ 0.2c downstream of the cascade. . . . 54
3.8 Spanwise evolution of dimensionless velocity $\widetilde{V_x}$ vs incidence. 54
3.9 Cartographies of pitchwise angle β 0.2c downstream of the cascade. 55
3.10 Spanwise evolution of pitchwise angle β vs incidence. 56
3.11 Cartographies of spanwise angle ϕ 0.2c downstream of the cascade. 56
3.12 Secondary streamlines. Coloured with $\widetilde{V_x}$. 57
3.13 Secondary streamlines zoomed in the corner region of the investigated channel. Coloured with $\widetilde{V_x}$. 57
3.14 Oil flow visualisation of the suction side and the endwall. TE : Trailing Edge. Adapted from Dawkins (2021). 58
3.15 Illustration of corner separation development within the channel (RANS results, i=4.9°). Region of negative axial velocity (in yellow). Streamlines are coloured with total pressure losses, stator and endwall surfaces with $C_{p,s}$. 58

4.1 Schematic of cascade showing key elements. 60
4.2 Details of the bleed slot. From (Dawkins, 2021). 61
4.3 Pressure tappings positions and measurement in a case of balanced flow rates. From (Dawkins, 2021). 61
4.4 Inlet boundary layer profiles, measured 0.25c upstream of the cascade leading edge at 3 pitch locations. From (Dawkins et al., 2021). 61
4.5 $C_{p,s}$ profiles at various incidences. Measurements (black crosses) vs MISES best fit (red lines). Incidences are deduced from the MISES database. From Dawkins et al. (2021). 62
4.6 Periodicity evaluation. ω and β at i=4.9° across two consecutive channels. Investigated (red) and neighbouring (black) channels at various spanwise locations. From the author. 62
4.7 Five-hole probe illustration. 63
4.8 Calibration maps. 63
4.9 Effects of pressure gradient correction on midspan values of β, ϕ, P_t, P_s. Investigated channel only. 65
4.10 Probe sampling grid. Total pressure losses at i=4.9°. 66
4.11 Geometrical description of the insertion system. Gray : fixed part. Black : removable platform. 68
4.12 Insertion system outside of the rig. Baseline and guide fin configurations. 68
4.13 Rear view of the cascade equipped with the system. 69

4.14 Effect of the insertion system on the endwall losses. Baseline configuration. . . . 69

5.1 Chain overview. . . . 70
5.2 Example of various guide fins. . . . 71
5.3 Examples of thickness and camber laws. t_M is expressed in guide fin chord unit and c_{GF} in stator chord unit. . . . 72
5.4 Example of aerofoil parametrised with the 7 construction parameters (in purple). 73
5.5 Stacking methodology. . . . 73
5.6 Illustration of the authorised surface (left) and chord (right) at hub. . . . 75
5.7 Illustration of parameters $\Delta\beta_1$ (left), and d_{sweep} and d_{lean} (right). . . . 76
5.8 Illustration of the parameter $\beta_{2,pc_\beta1}$. . . . 76
5.9 Illustration of the hybrid methodology. . . . 77
5.10 Illustration of the original structured mesh. *Black lines : blocks borders.* . . . 78
5.11 Unstructured block boundaries (in red). *Black lines : blocks borders. A second faded channel is added for visualisation purposes.* . . . 78
5.12 Portions of hybrid mesh with a guide fin. Grey elements : hexahedra (structured part). Green elements : prisms. Red elements : tetrahedra and pyramids. 24 layers are used for visualisation purposes. . . . 79
5.13 Effect of the number of layers (left) and of the wake refinement level (right). . . 80
5.14 No wake refinement (left) vs refinement level 3 (right). . . . 80
5.15 Computation domain. Inviscid (green) and no-slip (red) conditions. . . . 81
5.16 RANS predictions of the endwall losses and skin friction patterns using $k\omega - BSL$ turbulence model. . . . 82
5.17 Convergence of ω_{0D} for various incidences. . . . 83
5.18 Effect of turbulence model on losses distribution at high incidence (i=4.9°). . . . 84
5.19 Effect of the turbulence model on endwall losses. . . . 85
5.20 Effect of QCR correction on endwall losses. . . . 86
5.21 Radial profile (i=4.9°). . . . 86
5.22 Effect of the mesh type on endwall losses. Structured mesh of reference, hybrid mesh of reference (Tetrahedral) and intermediate hybrid mesh (Hexahedral). . . 87
5.23 Total pressure losses at design (0°) and high (4.9°) incidences. Experiment vs RANS. . . . 88

6.1 Correlation between diffusion factor and stall indicator. Reproduced from (Lei et al., 2008). Annotated with RANS computations on the current baseline. . . . 91
6.2 Illustrations of the geometrical criteria. LE=Leading Edge, TE=Trailing Edge. . 92
6.3 Evolution of the RANS database and candidate database predictions. . . . 94
6.4 Evolution of the Pareto fronts. . . . 95
6.5 Evolution of the HVI and Q2 criteria on the large input space. . . . 96
6.6 Shapes and positions in the RANS database of guide fins A and B. . . . 97
6.7 Surrogate predictions vs RANS computations. For each guide fin A and B, only H_{GF} varies from its minimum to its maximum value. . . . 97
6.8 RANS database coloured by depth values. Depths 1, 10, 20, 30 are highlighted. . 98
6.9 Guide fins used for computing Pearson coefficients (depth $\leq$ 10). The Pareto front is highlighted with blue diamonds. . . . 99
6.10 Evolution of the RANS database and Pareto fronts. . . . 102
6.11 Evolution of the HVI and Q2 criteria on the reduced input space (6p). . . . 103

6.12 Predictability near Pareto Front : guide fins selection on the surrogate Pareto front at Reft. 16 vs RANS evaluations. Global view (left) and zoom in the evaluated region (right). . . . 104
6.13 Comparison of 15p and 6p databases and Pareto fronts (PF). . . . 104

7.1 Characteristic shapes of RANS Pareto front (15p). RANS database (black) and intuitive repartition of Pareto optimal geometries into two groups (blue and red). 108
7.2 Hub chord vs absolute hub thickness of guide fins of depth ≤ 5. Coloured with $\Delta\omega_0$ and scaled with $-\Delta\omega_{4.9}$. . . . 108
7.3 Performance and characteristic shapes of the SF, 3D and LF families (15p). . . . 110
7.4 Pyramidal aspect of SF and 3D families. . . . 111
7.5 Investigation of local section convergence and twist. . . . 112
7.6 H_{GF} vs $\Delta\omega_{4.9}$. RANS database (red dots) and surrogate predictions (black faded lines). . . . 115
7.7 $\Delta\beta_{1,H}$ vs $\Delta\omega_{4.9}$. RANS database (red dots) and surrogate predictions (black faded lines). . . . 115
7.8 u vs $\Delta\omega_{4.9}$. RANS database (red dots) and surrogate predictions (black faded lines). . . . 116
7.9 v vs $\Delta\omega_{4.9}$. RANS database (red dots) and surrogate predictions (black faded lines). . . . 117
7.10 $t_{M,H}$ vs $\Delta\omega_{4.9}$. RANS database (red dots) and surrogate predictions (black faded lines). . . . 117
7.11 $c_{GF,H}$ vs $\Delta\omega_{4.9}$. RANS results : SF (red) and 3D (blue) guide fins. . . . 118
7.12 Limits of the LF family definition. . . . 119
7.13 Sensitivities to the parameters u, v and H_{GF}. . . . 120
7.14 Hub chord vs absolute hub thickness of guide fins of depth ≤ 5. Coloured with $\Delta\omega_0$ and scaled proportionally to $-\Delta\omega_{4.9}$. . . . 122
7.15 Parameter distributions of the 6p guide fins investigated against $\Delta\omega_{4.9}$. . . . 123
7.16 Performance and characteristic shapes of the SF, 3D and LF families (6p). . . . 124
7.17 Performance of SF guide fins (6p vs 15p). PF : Surrogate Pareto Front. . . . 126
7.18 Performance of 3D guide fins (6p vs 15p). PF : Surrogate Pareto Front. PF : Surrogate Pareto Front. . . . 127
7.19 Effects of H_{GF} and $c_{GF,H}$ depending on $\Delta\omega_{4.9}$ values. . . . 128
7.20 Performance of LF guide fins (6p vs 15p). PF : Surrogate Pareto Front. . . . 128
7.21 Comparison of SF, LF and surrogate Pareto fronts. . . . 129
7.22 Representative guide fins of the SF, LF and 3D families. . . . 130
7.23 Values of the objective functions, parameters and geometrical criteria associated to each representative guide fin. The main parameters are highlighted in green. . 131

8.1 Geometry of SF guide fin. . . . 133
8.2 Evolution of the endwall losses on the measurement plane. Baseline vs SF guide fin. Black arrow : guide fin wake. Black rectangle : low loss region. . . . 134
8.3 Total pressure losses with the SF guide fins at various incidences. RANS vs Experiment. . . . 134
8.4 Topological organisation. Baseline vs SF guide fin (i=4.9°). . . . 135
8.5 Topological organisation : zoom in guide fin leading edge and guide fin trailing edge regions (i=4.9°). . . . 136
8.6 Illustration of the short fence effect. . . . 136
8.7 Beneficial effects of the fence mechanism. . . . 137

8.8 Illustration of the SF guide fin tip vortex. . . . 137
8.9 Secondary streamlines and dimensionless axial velocity distributions at different axial positions. Slice D : experimental measurement plane. . . . 138
8.10 Validation of the presence and of the beneficial effect of the tip vortex (SF guide fin). Experimental data in the measurement plane. . . . 139
8.11 Experimental profiles in the measurement planes. SF guide fin (red) vs Baseline (black). H_{GF} : Guide fin height. δ_{ref} : inlet boundary layer thickness. . . . 140
8.12 Geometry of LF guide fin. . . . 141
8.13 Evolution of the endwall losses on the measurement plane. Baseline vs LF guide fin. . . . 142
8.14 Total pressure losses with the LF guide fins at various incidences. RANS vs Experiment. A : Stator corner separation. B : Low loss region (RANS only). C : Guide fin corner separation. D : Bulk flow guided with low losses. . . . 143
8.15 Topological organisation. Baseline vs LF guide fin (i=4.9°). . . . 144
8.16 Pressure distribution near the hub. . . . 144
8.17 Secondary streamlines and dimensionless axial velocity distributions at different axial positions. Slice D : experimental measurement plane. . . . 145
8.18 RANS predictability : experimental integrated losses and gains vs predictions for guide fins SF, LF and 3D. . . . 145
8.19 Streamlines seeded in low loss region and high loss pattern for i=0° and i=4.9°. 146
8.20 Zoom in guide fin leading edge. Skin friction and negative axial velocity region (in yellow) at design incidence i=0°. . . . 146
8.21 Comparison of experimental and RANS cartographies of $\widetilde{V_x}$ and $\beta - \beta_{MID}$. LF guide fins, i=4.9°. CS : Corner separation. Purple arrows : passage vortex. . . . 147
8.22 Experimental profiles in the measurement planes. LF guide fin vs Baseline. CS : Corner Separation. H_{GF} : Guide fin height. δ_{ref} : inlet boundary layer thickness. 148
8.23 Geometry of 3D guide fin. . . . 149
8.24 Evolution of the endwall losses on the measurement plane. Baseline vs 3D guide fin. . . . 150
8.25 Total pressure losses with the 3D guide fins at various incidences. RANS vs Experiment. Black arrow : guide fin wake. . . . 151
8.26 Topological organisation. Baseline vs 3D guide fin (i=4.9°). . . . 151
8.27 Effect of the guide fin 3D on near hub streamlines. Streamlines are seeded 1.5 mm away from the hub and coloured with their ID. The solid surfaces are coloured with $C_{p,s}$. . . . 152
8.28 Illustration of beneficial gradients induced by guide fin 3D at i=4.9°. Baseline (left) vs 3D guide fin (right). . . . 153
8.29 Experimental data : total pressure losses and pitchwise angle fluctuations at design and high incidences with guide fin 3D. Purple arrows : passage vortices. Black line : guide fin height. . . . 153
8.30 Experimental profiles in the measurement planes. 3D guide fin vs Baseline. CS : Corner Separation. BL : Boundary Layer. H_{GF} : Guide fin height. δ_{ref} : inlet boundary layer thickness. . . . 154
8.31 Evolution of the endwall losses when doubling the inlet boundary layer thickness. RANS results. BSL : Baseline configuration. . . . 155
8.32 RANS predictability : experimental integrated losses and gains vs RANS predictions for guide fins SF, LF and 3D. BSL : Baseline configuration. . . . 157

8.33 Left : Sensitivity of $\Delta\omega_{4.9}$ to the streamwise position of the guide fin leading edge (parameter u). Surrogate models and RANS predictions. Right : Positions corresponding to the investigated range of u, with respect to the Saddle/Focus pair observed on the baseline configuration at i=4.9°. 158

9.1 Evaluation of the baseline configuration and SF-03, LF-A and 3D-01 guide fins under compressible flow conditions. Evolution of the endwall total pressure losses (ω_{EW}) with the incidence. The inlet Mach number (M) varies between 0.11 and 0.47. The inlet Reynolds number is kept constant so that a similar boundary layer thickness develops on the hub and on the stator blades. 164

A.1 Design coefficients graphical interpretation V

B.1 Realisations of a Gaussian process replicating the Brownian motion and evolution of the probability density function f as a function of the time t. Adapted from Helbert (2020). X
B.2 Effect of the covariance function of the realisations of the Gaussian process, unconditioned and conditioned. Adapted from Helbert (2020) and Da Veiga (2019). XII

C.1 Distribution of the optimisation parameters against $\Delta\omega_0$. SF (red), 3D (blue) and LF (green) families. XIV
C.2 Distribution of the optimisation parameters against $\Delta\omega_{4.9}$. SF (red), 3D (blue) and LF (green) families. XV
C.3 Distribution of the hub chord $c_{GF,H}$ values against $\Delta\omega_0$ and $\Delta\omega_{4.9}$. $c_{GF,H}$ is expressed in stator chord unit. SF (red), 3D (blue) and LF (green) families. . . . XVI
C.4 Relative stagger angle vs twist for all guide fins of the 15p RANS database. Coloured with $\Delta\beta_{1,H}$. XVII
C.5 Distribution of all optimisation parameters against $\Delta\omega_0$. SF (red), 3D (blue) and LF (green) families. XVIII
C.6 Distribution of all optimisation parameters against $\Delta\omega_{4.9}$. SF (red), 3D (blue) and LF (green) families. XVIII
C.7 Comparison of 15p and 6p guide fins of each family in the objective function space.XIX
C.8 Investigation of SF (red) and LF (green) Pareto fronts. XX
C.9 Parameter evolution along the SF (red) and LF (green) Pareto fronts. XXI
C.10 Objective functions evolution with ($\Delta\beta_{1,H}$,H_{GF}) around SF-A. XXII
C.11 Objective functions evolution with (u,H_{GF}) around SF-A. XXII
C.12 Objective functions evolution with (u,H_{GF}) around LF-A. XXIII
C.13 Representative guide fins of the SF, LF and 3D families. XXIV
C.14 Surrogate predictions near guide fins SF-03, LF-01, 3D-01. Main parameter values vs $\Delta\omega_0$. XXIV
C.15 Surrogate predictions near guide fins SF-03, LF-01, 3D-01. Main parameter values vs $\Delta\omega_{4.9}$. XXV

D.1 Axial evolution of mass averaged total pressure losses in the measurement plane. Baseline configuration vs SF, LF and 3D guide fins. RANS results. XXVII
D.2 **Experimental measurement at i=0°.** Baseline configuration vs SF, LF and 3D guide fins. XXIX
D.3 **RANS in measurement plane at i=0°.** Baseline configuration vs SF, LF and 3D guide fins. XXX

D.4 **Experimental measurement at i=3.6°**. Baseline configuration vs SF, LF and 3D guide fins. XXXI
D.5 **RANS in measurement plane at i=3.6°**. Baseline configuration vs SF, LF and 3D guide fins. XXXII
D.6 **Experimental measurement at i=4.9°**. Baseline configuration vs SF, LF and 3D guide fins. XXXIII
D.7 **RANS in measurement plane at i=4.9°**. Baseline configuration vs SF, LF and 3D guide fins. XXXIV
D.8 **Experimental measurement at i=5.4°**. Baseline configuration vs SF, LF and 3D guide fins. XXXV
D.9 **RANS in measurement plane at i=5.4°**. Baseline configuration vs SF, LF and 3D guide fins. XXXVI

List of Tables

3.1 Cascade characteristics. Uncertainties were computed by Dawkins (2021). 49

5.1 Definitions of parameters sets defining guide fins. Parameters in white are common to both sets. $\%c$ / $\%c_{GF}$: percentage of stator chord / guide fin chord. LE : Leading Edge, TE : Trailing Edge, GF : Guide Fin. H refers to the Hub aerofoil, T to the Tip aerofoil. 71
5.2 Wake refinement levels. 80
5.3 RANS simulation parameters. 82

6.1 Parameters and ranges defining the initial rectangular input space. 92
6.2 Exploration of the large input space (15p) : summary of the iterative refinements. 93
6.3 Pearson coefficients with $\Delta\omega_0$. 99
6.4 Pearson coefficients with $\Delta\omega_{4.9}$. 99
6.5 Parameter ranges and values defining the reduced optimisation problem. Only 6 parameters vary (in blue). 100
6.6 Exploration of the reduced input space (6p) : summary of the iterative refinements. The input space is enlarged from Reft. 13 (Gray rows). 101
6.7 15p vs 6p : characteristics of the RANS databases. 105
6.8 15p vs 6p : characteristics of the surrogate models. 105

7.1 Number of guide fins in each family. Absolute number and percentage of the population investigated (depth ≤ 5). 109
7.2 Pearson coefficients with $\Delta\omega_{4.9}$ for SF and 3D families. Only parameters with Pearson coefficient of absolute values greater than 0.48 on at least one objective function are considered. 113
7.3 Efficient parameter ranges of SF and 3D guide fins (15p). 114
7.4 Geometrical specificities of SF and 3D families. LE refers to Leading Edge. . . . 121
7.5 Sensitivity and optimal ranges of main parameters for SF and 3D families. In this Table, the sensitivity is a qualitative evaluation of the rise in $\Delta\omega_{4.9}$ values when leaving the optimal range. It is evaluated with the curvature of the predictions of $\Delta\omega_{4.9}$ in the optimal range, and with the RANS trends for $c_{GF,H}$. 121
7.6 Number of guide fins in each family. Absolute number and percentage of the guide fin distribution (depth ≤ 5). 122
7.7 Efficient parameter ranges of SF guide fins (6p vs 15p). 125
7.8 Performance of best SF guide fins (6p, surrogate model). 126

7.9 Efficient parameter ranges of 3D guide fins (6p vs 15p). PF : Surrogate Pareto Front. . . . 126
7.10 Performance of best 3D guide fins (15p, RANS results). . . . 127
7.11 Performance of best LF guide fins. 15p RANS results (grey) and 6p surrogate model (white). . . . 128

8.1 Gains with SF guide fin. RANS vs Experiment. Gains are measured with an uncertainty of ± 0.15%. . . . 133
8.2 Gains with LF guide fin. RANS vs Experiment. Gains are measured with an uncertainty of ± 0.15%. . . . 142
8.3 Gains with 3D guide fin. RANS vs Experiment. Gains are measured with an uncertainty of ± 0.15%. . . . 150
8.4 Gains with doubled inlet boundary layer thickness. RANS results. . . . 156
8.5 Variations in endwall losses when doubling the inlet boundary layer thickness. RANS results. . . . 156
8.6 Elementary effects reducing the corner separation. . . . 160

9.1 Comparison between academic and realistic configurations. Characteristics likely to alter the guide fin efficiency. BL : Boundary Layer. . . . 164

A.1 Order of magnitude : CFM 56, LEAP-1A. . . . I

C.1 Parameters yielding more than a 0.1% variation in $\Delta\omega_0$ across their range. . . . XXV
C.2 Parameters yielding more than a 0.1% variation in $\Delta\omega_{4.9}$ across their range. . . . XXV

Nomenclature

Flow parameters

$i = \beta - \beta_{DES}$	Incidence (°)
i_{crit}	Critical incidence (°). $i < i_{crit} \Rightarrow$ single sided topology. $i > i_{crit} \Rightarrow$ double sided topology.
Re, Re_c	Reynolds number based on the stator chord (-)
M	Mach number (-)
Tu	Turbulence rate (%)
P	Pressure (Pa)
T	Temperature (K)
ρ	Density ($kg.m^{-3}$)
δ	Boundary layer thickness (m)
δ^*	Displacement thickness (m)
θ	Momentum thickness (m)
β	Pitchwise flow angle (°)
β_{DES}	Design inflow pitchwise flow angle (°). $\beta_{DES} = 52.8°$.
β_{MID}	Surface averaged pitchwise flow angle at midspan (°)
ϕ	Spanwise flow angle (°)
$Cp_s = \frac{P_s - P_{s,\infty}}{P_{t,\infty} - P_{s,\infty}}$	Static pressure coefficient (-)
$Cp_t = \frac{P_t - P_{t,\infty}}{P_{t,\infty} - P_{s,\infty}}$	Total pressure coefficient (-)
V	Velocity magnitude ($m.s^{-1}$)
V_x	Axial velocity ($m.s^{-1}$)
$\widetilde{V_x} = \frac{V_x/V_{x,\infty}}{< V_x/V_{x,\infty} >}$	Dimensionless velocity (-). <.> : surface average on measurement plane.
$\omega = -Cp_t$	Total pressure loss coefficient (-)
ω_{0D}	Integrated losses (-). Mass averaged loss coefficient on measurement plane.
ω_{MID}	Midspan losses (-). Mass averaged loss coefficient at midspan.
$\omega_{EW} = \omega_{0D} - \omega_{MID}$	Endwall losses (-).
$\Delta\omega_0$	Endwall loss variation at i=0° when adding a guide fin compared to the baseline case.
$\Delta\omega_{4.9}$	Endwall loss variation at i=4.9° when adding a guide fin compared to the baseline case.

Design parameters

Stator

c	Stator chord (mm)

Guide fin : construction parameters

$\beta_{1,H}$	(Hub) Metal angle at LE (°).
$\beta_{2,H}$	(Hub) Metal angle at TE (°).
$x_{M,H}$	(Hub) Relative position of maximum of camber (%c_{GF}).
$t_{M,H}$	(Hub) Relative maximum thickness (%c_{GF}).
$c_{GF,H}$	(Hub) Chord (%c).
$x_{bary,H}$	(Hub) Barycenter position (engine axis) (%c).
$y_{bary,H}$	(Hub) Barycenter position (azimuthal axis) (%c).
$\beta_{1,T}$	(Tip) Metal angle at LE (°).
$\beta_{2,T}$	(Tip) Metal angle at TE (°).
$x_{M,T}$	(Tip) Relative position of maximum of camber (%c_{GF}).
$t_{M,T}$	(Tip) Relative maximum thickness (%c_{GF}).
$c_{GF,T}$	(Tip) Chord (%c).
$x_{bary,T}$	(Tip) Barycenter position (engine axis) (%c).
$y_{bary,T}$	(Tip) Barycenter position (azimuthal axis) (%c).
H_{GF}	GF height (%c)

Guide fin : optimisation parameters

$\Delta\beta_{1,H}$	(Hub) Relative metal angle at LE with respect to the local camber (°)
$\beta_{2,pc_\beta1}$	(Hub) Metal angle at TE as a percentage of the metal angle at LE (-)
$x_{M,H}$	(Hub) Relative position of maximum of camber (%c_{GF})
$t_{M,H}$	(Hub) Relative maximum thickness (%c_{GF})
$\widetilde{c_{GF}}$	(Hub) Percentage of authorised chord at hub (-)
u	(Hub) LE position on authorised surface (streamwise direction) (-)
v	(Hub) LE position on authorised surface (pitchwise direction) (-)
$\Delta\beta_{1,T}$	(Tip) Relative metal angle at LE with respect to the local camber (°)
$\Delta\beta_{2,T}$	(Tip) Relative metal angle at TE with respect to the local camber (°)
$x_{M,T}$	(Tip) Relative position of maximum of camber (%c_{GF})
$t_{M,T,rel}$	(Tip) Percentage of maximum thickness with respect to hub thickness (-)
$c_{GF,T,rel}$	(Tip) Percentage of chord with respect to hub chord (-)
λ_{sweep}	(Tip) Sweep angle (along the hub chord direction) (°)
λ_{lean}	(Tip) Lean angle (normal to the hub chord direction) (°)
H_{GF}	GF height (%c)

Guide fin : other

$y_{TE,abs}$	Guide fin TE thickness (mm). Fixed to 0.5mm.
L	Maximum value of hub aerofoil chord to fit in the authorised region (mm)
λ_{tol}	Maximum value of lean or sweep angle at the guide fin LE and TE (°). Fixed to 45°.
$c_{GF,min}$	Minimum guide fin chord value (mm). Fixed to 2.5 mm=0.2c.
$H_{min,abs}$	Minimum guide fin height value (mm). Fixed to 1 mm=0.08c.
λ_{chord}	Trapezoidal angle in the direction of the average guide fin chord (°)
$\lambda_{thickness}$	Trapezoidal angle in the direction normal to the average guide fin chord (°)
$(\Delta\gamma)_{conv}$	Guide fin stagger angle relative to the local stator camber (°)
$(\Delta\gamma)_{twist}$	Guide fin twist (°)

Subscripts

s	Static quantity
t	Total quantity
∞	Relative to far upstream or freestream value
ref	Relative to baseline characterisics
H	Relative to guide fin hub aerofoil characteristics
T	Relative to guide fin tip aerofoil characteristics

Superscripts

$*$	Optimal value

Units

$\%c$	Percentage of stator chord (-)
$\%c_{GF}$	Percentage of guide fin chord (-)

Acronyms

Configurations	
BSL	Baseline (reference case without guide fin)
SF	Short Fence family
SF-03	Guide fin representative of the Short Fence family
LF	Long Fence family
LF-A	Guide fin representative of the Long Fence family
3D	Thick and Long family
3D-01	Guide fin representative of the 3D family
Optimisation	
6p	Relative to the 6 parameter design space
15p	Relative to the 15 parameter design space
HVI	HyperVolume Indicator
EHVI	Expected HyperVolume Improvement
NSGA2	Non-dominated Sorting Genetic Algorithm 2
DOE	Design Of Experiment
PF	Pareto Front
Other	
BL	Boundary Layer
CAD	Computer-Aided Design
CGNS	CFD General Notation System
elsA	Ensemble Logiciel de Simulation en Aérodynamique
LE	Leading Edge
LES	Large Eddy Simulation
LES-LBM	Lattice Boltzmann Method
LMFA	Laboratoire de Mécanique des Fluides et Acoustique
OGV	Outlet Guide Vane
QCR	Quadratic Constitutive Relation
RANS	Reynolds-Averaged Navier Stokes
TE	Trailing Edge

Introduction

Context

First aircraft appeared in the early 20th century. At this time, pilots flew with very little knowledge about aerodynamics, and people were thrilled by their courage and agility. The race for breaking records led to improvements in terms of piloting skills, aircraft architecture, motorisation and aerodynamics. However, the greatest improvements arose from military needs. During World War I, aircraft were used for spying missions and equipped with riffles, thus leading to the first air battles. World War II contribution was more about intensive industrial production. Aircraft needed to carry large numbers of troops, loads, and fly faster than before. This led to a fast development of more powerful aircraft engines, and to the invention of turbojet. In the second half of the century, the aeronautical sector had the industrial and technical capacity to transport people, and was thus ready for the apparition and the increasing use of aircraft for commercial purposes.

Nowadays, the intense growth of the global air traffic, is evaluated at 4.5% annually for the period 2016-2035 by the Airbus's Global Market Forecast and the IATA, which corresponds to more than doubling in 20 years. This leads to dangerous environmental repercussions in terms of air pollution, fossil fuel consumption and noise nuisance, and to an ever-increasing economical competitiveness. For these reasons, industrials seek for ever more efficient and compact engines, generating the same thrust while polluting less with a lower fuel consumption. Since compressors stages account for 40% to 50% of the total engine mass, industrial research particularly focuses on how to improve their efficiency. Indeed, for a given objective, this would result in a compressor with fewer or lighter stages, leading to a mass gain directly responsible for a fuel consumption decrease (Courtiade, 2012). Such an improvement in efficiency can be achieved by limiting losses and non desired secondary flows within the compressor. In addition, compressors stages are key components in terms of operability, reliability and safety of the engine. Indeed, compressing a fluid while reducing its velocity favours flow separation. Compressor stages are then highly sensitive to inflow disturbances, including operational changes, that can trigger unsteady phenomena such as surge or rotating stall. On top of a dramatic loss increase, these might induce mechanical stresses, and vibrations likely to damage the engine.

Objectives

One of the major phenomena limiting the operability of modern aeronautical compressors is the phenomenon of corner separation. This specific separation occurs at the blade/endwall junction of a compressor row, mostly at hub, both in stators and rotors. Corner separation is commonly reduced with three-dimensional blading techniques. However, these techniques start reaching their limits, as an increasingly large aerodynamic load is required on the blades. As such, the addition of technological control effects is of major interest to de-stress the design of

blades and improve their performance. However, the technological effects investigated so far rely on a strong empirical approach (Vortex Generator) or on optimisation techniques devoid of aerodynamic rules (3D Contouring). This work focuses on a technological effect called "guide fin", which is defined here as "a profiled device of a priori non-conventional shape fixed to the hub". This large definition aims at including existing conventional technological effects as well as potentially interesting intermediate shapes. In this work, guide fin shapes are defined with elementary aerodynamic constraints, and with a limited *a priori* on the physical mechanisms they should implement. The objectives of this thesis are thus to a) establish basic design rules for passive corner separation means of control, and b) identify the physical mechanisms yielding a corner separation reduction.

Thesis outline

In order to investigate the effects of a great variety of guide fin shapes, a sophisticated optimisation methodology is undertaken in this thesis. Guide fins are defined with parametrised shapes (15 parameters) constrained with elementary aerodynamic design rules. An optimisation strategy relying on iterative refinements of Kriging surrogate models fed with RANS results is implemented. A large design space is investigated in a first step, and main parameters influencing the corner separation size are revealed. Several efficient guide fins are selected, analysed, and their effect is validated with experimental measurements.

This manuscript is organised as follows :

- Chapter 1 : A literature review on corner separation in the context of aeronautical compressors is proposed. The mechanisms at the origin of corner separation, the challenges related to its prediction and common passive means of control are presented.
- Chapter 2 : Elements on Kriging surrogate models and their use within an optimisation process are presented.
- Chapter 3 : The configuration of reference (baseline) is presented and characterised experimentally. The objective of this chapter is to provide an overview of the corner separation to be reduced with guide fins.
- Chapter 4 : The experimental methodology used to control the experimental rig and perform the measurements is detailed.
- Chapter 5 : The numerical methodology used to define guide fin shapes and predict their performance with RANS computations is presented.
- Chapter 6 : The optimisation process is performed, and its convergence analysed. Two design spaces (15 parameters and 6 parameters) are defined and investigated.
- Chapter 7 : Guide fin shapes resulting from the optimisation process are investigated. Three families of guide fins are defined according to common geometrical characteristics and common sensitivities.
- Chapter 8 : A representative guide fin of each family is tested experimentally. The potential of guide fins is proven, the relevance of RANS in the design process is validated, and specific beneficial mechanisms implemented by each guide fin are revealed.
- Chapter 9 : A summary of major findings is proposed, as well as recommendations for future work.

Chapter 1

Corner separation in aeronautical compressors

Corner separation is one of the most limiting flow features in terms of performance and operability in modern aeronautical compressors. The objective of this thesis is to assess the potential of a passive technological effect (guide fins) for reducing the detrimental effects related to corner separation.

In this first chapter, general elements on the physics of aeronautical compressors are presented (Section 1.1). The phenomenon of corner separation and its consequences are then described (Section 1.2). Corner separation modelling strategies are then discussed, and their limitations underlined (Section 1.3). Finally, the sensitivity of corner separation to inflow conditions and stator blade details is discussed, and commonly studied passive means of control are presented (Section 1.4).

1.1 Physics of compressors

This section provides background information on aeronautical compressors.

1.1.1 Turbomachinery context

Turbomachinery describes machines that transfer energy between a rotating part and a fluid. Turbines extract mechanical energy from the fluid, while compressors (and pumps, fans...) provides mechanical energy to the fluid. A gas turbine is a type of continuous flow combustion engine, generally composed of three main components : a compressor, a combustion chamber, a turbine.

Jet engines are gas turbine designed to convert chemical energy into thrust, and are spread into two main categories : turbojets, in which most of the thrust is directly generated by the impulse of exhaust gases, and turbofans, in which most of the thrust is generated by a ducted fan powered by a turbojet-like engine. In a turbofan, the flow is divided into two streams called the bypass stream and the core stream. The ratio between the two corresponding mass flow rates (bypass ratio) is a major characteristic of a turbofan. While turbojets are more frequently used for military application as they allow for supersonic flight speed, modern commercial aircraft favour turbofan engines for their high efficiency in subsonic flow. The trend is then to design turbofans with ever-increasing fan diameters, leading to higher bypass ratios lower fuel consumptions. However, this potential gain is limited by the extra mass and drag induced by the larger engine size. Industrials research consequently focuses on more compact engines, and

particularly lighter compressor stages, which account for 40% to 50% of the total mass of the engine.

A schematic view of a turbofan and its corresponding Brayton cycle are presented in Figure 1.1. Such an engine is powered by a mixture of air and kerosene which ignition in the combustion chamber releases a large amount of thermal energy. The turbine stages located downstream will convert a small amount of this energy into thrust by acceleration and ejection from the nozzle (usually 20% of the total thrust), while the remaining energy will be used to power the upstream compressor stages (required for a most effective combustion process) and the fan that provides about 80% of the total thrust.

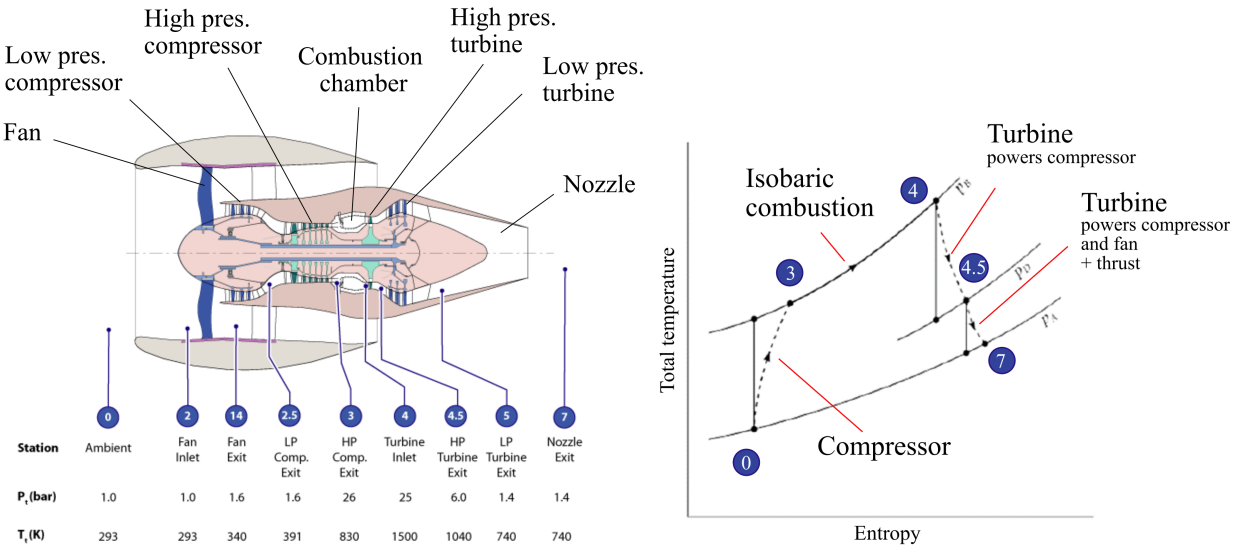

(a) From Wikipedia (2022). (b)

Figure 1.1: Typical modern turbofan architecture and specifications (left). Simplified Brayton cycle (left) for isentropic (solid lines) and real (dashed line) transformations.

1.1.2 Axial compressors performance and operating range limits

An axial compressor is usually composed of several stages defined by the association of an upstream rotor and a downstream stator. The rotor is entrained by the shaft, which is powered by the turbine, providing an enthalpy surplus to the fluid in the form of kinetic energy (dynamic pressure) and static pressure increase. The stator, or diffuser, is fixed and therefore does not provide any work to the flow. Yet, it is a crucial component as it decelerates and realign the flow, recovering the static pressure from the dynamic pressure increase induced by the rotor and providing an appropriate incidence for the following stage.

This process is usually illustrated on a two-dimensional schematic at constant radial height representing the evolution of the relative and absolute velocities across the stage, along with the entrainment and axial velocity, together forming the so-called velocity triangle. Figure 1.2a gives such an illustration, with V_x the axial component of the velocity. The deviation angles are then easily related to the enthalpy gain via the Euler equation (A.15) and Figure 1.2b illustrates how this surplus is eventually converted into static pressure. In an isentropic transformation this gain would directly correspond to a gain in total pressure, leading to p_{t2is}, but in a real transformation heat dissipation and viscous deformation lead to $p_{t2} < p_{t2is}$ even though the total enthalpy remains constant. The right part of the diagram illustrates the role of the stator, which converts kinetic energy into static pressure ($V_2 < V_3$, $p_2 > p_3$). On the other hand,

further total pressure losses, such as the ones induced by the phenomenon of corner separation, lead to $p_{t3} < p_{t2}$. Finally, this figure shows how the static pressure rises across the stage by comparing the three blue isobars. In this typical configuration, the contributions of the rotor and of the stator are roughly equal in terms of static enthalpy gain, leading to a reaction ratio of about 0.5.

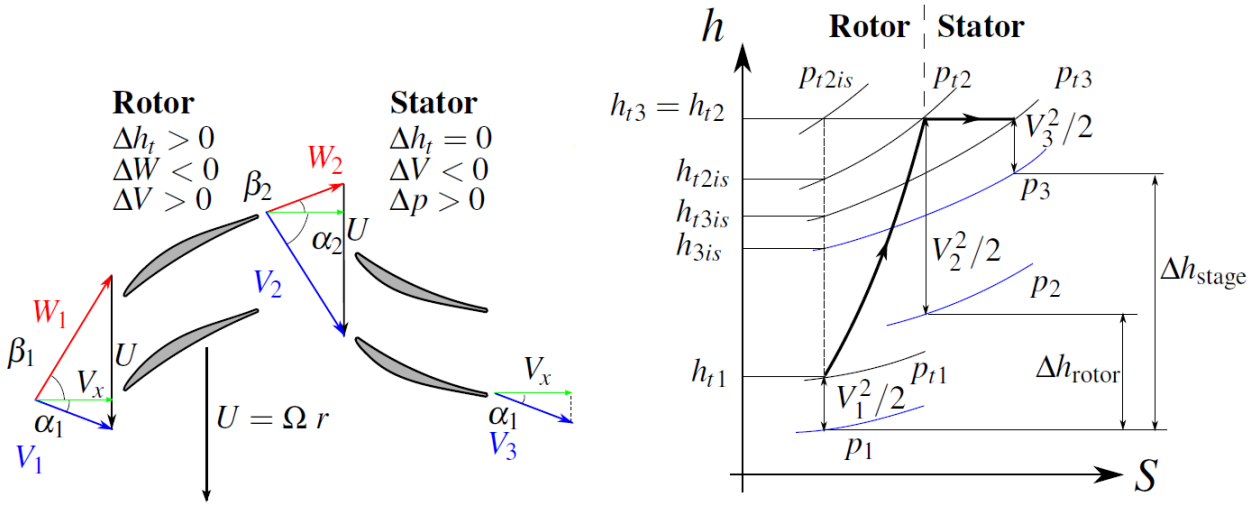

(a) Velocity triangle for an axial compressor stage

(b) Enthlapy diagram for a typical compressor stage with reaction ratio $R = \Delta h_{rotor}/\Delta h_{stage} \simeq 0.5$

Figure 1.2: Enthalpy gain and compression across an axial compressor stage. From Zambonini (2016).

The total to static pressure rise and the isentropic efficiency can then be computed :

$$\pi^{t-s}_{stage} = \frac{P_3}{P_{t1}} \tag{1.1}$$

$$\eta^{t-s}_{is,stage} = \frac{h_{3is} - h_{t1}}{h_{t3} - h_{t1}} = \frac{T_{t1}}{T_{t3} - T_{t1}} \left[(\pi^{t-s}_{stage})^{\frac{k}{k-1}} - 1 \right] \tag{1.2}$$

The main objective of a compressor is to increase the static pressure of a fluid as it flows downstream. This induces an axial adverse pressure gradient, opposed to the fluid motion, and therefore likely to trigger instabilities. The static pressure increase comes from the mechanical work provided by the rotor stages, which is conditioned by their rotating velocity. This velocity is progressively increased from the ground regime to the cruise regime. The main objective of an engine manufacturer is to ensure that no dramatic instabilities are triggered during this transient state, regardless of the inflow disturbances (vortex ingestion for instance).

For a given rotating velocity, several values of pressure gradients exist depending on the mass flow rate that passes though the compressor. The overall behaviour of a compressor is therefore quantified with a *performance characteristic* diagram (see Figure 1.3). To build such a diagram, the pressure ratio (corresponding to the axial pressure gradient) is artificially tuned with a throttled located downstream of the compressor. The stability limits of the compressor are then evaluated in terms of a maximum pressure ratio and a maximum mass flow rate before triggering instabilities, for various rotating velocities. In practice, a security margin is taken into account during the design steps to ensure avoiding these instabilities.

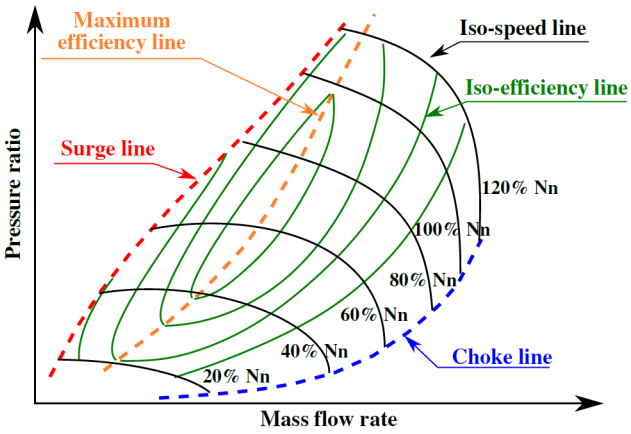

Figure 1.3: Performance characteristic map for an axial compressor. 100% Nn : rotating velocity of the cruise regime. From Zambonini (2016).

The efficiency can be added to such a diagram, and is represented by iso-efficiency lines that reveal the high efficiency regions. Ideally, a compressor should reach the desired pressure ratio, starting from 0 shaft velocity to 100% Nn (cruise regime) while following the maximum efficiency line.
The performance characteristic map is typically bounded by the surge line in the region of high pressure ratio and by the choke line in the region of low pressure ratio. Surge phenomenon corresponds to a cyclic low frequency and high amplitude axial mass flow oscillation. It causes cyclic stresses acting on the compressor, likely to drastically reduce the efficiency and to damage the compressor stages. Choke phenomenon occurs when the adverse pressure gradient is too weak, i.e. the throttle is too opened, leading to transonic flows. When the fluid is supersonic in a whole section, the induced shocks limit the mass flow rate to its maximum value. From then, the mass flow rate is insensitive to the pressure ratio value.

Corner separation is a major flow feature that can trigger surge. In order to increase the operability margins and avoid detrimental instabilities, the phenomenon of corner separation must be understood and controlled. Corner separation constitutes one of the main field of research in terms of aeronautical compressors aerodynamics.

1.2 Physics of corner separation

At the junction between blades and hub or casing, boundary layers developing on each solid body interact, leading to the accumulation of low momentum fluid likely to generate losses and trigger flow separation. This separation is called corner separation. In this section, a short introduction to boundary layer separation is first presented (Section 1.2.1). The flow mechanisms at the origin of the corner separation are then described (Section 1.2.2). A useful mathematical approach to analyse corner separation organisation is then presented (Section 1.2.3), followed by a description of the detrimental effects caused by corner separation in a stator row of aeronautical compressor (Section 1.2.4).

1.2.1 Elements on boundary layer separation

The notion of boundary layer constitutes a major field of research in fluid mechanics. Only basics of boundary layer separation are presented here. A thorough introduction to boundary

layers can be found in (Schlichting and Kestin, 1961) or (Lachmann, 1961) for instance, and a review focused on turbulent boundary layer separation is proposed by Simpson (1989).

A viscous flow features a no-slip condition at its boundary with a solid body, which induces a velocity gradient called the boundary layer (see Figure 1.4). In a context of two-dimensional boundary layers (no evolution in the directions normal to the freestream), boundary layers are characterised with the following characteristic lengths :

- Boundary layer thickness δ : distance to the solid boundary allowing to retrieve a similar velocity as in the freestream. A common criterion consists in defining δ such that 99% of the freestream velocity is retrieved.

- Boundary layer displacement thickness δ^* : distance by which the surface must be translated parallel to itself in an inviscid flow to retrieve the same mass flow. Quantifies the aerodynamic blockage induced by deceleration within the boundary layer.

- Boundary layer momentum thickness θ : distance by which the surface must be translated parallel to itself in an inviscid flow to retrieve the same momentum.

The presence of boundary layers induces an aerodynamic blockage, quantified with δ^*, and frictional losses, quantified with the wall shear stress τ_w :

$$\tau_w = \mu \frac{\partial u(x,y)}{\partial y}|_{y=0} \tag{1.3}$$

In some cases, the wall shear stress might vanish and become negative. The flow is thus ejected in the direction normal to the solid surface : this phenomenon is called *boundary layer separation* (see Figure 1.5a). Boundary layer separation notably occurs in the presence of adverse pressure gradients, which might induce a reverse flow near the solid surface. In the context of fully immersed bodies, boundary layer separation necessarily occurs downstream of the body, inducing a low momentum region convected downstream called the *wake*.

In realistic conditions boundary layers cannot be considered two-dimensional. Indeed, solid bodies are generally not planar (see Figure 1.5b), neither isolated. In particular, at the junction between two solid surfaces the two boundary layers developing on each surface necessarily interact, resulting in a three-dimensional boundary layer. In this specific case, the separation of such a three-dimensional boundary layer is called a *corner separation*. A dedicated mathematical apparatus is required to study three-dimensional separation, and is further developed in Section 1.2.3.

Flow around isolated junctions often feature corner separations, as reviewed by Gand et al. (2010). The wing/fuselage junction of an aircraft is an example of realistic junction flow that features a corner separation (Tinoco, 2006). However, this phenomenon is particularly amplified by the presence of neighbouring stator blades in the context of aeronautical compressor rows, as explained in next section.

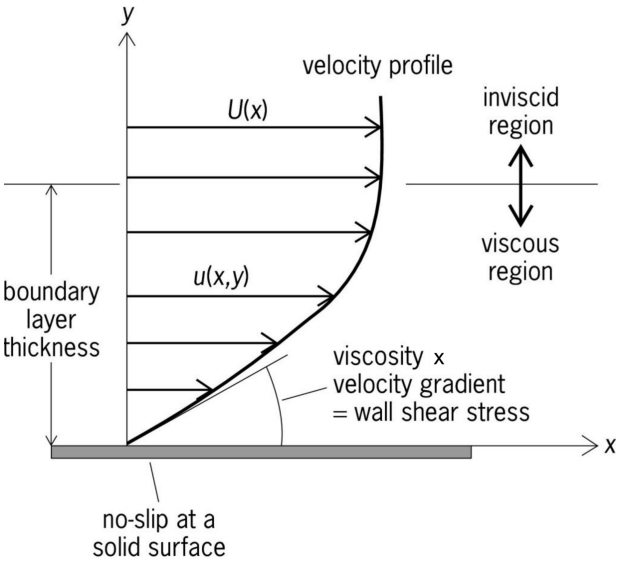

Figure 1.4: Schematic of a boundary layer, from Encyclopedia2 (2022).

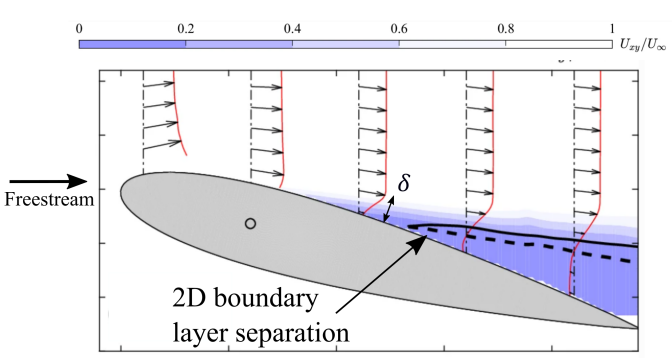

(a) Two-dimensional separation (Schematic).

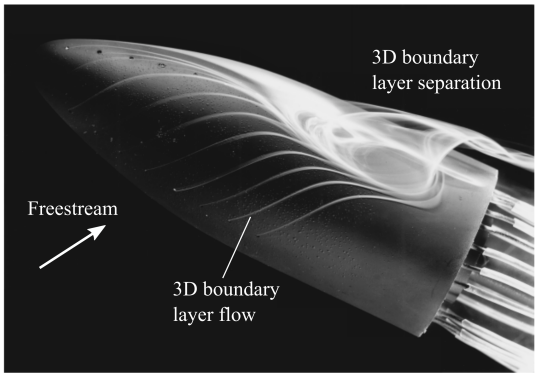

(b) Three-dimensional separation (Experiment). Adapted from Délery (2001).

Figure 1.5: Illustration of boundary layer separations.

1.2.2 Cause of corner separation in axial compressors

In a row of axial compressor, several blades are embedded on the hub, casing or both. The presence of these solid boundaries induces three-dimensional flows that amplify corner separation. These three-dimensional flows are called *secondary flows*, and are defined as any flow with a different orientation than the midspan flow. Horlock and Lakshminarayana (1973) offer a review on secondary flows in turbomachinery, and Kang and Hirsch (1991) a description of secondary flows in a compressor cascade composed of shrouded stators (both embedded at hub and shroud). In the context of shrouded stators, a famous secondary flow is the horseshoe vortex, that forms upstream of the stator leading edge near the endwall and splits into two legs. However, the strength of the horseshoe vortex largely depends on the blade leading edge thickness (bluntness factor) (Gand et al., 2010),(Bordji, 2015). In typical compressor stators, the leading edge is sharp and the horseshoe vortex does not play a significant role in corner separation, while it constitutes a major source of losses in the context of turbines (Langston, 2001).

In shrouded compressor stators, the main secondary flow participating to corner separation is the *passage flow*, also called cross flow. It consists in a transverse flow (in the blade to blade direction) induced by the pressure difference between the pressure side of one blade and the suction side of the neighbouring blade. A particle of fluid travelling through the blade passage will be deflected by this transverse pressure gradient, so that its local radius of curvature R in the blade to blade view respects the following equilibrium equation :

$$\frac{V^2}{R} = \frac{1}{\rho}\frac{\partial p}{\partial n} \tag{1.4}$$

With V the velocity magnitude, ρ the fluid density and $\frac{\partial p}{\partial n}$ the transverse pressure gradient. $\frac{\partial p}{\partial n}$ is entirely defined by the blade design, and is almost constant in the spanwise direction as isobars are almost straight in this direction*. With this assumption, comparing a particle FS (Freestream) and a particle BL (Boundary Layer), equation 1.4 yields $\frac{V_{FS}^2}{R_{FS}} = \frac{V_{BL}^2}{R_{BL}}$ with $V_{BL}^2 < V_{FS}^2$, yielding $R_{BL} < R_{FS}$ (see Figure 1.6). As such, fluid particles within the boundary layer are over deflected towards the suction side of the blade, generating the so-called passage flow.

The main consequence of this passage flow is that it drives low momentum fluid contained in the endwall boundary layer towards the suction side, as illustrated in Figure 1.7a. This induces an accumulation of low momentum fluid region in the junction region as described by Kang and Hirsch (1991), which interacts with the boundary layer developing on the stator suction side, thus increasing the phenomenon of corner separation (see Figure 1.7b). This mechanism is now acknowledged, and was notably evidenced numerically and experimentally in a subsonic annular compressor by Hah and Loellbach (1999). Let us underline that this phenomenon also occurs in rotor rows. However, this thesis focuses on corner separation occurring in stator rows.

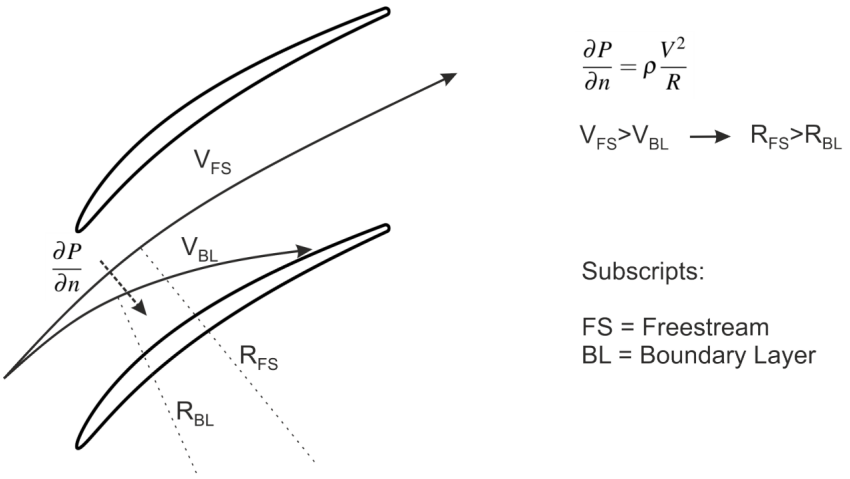

Figure 1.6: Overturning of the endwall boundary layer in the presence of the cross-passage transverse pressure gradient. From Dawkins (2021).

*An example of isobar contours in a modern stator row can be seen in (Taylor and Miller, 2017).

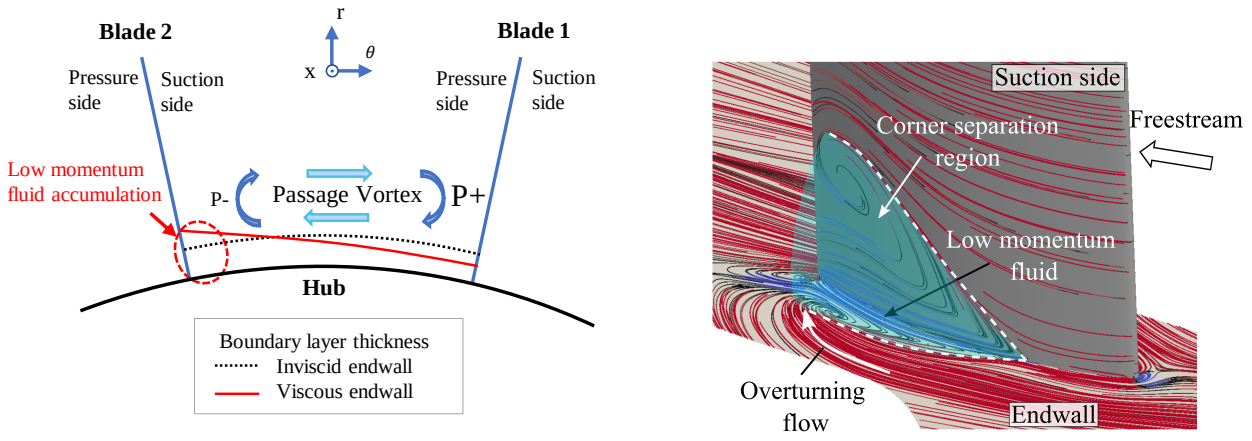

(a) Accumulation of low momentum fluid induced by passage flow.

(b) Interaction of overturned endwall boundary layer with suction surface boundary layer. Red : positive axial velocity. Blue : reversal flow. Black : axial velocity equals to 0.

Figure 1.7: Effect of passage flow on corner separation.

By mass flow conservation in the blade to blade direction, the passage flow also induces a transverse flow in the opposite direction, thus creating the so-called *passage vortex* (see Figure 1.7a). An approach relying on vorticity convection is proposed by Dixon (1998) to describe the development of the passage vortex. In this approach, the inlet boundary layer vorticity in the transverse direction is related to the outlet passage vortex vorticity in the streamwise direction with the following equations :

$$\begin{cases} \omega_1 &= dV_x/dz \\ \omega_2 &= -2\theta_{12}\ \omega_1 \end{cases} \qquad \rightarrow \omega_2 = -2\theta_{12}\frac{dV_x}{dz} \tag{1.5}$$

with dV_x/dz the inlet velocity gradient in the direction normal to the endwall (inlet flow considered entirely axial) and θ_{12} the deflection imposed by the stator.

As such, it becomes evident that three main characteristics influence the strength of the passage flow : the aerodynamic load (that acts on $\frac{\partial p}{\partial n}$), the inlet boundary layer thickness (low momentum introduced in the channel), and the stator deflection.

1.2.3 Topological description of corner separation

Limiting streamlines The corner separation is an intrinsically three-dimensional phenomenon, and can not be studied with the mathematical apparatus developed for two-dimensional separations. The major difference between these two approaches lies in the friction vector. In two-dimensional cases, it can be reduced to a scalar that indicates a separation when becoming nil, while in three-dimensional cases, transverse flow is allowed and induces a transverse component of the friction vector. Separation is then no longer detected by a scalar threshold but by the study of the whole skin-friction field. It is usually investigated with skin friction lines, defined as lines to which the friction vector is tangent. Mathematically, this is equivalent to the following differential system:

$$\frac{dy}{dx} = \frac{\tau_{wy}}{\tau_{wx}} \tag{1.6}$$

with $\tau_{wx}(x,y)$ and $\tau_{wy}(x,y)$ the components of the skin friction vector τ_w, and dx, dy the spatial representation of the skin friction lines. In the same manner, we recall the mathematical definition of streamlines, the set of lines to which the fluid velocity vector is tangent

$$\frac{dx}{u} = \frac{dy}{v} = \frac{dz}{w} \tag{1.7}$$

with u, v and w the components of the fluid velocity. Streamlines infinitely close to the surface tend to skin friction lines, and are called surface or limiting streamlines. They verify the following equation (Gbadebo et al., 2005):

$$\frac{dy}{dx} = \lim_{h\to 0}\frac{v}{u} = \frac{\partial v/\partial z}{\partial u/\partial z} = \frac{\tau_{wy}}{\tau_{wx}}|_{h=0} \tag{1.8}$$

with h the distance to the solid body. As stated by Délery (2001), limiting streamlines are not physical objects and remain a fictitious concept, as the velocity at the wall is strictly zero due to viscosity. However, it is a useful concept that allows to link three-dimensional flow patterns to two-dimensional friction patterns.

Critical points Positions where the skin friction components are both nil denotes an attachment or a detachment of the flow onto the surface, and are called *critical points*. These critical points can be classified depending on the behaviour of the surrounding limiting streamlines. Délery (2001) presented a mathematical classification of critical points, introducing the Jacobian matrix J, the quantities p=-(trace of J) and q = (determinant of J) and its eigenvalues (Equations 1.9 and 1.10).

$$\tau_w = \begin{cases} \tau_{wx}(x,y) \\ \tau_{wy}(x,y) \end{cases} \qquad J = \begin{bmatrix} \frac{\partial \tau_{wx}}{\partial x} & \frac{\partial \tau_{wx}}{\partial y} \\ \frac{\partial \tau_{wy}}{\partial x} & \frac{\partial \tau_{wy}}{\partial y} \end{bmatrix} \tag{1.9}$$

$$S_{1,2} = \frac{-p \pm \sqrt{p^2 - 4q}}{2} \tag{1.10}$$

Any critical point can then be positioned in the [p-q] plane of Figure 1.8, where each sketch represents the skin friction lines in the vicinity of the critical point. It was shown by Tobak and Peake (1982) that all critical points on the axes $q = 0$ and $p = 0$ or on the parabola $q = \frac{p^2}{4}$ are unstable in the sense that slight modifications of the flow will result in their disappearance or evolution. As defined by Gbadebo et al. (2005), stable critical points are :

- **Saddle point S** : a point through which two critical lines pass, each acting as barriers in the field of limiting streamlines, making one set of streamlines inaccessible to the adjacent set. The critical line along which limiting streamlines converge (resp. diverge) is called a separation line (resp. attachment line).
- **Node N** : a point common to an infinite number of limiting streamlines. It can be seen as a separation (resp. attachment) point if all the limiting streamlines converge to it (resp. diverge from it).
- **Focus F** : a point around which an infinite number of limiting streamlines spiral, which can denote a vortex lifting off the surface. A Focus spiralling inward (resp. outwards) denotes a separation point (resp. attachment point).

These three critical points are represented in Figure 1.8.

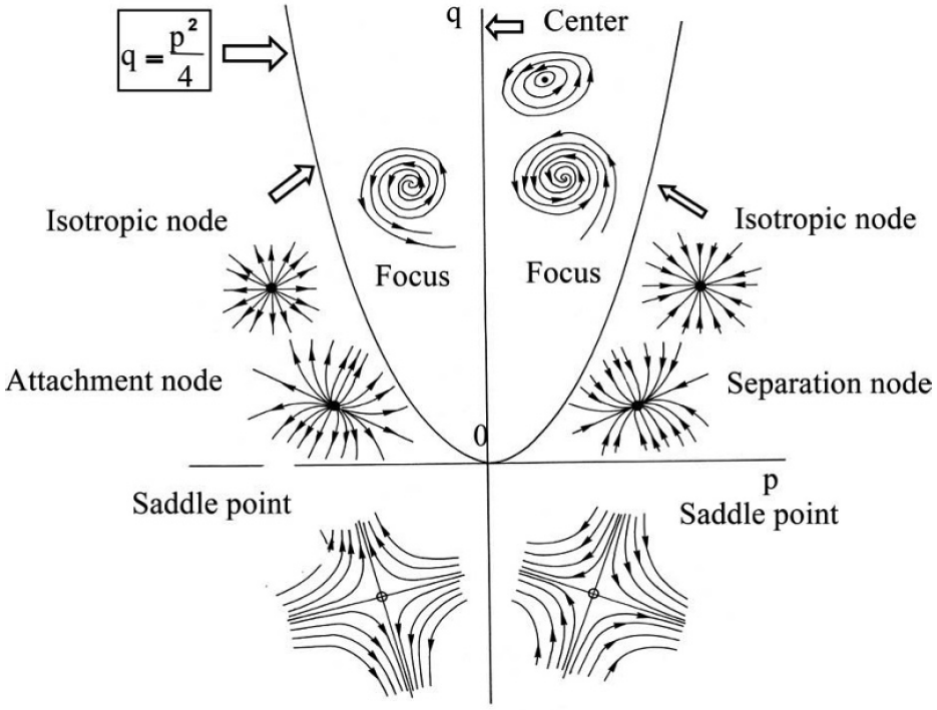

Figure 1.8: Classification of critical points and surrounding skin friction field in the eigen vector plane [p-q], from Délery (2013)

From 2D skin friction field and 3D flow feature The three elementary critical points (Node, Focus, Saddle) are related to three-dimensional flow structure near the surface. As illustrated in Figure 1.9a, a Node corresponds to a separation or attachment point where streamlines are ejected or absorbed onto the surface. As illustrated in Figure 1.9b, a Focus corresponds to a vortical structure around a separation (or attachment) three-dimensional streamline.

A saddle point is characterised with the presence of two separation lines, along which fluid is ejected or attached onto the surface. This is illustrated in Figure 1.10 by considering the stream tube passing through the rectangular sections highlighted with arrows. By mass conservation, the surface of this stream tube is constant. The tightening of the limiting streamlines (or surface streamlines) about the separation lines induces a decrease in the rectangular section width w, which induces an increase in its height h. This requires the streamlines above the limiting streamlines to move further away from (respectively get closer to) the surface, meaning that the fluid is ejected from (respectively absorbed onto) the surface.

Index rule Flegg (1974) provides an *index rule* that links the number of Nodes and Foci with the number of Saddles depending on the surface topology. This index rule can be expressed as

$$\sum (Nodes + Foci) - \sum (Saddles) \quad = \quad 2 - 2g \tag{1.11}$$

where the genus g is a scalar topological property the surface. Munkres (2014) offers a thorough mathematical introduction to the notion of genus, and provides a simple definition : g corresponds to the maximum number of cutting along a surface without disconnecting it. Duquesne et al. (2022) provides a methodology to compute the genus in realistic turbomachinery configurations. For instance, the genus of a shrouded annular stator row with N_b blades is N_b.

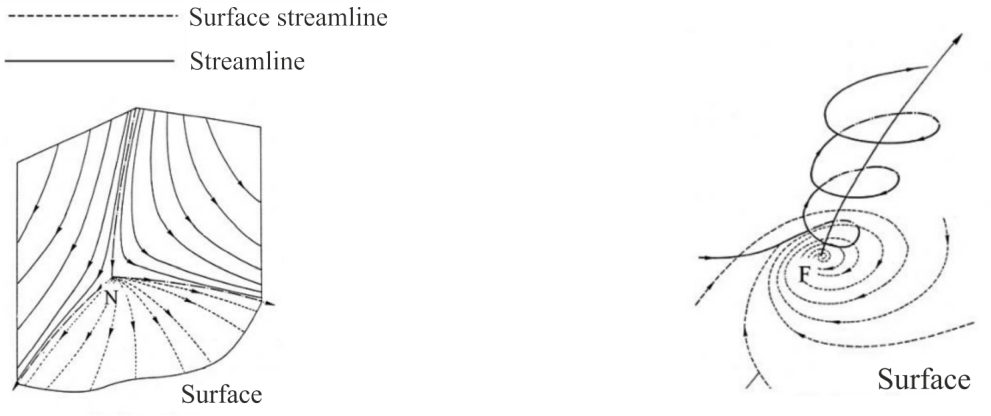

(a) Node (b) Focus

Figure 1.9: Three-dimensional flow in the vicinity of a Node or a Focus. From Délery (2013).

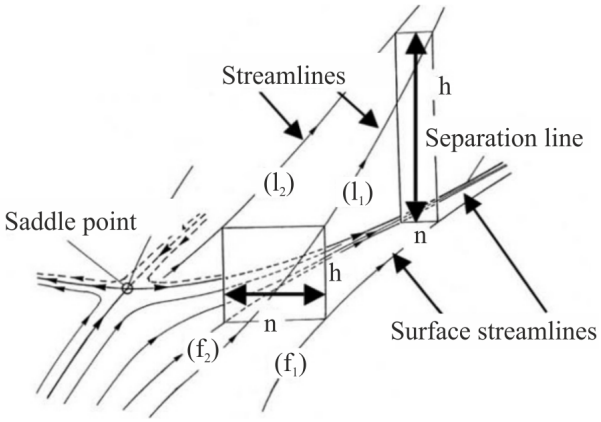

Figure 1.10: Three-dimensional flow in the vicinity of a Saddle point. Adapted from Délery (2013).

Gbadebo et al. (2005) validated this topological rule experimentally and numerically on two configurations of compressor cascades equipped with NACA65 profile blades with no tip gap. The authors use both the number of critical points and the thickness of the separated region to quantify the complexity of the flow. They show that both increase with the incidence (see Figure 1.11) and that the flow always verify the index rule.

The index rule provides a major result : in a given configuration, critical points can only appear by Node/Saddle or Focus/Saddle pairs. This result is of particular interest in the context of corner separation as it enables to distinguish two principal corner separation topologies.

Topology of corner separation The precise description of the corner separation topology is an intricate problem. This three-dimensional separation is unsteady in essence and sensitive to small scale disturbances, thus requiring *a priori* the use of high fidelity CFD methods or detailed experimental measurements. Dawkins et al. (2021) set up a precise experimental set up which enables to reveal the instantaneous and averaged topological organisation in a compressor cascade using PIV (Particle Image Velocimetry) techniques. The instantaneous organisation (Figure 1.12a) reveals numerous critical points, organised in pairs consistently with the index rule. Figure 1.12b reveals that the average topological organisation is much simpler, and can

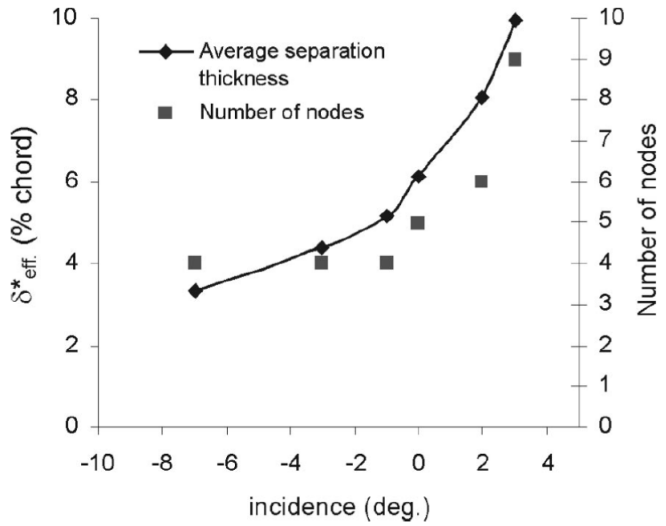

Figure 1.11: Evolution of the number of nodes and of the boundary layer thickness when increasing the flow incidence. From (Gbadebo et al., 2005).

be summarised either with no critical points or with a single Focus/Saddle pair.

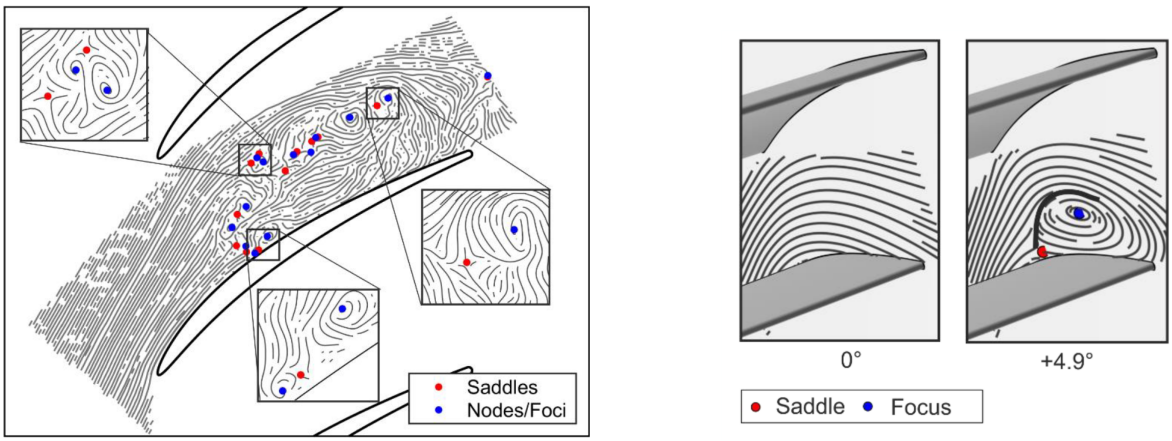

(a) Instantaneous topology organisation. i=4.9°.

(b) Average topological organisation.

Figure 1.12: Experimental investigation of the corner separation in a compressor cascade. PIV (experimental) measurements near the endwall (i : inflow incidence). From (Dawkins et al., 2021).

Numerical studies on the corner separation topology most often rely on RANS, which enables numerous investigations of the average corner separation topology. Notably, Lei et al. (2008) performed numerous computations on various configurations and show that RANS only predicts two topological organisations. This finding is notably confirmed by Taylor and Miller (2017), who proposed to qualify these separations as *single sided* and *double sided*. Figure 1.13 illustrates these two organisations. The single sided topology features a single separation line on the stator suction side, which does not necessarily induce reversal flows. The double sided topology is characterised with the appearance of a second separating line on the hub, associated to the appearance of a pair a critical point (Saddle located near the junction, Focus located in the channel). It is interesting to notice that the Saddle/Focus pair appearance is detected experimentally by Dawkins et al. (2021) when the inflow incidence is raised.

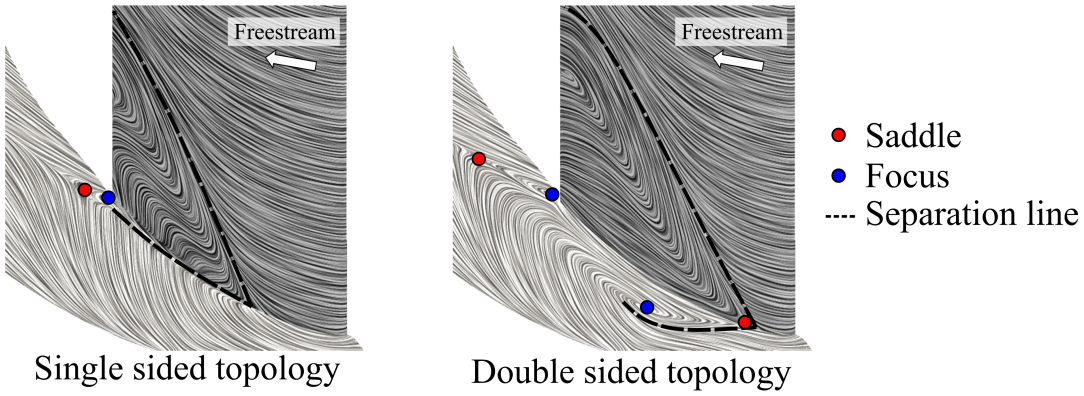

Figure 1.13: Illustration of the single sided and double sided topology (RANS).

1.2.4 Impact of corner separation in axial compressors

Losses In a stator with no hub clearance, 3 types of losses are at stake : frictional losses due to viscous stresses on solid surfaces, wake losses due to the mixing of the wake downstream of the blade and three-dimensional losses, mainly composed of secondary flow losses and corner separation losses. Figure 1.14a illustrates three regions where these losses appear with a two-dimensional cartography of total pressure losses downstream of a compressor cascade (Zambonini, 2016). In this cartography, it is evident that three-dimensional losses account for a large part of the total losses. In the configuration studied by Dawkins et al. (2021), the midspan losses (two-dimensional wake) represent about 2.1% of the inlet dynamic pressure. With inviscid endwalls, the total integrated losses would be of that value. In reality, at design incidence the integrated losses are about 3%, and at high incidence about 5%, thus revealing a major contribution of the endwall losses to the integrated losses. In both configurations used by Zambonini (2016) and Dawkins et al. (2021), the compressor cascades are designed with a large span/pitch ratio to uncouple the corner separations occurring on both tips of the blades. However, high pressure compressors usually feature a low value of the span/pitch ratio, and the relative importance of endwall losses is even larger in these cases.

Blockage Corner separation induces a large region of low momentum that must be bypassed by the freestream as illustrated in Figure 1.14b. This blockage induces spanwise flows that result in an acceleration of the fluid in the midspan region, as well as a circumferential deviation that might alter the flow incidence seen by the downstream stage. The blockage B induced by the corner separation is theoretically quantified with the displacement thickness δ^* as

$$B = 1 - \frac{\text{effective flow area}}{\text{geometric flow area}} = 1 - \frac{(A - \sum \delta^*)}{A} \tag{1.12}$$

$$\delta^* = \int \left(1 - \frac{\rho u}{\rho_\infty V_\infty}\right) dy \tag{1.13}$$

where ρ_∞ and V_∞ are respectively the freestream density and velocity upstream of the blade. However, it is difficult to define freestream conditions in the context of turbomachinery (Cumpsty, 1989). Gbadebo et al. (2008) then offered to link the blockage coefficient with the ideal static pressure rise coefficient across the blade row, defined as

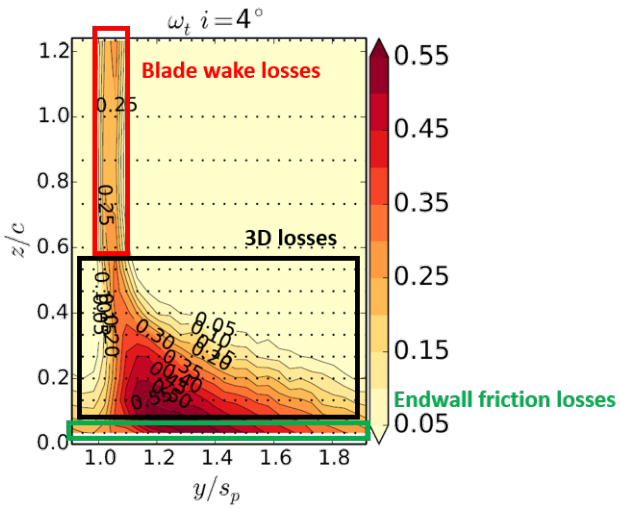

(a) Cartography of total pressure losses downstream of the NACA65 compressor cascade. Adapted from Zambonini (2016).

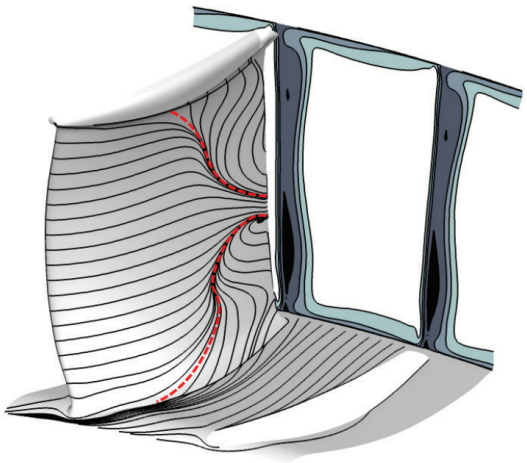

(b) Streamline contraction due to corner separation in a shrouded stator representative of a modern high pressure compressor stator. From Auchoybur and Miller (2018).

Figure 1.14: Losses and blockage induced by corner separation.

$$C_{p,rise} = \frac{P_2 - P_1}{\frac{1}{2}\rho V_1^2} = 1 - \left(\frac{V_2}{V_1}\right)^2 \tag{1.14}$$

where V_1 and V_2 are the midspan velocity upstream and downstream of the blade row respectively. In this definition, V_2 can be replaced by the velocity averaged in both the pitchwise and spanwise directions ($\overline{V_2}$) to get an averaged exit static pressure rise. The effective flow area is then defined as the section of a fictitious inviscid tube with a uniform velocity distribution equals to $\overline{V_2}$. In that case, mass conservation yields $A_{2e} = A_1 V_1 / \overline{V_2}$. Using Equation (1.14), the blockage is therefore given by

$$B = 1 - \frac{A_{2e}}{A_2} \tag{1.15}$$

$$= 1 - \frac{A_1}{A_2}(1 - C_{p,rise})^{-1/2} \tag{1.16}$$

$$= 1 - \frac{\cos\ \alpha_1}{\cos\ \alpha_2}(1 - C_{p,rise})^{-1/2} \tag{1.17}$$

where α_1 and α_2 are the nominal inlet and exit flow angles at the midspan and $C_{p,rise}$ the averaged exit static pressure rise coefficient. As such, Equation 1.17 shows that an increase in blockage leads to a reduction in the static pressure rise in the blade row.

Effect on operability The blockage induced by the corner separation was reported as a cause of pre-stall rotating disturbances by McDougall et al. (1990) for instance. Conversely, modifications of the stator design in order to reduce the corner separation blockage were found to successfully delay rotating instabilities in studies such as (Taylor, 2019) and (Beselt et al., 2013). In the latter, the corner separation blockage was found to deviate the flow from one passage to the adjacent, causing a hub separation upstream of the leading edge and its propagation in the circumferential direction.

The phenomenon of corner separation therefore induces deleterious effects in terms of performance and operability of the compressor. These effects are particularly detrimental when operating at off-design conditions, and the accurate prediction of corner separation constitutes a major challenge for designing modern compressors.

1.3 Prediction of corner separation

Corner separation prediction is an active challenge for designing a compressor. In this section, empirical criteria built to anticipate corner separation in early design steps are presented. They appear not sufficient to fully anticipate stall phenomena, and high fidelity numerical methods are required to provide a more precise description of the corner separation impact. The advantages and limitations of conventional CFD methods are described in a second part.

1.3.1 Corner separation prediction with criteria

The stator blade of a compressor can be seen as a diffuser that decelerates the flow, and separation is likely to arise if the velocity drops too rapidly. Several criteria were developed to anticipate corner stall (corner separation inducing blade failure) based on this idea for blade design purposes.

De Haller criterion The simplest criterion to predict stall on a compressor blade row relies on a one-dimensional evaluation of the diffusion occurring across the blade row, based on the inlet and outlet velocity magnitude. This criterion is not specific to corner separation, and accounts for all phenomena yielding complete aerodynamic failure of the blade. Experimentally, De Haller (1953) established that the outlet velocity should not be less than 0.72 times the inlet velocity, which is

$$DH = \frac{V_2}{V_1} < 0.72 \Rightarrow \text{separation} \tag{1.18}$$

Lieblein diffusion factor Lieblein et al. (1953) offered another empirical one-dimensional criterion, more precise than the De Haller criterion although still not specific to corner separation. This criterion takes into account the maximum flow velocity across the blade passage, which is related to the the flow deviation ΔV_θ and blade solidity σ. The general expression is given by Equation 1.19. This equation is composed of two main contributions : the overall change in velocity magnitude $\frac{V_2}{V_1}$, and a term proportional to the lift coefficient of the section based on the inlet velocity $C_L = \frac{2\Delta V_\theta}{\sigma V_1} \frac{cos\ \alpha_1}{cos\ (\alpha_1+\alpha_2)/2}$. In the case of an incompressible fluid with constant axial velocity, it can be reduced to Equation 1.20.

$$\begin{aligned} DF &= 1 - \frac{V_2}{V_1} + \frac{\Delta V_\theta}{2\sigma} && (1.19)\\ &= 1 - \frac{\cos\ \alpha_1}{\cos\ \alpha_2} + \frac{\cos\ \alpha_1}{2\sigma}(\tan\ \alpha_1 - \tan\ \alpha_2) && (1.20) \end{aligned}$$

Stall may generally occur for value of DF greater than 0.6, and a typical design is 0.45. However, this formulation is only valid near the design operating point. Lieblein extended this criterion to off-design operating conditions with the *equivalent diffusion factor* :

$$DF_{eq} = \frac{\cos\ \alpha_2}{\alpha_1}\left[1.12 + a(i - i^*)^{1.43} + 0.61\frac{\cos^2\alpha_1}{\sigma}(\tan\ \alpha_1 - \tan\ \alpha_2)\right] \tag{1.21}$$

where i^* is the optimal incidence generating the minimum of losses and a is a constant coefficient ($a = 0.117$ for the NACA65(A_{10}) blade family). The new critical value not to exceed is $DF_{eq} = 2$.

The De Haller and Lieblein criteria are widely used in early design steps. However, they rely on a too simplistic global approach to provide precise information on how to reduce the corner separation size. The next criteria were developed recently and are based on RANS evaluations.

Lei criterion In their work, Lei et al. (2008) provide two major results : a) among hundreds of RANS computations, only two corner separation topologies are found, the double sided topology (of open type in their work) and the single sided topology (of closed type in their work) b) based on these computations a diffusion factor is proposed to anticipate the apparition of the double sided topology (yielding large losses and blockage). Their study relies on the definition of two criteria. The stall indicator (S) is a measure of blade loading near the endwall relative to midspan. It is defined in Equation 1.25 and illustrated in Figure 1.15a. The diffusion factor D is based on blade geometrical parameters, but effectively corresponds to a measure of the inflow incidence (see Equation 1.26).

Dimensional analysis shows that the stall indicator depends *a priori* on many flow parameters. However, numerous computations are performed, and show that the stall indicator has little or no appreciable sensitivity to the Reynolds number, the Mach number, the inlet boundary layer thickness and the blade aspect ratio. Actually, it appears to only depends on the diffusion factor D, which features three distinct regimes as shown on Figure 1.15b. For diffusion factor values lower than 0.35, only single sided separations are found. For values greater than 0.45, only double sided separations are found. For values between 0.35 and 0.45, both separation types coexist. The critical value of $D_{crit} = 0.4 \pm 0.05$ is therefore retained, and Lei criterion can be summarised as

$$D > 0.45 \quad \Rightarrow \quad \text{stall} \tag{1.22}$$

$$0.35 < D < 0.45 \quad \Rightarrow \quad \text{possible stall} \tag{1.23}$$

$$D < 0.35 \quad \Rightarrow \quad \text{corner separation without stall} \tag{1.24}$$

Remark : The criteria are formally defined as :

$$S = \left[\int_0^1 \frac{p_{ps}(x) - p_{ss}(x)}{p_{t_1} - p_{s_1}}\left(\frac{dx}{c_a}\right)\right]_{z/c=0.5AR} - \left[\int_0^1 \frac{p_{ps}(x) - p_{ss}(x)}{p_{t_1} - p_{s_1}}\left(\frac{dx}{c_a}\right)\right]_{z/c=0.1AR} \tag{1.25}$$

$$D = \frac{s}{c}\left\{1 - \left[\frac{\cos(i + \gamma + \theta/2)}{\cos(\gamma - \theta/2)}\right]^2\right\}(i + \theta + \Delta\beta) \tag{1.26}$$

where c_a is the blade axial chord length, p_{ps} and p_{ss} are the static pressures on the pressure and suction side respectively, p_{t1} is the upstream total pressure, p_{s1} the upstream static pressure and AR the span/chord aspect ratio. The angles i and β denote the flow incidence and the azimuthal angle respectively, and γ and θ are linked to the blade geometry and illustrated on Figure 1.15a.

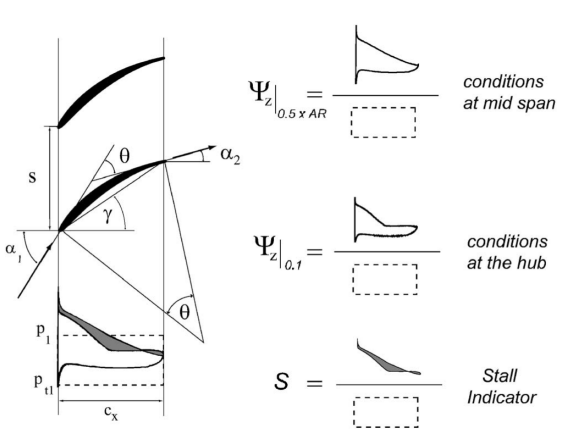

(a) Illustration of stall indicator and geometrical parameters

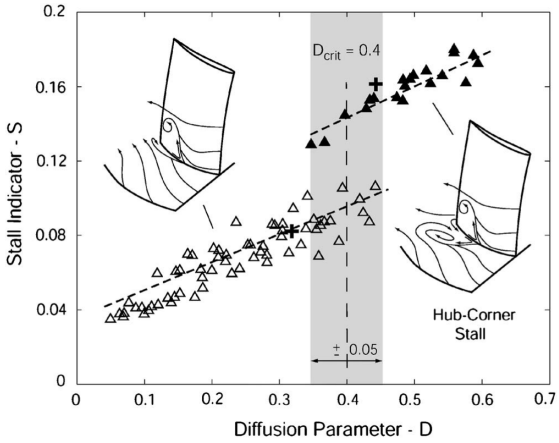

(b) Correlation between diffusion factor and stall indicator. Overlapping region centred on critical value

Figure 1.15: Lei criterion. From (Lei et al., 2008).

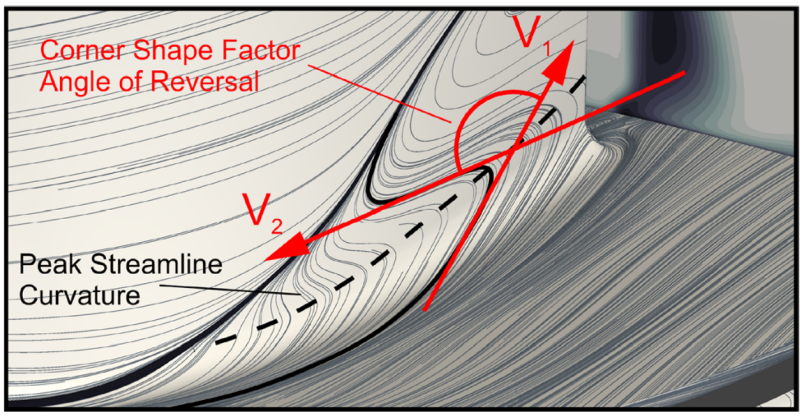

Figure 1.16: Definition of the corner shape factor. From Taylor and Miller (2017).

Corner shape factor Taylor and Miller (2017) studied the impact of 3D blade designs on the size and the topological type of the corner separation. They deduced from these investigations a criterion called the *corner shape factor* matching their observations, based on the skin friction field.
The corner shape factor is defined as the angle between the forward facing flow vector V_1 and the reversed flow vector V_2 as illustrated in Figure 1.16. It therefore varies between 0 and π. As the angle tends toward π, the local streamline surface curvature tends toward infinity and the topology changes with the apparition of a Saddle/Focus pair. Thus, this criterion has no meaning for an established double sided separation : it is used to measure the proximity of a single sided separation to its switch towards a double sided topology. Taylor and Miller (2017) used this criterion as a stability criterion to compare and rank several blade designs with various lean angles.

These two last criteria rely on higher fidelity methods than the first ones, and are based on a measure of the corner separation size. More specifically, their limit values are set by the phenomenon of topological switch (from the single to double sided topology). However, the topological switch is yet an unclear process, and its prediction constitutes a real challenge for modern RANS methodologies as detailed in next section.

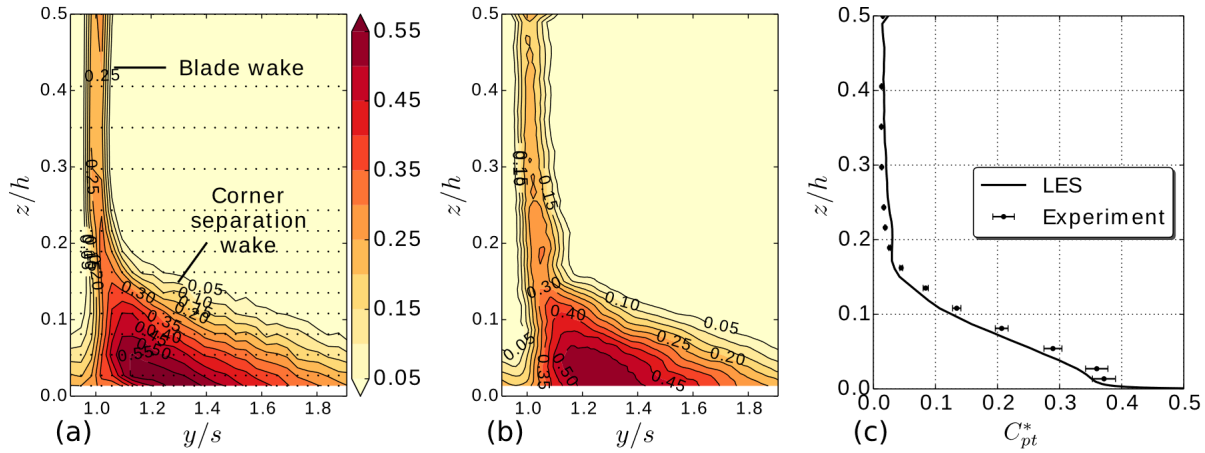

Figure 1.17: Total pressure losses measured downstream of the NACA65 compressor cascade. Full cartography : Experimental (a) vs Wall resolved LES (b). Pitchwise mass-averaged total pressure loss coefficient (c). From Gao et al. (2015).

1.3.2 Corner separation prediction with CFD methods

Large Eddy Simulation methods High fidelity methods such as LES (Large Eddy Simulation) are too costly to be used during design iterations of a realistic compressor configuration. Most high fidelity studies are performed on academical cases to get a deeper understanding of the physical phenomena, and are still too expensive in most cases to enable parametric studies. The capability of LES to predict corner separation is illustrated on a compressor cascade equipped with NACA-65009 blades set up at the LMFA. The characteristics of this cascade are summarised in (Zambonini et al., 2017) and thoroughly described in (Zambonini, 2016).

Gao et al. (2015) performed a conventional Navier-Stokes LES computation (wall-resolved) of that configuration, which is found to successfully retrieve the experimental measurements in a high incidence configuration (large corner separation). Boundary layer profiles were compared, as well as time-averaged total pressure losses downstream of the cascade. The latter are shown in Figure 1.17. This resolved approach therefore enables detailed and reliable investigations, but requires large computational resources (Mesh size : about 200×10^6 grid points. CPU hours : about 2×10^6).

In a recent work, Boudet et al. (2022) successfully retrieved both the experimental results and Navier-Stokes LES results with a LES-LBM (Lattice Boltzmann Method) approach (see Figure 1.18), for a much more affordable numerical cost. Their computations relied on an incompressible Lattice Boltzmann approach with a wall law, over a shorter time, yielding a decrease in computational time of a factor 300. However this speed up is over-estimated as the modelling hypotheses are stronger. Still, Boudet et al. (2022) estimate a very interesting net speed up factor of 5 (with comparable numerical conditions) compared to the LES approach proposed by Gao et al. (2015). As such, in this context LES-LBM methods appear as a promising numerical approach for investigating the sensitivity of corner separation through parametric studies. However, LES-LBM methods are mostly restrained to incompressible flows, and still constitute an active field of research.

RANS modelling RANS modelling features an affordable cost that enables design optimisations. However, and as previously stated, RANS computations can only predict two distinct corner separation topologies. Taylor and Miller (2017), Dawkins et al. (2021), Ma et al. (2019) observed a sudden switch from the single to the double sided topology when the incidence is

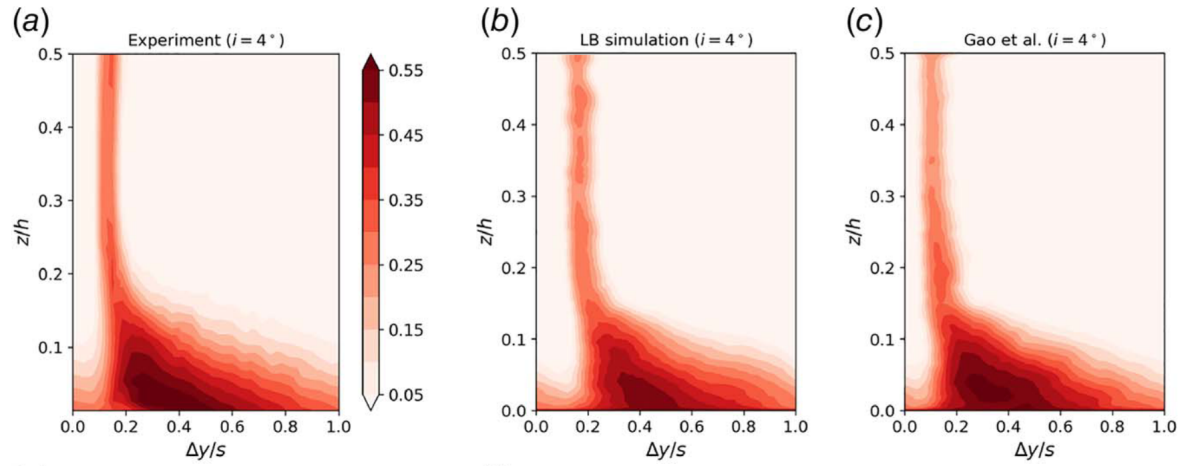

Figure 1.18: Total pressure losses measured downstream of the NACA65 compressor cascade. Full cartography : Experimental (a) vs LES-LBM wall modelled (b) vs Navier-Stokes wall resolved LES (c). From Boudet et al. (2022).

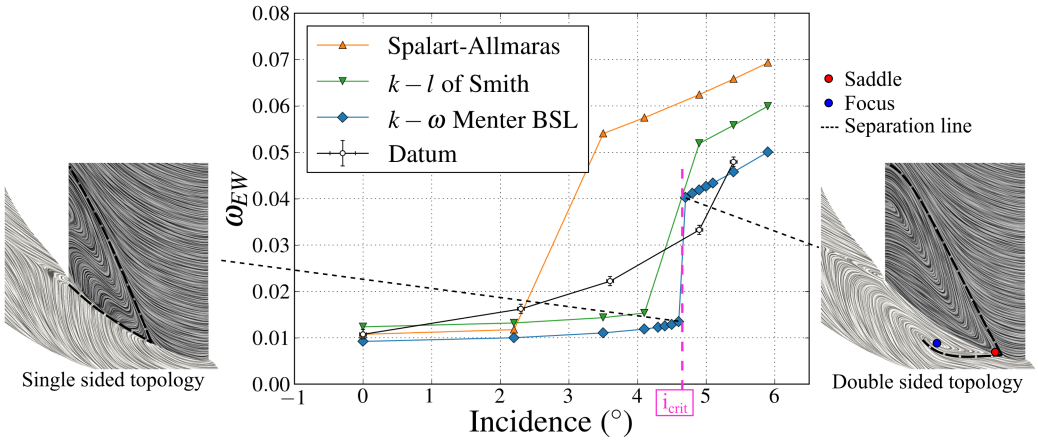

Figure 1.19: Evolution of integrated total pressure losses downstream of the compressor cascade studied in this work. Experimental results (Datum) vs RANS predictions with three commonly used turbulence models.

raised above a so-called *critical incidence*, thus inducing a sudden increase in the losses and blockage. Dawkins et al. (2021) show that this sudden switch is not retrieved experimentally and originates from a pure numerical defect of RANS methods. This is confirmed by the author of this thesis on the same configuration, even when using different turbulence models (see Figure 1.19).

The work of Gao et al. (2017) focuses on the effect of the numerical environment on the prediction of corner separation at a high incidence (i=4°) in the NACA65 compressor cascade. Even though this is not explicitly mentioned in their work, the extension and shape of the corner separation predicted with their RANS methodology is typical from a double sided corner separation. In their work, several turbulence models are evaluated ($k-\omega$ Wilcox, $k-\omega$ Kok, Spalart-Almaras and DRSM) together with several spatial schemes (1st-order upwind, 2nd-order upwind, 3rd-order Roe/MUSCL/AUSM/SLAU, 4-pt Jameson centre) and different turbulent kinetic energy inflow conditions. Even though slight differences are observed between these set up, the shape and extension of the corner separation remains over predicted and typical of a double sided separation. By comparison with LES results, Gao et al. (2017) then

concluded that the misprediction of RANS was probably due to the turbulence modelling itself. This statement is understandable, as the Reynolds stress tensor is considered isotropic when using the Boussinesq hypothesis (Boussinesq, 1877) while it is proven to be highly anisotropic in the corner region (Gessner, 1973), (Monier, 2018). Several corrections were proposed to better take into account this anisotropy, and notably the Quadrative Constitutive Relation (QCR) proposed by Spalart (2000). The effect of the QCR correction was notably assessed by Monier et al. (2018). The QCR correction is also evaluated in this work (see Section 5.3.4) and successfully improves the prediction of loss gradients in double sided separations, but does not manage to prevent the topological switch artefact.

Still, RANS is found to correctly predict the corner separation at design operating conditions, as in the work of Dawkins et al. (2021) and Hergt et al. (2013) for instance. Moreover, Gbadebo et al. (2005) underlines that RANS computations lead to skin friction fields consistent with the physics at stake, which allows a reliable topological interpretation of the flow. In addition, Auchoybur and Miller (2018) present an interesting work in which corner separation is remarkably well predicted with RANS at off-design condition (stator representative of modern high pressure compressor, single sided topology). From a design perspective, Gbadebo et al. (2008) and Gao et al. (2017) notice that the extent of the corner separation is overestimated, highlighting that RANS should be conservative in design. Moreover, it is intuitively understandable that reducing the corner separation size should increase the RANS predictability, as anisotropic regions would be of lesser importance. Beside such limitations, RANS remains the most suitable computational method in turbomachinery because of its low computational cost. It is widely used to design corner separation control devices as in the work of Sun et al. (2021) and (Hergt et al., 2009), and to investigate blade design impact on corner separation, as in the work of Beselt et al. (2014) or Taylor and Miller (2017) for instance.

In the context of this thesis, RANS constitutes an interesting compromise between numerical cost and fidelity. Because of the reasons mentioned above, a RANS-based methodology should be able to provide reasonable trends for designing a control device such as the guide fins. Indeed, efficient guide fins would yield a smaller and therefore better predicted corner separation.

1.4 Control of corner separation

Corner separation control strategies can be gathered into two main families, the passive and active strategies. A thorough review on corner separation control techniques is given by Lin et al. (1990), and Figure 1.20 gives an overview of the most studied control strategies. This literature review only focuses on passive control.

In the context of corner separation control, it is crucial to understand the main parameters to which corner separation is sensitive. The sensitivity to inflow conditions is therefore first described (Section 1.4.1), followed by the sensitivity to some blade details (Section 1.4.2). Control strategies relative to blade design are then presented (Section 1.4.3). Finally, control strategies relying on technological effects are described (Section 1.4.4).

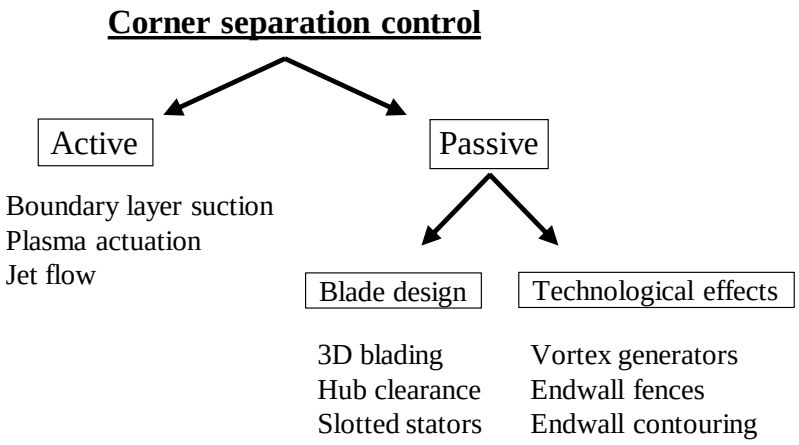

Figure 1.20: Overview of existing corner separation control strategies.

1.4.1 Sensitivity to inflow conditions

The corner separation is mainly affected by two inflow parameters : the inflow incidence and the inlet boundary layer developing on the endwall.

Inflow incidence Many studies assessed the influence of the incidence on the corner separation, notably (Joslyn and Dring, 1985) or Gbadebo et al. (2005), with the conclusion that the corner separation size increases when the incidence is raised. Indeed, increasing the incidence (or the aerodynamic loading) results in an increased adverse pressure gradient along the stator chord, which notably decelerates the flow near the endwalls. Moreover, increasing the incidence increases the transverse pressure gradient, and therefore the strength of the passage flow. Consequently, more low momentum flow will be driven from the hub boundary layer towards the stator suction side, thus increasing the size of the corner separation.

Inlet boundary layer The inlet boundary layer developing on the endwall contains low momentum fluid, that will be driven towards the stator suction side under the effect of the passage flow. As such, increasing the inlet boundary layer thickness enhances the corner separation phenomenon and its related losses (Gbadebo, 2003). A recent illustration of this effect is proposed by Boudet et al. (2022), who compare two boundary layer thicknesses with LES-LBM high fidelity computations of the NACA65 compressor cascade (see Figure 1.21). They indeed retrieve that reducing the boundary layer thickness reduces the corner separation. In their work, an academic inlet boundary layer profile is generated upstream of the cascade from a uniform flow imposed far upstream of the cascade. A recent study proposed by Auchoybur and Miller (2018) presents the main characteristics of a realistic boundary layer profile seen by a stator in a multi-stage high pressure compressor. They propose to consider three regions at different positions of the span. From midspan to the hub, these regions are : the freestream region (where the mass flow is uniform), the low momentum endwall region (regions of low velocity due to the cumulative effect of secondary flows in upstream stages) and the endwall boundary layer (region of energised and skewed flow due to the rotation of the platform of the upstream rotor). They investigate the sensitivity of the corner separation to each region by replacing them iteratively with uniform flow conditions. Figure 1.22 summarises these effects.

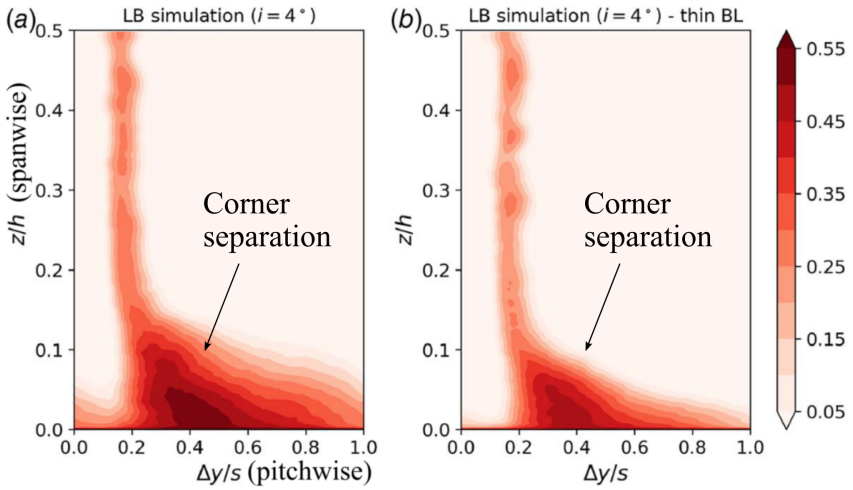

Figure 1.21: Effect of boundary layer thickness on total pressure losses downstream of the NACA65 compressor cascade (Boudet et al., 2022): (a) with the reference inlet boundary layer, (b) with a 3 to 5 times thinner inlet boundary layer. LES-LBM results.

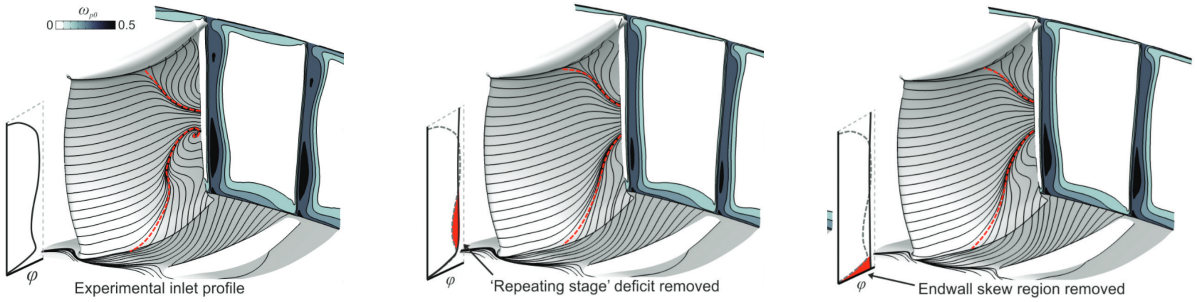

(a) (b) (c)

Figure 1.22: Effect of inlet boundary layer profile details on corner separation (Auchoybur and Miller, 2018).

In Figure 1.22a, the full experimental profile is used, resulting in a large corner separation. In Figure 1.22b, the low momentum endwall region is replaced with a uniform portion equivalent to the freestream. The corner separation appears to be significantly reduced. Finally, in Figure 1.22c the endwall boundary layer is replaced with a non-skewed portion, of characteristic equivalent to the freestream. Little difference is observed with Figure 1.22b, indicating that corner separation is less sensitive to the endwall boundary layer.

Other inflow characteristics Gao et al. (2017) offers a bibliographic review on the impact of inflow conditions on corner separation. It results from this review that the inlet Reynolds number has little impact on the corner separation losses. The inlet turbulence rate might have a significant impact in cases where recirculation bubble exists on the stator suction side. Indeed, a large value of the turbulence rate might remove this bubble, thus reducing the corner separation losses. The effect of Mach number is also discussed. In cases where the Mach number is sufficiently large, shock waves might appear and trigger the corner separation near the stator leading edge, thus yielding an important increase in the endwall losses (Weber et al., 2002), (Bailie et al., 2008). Finally, the effect of an incoming wake from an upstream rotor is studied by Schulz et al. (1990). Such a wake induces periodic increase in the local turbulent rate seen

by the stator boundary layer, thus periodically suppressing the laminar recirculation bubble that was observed in their configuration. This results in a significant decrease in the endwall losses.

1.4.2 Sensitivity to blade details

Slight changes in the blade details might play a major role in the development of corner separation. The three following blade details are commented in this section : the stator leading edge shape, the blade and endwall roughness, the presence of fillet.

The effect of the Leading Edge (LE) shape plays a major role if a laminar portion exists on the upstream part of the blade. In their work, Goodhand and Miller (2012) evaluated this effect in a low-speed, single stage, large-scale model of an embedded high-pressure compressor stage. They compared the endwall losses generated when using an elliptical LE (laminar portion from LE to peak suction on the suction side) and when a circular LE is used (transition triggered from the LE). Their results show that removing the laminar portion greatly increases the endwall losses.

In the same study, Goodhand and Miller (2012) also evaluated the effect of roughness on the LE region (see Figure 1.23a). They compared a roughness equivalent to a new blade (hence low) and equivalent to the one encountered in real engines after 4000 engine cycles (hence much larger). Adding this roughness increases the losses, both in the elliptical and circular LE cases. In the elliptical case, this is explained by the fact that the greater roughness triggers a premature transition, yielding a loss increase consistent with the conclusion drawn when comparing elliptical and circular LEs. When using the circular case, the increase in endwall losses is lower, but still observable, and is attributed to the additional thickening of the turbulent boundary layer induced by the greater roughness. Auchoybur and Miller (2018) assessed the impact of roughness on a modern stator configuration, supposedly robust to that parameter. Interestingly, the corner separation features a binary behaviour depending on the roughness value. Below a critical roughness, no sensitivity of the corner separation to the roughness is observed while a complete aerodynamic failure is observed passed this value. In their work, the effect of the endwall roughness is also investigated. The hub corner separation appears particularly insensitive to the hub roughness, even up to large roughness values.

Goodhand and Miller (2012) also evaluated the impact of the presence of fillets at the blade/endwall junction. Their results show that when a fillet is added, the spanwise extension of the corner separation is simply shifted radially by a length corresponding to the fillet height. This mechanism induces negligible additional losses. However, they found that removing completely the fillet increases the losses, regardless of the shape of the LE used (circular or elliptical). As such, adding a fillet to the blade/endwall junction reduces the endwall losses.

Figure 1.23b summarises and help ranking these effects. Surface roughness, responsible for a premature transition and a faster thickening of the induced turbulent boundary layer, is shown to have the greatest impact on losses. The second effect is about the circular leading edge, also responsible for a premature transition. The other effects deal with different types of fillets tested, and are of secondary importance.

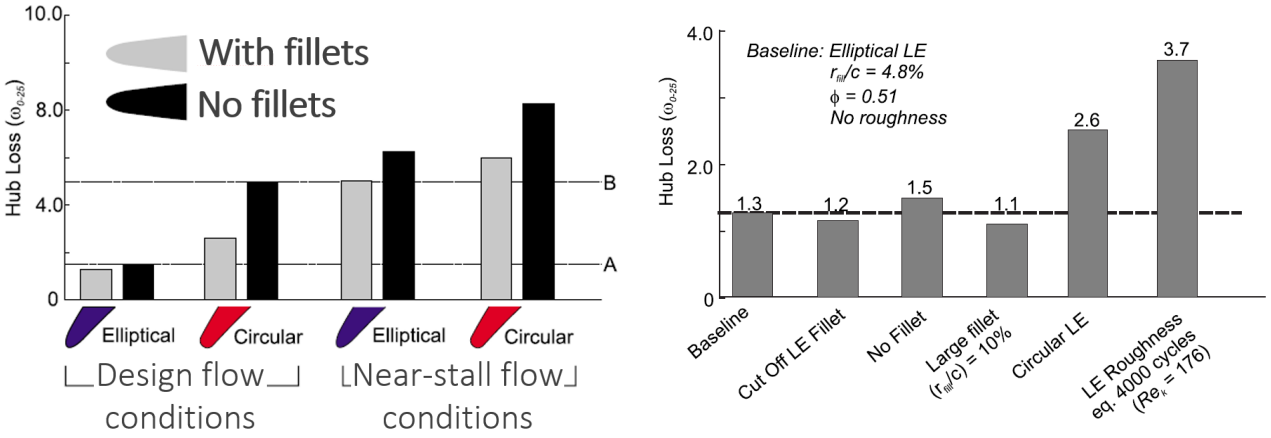

(a) Sensitivity of losses to the LE shape and suction surface roughness.

(b) Summary and ranking of endwall effects

Figure 1.23: Effect of small geometry changes on hub losses (Goodhand and Miller, 2012).

1.4.3 Control with blade design

A first step to reduce the detrimental effects of corner separation consists in adapting the blade design. Three-dimensional blading is systematically used in modern compressors. In addition, stator design can be modified with the addition of a hub clearance or slots, which implement a flow from the pressure side to the suction side.

Three-dimensional blading design Three-dimensional blading is a vast topic of research, and a thorough review of this field is proposed by Bolger (1999) and Steinhardt (2003). Gallimore et al. (2002) offers a synthetic review of three-dimensional blading characteristics. Two main characteristics are briefly discussed : the sweep and lean aspects, and the leading edge re-cambering.

The effects of sweep and lean correspond to a displacement of a given aerofoil along the chord line (sweep) or in a direction normal to the chord line (lean) (see Figure 1.24a). The effect of a forward sweep is to bring high momentum flow in the endwall region, thus energising the endwall boundary layer. This tends to lower the extent of the corner separation. The lean is typically set such that an obtuse angle is obtained between the endwall and the aerofoil suction surface. Such a lean tends to impose a radial migration of the low momentum fluid located in the corner region towards midspan, thus reducing the phenomenon of corner separation. Taylor and Miller (2017) investigated this effect on corner separation. Several three-dimensional blades with increasing lean angles were designed while keeping the same loading distribution along the span. The increase in lean induces an increase in spanwise pressure gradients (see Figure 1.25a), thus imposing a radial migration of the flow towards midspan. Using the corner shape factor (see Section 1.3.1), they show that increasing the lean value has a beneficial effect on the proximity to forming an open corner separation, hence on its stability range. However, higher lean values induce additional losses at design and off-design incidences (see Figure 1.25b).

As illustrated in Figure 1.6 (Section 1.2.2) the passage flow causes an overturning of the endwall boundary layer. This overturning induces an increase in the incidence value seen by the downstream blade. The camber line of the endwall aerofoil of the downstream blade should anticipate this larger incidence, resulting in blades whose aerofoils are generally more cambered near the endwalls (see Figure 1.24b). This change in camber is called leading edge re-cambering. It strongly interacts with the intermediate aerofoils of the same blade, thus requiring numerous

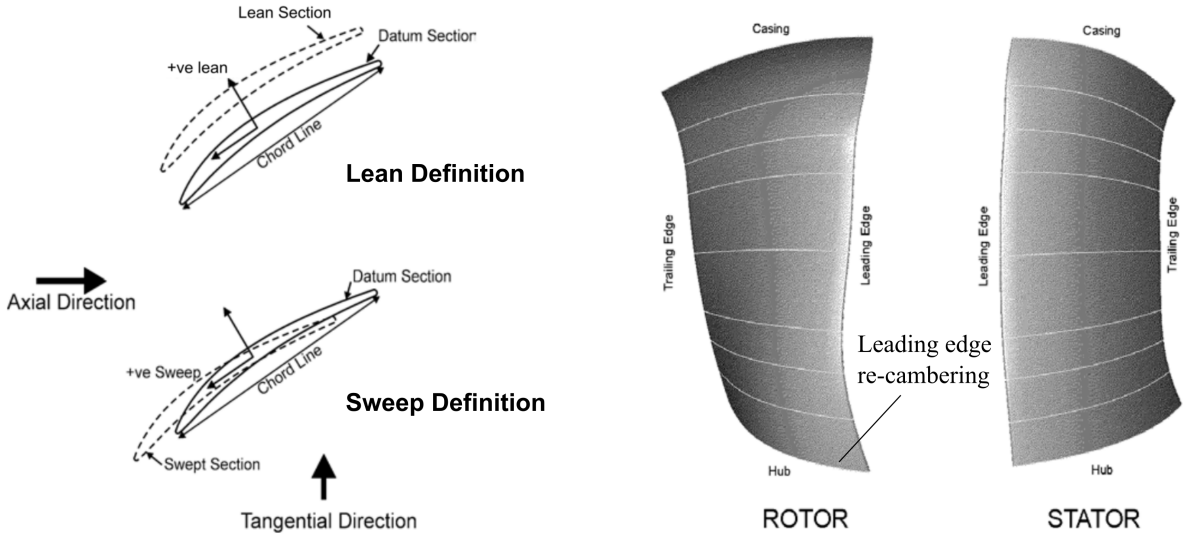

(a) Definition of lean and sweep.

(b) Front view onto suction surface of a three-dimensional stage.

Figure 1.24: Illustration of three-dimensional blading (Gallimore et al., 2002).

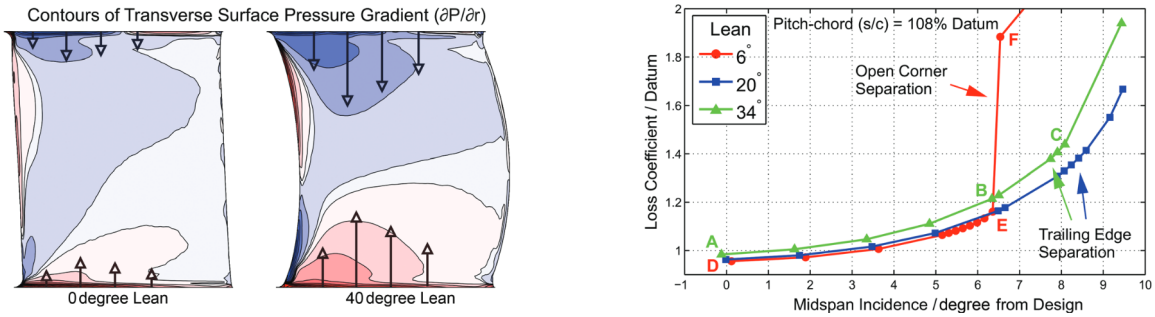

(a) Effect of lean on spanwise surface pressure gradient.

(b) Integrated losses downstream the blade row. Evolution with the incidence for different lean angles.

Figure 1.25: Effect of lean angle on pressure surface and downstream losses (Taylor and Miller, 2017).

design iterations.

Hub clearance In stator configurations with hub clearance, the pressure difference between the suction side and pressure side of the blades induces a flow through this clearance, inducing a new secondary flow called the hub clearance vortex (similar to the tip leakage vortex occurring in rotor configurations). The clearance flow brings high momentum fluid through the gap, and might have beneficial effects regarding the corner separation as it can re-energise the boundary layer, increase the flow turning and lower the local diffusion factor.

Lakshminarayana and Horlock (1967) showed that an optimal clearance value exists but depends on the operating point, and can yield larger losses at off-design conditions. As a consequence, the hub clearance gap should be adapted to the operating point, as stated in the experimental study on a NASA low speed compressor (Barankiewicz and Hathaway, 1998), which is difficult to implement in practice. Partially sealed hub have also been studied in this work, but also exhibits a lack of robustness. Finally, Beselt et al. (2014) presents a detailed experimental, numerical and topological investigation at different operating points of an annular compressor cascade with hub clearance. They evidence a complex interaction between

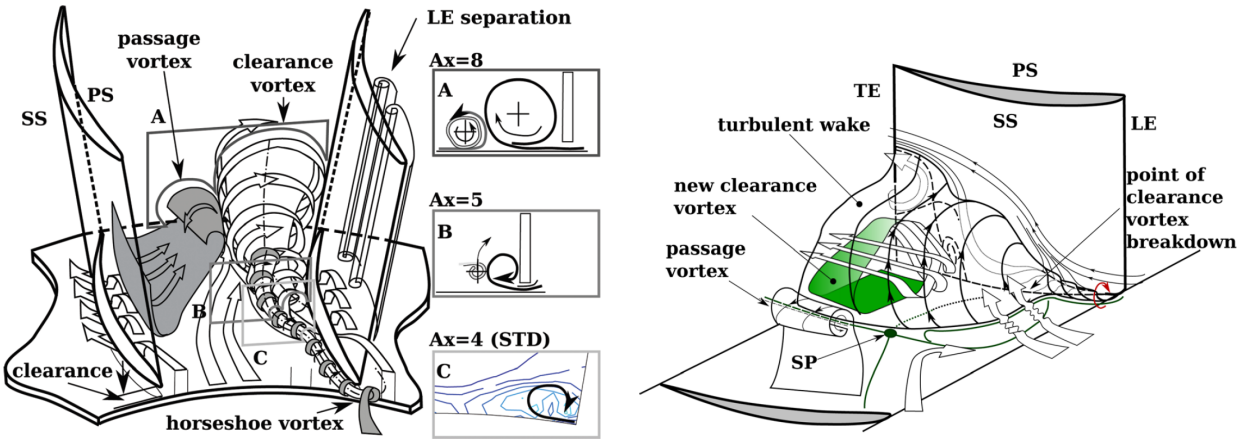

(a) Clearance Vortex. Incidence i=0°

(b) Clearance vortex breakdown and induced separation. Incidence i=9.8°

Figure 1.26: Schematic illustrations of secondary flows interaction in the presence of hub clearance. From Beselt et al. (2014)

the clearance, horseshoe and passage vortices (see Figure 1.26a) at different operating points. Moreover, the hub clearance vortex appears to break down above an incidence of 7.9° in their configuration, causing the flow to separate and to block the passage (see Figure 1.26b).

Slotted stators Other clearance flow with slots of more sophisticated shapes are also investigated in the literature. Notably, Sun et al. (2021) present an experimental validation of the beneficial impact of an optimised slot geometry in a compressor cascade (see Figure 1.27). Relative gains of 5.6% to 23% are measured on a large range of incidence ($i \in [2°, 7°]$).

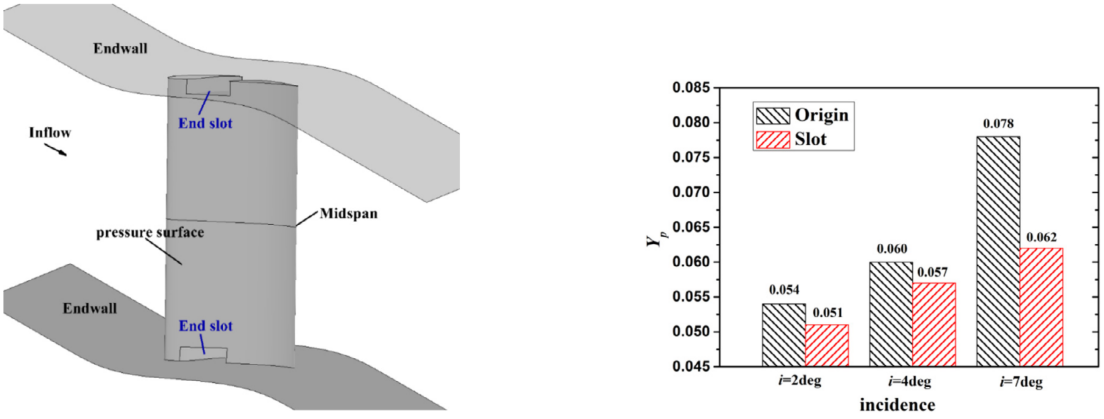

(a) Slot geometry

(b) Total pressure losses downstream of the cascade : reference vs slotted configuration (Experiment).

Figure 1.27: Illustration of a slotted configuration (Sun et al., 2021).

1.4.4 Control with technological effects

In some configurations, corner separation limits the operability of the stator row even after conventional re-blading. The design of stator blades is therefore dedicated to sustain off-design conditions, which in turns results in poor performance at design operating points. This is typically the case when using large lean angles (see Figure 1.4.3). Several technological

effects were studied in the literature to reduce the corner separation size. This section offers an overview of the most studied passive technological effects for reducing corner separation : Vortex generators, Endwall fences and Endwall contouring.

Vortex generator Vortex generators (VG) are small aerodynamic devices fixed on a surface, generally designed to produce a tip vortex similar to the one generated at the tip of a wing (see Figure 1.28). The main objectives of such a vortex are to mix two regions of the flow (boundary layer energisation) and to induce a flow deflection. Vortex generators can be used to reduce separation, but can produce a measurable increase of drag at cruise. The fundamental principles of vortex generators were thoroughly described by Pearcey (1961). Vortex generators are usually thin devices that are used in groups, as in the top right configuration in Figure 1.28b. The choice of their shape, dimensions, number, relative distance, stagger angle etc ... is largely empirical. Recommendations from Pearcey (1961) and Chima (2002) are commonly used :

- Shape : in a context of vortex generators for heat transfer improvement, Liou et al. (2000) studied 12 different shapes of vortex generators. The most commonly used are triangular, or rectangular. Figure 1.28b presents more complex shapes.

- Camber and thickness : vortex generators are mainly made of flat plates or created at edges of plow-like shapes. Chima (2002) is a rare work that uses profiled vortex generators (inspired from a NACA 64-006 aerofoil).

- Stagger angle : a common value is $\pm 20°$ relative to the engine axis. Zheng et al. (2015) studied vortex generators with stagger angles from $+20°$ to -15°.

- Rotation direction : most vortex generators are used to organise co-rotating vortices, as in Chima (2002). An example of counter-rotating vortex generators (grouped in pairs with alternating stagger angles) is studied in Godard and Stanislas (2006).

- Solidity and arrangement : as vortex generators are usually made of simple geometries, their effects on the flow mainly depends on their aspect ratios h/l (h : height ; l : length) and on the distance between two adjacent vortex generator (d). A common practice consists in taking $d \in [4h, 8h]$ and a solidity $l/d = 1$.

- Height : h is commonly set with respect to the boundary layer thickness value (δ) depending on the objective of the vortex generator. Chima (2002) shows that the effect of mixing and deflection are increased when h is raised, together with additional losses caused by the device. In their work, vortex generators of $h \in [0.5\delta, 1.3\delta]$ were tested.

Vortex generators are commonly used in the airframe aerodynamics of aircraft since the late 1950's (Meyer et al., 2003). In the context of aeronautical compressor, they can be used to induce a rotor pre-swirl, as part-span splitters, or for secondary flow control (Chima, 2002). Increasingly complex arrangements were tested at the German Aerospace Center (DLR) for reducing the corner separation in a compressor cascade (all at a Mach number of about 0.67), and their main results are summarised hereafter :

- (Meyer et al., 2003) : a single rectangular vortex generator is fixed on the suction side of the blades. A significant reduction of the separated zone is observed experimentally with oil visualisation.

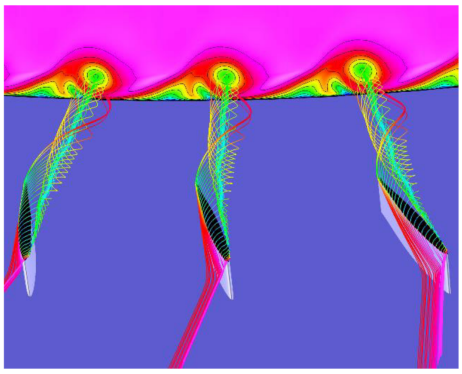

(a) Effect of mixing : streamlines and total pressure losses downstream of a vortex generator (Chima, 2002).

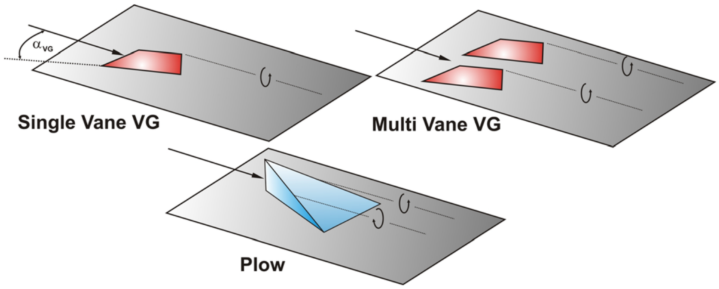

(b) Examples of vortex generator geometries and arrangements (Hergt et al., 2013).

Figure 1.28: Illustration of the concept of vortex generator.

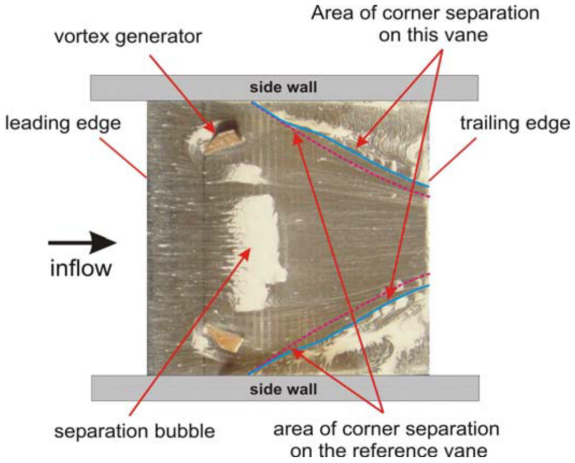

(a) From (Hergt et al., 2006).

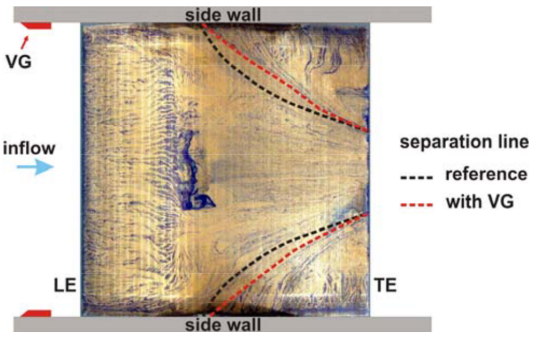

(b) From (Hergt et al., 2008).

Figure 1.29: Effect of VG on separated region (oil visualisation) at design incidence ($Mach = 0.66$).

- (Hergt et al., 2006), Figure 1.29a : a more sophisticated shape is tested (single vane in Figure 1.28b), dimensioned from recommendations of Chima (2002). The vortex generator is successively placed at 9 spanwise positions. In all cases an increase in total pressure losses is observed (between +2% and +8.5%), even though a reduction of the separated region is observed with oil visualisation.

- (Hergt et al., 2008), Figure 1.29b : an arrangement of 3 vortex generators of vane-type is fixed on the hub, upstream of all channels. A beneficial effect on the losses is observed on incidences near the design incidence ($i \in [-4°, +4°]$) with a maximum relative loss reduction of 4.6% at design incidence.

- (Hergt et al., 2013), Figure 1.30: Combinations of 3 arrangement were tested. A new shape (plow in Figure 1.28b) is tested while others (vane type on the hub and on the suction side) are inspired from their previous work. An interesting reduction in losses is observed on a larger range of incidence, from -4° to +6°, with a maximum relative reduction of 9% at design with the plow geometry.

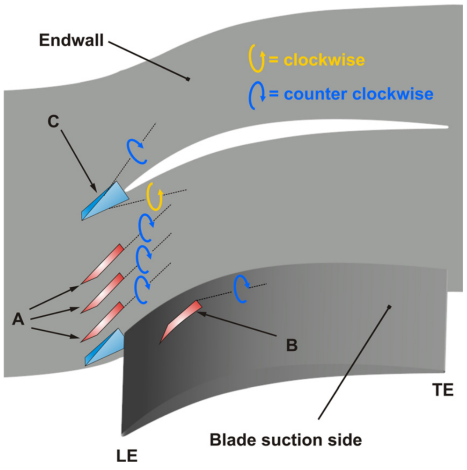

(a) Arrangements tested.

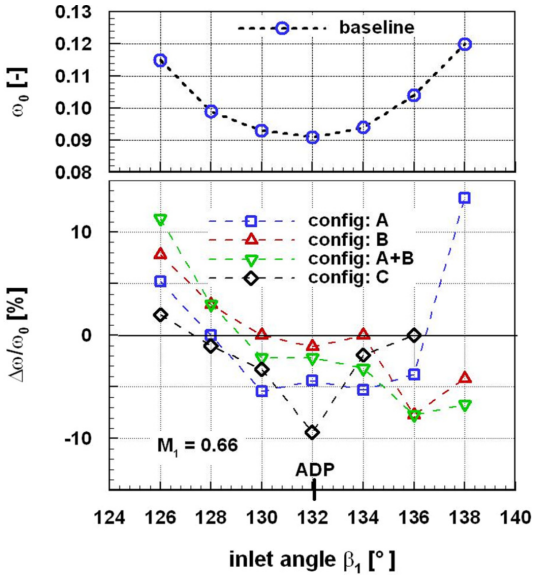

(b) Evolution of the integrated total pressure losses with the incidence for different combinations of VG arrangement.

Figure 1.30: Evaluation of various vortex generator arrangements in a compressor cascade ($Mach = 0.66$) (Hergt et al., 2013).

As such, vortex generators are able to reduce the corner separation size and losses on a relatively large range of incidence. However, without specific caution they are likely to induce more losses than what is gained when reducing the corner separation size. In addition, vortex generators suffer from their empirical approach, as a decade of iterative work was necessary to obtain these results. Their interaction with corner separation is therefore not well understood yet. Finally, it is interesting to notice that efficient vortex generators are systematically shorter than the local boundary layer thickness in these studies.

Endwall fences Endwall fences, or endwall boundary layer fence, are short and relatively long profiled devices that act as a physical barrier that breaks the passage flow and guide the near-endwall flow (see Figure 1.31). This concept is mostly investigated in the context of turbines (Kawai et al., 1989),(Cho et al., 2011), but was recently applied in the context of axial compressors. Endwall fences usually feature a simple design, with a constant and rather little thickness, a simple camber line and a short height. Their main design parameters consist in their length, height, axial and pitchwise positions.

A parametric RANS study was performed by Chen et al. (2019b) on a high speed compressor cascade at design operating point. The length, thickness and height are varied independently, and results in most configurations in an increase in total pressure losses. In another RANS parametric study on the same configuration, Chen et al. (2019a) varied the axial and pitchwise position of the fence. A relative loss reduction of -6.3% is observed at design operating condition for the best configuration. The axial position of this fence leading edge is the stator leading edge, located at 50% pitch, with a chord of 75% of the stator chord and a height corresponding to 10% of the inlet boundary layer thickness. The investigation of their numerical results show a strong interaction of the endwall fence with the secondary flows, locally reducing their vorticity. However, the beneficial effect of the fence disappears for positive incidence values.

An experimental and RANS investigation of several arrangement of fences is carried out by Hergt et al. (2011) in a high speed compressor cascade. In these arrangements, the number of fence is varied from 1 to 8, and different height distributions are tested. The best arrangement is shown in Figure 1.32a. It manages to contain the passage flow, and yields a maximum relative loss reduction of 8% (see 1.32b). However, a loss increase is found for angles of incidence greater than 4°.

As such, the efficiency of endwall fences is not proven yet. This mean of control was little studied in the context of compressor so far, and requires further investigations and experimental campaigns.

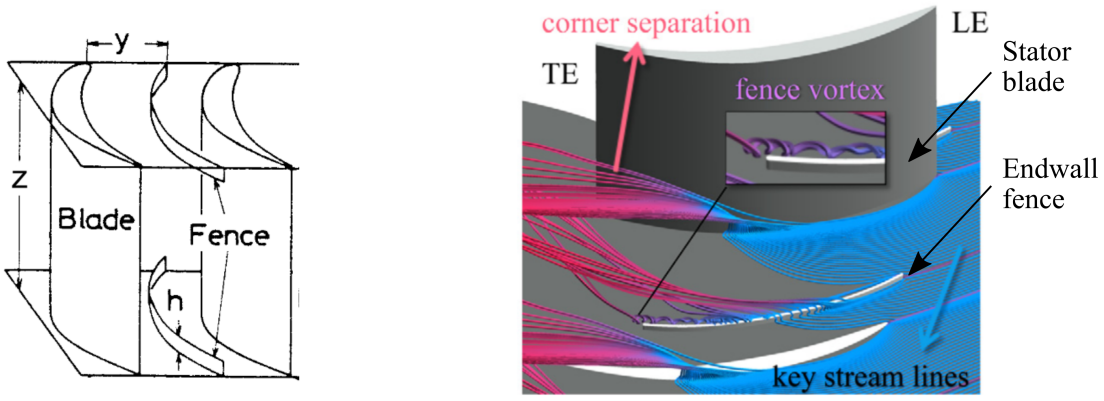

(a) Concept of fence. Adapted from (Kawai et al., 1989).

(b) Influence on near endwall streamlines (Chen et al., 2019b).

Figure 1.31

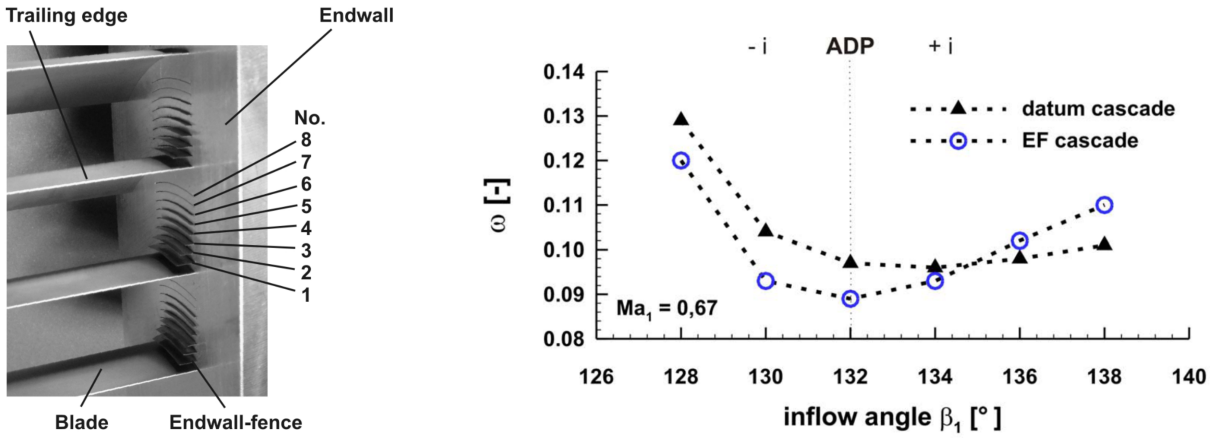

(a) Optimal selected configurations of endwall fences.

(b) Total pressure losses variation. Black triangles : baseline configuration. Blue dot : with endwall fences.

Figure 1.32: Illustration of endwall fences concept and its influence of loss variation with the incidence (Hergt et al., 2011).

Endwall contouring The shape of the endwall can be modified to alter the development of corner separation. Two types of endwall design must be distinguished : the axisymmetric (2D) and non-axisymmetric (3D) endwall contouring. The 2D contouring consists in varying

the radial position of the endwall along the engine axis (see Figure 1.33), and is widely used in the design of modern compressors. Such a variation is naturally present in a real engine, but can be altered to reduce corner separation (LeJambre et al., 1995). A summary of early work in designing axisymmetric contouring is given by Denton and Xu (1998).

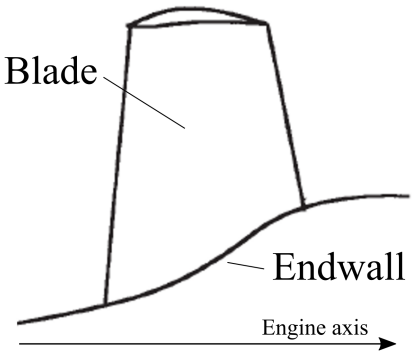

Figure 1.33: Schematic of an axisymmetric (2D) endwall contouring, from (Denton and Xu, 1998).

In 3D contouring, the radial position of the endwall is a function of both the axial and azimuthal position. This additional degree of freedom is interesting to better influence the secondary flows but induces a greater complexity of shape. Their designs therefore require a case by case study, and usually involve complex optimisation procedures.

Harvey and Offord (2008) and Harvey (2008) investigated the effect of 3D contouring (Profiled Endwall in their work) on two different configurations. In Harvey and Offord (2008), the 3D endwall is designed with manual iterations, in a high speed compressor cascade (Mach number of 0.67). Experimental and CFD studies are carried out at design and off-design conditions. Their 3D endwalls merely affect the cascade performance, with a best improvement of 1° in the cascade deflection. However they notice a potentially beneficial mechanism of radial migration of the passage flow. In Harvey (2008) an optimisation process is carried out to design a 3D endwall in a high-speed annular cascade with two-dimensional blades. A numerical investigation is performed at design and off-design conditions. In this case, the optimised 3D endwall shows a large improvement at both operating points, equivalent to the best one found when using three-dimensional re-blading of the blades. The beneficial mechanisms of radial flow migration, similar to the one induced with the use of lean, is confirmed.

Hergt et al. (2009) carried out an experimental evaluation of an optimised 3D endwall in a high speed compressor cascade. This endwall features a shape characteristic of a groove, as illustrated in Figure 1.34a. This 3D endwall efficiently reduces the corner separation losses, with a relative loss reduction of 20% at design condition and 30% at off-design condition. A numerical investigation shows that the groove generates a vortex that acts as an aerodynamic separator. This vortex interacts with the passage flow and limits its azimuthal extension (see Figure 1.34b). An advanced numerical study of this configuration is proposed by Dorfner et al. (2011), which confirms the role of the groove as an aerodynamic separator. This 3D endwall was successfully transferred (RANS results) to a high pressure compressor single stage, with an increase in isentropic efficiency of +2.5% at design operating conditions, and with no effect at off-design conditions.

In a recent numerical study, Reutter et al. (2017) designed a 3D endwall via an optimisation process, for a high speed compressor cascade with optimised (although two-dimensional) blades.

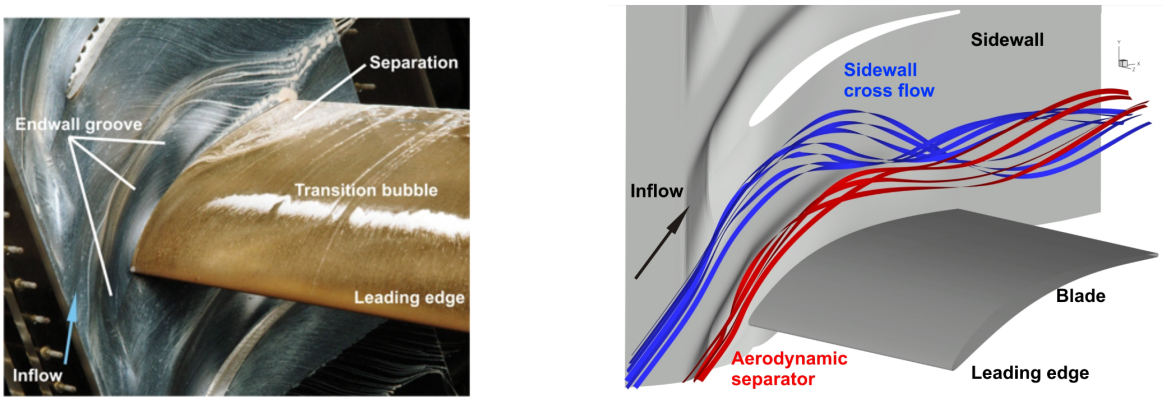

(a) Oil visualisation on the blade suction surface and endwalls with grooves

(b) Aerodynamic separator (red) - passage flow (blue) interaction. Streamlines (RANS).

Figure 1.34: Illustrations from Hergt et al. (2009)

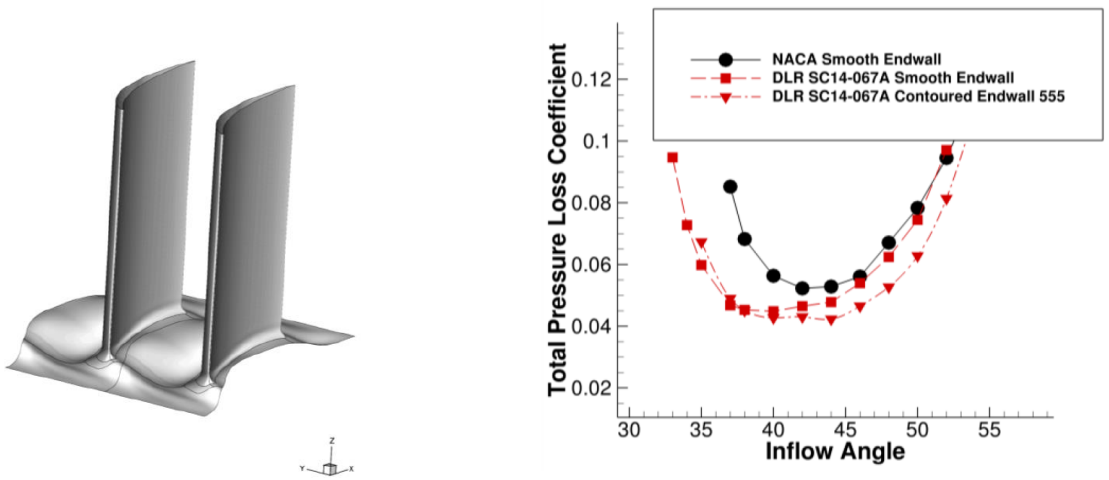

(a) (b)

Figure 1.35: From Reutter et al. (2017). Left : optimised 3D endwall. Right : Evolution of losses with the incidence. Non optimised blade (black dots), optimised 2D blades (red squares), optimised 2D blades + optimised 3D endwall (red triangles).

Three incidences were incorporated in the objective functions to secure a wide operating range (i=-6°, 0°, +7°). The best candidate is shown in Figure 1.35a and its performance is shown in Figure 1.35b (comparison of red lines). This 3D endwall notably yields a relative total pressure loss reduction of 0.5% at 0°, 9% at -6° and 16% at 7°, hence on a wide range of incidences.

These studies reveal a very interesting potential of 3D contouring for increasing the performance and operability of a compressor stator. However, most of the efficient 3D contouring encountered in these studies feature a negative height, which might lead to practical issues in real configurations. Moreover, their design required heavy optimisation processes, and their geometry is probably strongly linked to their related channel geometry.

1.5 Summary

The main results of this literature review on corner separation can be summarised as follows :

- Corner separation generates losses and blockage that strongly limits the operability of aeronautical compressors.
- Corner separation originates from the interaction of the suction side boundary layer and endwall boundary layer. In compressors, it is mainly caused by the passage flow, whose strength increases with the inlet boundary layer thickness, the aerodynamic load and the deflection.
- RANS modelling only predicts two corner separation topologies : single sided and double sided. The associated loss and blockage suddenly increase when switching from single to double sided. This is a numerical artefact called the topological switch.
- Three-dimensional blade design techniques efficiently reduce corner separation but reach their limits and induce sub-optimal performance at design operating conditions.
- Passive technological effect relies on a strong empiricism or on complex optimisation procedures. Their beneficial interactions with corner separation are not yet fully understood. Generally, they aim at energising the endwall boundary layer or help deflecting the passage flow.

In this thesis, a new approach on passive technological effect is undertaken with the concept of guide fins. The definition of guide fin shapes rely on elementary aerodynamic constraints with a limited *a priori* on the physical mechanisms they should implement. The underlying idea is to investigate all conventional technological effects at once, as well as potentially interesting intermediate shapes. However, this approach requires to investigate a large design space, at least in a first step. A sophisticated optimisation process is therefore set up to enable such an investigation in a context of expensive numerical estimation (RANS), as presented in Chapter 2.

Chapter 2

Elements on Kriging-based optimisation

As presented in Chapter 1, the phenomenon of corner separation originates from complex interactions and is difficult to predict with conventional computational flow modelling. In this thesis, the effect of guide fins of various shape on the corner separation is evaluated through an optimisation process. High fidelity methods are required to evaluate their effect on the flow, but induce a high computational cost. RANS is selected as a good compromise between fidelity and cost, but is still expensive. The optimisation methodology must be fitted to this context, and the iterative refinement of Kriging surrogate models is retained in this thesis.

The concept of Kriging surrogate model is first presented (Section 2.1). The use of such surrogate models within an optimisation process is then detailed (Section 2.2). Finally, the concept of Pearson correlation coefficient is recalled (Section 2.3).

2.1 Kriging surrogate modelling

The concept of surrogate model and Kriging surrogate model is described in this section. Kriging models are trained on an initial observation set called the Design Of Experiment (DOE). Properties and algorithms commonly used to generate DOEs are discussed in a second part.

2.1.1 Concept of Kriging surrogate models

Concept of surrogate model A surrogate model consists in the continuous approximation of a response function from a discrete set of evaluations (observation set), as illustrated in Figure 2.1. The objective of such a surrogate is to promptly return an approximation of a costly function whose direct discretisation is too expensive.

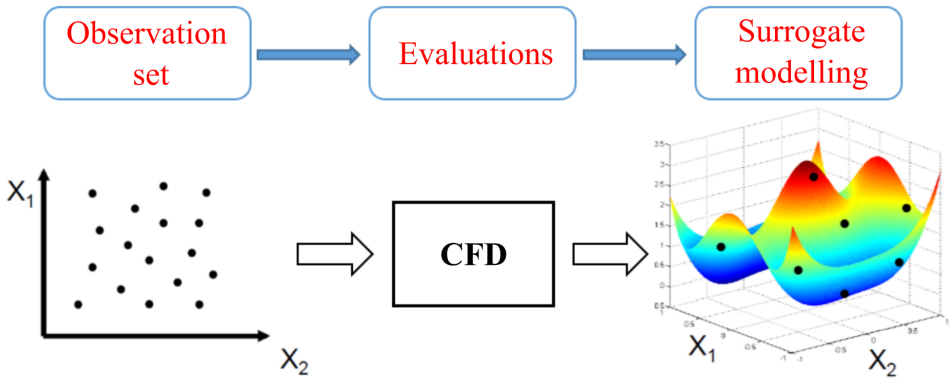

Figure 2.1: Illustration of the construction of a surrogate model. Adapted from Da Veiga (2019).

Several types of surrogate model exist, such as the polynomial regression (Box and Wilson, 1951), Radial Basis Functions (Hardy, 1971), Artificial Neural Network (McCulloch and Pitts, 1943), or Kriging surrogate models. No approach is drastically more powerful than the others, and Kriging modelling is widely used in modern applications (Martin and Simpson, 2005), (Jeong et al., 2005), (Kleijnen, 2009). Moreover, Kriging modelling is particularly fitted to the framework of this thesis through two properties :

- Kriging modelling is interpolating : the predicted response is strictly equal to the values of the response function on the observation set. This is fitted to replicate the response of deterministic functions, such as a CFD code.
- Kriging modelling natively includes a measure of local uncertainty, which is interesting to implement refinement strategies (See Section 2.2.2).

Kriging modelling In Kriging modelling, the response function is approximated as the realisation of a Gaussian process, i.e. a stochastic process described with Gaussian probability density functions. The notion of Gaussian process is defined and illustrated in the Appendix (Section B.1). Let us illustrate the principle of Kriging modelling on a simple one-dimensional example. One seeks to approximate the evolution of a scalar function y as a function of a single parameter p. In the frame of this work, y can be seen as a quantification of aerodynamic losses (output from a CFD code), and p a design parameter describing the guide fins shape, the height for instance.

- The true evolution of $y(p)$ is represented in black in Figure 2.2a. In this example, y is evaluated at 4 values of p (red squares).
- One seeks to approximate the response function as the realisation of a Gaussian process $(Y(p))$. Several realisations of this Gaussian process are represented in Figure 2.2b.
- To be representative of the response function, only the realisations conditioned with the observation values are retained $(Y(p)|Y_{obs}$, Figure 2.2c). All the possible realisations of this Gaussian conditioned process constitute the Kriging model.
- In practice, the average value of these realisations for each value of p is computed and constitute the average value of the Kriging prediction ($\mathbb{E}[Y(p)|Y_{obs}]$, solid blue line, Figure 2.2d). The variance of the Kriging model can also be computed, which enables to define 95% confidence intervals (dashed blue line, Figure 2.2d) and provides a local Kriging

uncertainty. Let us underline that in Kriging modelling, the uncertainty increases with the distance to an observation point, which is indeed observed in this example.

This simple example illustrates the two main characteristics of Kriging modelling : it is interpolating of the observation points and includes a measure of a local uncertainty.

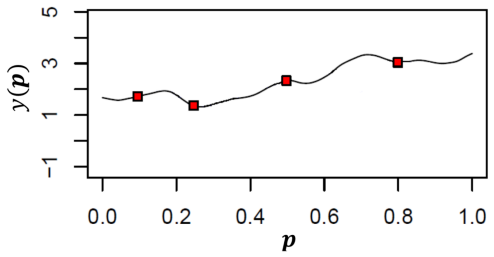

(a) 4 observation (red squares) of the response function y(p).

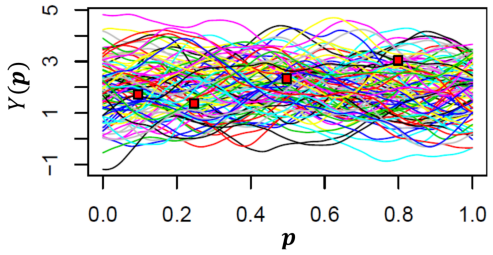

(b) Realisations of Gaussian Process.

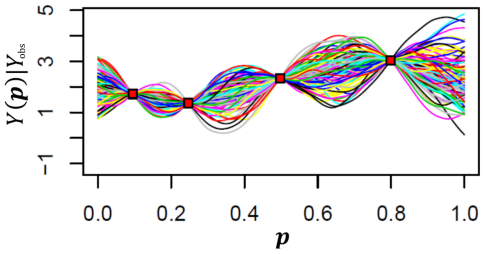

(c) Realisations of Gaussian process conditioned with the 4 observations (red squares).

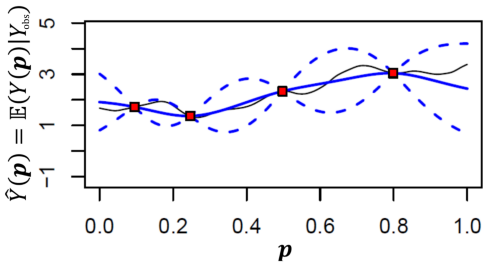

(d) Kriging prediction : Mean value (solid blue line) and 95% confidence interval (dashed blue line).

Figure 2.2: Principle of Kriging modelling. Adapted from Helbert (2020).

Quality of Kriging predictions Kriging modelling requires user inputs whose values might alter the Kriging predictions (see Appendix, Section B.2). It is therefore crucial to assess the quality of its prediction (predictability). By definition, these surrogate models are used in a context of expensive evaluations of the response function. It is therefore difficult to split the observation set in a training part and an evaluation part. The following strategy (Leave One Out or LOO strategy) is commonly used to bypass this issue :

- a single point is removed from the observation set
- a new surrogate is trained on the reduced observation set
- this new surrogate is used to predict the value at the removed point

This is done for every point of the observation set. If the observation set contains N points, this results in N predictions of surrogate models generated with N-1 points. The predicted vs true value graph then enables to evaluate the predictability of the surrogate model around every observation point (see Figure 2.3). The Q2 criterion, analogous to the R^2 regression coefficient, is computed, and gives a scalar value quantifying the average predictability of the surrogate model :

$$Q2 = 1 - \frac{\Sigma_i (y_i - \tilde{y}_i)^2}{\Sigma_i (y_i - \bar{y})^2} \tag{2.1}$$

With y_i the response value at observation point i, $\tilde{y_i}$ the predicted value at point i given by the surrogate model trained without this point, and $\bar{y}$ the average of the response values on the observation set. The predictability is commonly considered very poor for Q2 values below 0.7, to give reasonable trends for values within $[0.7, 0.9]$, and excellent for values above 0.9.

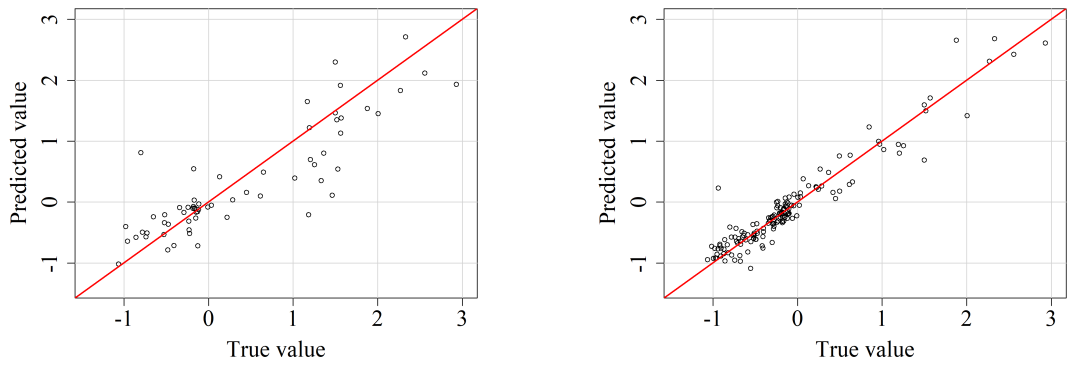

(a) Q2=0.70, poor confidence

(b) Q2=0.91, high confidence

Figure 2.3: Predicted vs true value. Each dot corresponds to an observation point. The red line is represents the region of perfect predictability (True value = Predicted value).

2.1.2 Design of experiment

In this manuscript, a *rectangular space* refers to a mathematical space of dimension n described when n parameters vary continuously between their minimum and maximum finite bounds. For instance, a rectangular space of dimension 2 is a rectangle, of dimension 3 a hexahedron.

Building a Kriging surrogate model requires an initial observation set, or Design Of Experiment (DOE). In the context of a limited number of observations, one may wonder if there is a particularly interesting set of points to evaluate at first. With no *a priori* knowledge of the function to evaluate, the objective of the DOE is to get an insight of the function evolution on the whole input space (with respect to all parameters on their whole range of variation). An efficient DOE must therefore feature two main characteristics : a) explore the entire input space (space-filling) b) uniformly explore each subspace of the input space (no redundancy by projection). These characteristics are illustrated with a two dimensional input space in Figure 2.4.

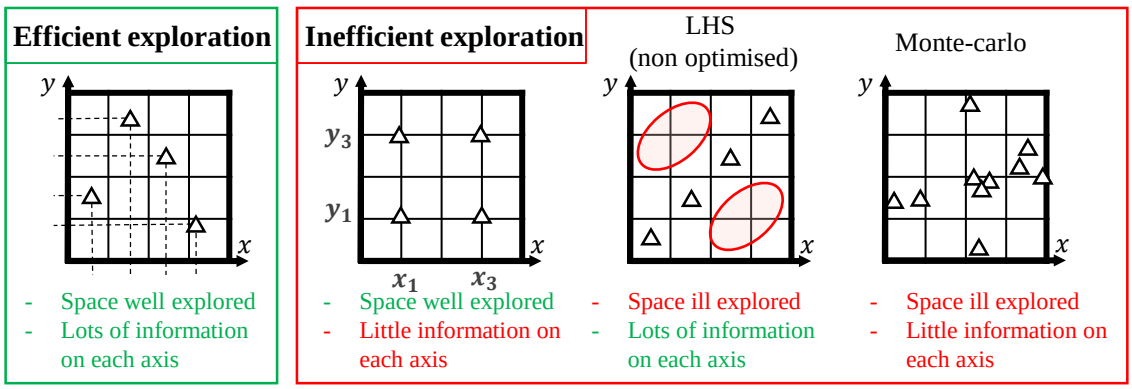

Figure 2.4: Examples of DOEs on a two-parameter space. Triangles : observation set.

A famous method to avoid the redundancy by projection is the Latin Hypercube Sampling (LHS) (McKay et al., 1979). For a DOE of size n, each parameter range is discretised in n intervals of same size. The n points are selected such that each interval of each parameter contains a unique point. However, this sampling needs to be optimized to be space-filling, as illustrated in Figure 2.4. Several space-filling techniques have been developed to reach that purpose, such as the minimax and maximin (Johnson et al., 1990) algorithms, the maxproj algorithm (Joseph et al., 2015), or low-discrepancy sequences (Niederreiter, 1988), (Sobol, 1967) among the most common techniques.

However, these methods are fitted to explore rectangular input spaces, which rarely occur in engineering applications. Indeed, a rectangular space supposes no constraints between inputs, and that any combination of parameter values yields a viable point (i.e. that can be associated to a response value). In this work, several aerodynamic and positioning constraints induce inaccessible portions of the input space, and a more sophisticated methodology is required. First a large database of input points is generated using a Monte Carlo methodology in a rectangular space. Only points satisfying specific viability criteria are retained, resulting in a discretised input space. The DOE is then built by picking a small subset which spans as best as possible the entire database. To achieve this, the "kernel herding " algorithm proposed by Chen et al. (2010) is used. The main assumption in this algorithm is that such a large database is representative of the set of all viable points.

In this work, the LHS technique together with the maxproj algorithm is used when possible. Otherwise, the approach relying on the kernel herding algorithm is selected.

2.2 Optimisation based on iterative refinement of surrogate models

This work aims at finding guide fins that efficiently reduce the phenomenon of corner separation. This correspond to the implementation of a complex optimisation problem, with a large number of input parameters ($\simeq 15$) and a limited number of observations (RANS). The optimisation strategy relying on the iterative refinement of Kriging surrogate model is *a priori* fitted to this context. Basic notions of optimisation are first recalled (Section 2.2.1), and the optimisation methodology relying on Kriging model refinement is then described (Section 2.2.2).

2.2.1 Basics of optimisation

The definition of an optimisation problem relies on the definition of one or several scalar functions F_j (objective functions) from a single input parameter space $D \subset \mathbb{R}^p$ of dimension p to an output space $F \subset \mathbb{R}^k$ of dimension k, the number of objective functions. Figure 2.5 presents an illustration of such a configuration in the case of two objective functions depending on two parameters.

A mono-objective optimisation process consists in finding the points (parameter sets) from the input space minimising a single objective function. A multi-objective optimisation process consists in finding the sets of points that reveal the best compromises to reduce the value of a given objective function while least deteriorating the values of the others. In the context of this work, a bi-objective ($k = 2$) optimisation is carried out. In order to quantitatively define the notion of best compromise, the notions of dominance and of Pareto front are introduced. A point of the input parameter space is said to *dominate another one in the Pareto sense* if it is associated to a lower value on at least one objective function (see Figure 2.6). The set of

points that are non-dominated is called the *Pareto front*, and is represented with the red line in Figure 2.5.

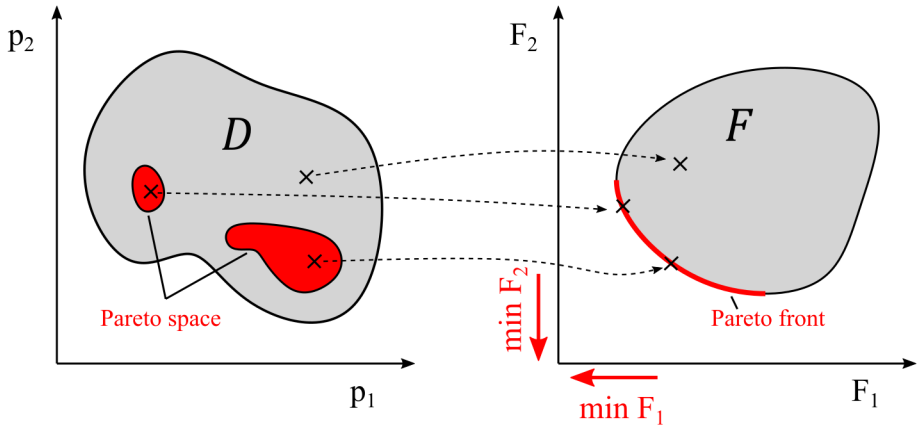

Figure 2.5: Illustration of a bi-objective, bi-parameter optimisation problem. The red line on the right hand side figure corresponds to the optimal region, or Pareto front.

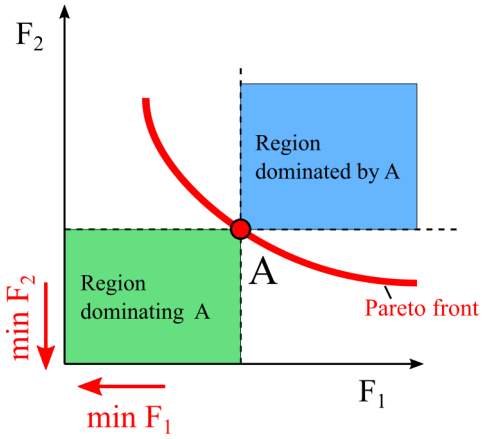

Figure 2.6: Illustration of the principle of dominance in the Pareto sense.

Setting up an optimisation process requires to select an algorithm that iteratively evaluate the objective functions and converge towards the optimal regions. A comprehensive summary of existing algorithms for solving optimisation problems, together with application cases, is proposed by Collette and Siarry (2004). The choice of an optimisation algorithm is largely dependant on the complexity of the optimisation process. This complexity notably depends on the number of input parameters, the number of objective functions, their complexity, and the authorised budget (i.e. the maximum number of evaluations). In this thesis, a bi-objective problem from a 15-parameter input space is considered (see Section 6). The objective functions are built to characterise a complex physics related to the phenomenon of corner separation. A non linear behaviour with potentially many local minima is therefore assumed. The optimisation strategy must therefore tackle a global, multi-parameter, multi-objective, non linear optimisation problem.

In this work the objective functions are evaluated with two numerical methodologies of different cost. The first methodology consists in CFD evaluations (limited budget, of the order of few hundreds evaluations). To best explore the input design space in this context, a strategy

based on iterative refinements of Kriging surrogate models will be used. This strategy is described in Section 2.2.2. The second methodology consists in evaluating a Kriging surrogate model trained with CFD results. In this case, the evaluation of the surrogate is particularly inexpensive and a conventional optimisation strategy will be used to detect the optimal regions. In this context of global multi-objective optimisation with a large budget, the NSGA2 algorithm (Deb et al., 2002) is particularly efficient and widely used. This algorithm belongs to the category of Genetic Algorithm, and enables to get a population of optimal solutions uniformly distributed along the Pareto front. It is worth noticing that its convergence requires about $\mathcal{O}(MN^2)$ evaluations, where M is the number of objectives and N the population size on the resulting Pareto front (user input). This corresponds to a fast convergence among genetic algorithms. However, a population of several dozens of individuals is generally used, thus discarding a direct use of NSGA2 with CFD computations.

2.2.2 Iterative refinement of surrogate models

Kriging surrogate models are trained on an observation set, which results from RANS evaluations in this work. The initial training database (DOE) might evaluate the response function far from its minima, resulting in a Kriging model of poor predictability. An iterative refinement strategy is thus implemented to a) ensure the evaluation of efficient guide fins with RANS b) increase the predictability of the surrogate model in the regions of local minima. Such an approach was proposed by Jones et al. (1998), and is notably evaluated in (Jones, 2001).

Refinement criteria Let us assume that a DOE is available and that a first Kriging model is trained on that database. Refining the surrogate model consists in evaluating new observation points. It might be interesting to evaluate new points where the model predicts low values (exploitation) or where it features a high uncertainty (exploration).

Let us illustrate the notion of iterative refinement in a mono-objective mono-parameter case. Several criteria taking into account both the predicted value and the local uncertainty were developed in this framework, such as the Probability of Improvement (Kushner, 1964), the Expected Improvement (Mockus et al., 1978) or the GP Upper Confidence Bound (Srinivas et al., 2012). The Expected Improvement (EI) is used in this example. The EI is computed on the whole input parameter space, using the Kriging average prediction and local uncertainty with a similar weight. In Figure 2.7, the investigated response function is represented with a red dashed line. An initial set of 3 observations is used to build an initial Kriging surrogate model (black line : average prediction ; grey envelope : local uncertainty). The values of the EI criterion are computed and represented with a purple area. The point maximising the EI criterion is selected to refined the surrogate model (refinement point). At iteration 1, the proposed refinement point is evaluated (blue arrow) and a refined Kriging surrogate model is built using all the available data (initial observations + refinement point). The same sequence is then repeated : computation of the EI criterion, new selection and evaluation. After 5 iterations, two local minima are detected and the behaviour of the response function in their vicinity is well predicted.

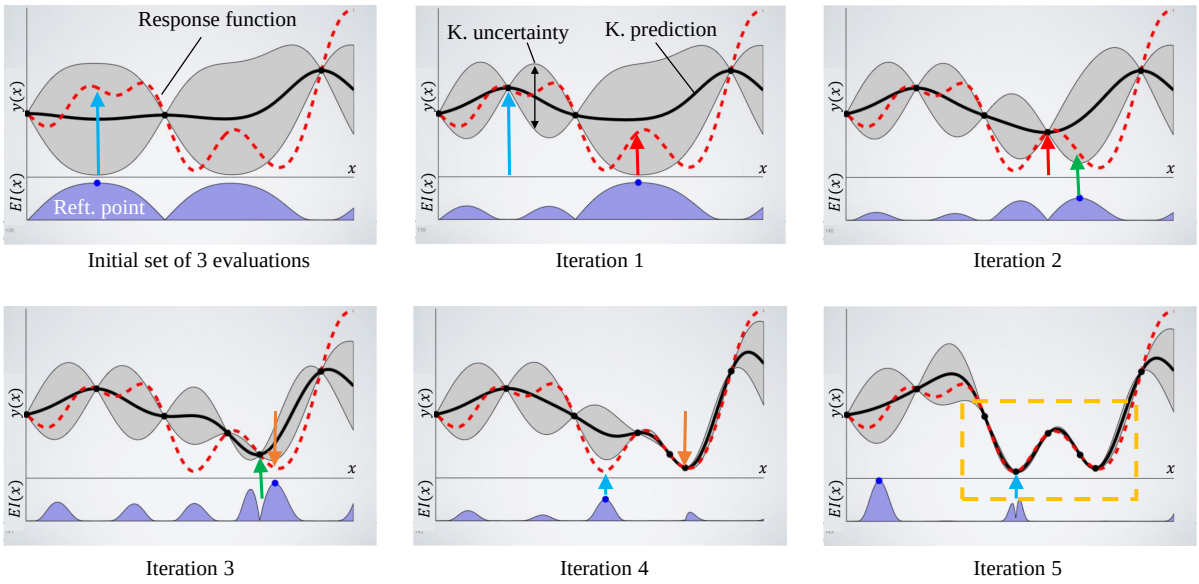

Figure 2.7: Illustration of surrogate refinement process. Arrows indicate the previous and next refinement points. The yellow frame indicates a region of minima well predicted by the surrogate model. Adapted from (Da Veiga, 2019).

The refinement strategy is more complex in a multi-objective context. In such a context, the objective of the refinement process is to improve the values of the predicted Pareto front and not to minimise each objective function independently. New refinement criteria relying on the predicted Pareto front are therefore required. Several refinement criteria dedicated to the multi-objective context were developed, such as the Estimation criterion (Shimoyama et al., 2012), the Expected Hypervolume Improvement (EHVI) (Emmerich et al., 2006) (Emmerich et al., 2011),(Svenson, 2011), the maximin improvement (Svenson, 2011) or the Expected Excursion Volume (Picheny, 2015). No clear superiority of these criteria is commonly assessed, and the EHVI criterion is retained for this work. Its performance and robustness were assessed by Wagner et al. (2011) and Svenson (2011). Moreover, an analytic formulation of this criterion exists in the particular case of a bi-objective context, which is the context of this work, thus considerably reducing the computational cost related to its evaluation.

The concept of the EHVI criterion is illustrated in Figure 2.8. This criterion provides a single refinement point that maximises an improvement function defined as in (Emmerich et al., 2006),(Emmerich et al., 2011). This improvement function describes the potential improvement of the hypervolume bounded by the non-dominated points of the observation set and by a reference point y_{ref}. In this work, the EHVI criterion is computed with the GPareto library (**R** software) developed by (Binois and Picheny, 2019).

The EHVI criterion only provides a single refinement point. This is not specific to this criterion, as a lack of multi-objective multi-observation criteria is observed in the literature (Martínez-Frutos and Herrero-Pérez, 2016). In this work, a naive multi-observation refinement strategy is undertaken : the EHVI criterion provides a first refinement point, which prediction is temporary considered as the true value of the response function. The EHVI criterion provides

a second refinement point while considering the prediction of the first refinement point as an evaluated point. This is done iteratively to generate batches of refinement points. This naive multi-observation strategy is sub-optimal, but greatly facilitates the optimisation process when the evaluation/refinement sequence can not be automated.

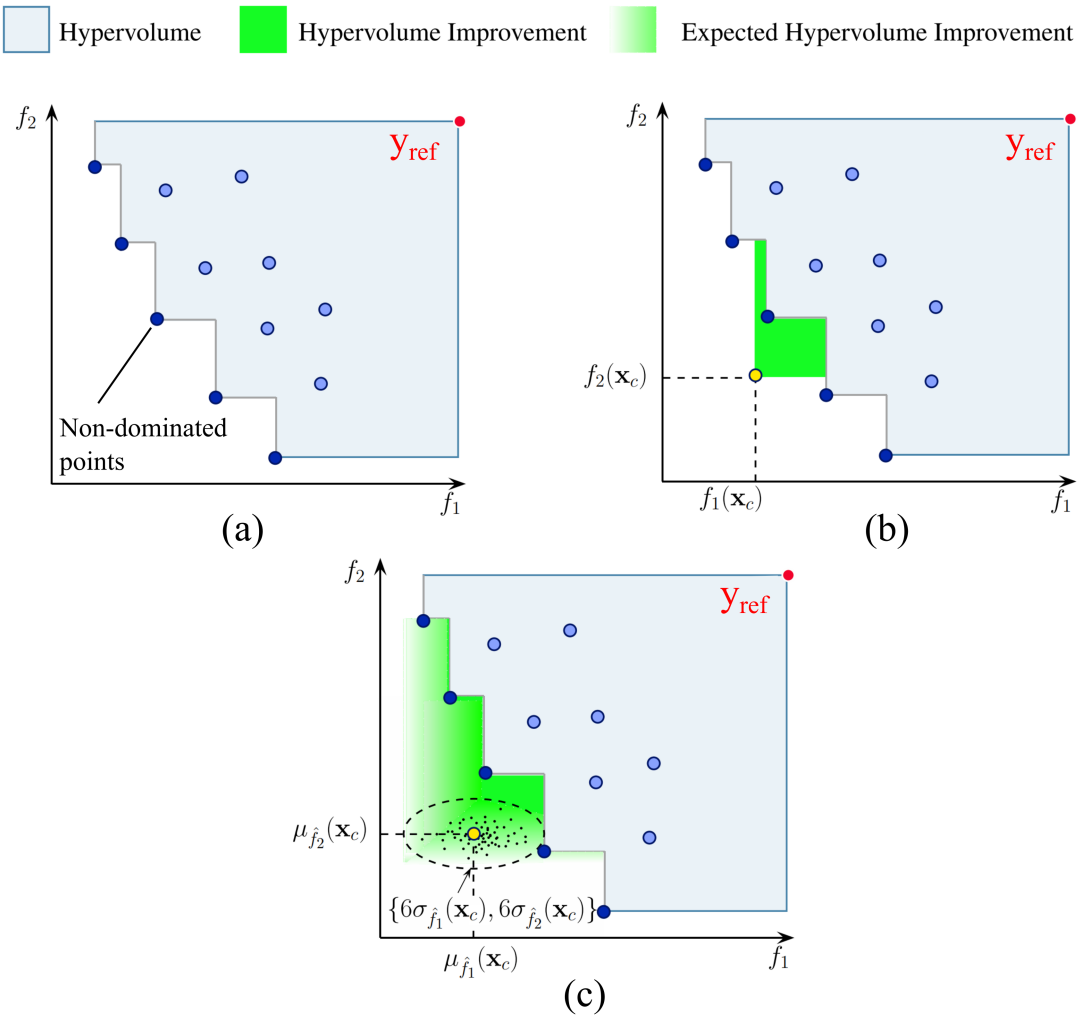

Figure 2.8: EHVI in a bi-objective context : (a) hypervolume on a given set of Pareto solutions, (b) improvement of the hypervolume by the deterministic inclusion $[f_1(x_c), f_2(x_c)]$ of a new candidate x_c, and (c) EHVI by the uncertain inclusion $[\hat{f}_1(x_c), \hat{f}_2(x_c)]$ of a new candidate x_c in the front. f_i : Kriging average prediction of objective function i. $\hat{f}_i$: Probabilistic values of objective function i (Kriging uncertainty). Adapted from (Martínez-Frutos and Herrero-Pérez, 2016).

The EHVI balances the exploration and exploitation of the surrogate model by taking into account both the average prediction and the uncertainty of the Kriging surrogate model. Other refinement strategies might be of interest :

- **Exploitation only :** A basic exploitation strategy consists in evaluating a selection of points among the predicted Pareto front. This strategy is proposed by Shimoyama et al. (2012) and corresponds to the Estimation criterion. The main difficulty of this strategy is to select which points of the Pareto front should be evaluated. Moreover, this strategy tends to focus the optimisation near the local minima already detected (no exploration) and hence does not constitute a robust global optimisation strategy. In this work, this

strategy is applied at specific iterations to evaluate the predictability of the surrogate model in its Pareto front region.

- **Exploration only :** The Global Accuracy algorithm (Active Learning MacKay in (Seo et al., 2000)) provides refinement points where the Kriging uncertainty is maximal (MacKay, 1992). It therefore aims at reducing the uncertainty on average over the whole input space.

Convergence of the iterative refinement The optimisation process might be stopped because the maximum computational budget is reached, or ideally when the Pareto front of the evaluated dataset has converged. In both cases, a metric to measure the convergence of the optimisation process is required. Two main metrics are commonly used, the Inverted Generational Distance (IGD, Coello Coello and Reyes Sierra (2004)) and the Hypervolume Indicator (HVI, (Zitzler and Thiele, 1998)). The HVI is used in this work, and simply consists in the measure of the hypervolume at each iteration (see Figure 2.8). For consistency of the HVI values, the same reference point y_{ref} is used at each iteration. The value of this criterion increases when the Pareto front is improved. A stagnation of this indicator reveals the convergence of this process. The slope and curvature of this indicator might also gives an insight on how far from the converged Pareto front the current Pareto front is, which is useful if the optimisation stops for computational budget reasons.

2.3 Pearson correlation

Definition The Pearson correlation coefficient is widely used to assess whether two random variables are linearly correlated. It is defined as :

$$\rho_{X,Y} = \frac{Cov(X,Y)}{\sqrt{(Var(X) \times Var(Y))}} \tag{2.2}$$

where Var and Cov respectively refers to the variance and covariance operators (see Appendix, Section B.1). By definition, its value varies between -1 (decreasing trends) and +1 (increasing trend). A value close to 0 indicates no linear correlation.

In practice, the Pearson correlation coefficient is computed on sample points $(x_i, y_i)_{1 \leq i \leq n}$, corresponding to n realisations of X and Y, and is then denoted r. With $\bar{x}$ (resp. $\bar{y}$) the mean value of x (resp. y), and σ_x (resp. σ_y) its standard deviation :

$$r_{x,y} = \frac{\Sigma_i (x_i - \bar{x})(y_i - \bar{y})}{\sigma_x \times \sigma_y} \tag{2.3}$$

Typical values of the Pearson correlation coefficient are illustrated on various samples in Figure 2.9. In this work, x typically refers to a given guide fin parameter (design parameter) and y to a given objective function (typically aerodynamic losses). The computation of the Pearson correlation coefficient therefore provides indications on the potential linear relation between a design parameter and the aerodynamic losses. Let us underline that x and y can be correlated and feature a Pearson correlation coefficient equal to 0 if this correlation is non linear (last line in Figure 2.9).

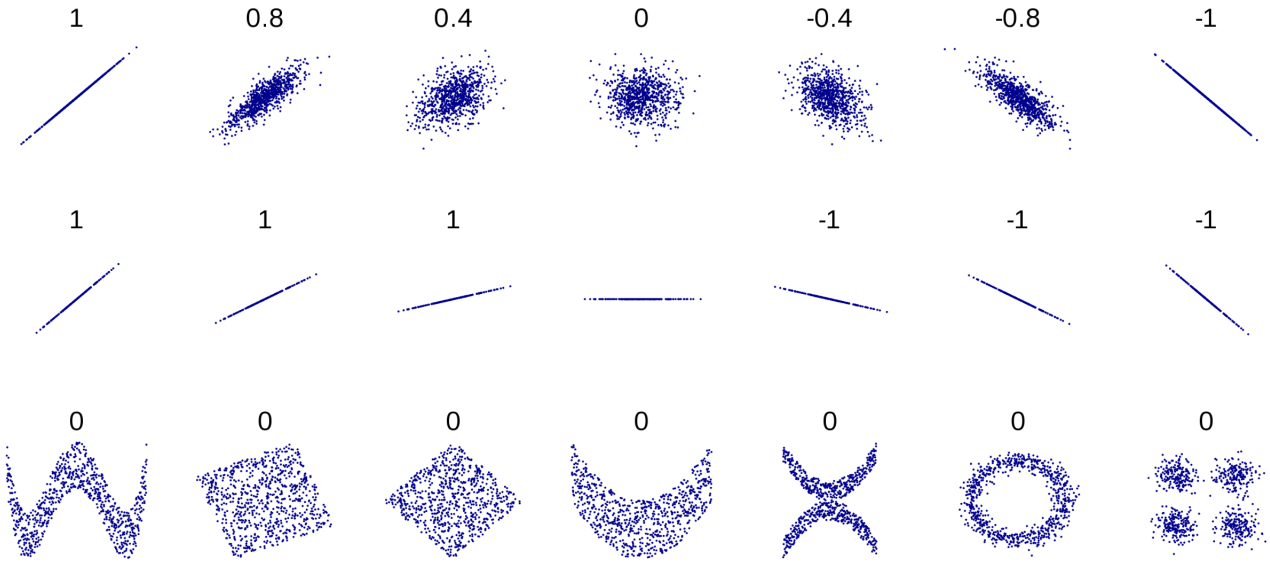

Figure 2.9: Values of Pearson correlation coefficient computed on samples of various shapes. From *https://en.wikipedia.org/wiki/Pearson_correlation_coefficient.*

Significance The Pearson correlation computed on a sample (r) is an estimate of the Pearson correlation of the underlying random variable (ρ). If a correlation is detected on the sample (r significantly different from 0), a statistical test should be performed to assess whether a correlation indeed exists between X and Y (ρ significantly different from 0) or if this value originates from pure randomness. Figure 2.10 illustrates this principle. From a test sample of 5 observations, a Pearson correlation coefficient of 0.80 is measured. This coefficient might reveal a true correlation between X and Y (case A), but might also result from pure randomness with X and Y uncorrelated (case B). The statistical test consists in computing the p-value* associated to the Pearson correlation r. The p-value is then compared to the commonly accepted threshold of 0.05 : if $r \neq 0$ and its p-value is below 0.05, $\rho \neq 0$ with a probability greater than 95%. In Figure 2.10, the p-value computed on the test sample is 0.10 : the correlation measured on the test sample reveals a true linear correlation with a probability of 90%. This is below the commonly accepted threshold of 95% : the Pearson correlation coefficient is not significant in this case.

Remark : When a true linear correlation exists, the p-value rapidly drops with the number of samples†. A minimum value of 20 samples is commonly sufficient to reveal the existence of a linear correlation.

*Probability that an inferred correlation originates from pure randomness. A thorough definition of the p-value can be found in (Witte and Witte, 2017).

†The samples of this example were generated with a random variation about a linear function ($0.5x + 0.7 \times rand(0, 1)$). For 4 samples, a p-value of 0.25 is measured. For 5, 0.10. For 7, 0.02, already below the 5% threshold.

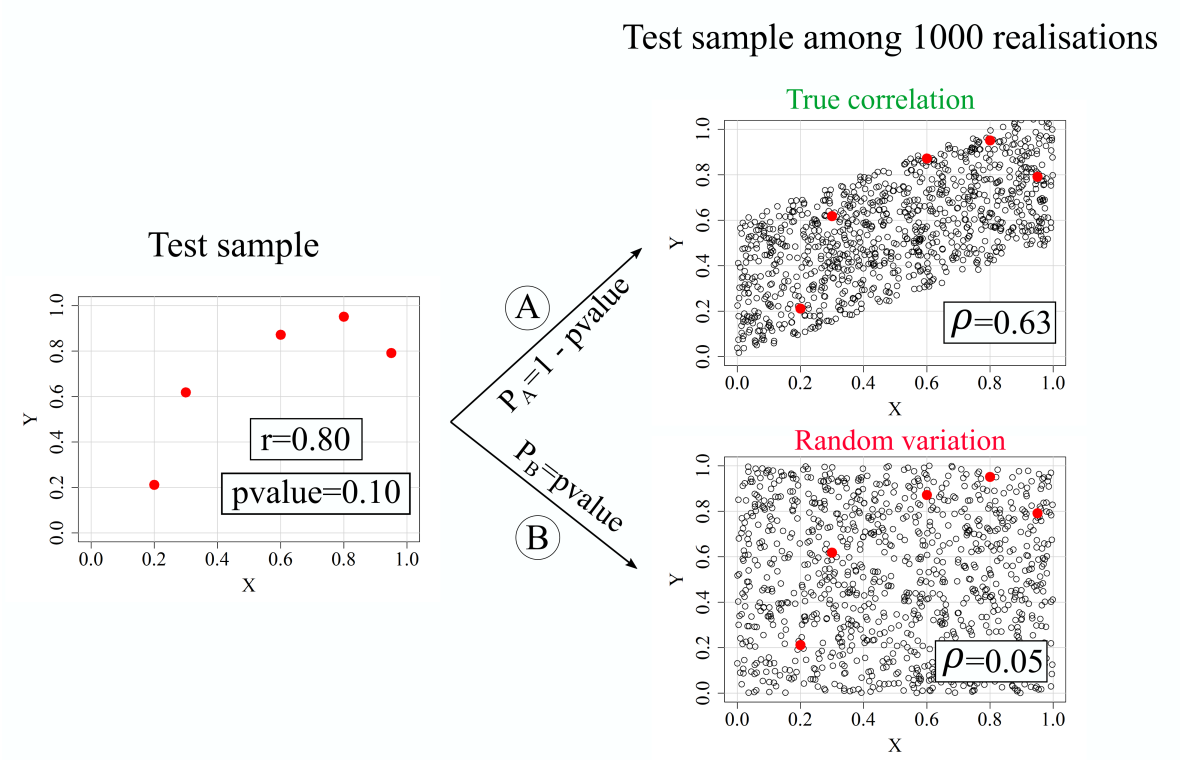

Figure 2.10: Illustration of Pearson correlation coefficient significance. The p-value is the probability that the inferred linear correlation on the sample originates from pure randomness (case B).

Chapter 3

Configuration of reference

In this work, the efficiency of guide fins is evaluated on a configuration of reference (baseline configuration). This configuration corresponds to an experimental rig available at the LMFA, which was set up by Ivo Dawkins during his PhD thesis (Dawkins, 2021). This chapter offers a clear overview of the baseline configuration performance with experimental measurements performed by the author of this thesis. The methodology used to obtain these experimental results is described in Chapter 4.

3.1 Overview of the rig

The baseline configuration consists in a linear stator cascade whose characteristics are summarised in Table 3.1. Figure 3.1 presents a side view of the rig.

Blade details This linear cascade is composed of 12 to 15 stators of CDA type (Controlled Diffusion Aerofoil) with elliptical leading edges. They are representative of stators in a 50% reaction stage with a loading coefficient of 0.45 and a design flow coefficient of 0.55. These stators result from the two-dimensional extrusion of the aerofoil presented in Figure 3.2a, with no fillets at the blade/endwall junction. The blade aspect ratio is relatively large (span / chord=2.32) to ensure that the endwalls do not interact with one another. The blades rugosity was measured by Dawkins (2021). The centreline-averaged roughness height R_a is $2\mu m$, yielding a roughness-based Reynolds number of $Re_k \simeq 5$ based on R_a and the inlet velocity (Dawkins, 2021). This is comparable to the typical roughness of a newly manufactured blade in an engine ($Re_k = 4.3$) according to Brendel et al. (2008).

Operating conditions The rig operates at a chord-based Reynolds number of 3.2×10^5, yielding a Mach number of 0.11, with an inlet turbulence rate of 2.4%. The flow passing through the cascade is therefore considered incompressible . The inlet boundary layer thickness is finely controlled and kept constant throughout all measurements (see Section 4.1.2). The cascade operate at incidences within [-1°,+8°] with an excellent downstream flow periodicity (see Section 4.1.2). The incidence is defined as the inflow pitchwise angle upstream of the stator leading edge minus the design pitchwise angle (52.8°). The latter corresponds to the angle yielding the minimum of losses downstream of the cascade.

Performance measurements The upstream static and total pressures ($P_{s,\infty}$,$P_{t,\infty}$) are measured one stator chord (c) upstream of the stator leading edge with a five-hole probe. Down-

stream measurements are performed in a plane 0.2c downstream of the trailing edge (measurement plane in Figure 3.1). A five-hole probe is used to measure the static pressure (P_s), total pressure (P_t), pitchwise flow angle (β) and spanwise flow angle (ϕ). To evaluate the flow periodicity, downstream measurements are performed across two consecutive channels.

Modification of the baseline configuration compared to (Dawkins, 2021) In this work, the baseline configuration is equipped with insertion systems enabling to insert guide fins. This system can also replicate the baseline configuration with a negligible impact on the cascade performance (see Section 4.3). In this work, the baseline configuration refers to the baseline set up by Dawkins (2021) equipped with the insertion systems with no guide fins.

Cascade parameters	**Value**
Profile type	Controlled Diffusion Aerofoil
Stator chord (c)	125 mm
Pitch	70.6 mm
Span	290 mm
Design inflow angle	52.8°
Blade Stagger	35.4°
Inlet metal angle	59.0°
Outlet metal angle	22.5°
Chord-based Reynolds number	$3.2 \times 10^5 \pm 0.15\%$
Inlet Mach number	0.11
Inlet Turbulence rate	$2.4\% \pm 0.1\%$
Inlet Momentum thickness (θ/c)	$0.0030 \pm 6\%$

Table 3.1: Cascade characteristics. Uncertainties were computed by Dawkins (2021).

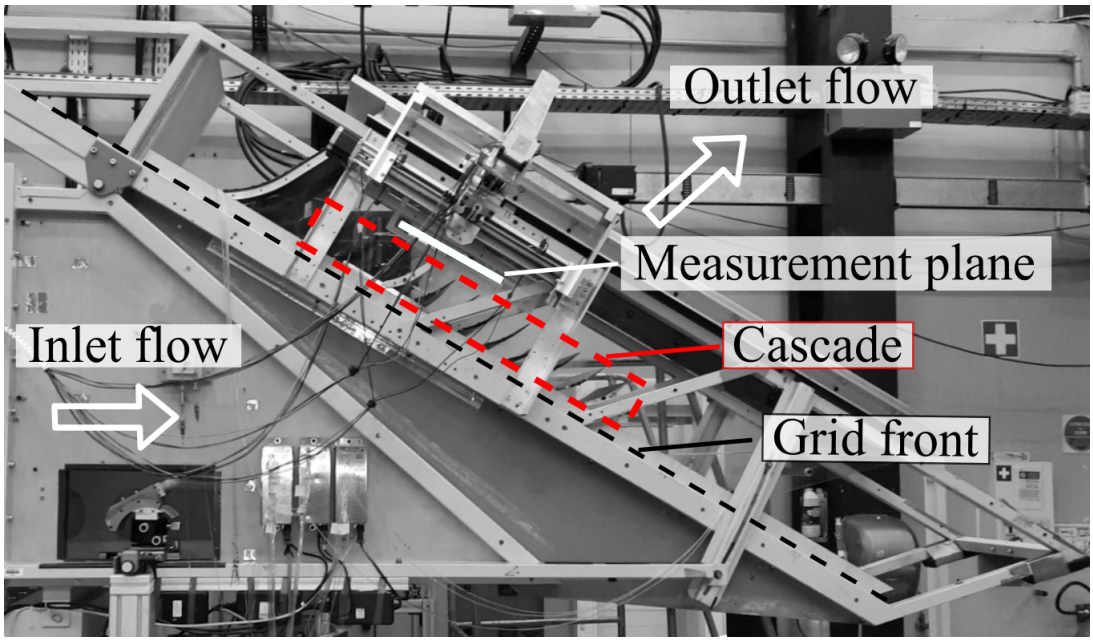

Figure 3.1: Side view of the rig.

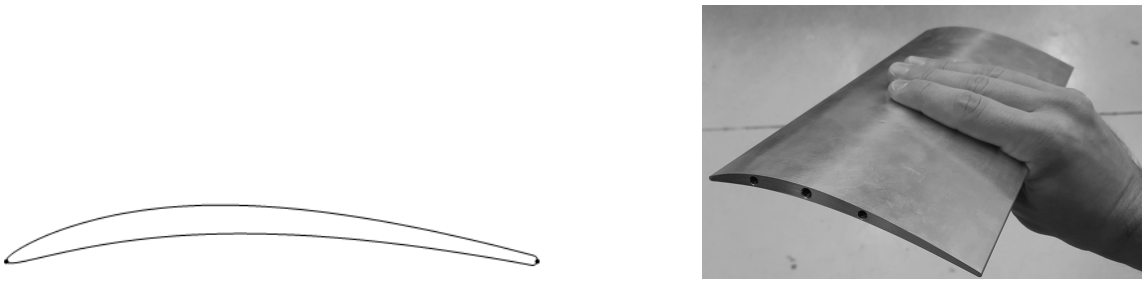

(a) Stator aerofoil.

(b) Stator blade.

Figure 3.2

3.2 Performance of the cascade

An overview of the aerodynamic characteristics of the rig is proposed in this section with experimental results. The aerodynamic load at midspan is first presented. Results obtained on full measurement cartographies are then presented, and enable to quantitatively observe the corner separation and its evolution as the incidence increases.

3.2.1 Aerodynamic load at midspan

The aerodynamic load at midspan is measured with the static pressure coefficient ($C_{p,s}$) along the blade :

$$C_{p,s} = \frac{P_s - P_{s,\infty}}{P_{t,\infty} - P_{s,\infty}} \tag{3.1}$$

with P_s the local static pressure, P_t the local total pressure, $P_{s,\infty}$ the reference upstream static pressure and $P_{t,\infty}$ the reference upstream total pressure. The distributions of $C_{p,s}$ along the blade at midspan at various incidences are presented in Figure 3.3.

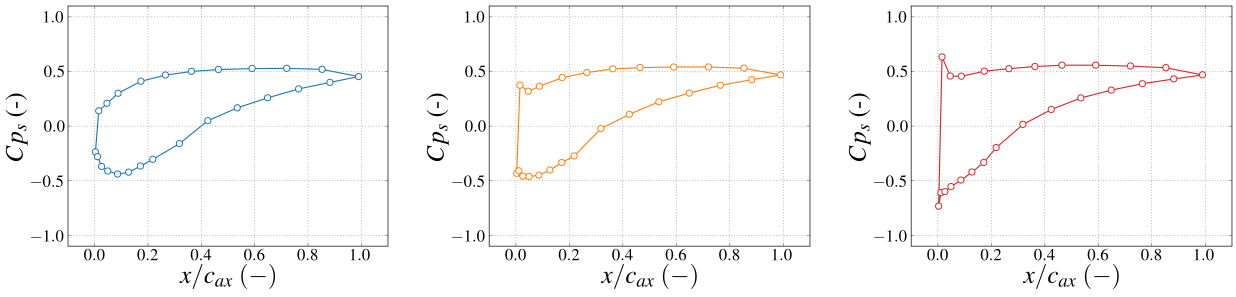

(a) i=0°

(b) i=2.3°

(c) i=4.9°

Figure 3.3: Pressure coefficient distribution ($C_{p,s}$) along the blade at midspan. Experimental data. c_{ax} : axial stator chord.

3.2.2 Total pressure losses

The total pressure losses are computed downstream of the cascade as follows :

$$\omega = \frac{P_{t,\infty} - P_t}{P_{t,\infty} - P_{s,\infty}} \tag{3.2}$$

with P_t the local total pressure, $P_{s,\infty}$ the reference upstream static pressure and $P_{t,\infty}$ the reference upstream total pressure. The midspan losses (ω_{MID}) are defined as the mass averaged total pressure losses across one pitch at midspan. With ρ the local flow density and V_x the axial velocity :

$$\omega_{MID} = \frac{\int \omega \rho V_x \, dy}{\int \rho V_x \, dy} \tag{3.3}$$

The integrated losses (ω_{0D}) are defined as the mass averaged losses across one pitch and from the endwall to midspan :

$$\omega_{0D} = \frac{\int \int \omega \rho V_x \, dS}{\int \int \rho V_x \, dS} \tag{3.4}$$

In order to characterise the additional losses induced by the presence of the endwall (secondary flow, corner separation), the endwall losses (ω_{EW}) are introduced :

$$\omega_{EW} = \omega_{0D} - \omega_{MID} \tag{3.5}$$

Figure 3.4 presents the cartographies of total pressure losses as the incidence is increased. These cartographies reveal three characteristic regions : the stator wake, the corner separation region and the endwall boundary layer. The extent of the corner separation increases as the incidence is raised from 0° to 5.4°. At 7.8°, a separated region at midspan appears. Dawkins (2021) estimates that the midspan profile starts separating from i=5.5°.

Figure 3.5 presents the pitchwise mass averaged integration of the loss cartographies as the incidence increases. The integration is performed on a single channel (investigated channel). Here again, the extension of the corner separation increases with the incidence, while the midspan losses remains at a similar level. The spanwise position of the maximum losses (white dots) appears to increase as the incidence is raised from 0° to 4.9°.

Finally, the evolution of the endwall losses with the incidence is presented in Figure 3.6. A smooth increase of the endwall losses is observed as the incidence is raised from 0° to 5.4°. Except for i=5.4°, the difference in the endwall losses between the investigated and neighbouring channels is below the experimental uncertainty, showing an excellent periodicity.

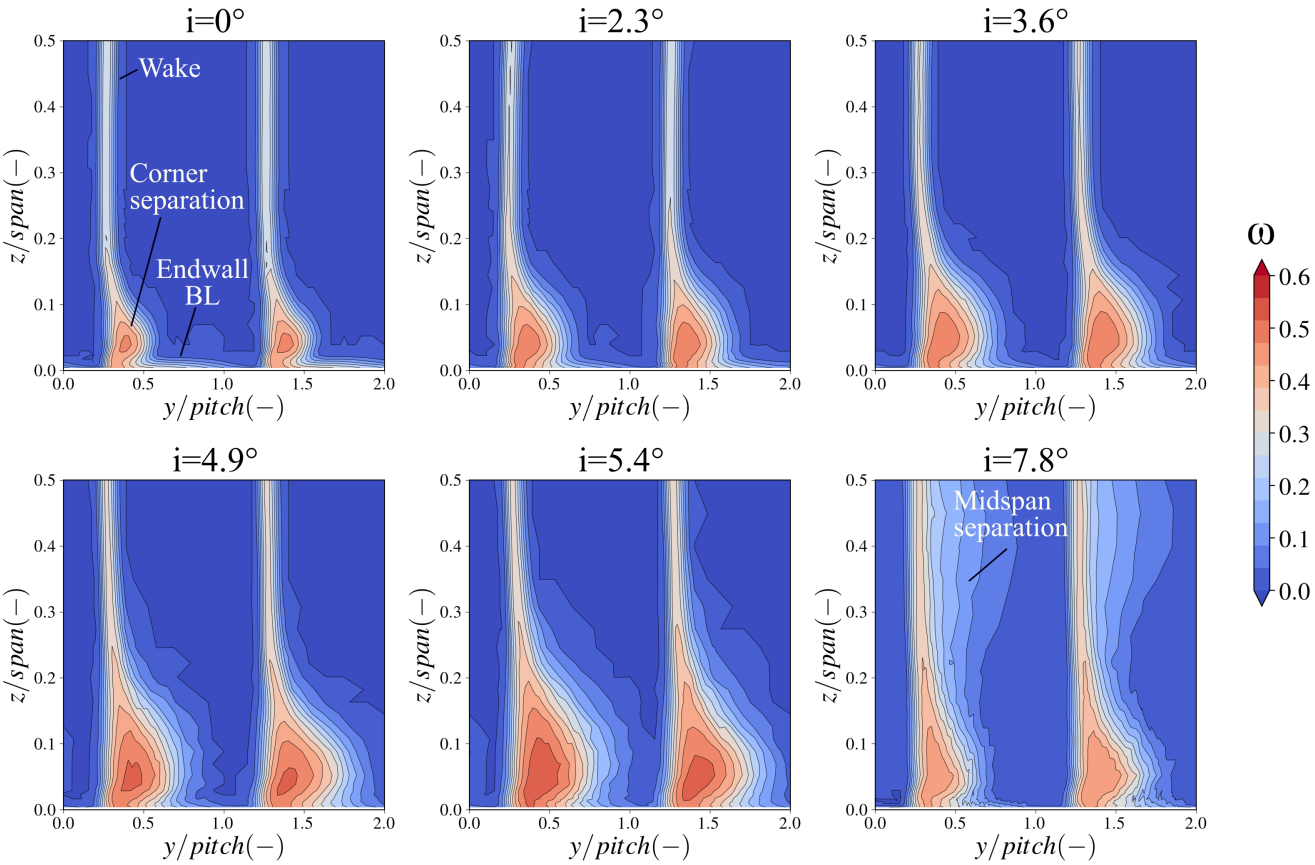

Figure 3.4: Cartographies of total pressure losses ω 0.2c downstream of the cascade. BL : Boundary Layer.

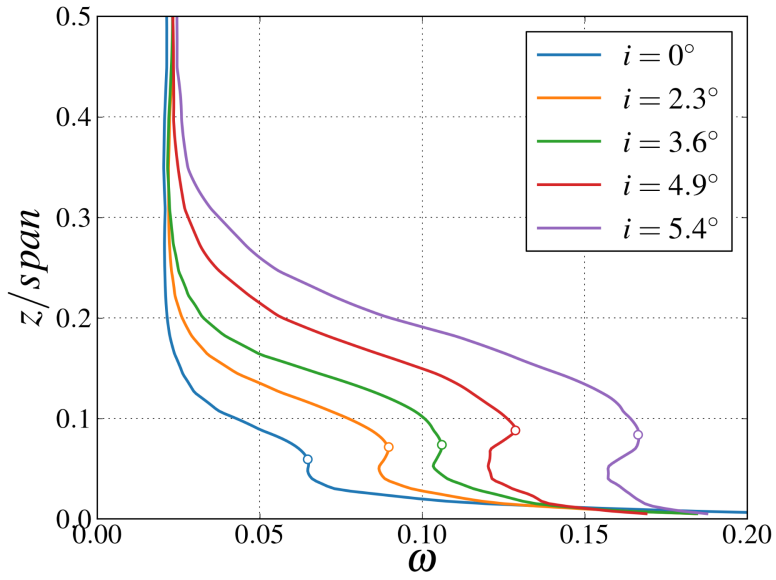

Figure 3.5: Spanwise evolution of total pressure losses ω as the incidence increases.

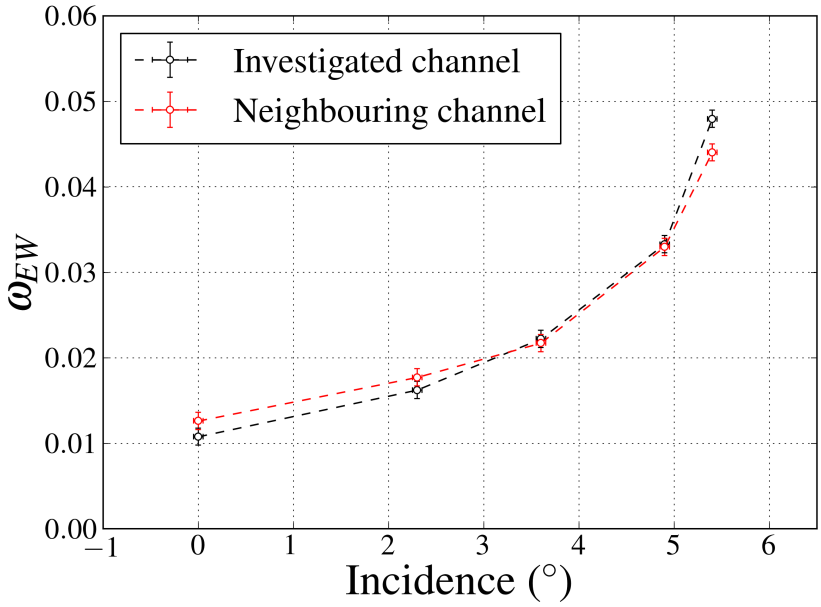

Figure 3.6: Evolution of endwall losses ω_{EW} with the incidence. Experimental data.

3.2.3 Blockage

The corner separation induces a region of low momentum, which results in an effect of blockage. To visualise the effect of blockage, the axial velocity distribution (V_x) is of interest. To get comparable results, the normalised axial velocity should be considered (axial velocity over upstream axial velocity). However, it is difficult experimentally to guarantee the mass flow conservation in a linear cascade. As a consequence, the surface averaged value of the normalised axial velocity might differ by a few percent from the theoretical value of 1 depending on the incidence and the settings of the rig. In order to compare the velocity gradients at different incidences (and later on with RANS results), the normalised axial velocity is itself normalised by its averaged value, resulting in the dimensionless axial velocity ($\widetilde{V_x}$) :

$$\widetilde{V_x} = \frac{V_x/V_{x,\infty}}{< V_x/V_{x,\infty} >} \tag{3.6}$$

with $V_{x,\infty}$ the upstream axial velocity and $< . >$ the surface average operator. Figure 3.7 presents cartographies of $\widetilde{V_x}$ downstream of the cascade. The gradients of the dimensionless velocity appear to be clearly related to the gradients of losses (see Figure 3.6), and the same three zones are observed (stator wake, corner separation, endwall boundary layer). The blockage induced by the corner separation increases as the incidence is raised from i=0° to i=5.4°, thus inducing an acceleration in the bulk region. An acceleration near the endwall is also observed for incidences 3.6° and 4.9°. At 7.8 °, the blockage induced by the midspan separation forces the flow to pass in the near endwall region, thus reducing the extension of the corner separation.

Figure 3.8 presents the pitchwise surface averaged integration of the dimensionless axial velocity for different incidences. This figure reveals the mass flow redistribution induced by the corner separation blockage. The upper limit of the blockage region increases from about 0.15 span (i=0°) to about 0.35 span (i=5.4°). The spanwise position of the maximum blockage (white dots) appears to increase when the incidence is raised, from about 0.05 span (i=0°) to about 0.08 span (i=5.4°).

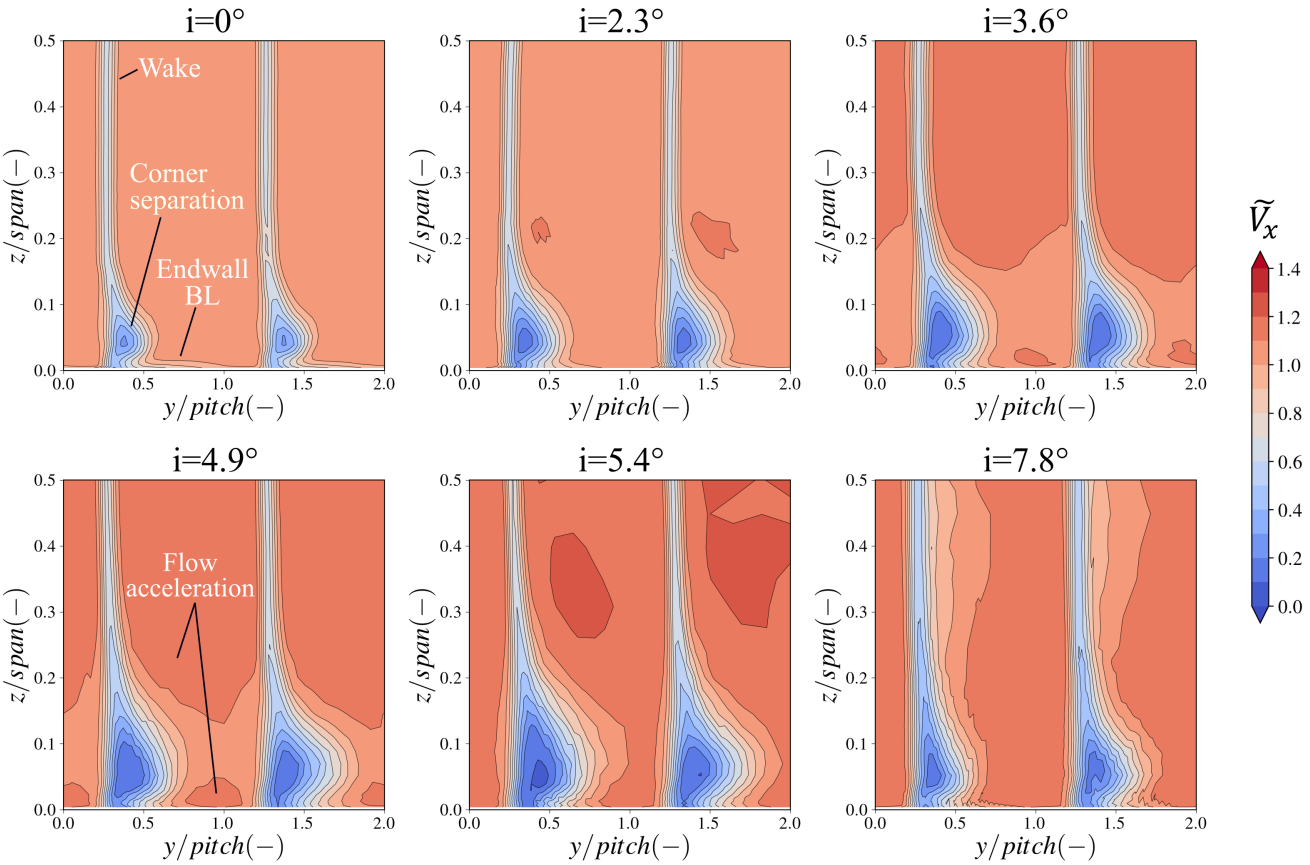

Figure 3.7: Cartographies of dimensionless velocity $\widetilde{V_x}$ 0.2c downstream of the cascade.

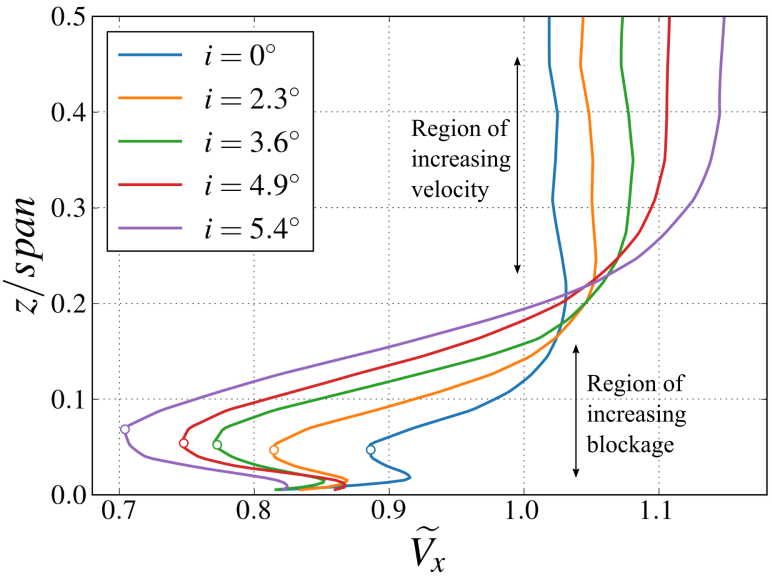

Figure 3.8: Spanwise evolution of dimensionless velocity $\widetilde{V_x}$ vs incidence.

3.2.4 Flow angles

The pitchwise flow angle (β) values downstream of the stator is of primary importance as it quantifies the deflection performed by the stator. The spanwise angle (ϕ) reveals regions of

spanwise flows. Both angles are used to visualise secondary flows, which are characterised with local angles different that the midspan angles.

Figure 3.9 presents the experimental cartographies of β. The region of over deflected flow near the endwall reveals the passage flow. The passage flow plays a major in role in the corner separation development as it drives the low momentum fluid developing on the endwall towards the stator suction side. A region of under deflected flow is observed in the core of the corner separation, and is referred to as the transverse flow in this work. This flow is induced to counter-balance the mass flow brought in the pitchwise direction by the passage flow, resulting in the so-called passage vortex (in pink).

Figure 3.10 presents the pitchwise surface averaged integration of β for different incidences, and reveals the spanwise extent of the under deflected region (compared to the midspan value). The maximum under deflection value and its corresponding spanwise position increases when the incidence is raised (white dots).

Figure 3.11 presents the experimental cartographies of ϕ. The values of ϕ are mainly negative (in blue) which reveals a descending flow towards the endwall. This descending motion results from the decreasing blockage of the corner separation passed the stator trailing edge. The concentrated regions of positive values (in red) in the corner region reveal the ascending component of the passage vortex. The extent of both regions increase when the incidence is raised, consistently with an increasing blockage and secondary flows intensity.

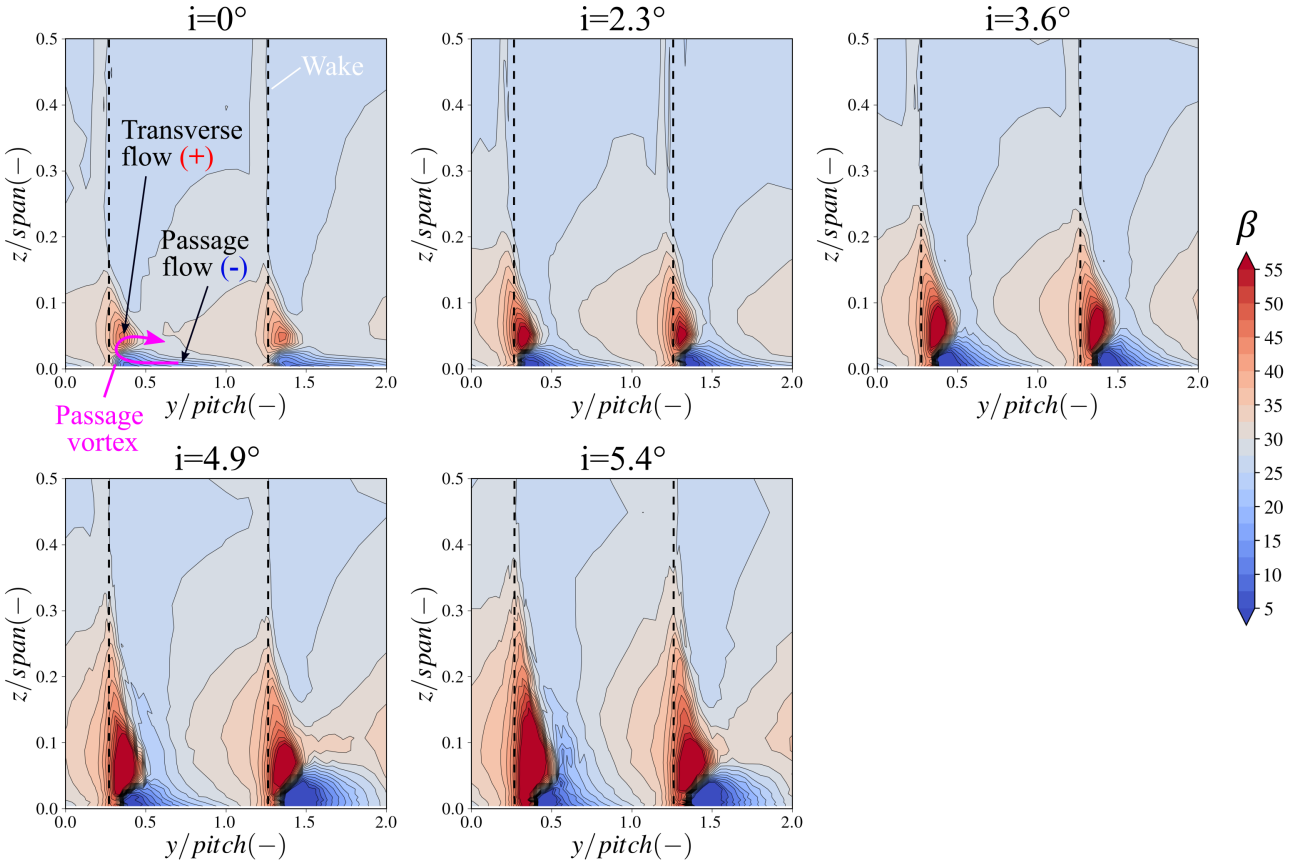

Figure 3.9: Cartographies of pitchwise angle β 0.2c downstream of the cascade.

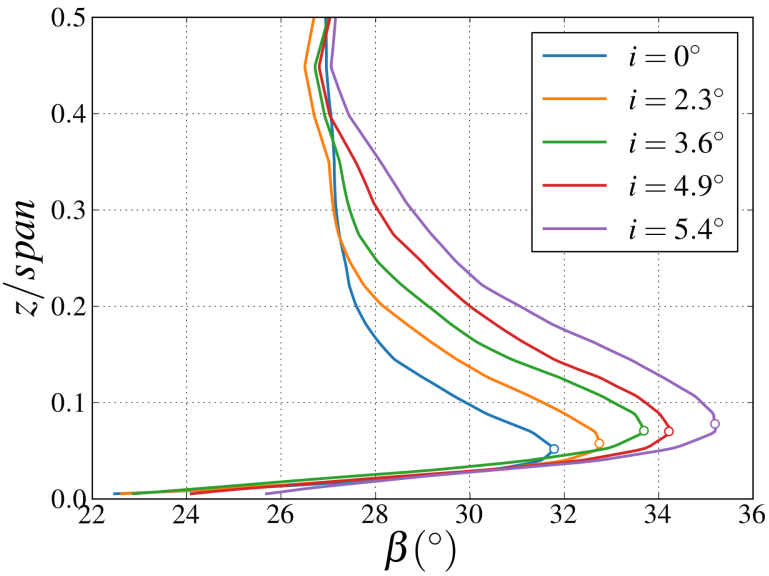

Figure 3.10: Spanwise evolution of pitchwise angle β vs incidence.

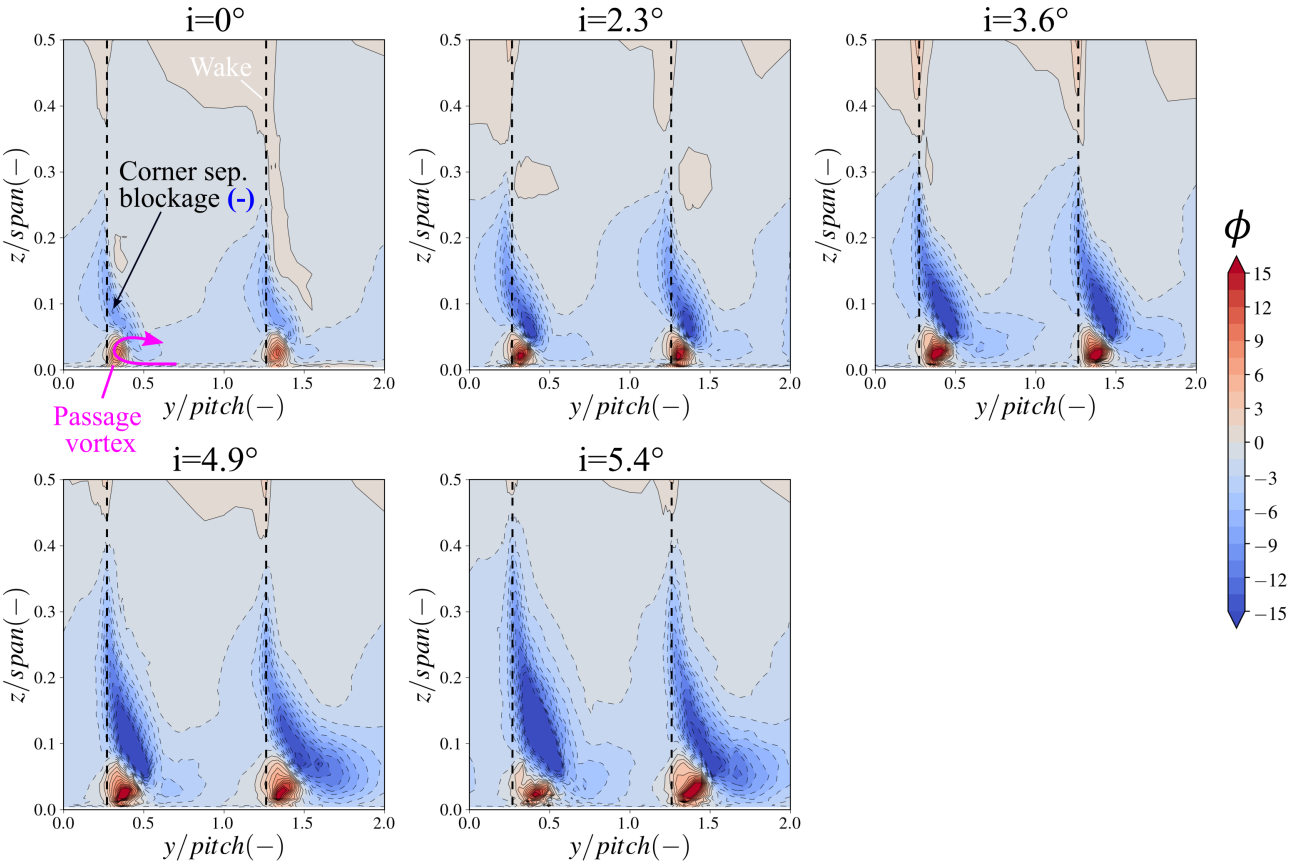

Figure 3.11: Cartographies of spanwise angle ϕ 0.2c downstream of the cascade.

3.2.5 Secondary streamlines

The secondary streamlines in the measurement plane are computed. They correspond to two-dimensional streamlines computed with the local velocity minus the midspan velocity at the

same pitchwise position. The objective of the secondary streamlines is to highlight the fluid motion which differs from the midspan behaviour, hence the motion of secondary flows. Global views (Figure 3.12) and zooms in the corner region of the investigated channel (Figure 3.13) are presented at design and high incidences.

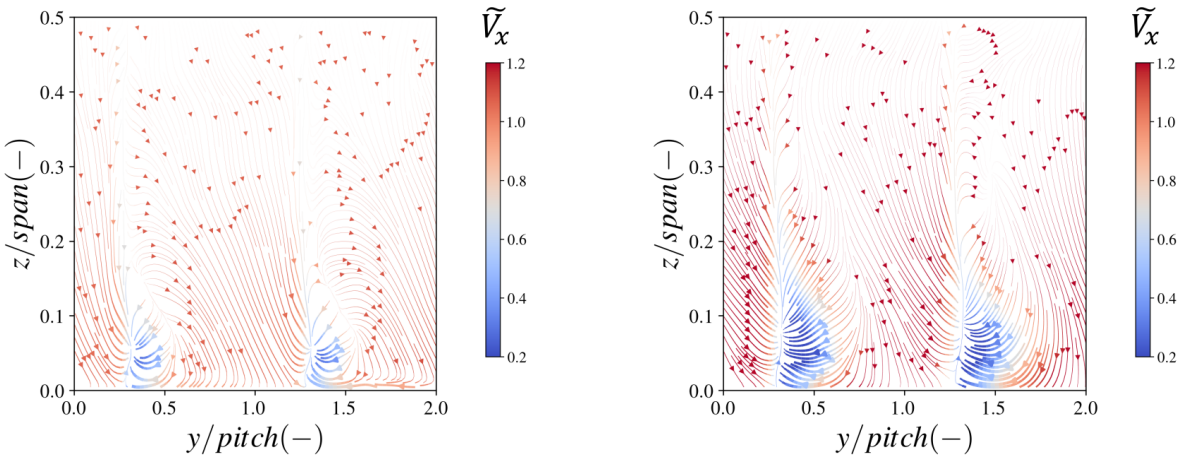

(a) i=0° (b) i=4.9°

Figure 3.12: Secondary streamlines. Coloured with $\widetilde{V_x}$.

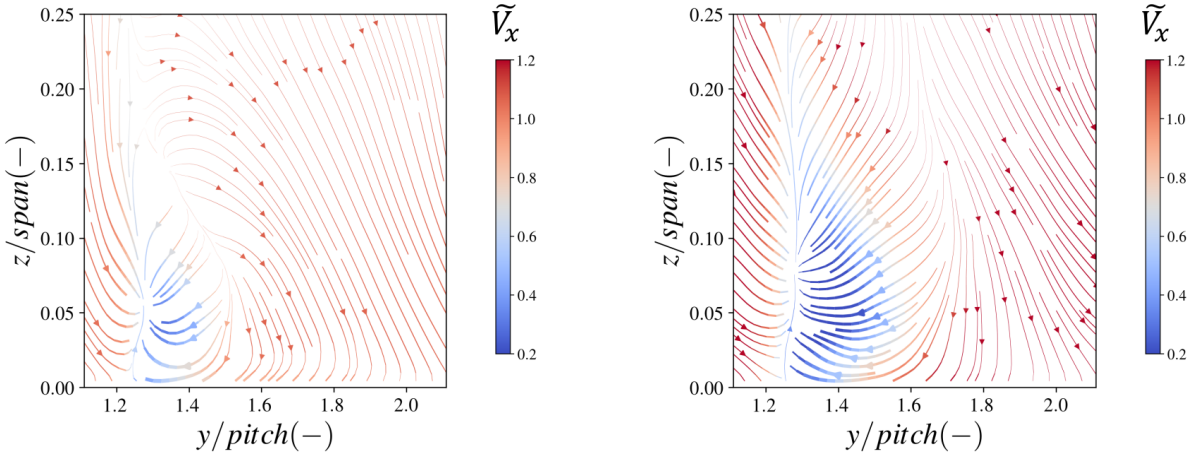

(a) i=0° (b) i=4.9°

Figure 3.13: Secondary streamlines zoomed in the corner region of the investigated channel. Coloured with $\widetilde{V_x}$.

3.2.6 Skin friction patterns

Finally, the skin friction patterns are investigated from results measured by Dawkins (2021). Figure 3.14 presents oil flow visualisations revealing the average topological organisation of skin friction lines. A separating line is systematically present on the suction side and is symptomatic of the blockage induced by the corner separation. More importantly, critical points are revealed on the endwall for incidences 2.3° and 4.9°, showing the presence of a double sided separation.

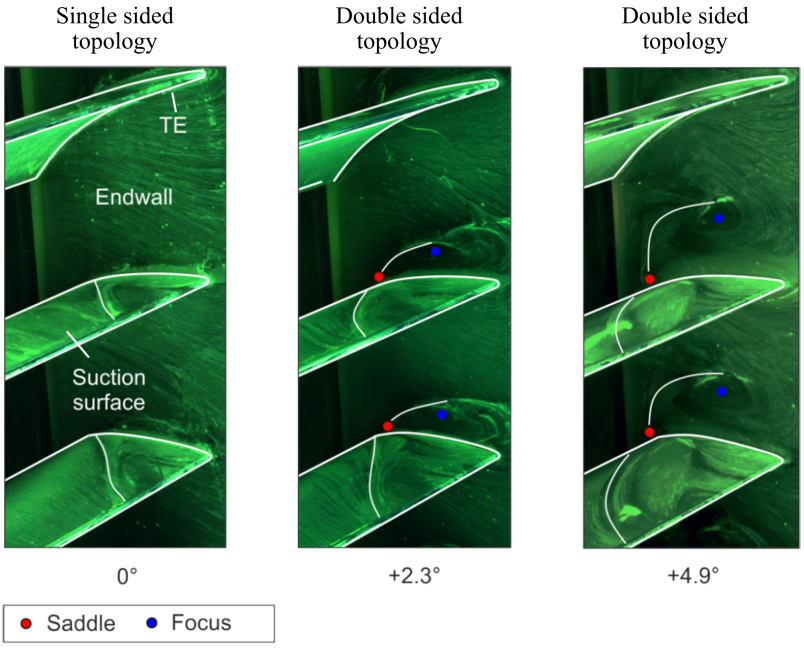

Figure 3.14: Oil flow visualisation of the suction side and the endwall. TE : Trailing Edge. Adapted from Dawkins (2021).

3.3 Numerical illustration

The three dimensional flow structures developing within the channel are difficult to investigate experimentally, and cannot be evaluated with the measurement techniques used in this thesis. An illustration based on RANS results is proposed to visualise the development and the effect of the corner separation within the channel (see Figure 3.15). The region of negative axial velocity (in yellow) gives an estimate of the extent of the separated region, which grows as the flow is convected downstream. Streamlines seeded in the pitchwise position near the stator leading edge illustrate the corner separation blockage compared to the midspan flow.

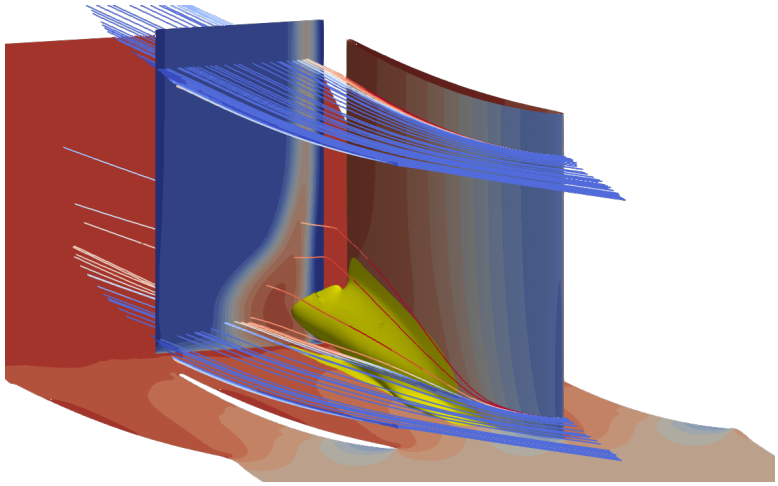

Figure 3.15: Illustration of corner separation development within the channel (RANS results, i=4.9°). Region of negative axial velocity (in yellow). Streamlines are coloured with total pressure losses, stator and endwall surfaces with $C_{p,s}$.

Chapter 4

Experimental methodology

In this chapter, the experimental methodology used to characterise the baseline configuration and the configuration with guide fins is presented. The control of the inflow conditions is first described (Section 4.1), followed by the description of the measurement technique (Section 4.2). The system enabling to insert guide fins in the rig is then presented (Section 4.3).

4.1 Controlling the rig

The main characteristics of the linear cascade used in this work are described in Section 3.1 and summarised in Table 3.1. This section describes the protocol used to monitor the operating flow conditions.

4.1.1 Overview of the control system

Figure 4.1 presents a schematic of the rig with key instrumentation. The inlet Reynolds number is measured far upstream of the cascade with two pitot tubes and two thermocouples located on both sides of the rig (Freestream temperature, Freestream pressure). The Reynolds number is adjusted with the inlet velocity. The upstream pressure references ($P_{t,\infty}$,$P_{s,\infty}$) are measured with a five-hole probe located at about one chord upstream of the cascade and one pitch above the investigated channel. The relative position of this probe with respect to the grid front is fixed. A five-hole probe was selected to avoid the need to re-align the probe with the flow when the grid front angle is varied. The incidence is checked using pressure measurements around the blade of reference, with a dedicated protocol detailed in Section 4.1.2. The boundary layer that develops on the endwall from the entrance of the rig is evacuated through a bleed slot (detailed in Figure 4.2). The bleeding flow is precisely adjusted so that the boundary layer developing on the endwall has a repeatable, well controlled thickness. The bleeding flow is adjusted with a throttle grid located at the exit of the rig. The throttle grid generates a fixed level of losses set by the user, which enables to adjust the static pressure upstream of the cascade and control the bleeding flow. The periodicity (similar flow in consecutive channels) is adjusted with a tailboard located at the exit of the rig. The latter induces a static pressure gradient in the pitchwise (blade to blade) direction depending on its relative orientation with respect to the front grid. This pressure gradient alters the mass flow entering in consecutive channels, and therefore the local incidence.

Finally, the operating flow conditions are set with the following steps :

1. Rotation of the front grid (incidence).

2. Adjustment of the tailboard position (periodicity).

3. Adjustment of the throttle level (bleeding flow adjustment).

These steps are performed iteratively as the two last steps modify the incidence value on the investigated blade. This is only necessary when targetting a new incidence value, the same combination of these elements yielding the same incidence.

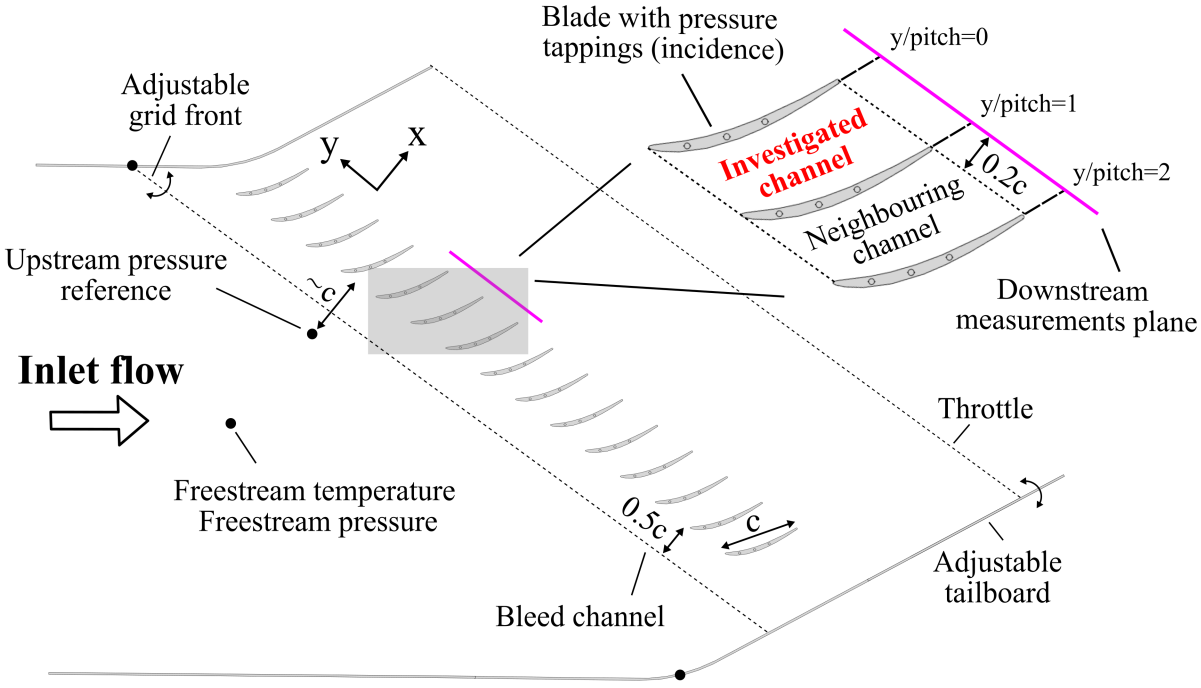

Figure 4.1: Schematic of cascade showing key elements.

4.1.2 Detailed settings

Inlet freestream Dawkins (2021) verified that the inlet freestream was uniform outside of the boundary layers. The inlet Reynolds number is set to 3.2×10^5, yielding a Mach number of about 0.11. At high incidence (i=4.9°), a variation in the endwall losses below 0.1% is observed when varying the Reynolds number by $\pm$ 10%, hence showing little sensitivity to that parameter. Several turbulence grid were tested by Dawkins (2021), and the retained set up yields a turbulence rate of 2.4% $\pm$ 0.1% 0.25c upstream of the cascade.

Inlet boundary layer thickness The inlet boundary layer strongly impacts the corner separation magnitude. To ensure repeatable inflow conditions, the inlet boundary layer developing on the walls of the rig upstream of the stator is bled off through lateral channels (see Figure 4.2). An exit throttle downstream of the stators is set up and enables to monitor the flow rate of the bleeding flow. In order to ensure a similar development of the new boundary layer on the hub, pressure tappings are mounted around the bleed lip (see Figure 4.3). For each incidence, the exit throttle is then altered until the stagnation point is located at tapping 4. As such, the pressure profile around the bleed lip is held constant, resulting in consistent boundary layer developments between runs. The efficiency of this system was assessed by Dawkins et al. (2021). Figure 4.4 shows this profile at 3 pitch locations.

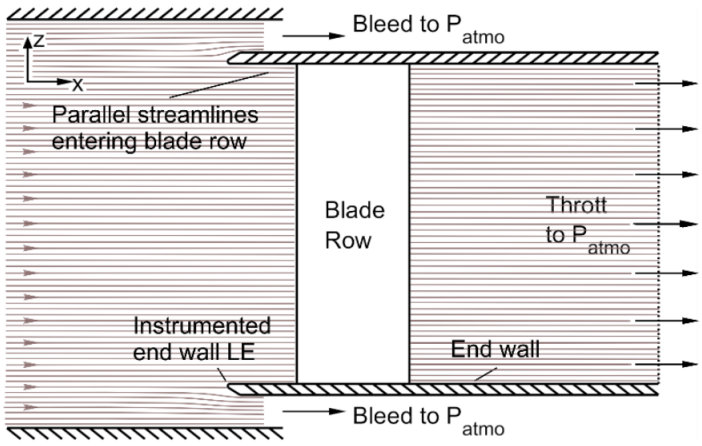

Figure 4.2: Details of the bleed slot. From (Dawkins, 2021).

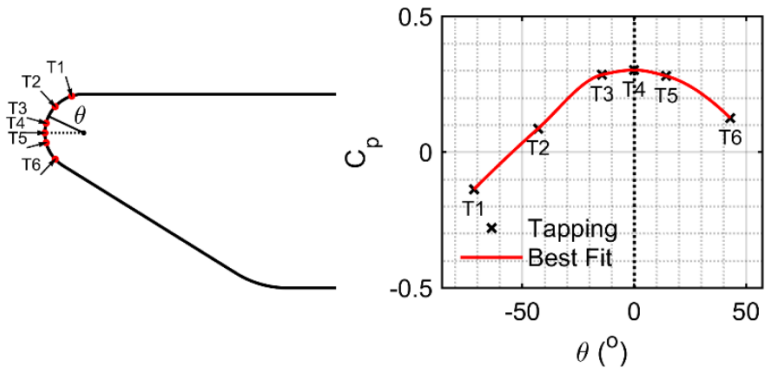

Figure 4.3: Pressure tappings positions and measurement in a case of balanced flow rates. From (Dawkins, 2021).

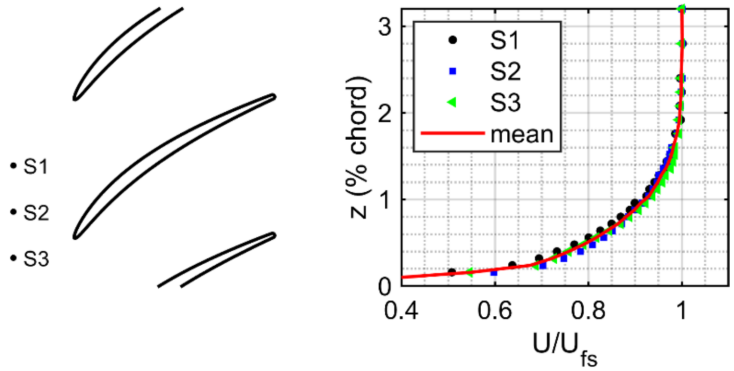

Figure 4.4: Inlet boundary layer profiles, measured 0.25c upstream of the cascade leading edge at 3 pitch locations. From (Dawkins et al., 2021).

Incidence The inflow incidence has a major effect on the corner separation phenomenon. It is determined using the midspan pressure distribution (25 pressure tappings). This distribution is compared to a database of MISES flow predictions of the midspan flow obtained at angle increments of 0.1°, which best fit provides the corresponding incidence. MISES is an Euler code coupled with a boundary layer solver (Drela, 1985). Its prediction of the pressure distribution

is particularly sensitive to the incidence and insensitive to the precision of the boundary layer prediction. This method therefore enables to accurately measure the incidence at midspan, with a precision of approximately ±0.1°, much better than with conventional probes.

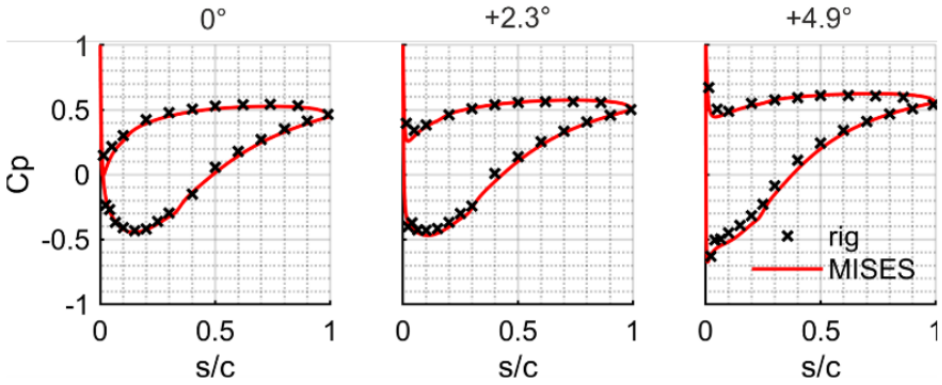

Figure 4.5: $C_{p,s}$ profiles at various incidences. Measurements (black crosses) vs MISES best fit (red lines). Incidences are deduced from the MISES database. From Dawkins et al. (2021).

Periodicity Setting the periodicity of a linear cascade is a delicate operation. In this work, the incidence is monitored on a single blade, and the incidences of the neighbouring blades are unknown. To ensure a reasonable periodicity of the channels, a first set of coarse measurements across two consecutive channels is performed at three spanwise locations : at midspan ($z/span = 0.5$), in the core loss ($z/span = 0.08$) and close to the endwall ($z/span = 0.01$). The grid front angle and the tailboard position are then iteratively adjusted in order to minimise the discrepancies between the values of the total pressure losses across these two channels (see Figure 4.14) while keeping the same incidence. Finally, detailed cartographies across these two channels from the hub to midspan are performed. The periodicity is then assessed *a posteriori* by comparing the integrated losses on each of these two channels.

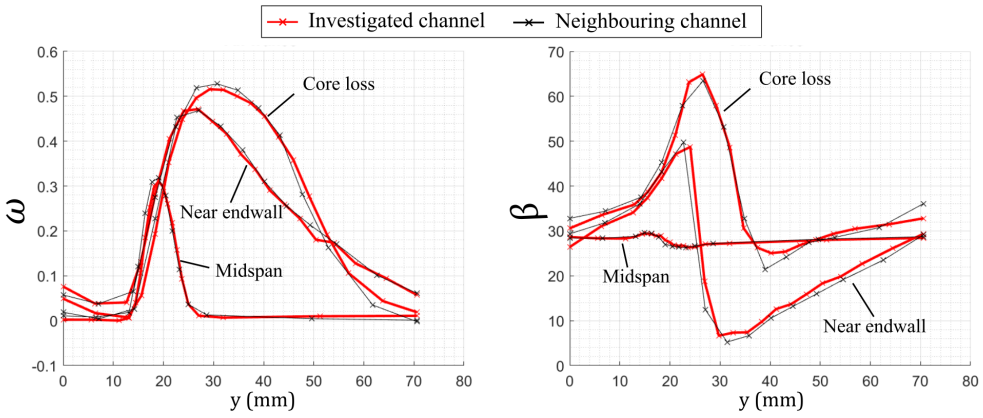

Figure 4.6: Periodicity evaluation. ω and β at i=4.9° across two consecutive channels. Investigated (red) and neighbouring (black) channels at various spanwise locations. From the author.

4.2 Measurement techniques

Five-hole probe measurements are performed 0.2c downstream of the cascade to quantify the aerodynamic performance of the rig. Examples of these measurements are presented in Section

3.2. The protocol implemented to perform these measurement is detailed in this section.

4.2.1 Pneumatic five-hole probe

A five-hole probe consists in five pressure tappings positioned on the head of a probe, on facets of different orientations (see Figure 4.7a). These pressure tappings enable to measure the local static pressure, total pressure and flow angles. Velocity components and magnitude are then deduced from these measurements.

Probe calibration The pressures and flow angles are deduced from the measured pressure on each pressure tapping and from calibration coefficients. The calibration coefficients are generated during a calibration step, where the probe is placed in a precisely known flow. Calibration maps are generated, such as the one presented in Figure 4.8. During this calibration step, the pitchwise and spanwise flow angles are varied from -45° to +45° by steps of 3°. The values of the calibration coefficients at each couple of angles is measured and constitutes the calibration data.

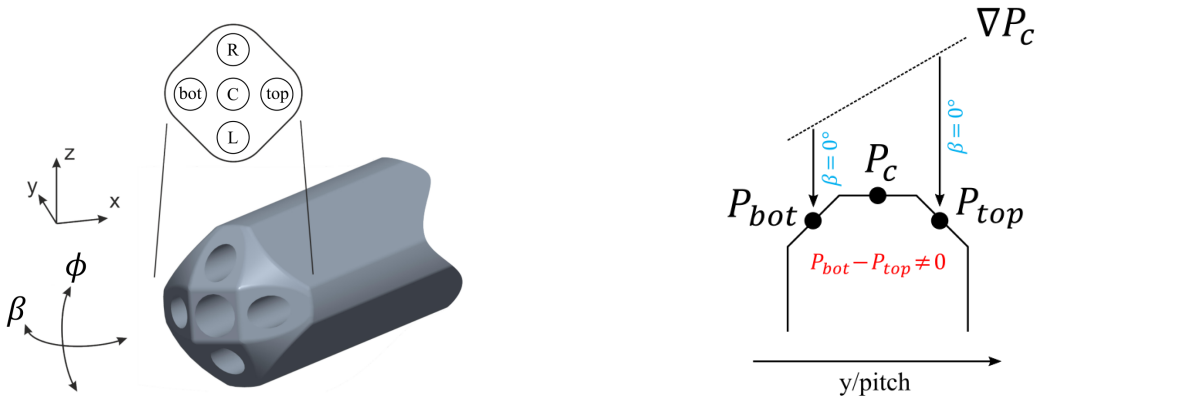

(a) Five-hole probe head details.

(b) Illustration of the effect of pressure gradient on angle measurement.

Figure 4.7: Five-hole probe illustration.

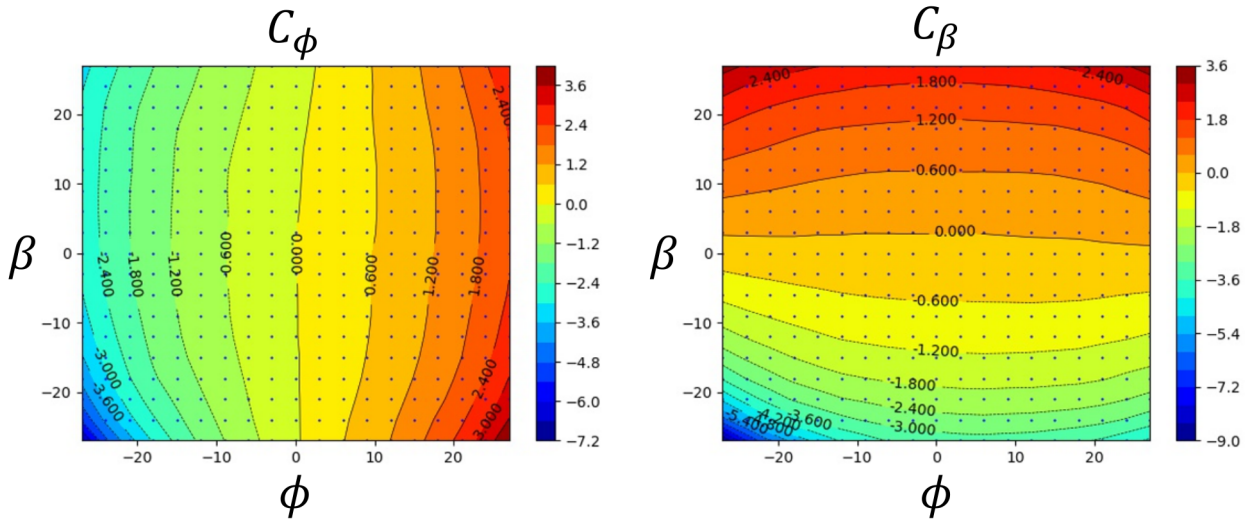

Figure 4.8: Calibration maps.

The relations between the local pressures, calibration coefficients and total pressure, static pressure and flow angles are given with the following equations :

$$\bar{P_s} = \frac{P_l + P_r + P_{top} + P_{bot}}{4} \tag{4.1}$$

$$C_\beta = \frac{P_{bot} - P_{top}}{P_c - \bar{P_s}} \tag{4.2}$$

$$C_\phi = \frac{P_l - P_r}{P_c - \bar{P_s}} \tag{4.3}$$

$$C_{total} = \frac{P_c - P_{t,\infty}}{P_c - \bar{P_s}} \tag{4.4}$$

$$C_{static} = \frac{\bar{P_s} - P_{s,\infty}}{P_c - \bar{P_s}} \tag{4.5}$$

$$P_t = P_c - C_{total}(P_c - \bar{P_s}) \tag{4.6}$$

$$P_s = \bar{P_s} - C_{static}(P_c - \bar{P_s}) \tag{4.7}$$

where P_c, P_l, P_r, P_{top} and P_{bot} are the pressure at centre, left, right, top and bottom holes, respectively and C_β and C_ϕ are the angle coefficients of β (pitchwise) and ϕ (spanwise) flow angles. $P_{t,\infty}$ and $P_{s,\infty}$ respectively refer to the upstream total and static pressures. In order to compute β, ϕ, P_s and P_t, the following steps are performed :

1. Measurement of $P_{bot} - P_{top}$, $P_l - P_r$ and P_c.

2. Computation of $\bar{P_s}$, C_β, C_ϕ.

3. Interpolation of the calibration data to deduce (β,ϕ) from (C_β,C_ϕ).

4. Interpolation of the calibration data to deduce (C_{total},C_{static}) from (β,ϕ).

5. Computation of P_t and P_s.

Pressure gradient correction A uniform flow is used to calibrate the probe, without transverse pressure or velocity gradients. For a perfectly symmetric probe, $P_{top} = P_{bot}$ thus induces $\beta = 0$ and $P_r = P_l$ induces $\phi = 0$. During the measurement, if the real value of β is 0 but that a pitchwise pressure gradient exists, $P_{top} \neq P_{bot}$ because of the finite size of the probe head, and the measured value of β is non zero (see Figure 4.7b). Ma (2012) proposed to take into account the effect of the total pressure gradient with the gradient of P_c : P_c values are interpolated at each probe hole location, and the gradient of P_c is subtracted to the pressure difference measured. Moreover, the values of lateral pressures are interpolated at the location of the centre hole in the computation of the average static pressure coefficient ($\bar{P_s}$) to replicate an infinitely thin probe. This yields the following corrected coefficients :

$$\bar{P_s}' = (P_{l\to c} + P_{r\to c} + P_{top\to c} + P_{bot\to c})/4 \tag{4.8}$$

$$C'_\beta = \frac{P_{bot} - P_{top}}{P_c - \bar{P_s}'} - \frac{P_{c\to bot} - P_{c\to top}}{P_c - \bar{P_s}'} \tag{4.9}$$

$$C'_\phi = \frac{P_l - P_r}{P_c - \bar{P_s}'} - \frac{P_{c\to l} - P_{c\to r}}{P_c - \bar{P_s}'} \tag{4.10}$$

$$C'_{total} = \frac{P_c - P_{t,\infty}}{P_c - \bar{P_s}'} \tag{4.11}$$

$$C'_{static} = \frac{\bar{P_s}' - P_{s,\infty}}{P_c - \bar{P_s}'} \tag{4.12}$$

$$P'_t = P_c - C'_{total}(P_c - \bar{P_s}') \tag{4.13}$$

$$P'_s = \bar{P_s}' - C'_{static}(P_c - \bar{P_s}') \tag{4.14}$$

The superscript (') denotes the corrected coefficients. The parameters indexed with an arrow correspond to interpolated parameters. $P_{c\to l}$, $P_{c\to r}$, $P_{c\to top}$ and $P_{c\to bot}$ are interpolated values of P_c at left, right, top and bottom hole locations, respectively. $P_{l\to c}$, $P_{r\to c}$, $P_{top\to c}$, $P_{bot\to c}$ denote the interpolated values of P_l, P_r, P_{top}, P_{bot} at the centre hole position. Figure 4.9 illustrates the effect of this correction on a measurement at midspan, across one pitch. As expected, the corrective terms act only in the region with a total pressure gradient ($y/pitch \in [0.2, 0.4]$). As this gradient evolves only in the pitchwise direction, only β values are affected. In this example, the pressure gradient correction reduces the gradient of β. The resulting evolution is more consistent with typical CFD results, where numerical probes are infinitely thin.

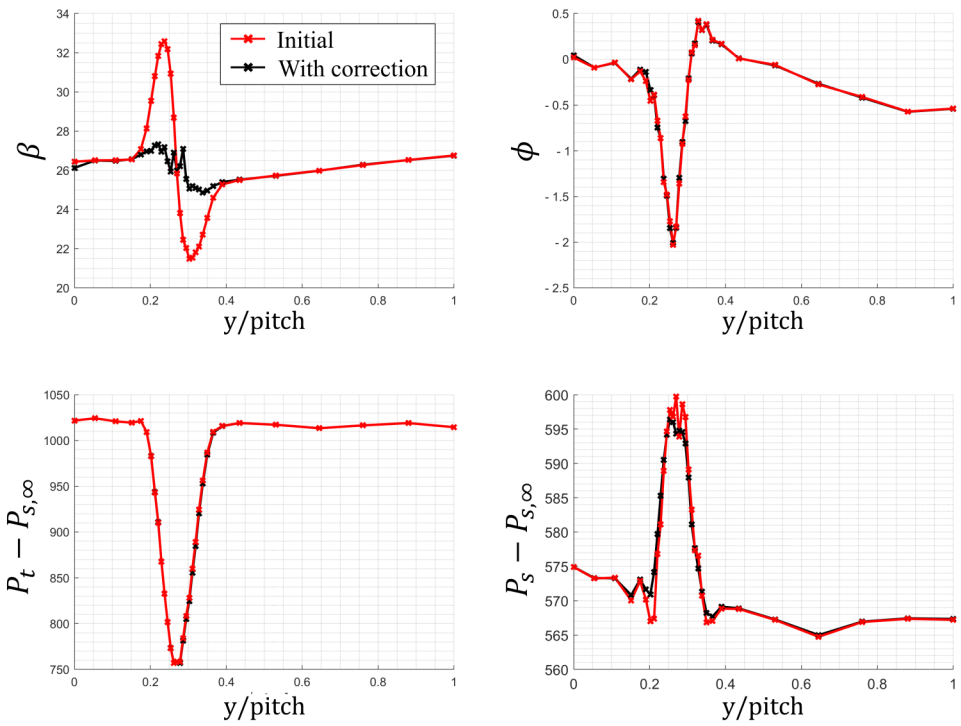

Figure 4.9: Effects of pressure gradient correction on midspan values of β, ϕ, P_t, P_s. Investigated channel only.

Probe sampling grid Measurements are recorded using the sampling grid shown in Figure 4.10, with sample points clustered in regions of high total pressure gradients. The investigated channel is refined with 825 samples, the neighbouring one with 550 samples.

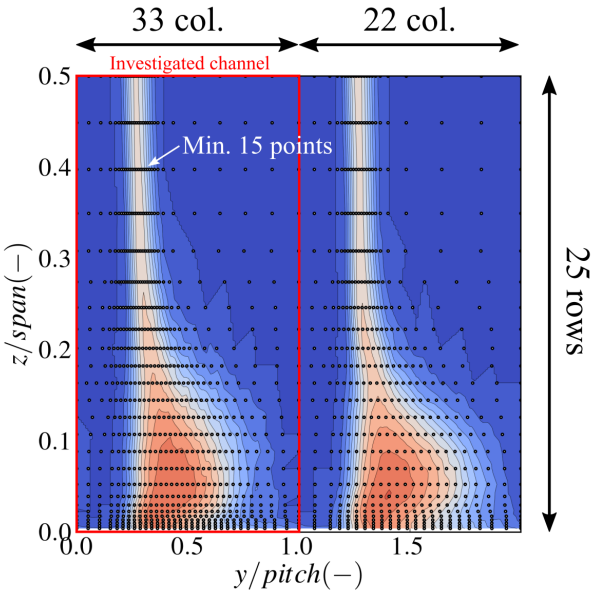

Figure 4.10: Probe sampling grid. Total pressure losses at i=4.9°.

4.2.2 Uncertainty quantification

In this work, the corner separation is notably characterised with the values of the endwall losses ω_{EW}. The uncertainties related to these quantities must therefore be evaluated. The following approach is undertaken by the author, and is inspired from Dawkins (2021).

Acquisition uncertainty For a single run, the uncertainty of the acquisition system (five-hole probe and pressure transducer) is evaluated using a Monte-Carlo approach. This uncertainty comes from the pressure acquisition system during a) the measurement b) the recording of the calibration data. The same pressure acquisition system is used during the measurement and the calibration process, and is characterised with an uncertainty of $\pm 1.25\ Pa$. The calibration angles were measured with a precision of $\pm$ 0.1°. The measured pressures and the calibration data were randomly altered within these ranges for a given cartography at i=4.9°. 500 altered cartographies are obtained, yielding a Gaussian distribution of ω_{EW} with a thickness of $\pm 2\sigma = 0.025\%$ (equivalent to $\pm 0.25 Pa$) of total pressure losses.

Repeatability The downstream five-hole probe was mounted and unmounted several times during the experimental campaign, which spanned over a one-year period. During this campaign, the average pitchwise angle value at midspan was found to vary by $\pm$ 1.5°. To evaluate the effect of such a variation, the pitchwise and spanwise angle distributions measured at i=4.9° were artificially offset with a variation of $\pm$ 1.5°, resulting in a variation in the endwall losses of $\pm$ 0.05%. All configurations (baseline and tested guide fins) were then ran consecutively within a single day. The average pitchwise angle at midspan varies by $\pm$ 0.2° in this case. Because of the low impact of an angle offset on the endwall losses and to facilitate the angle comparisons, the cartographies were offset so that their midspan angles match the ones measured during these runs.

Systematic error In this linear cascade, the settings maximising the periodicity in terms of endwall losses induce a systematic error in the integrated mass flow rate. The axial velocity is measured downstream of the cascade and divided with the upstream axial velocity of reference, measured at the same instant. Integrating this quantity should result in a value of 1 by mass flow conservation, but values of 1.02±0.01 at i=0° and 1.09±0.02 at i=4.9° are found. This discrepancy is suspected to come from an error in the upstream velocity measurement and not from an additional incoming flow. Indeed, the control of the pressure tappings around the bleed lip ensures that the bleeding flow is correctly set, the average value of the spanwise angle at midspan is systematically close to 0° and an excellent periodicity in the pitchwise angle is found at several spanwise locations. To assess the effect of this error on the endwall losses, the inlet axial velocity is varied by ± 10%. A variation of ω_{EW} of about ± 0.1% is measured. In order to compare the velocity gradients at different incidences and with RANS results, the normalised axial velocity is divided by its averaged values, resulting in the dimensionless axial velocity ($\widetilde{V_x}$, see Equation 3.6).
The uncertainty in the values of the endwall losses is finally estimated to about ± 0.1%. The performance of guide fins will be assessed as the difference in endwall losses obtained with a guide fin and in the baseline configuration. The uncertainty of this quantity is estimated with the square root of the sum of the squares of the uncertainty on endwall loss measurements, hence to about ± 0.15%.

4.3 Guide fin insertion system

An insertion system is designed to place guide fins on the endwall of the cascade with two main objectives : a) to easily insert and remove a new set of guide fins b) to least possible affect the flow.

This system is composed of a fixed part fitting the stator profile in which a removable part containing the guide fin can be slid in. Its geometrical characteristics are presented in Figure 4.11. Figure 4.12 illustrates this principle and 4.13 its implementation in the cascade. The system is 2 mm thick, yielding a section reduction of about 1.3%. Its upstream part starts at an axial position 0.29c upstream of the stator leading edge. It consists of a ramp that smoothly brings the flow up, from the endwall to the top of the platform, with an angle seen by the flow of 3.8°. This system, including the guide fin, is manufactured with a Fuse Deposition Modelling (FDM) method, using ABS plastic. A nozzle of 0.4 mm diameter is used, with a resolution of 0.09 mm per layer. With this system, a complete set of 12 guide fins is manufactured in about 30 hours, which is much faster than with a conventional process. In order to limit extra losses and the inlet boundary layer thickening, the fixed part is sanded down to a rugosity of $0.5\mu m$.

The same operating points are reached with and without the insertion system. In order to assess the effect of the insertion system on the flow, flat platforms are slid in the insertion system to mimic the initial baseline configuration (see Figure 4.12). This modified baseline is characterised experimentally by the author, and is the one used in this work. The gains measured when replacing the flat platform by a platform with a guide fin are thus independent of the insertion system. Figure 4.14 compares the evolution of the endwall losses as the incidence increases, with the initial baseline and the modified baseline. The same evolution of the losses is retrieved. A small increase in losses is observed, which is understandable. This offset is below the experimental uncertainty for the investigated channel, hence small. Moreover, the periodicity of the rig remains excellent up to 4.9°.

Finally, several guide fins are manufactured and tested in this work. 6 neighbouring channels are equipped with the insertion system, on both endwalls to maintain the spanwise symmetry of the configuration. The 6 equipped channels are chosen so that the investigated and the neighbouring channels are the middle ones (see Figure 4.13). The periodicity is found to be excellent with the tested guide fins, with a variation in endwall losses below 0.1% between the investigated and neighbouring channels. This proves *a posteriori* that equipping 6 channels is sufficient.

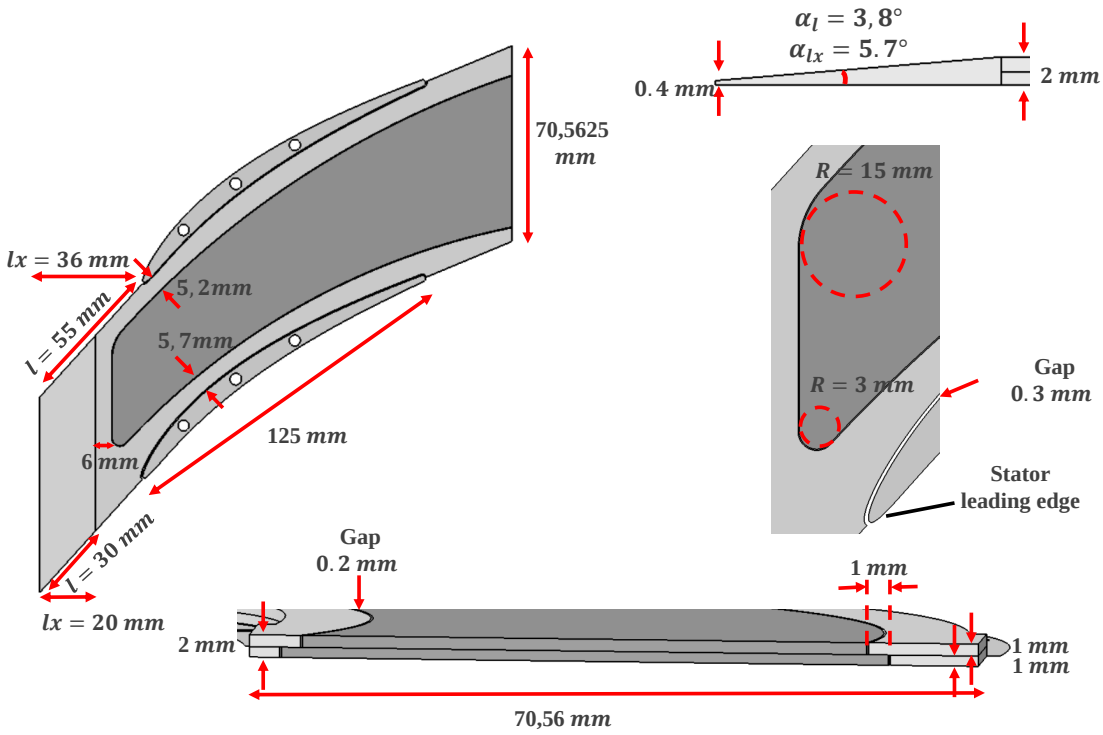

Figure 4.11: Geometrical description of the insertion system. Gray : fixed part. Black : removable platform.

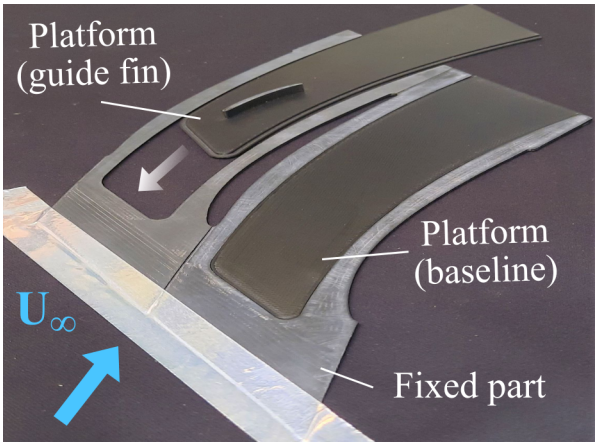

Figure 4.12: Insertion system outside of the rig. Baseline and guide fin configurations.

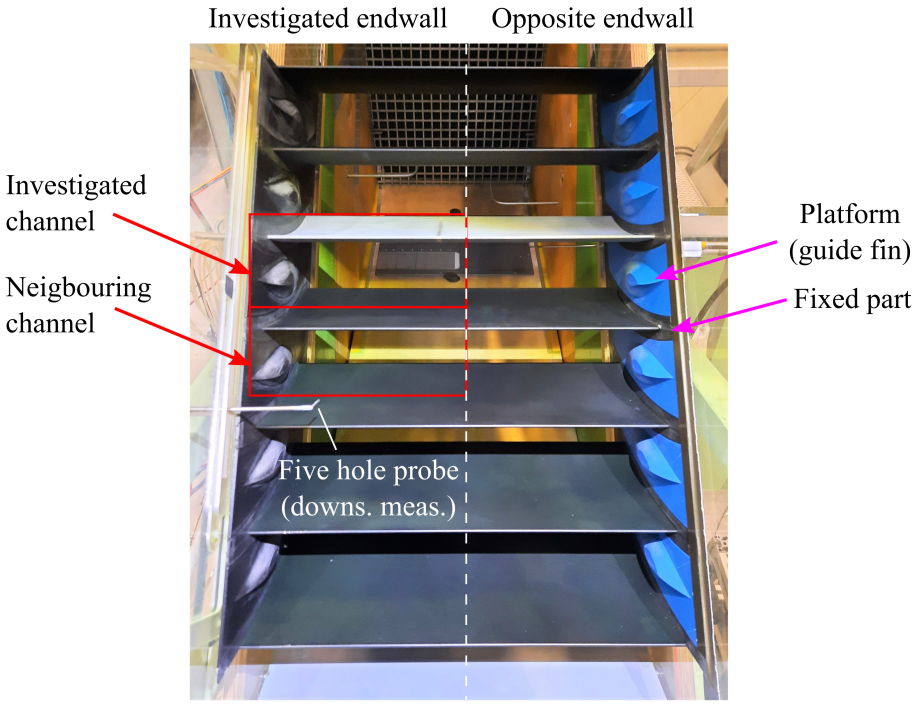

Figure 4.13: Rear view of the cascade equipped with the system.

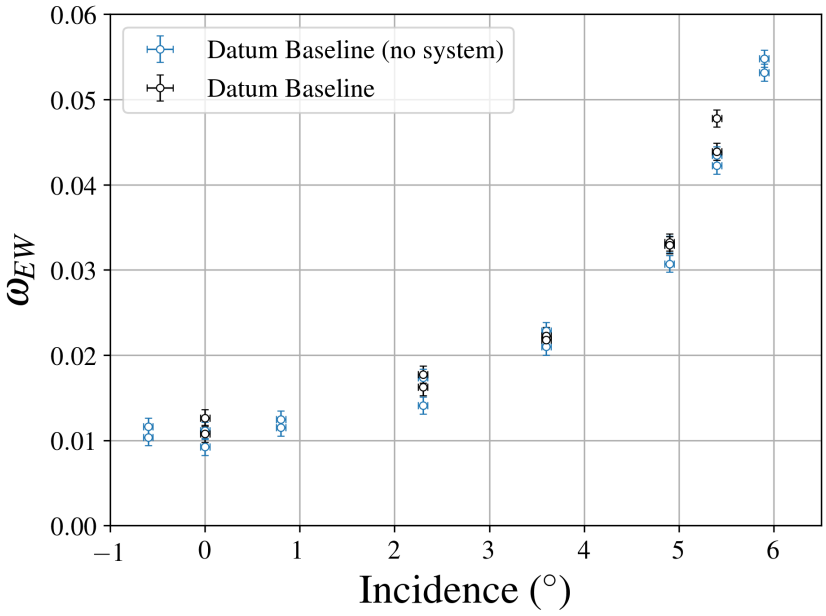

Figure 4.14: Effect of the insertion system on the endwall losses. Baseline configuration.

Chapter 5

Numerical methodology

This chapter describes the numerical methodology implemented for evaluating guide fins. This methodology goes from the definition of the guide fin geometries to the simulation of their effects on the flow field. The first main objective of this methodology is to evaluate the influence of guide fins on the physics of the corner separation. The second main objective is to characterise the guide fins performance with integral values in order to feed an optimisation process. This process forbids the use of high fidelity methods such as LES because of their computational cost. RANS methods are more affordable, but show some limits when it comes to predicting separations, as pointed out in the literature review (Section 1.3.2). This chapter discusses these limits in the current framework and show encouraging results. RANS is therefore considered as an interesting compromise.

This numerical methodology can be seen as a numerical chain that associates a set of parameters to CFD results through several steps. These steps are a) the conversion of guide fin parameters into a CAD surface b) the meshing process c) the RANS evaluation (see Figure 5.1). The entire process must be automated and robust as numerous guide fins of *a priori* unknown shapes will be assessed.

The complexity of an optimisation process notably depends on the dimension of the parameter space to be explored. Section 5.1 presents a parametrisation defining various guide fin geometries with a restrained number of parameters to ease this process. Two sets of parameters are introduced : the *construction* parameter set and the *optimisation* parameter set. Construction parameters define basic aerodynamic shapes (Section 5.1.1). Optimisation parameters constrains these aerodynamic shapes to meet geometrical constraints and basic aerodynamic design rules (Section 5.1.2).

Evaluating guide fins of various shapes is challenging for conventional, structured meshing approaches. Hybrid meshes, including structured and unstructured zones, are used to ensure a high quality and a robust meshing process. The methodology to create hybrid meshes is presented in Section 5.2.

Finally, the numerical set up used to compute RANS simulations is described in Section 5.3. The effect of the turbulence model and of the Quadrative Constitutive Relation (QCR) correction are notably discussed.



Figure 5.1: Chain overview.

5.1 Guide fin parametrisation

Guide fins must feature aerodynamic characteristics. For that purpose, a set of 15 construction parameters is introduced, and define a guide fin as a set of stacked aerodynamic aerofoils. In practice, only the tip and the hub aerofoils are parametrised, and intermediate aerofoils are deduced *a posteriori*. Moreover, guide fins must be placed and positioned consistently with the stator, and respect basic aerodynamic rules. A set of 15 optimisation parameters is thus define to introduce these constraints.

Examples of guide fins of various shapes obtained with these parametrisations are shown in Figure 5.2. For the sake of clarity, the definitions of the parameters used in this section are summarised in Table 5.1.

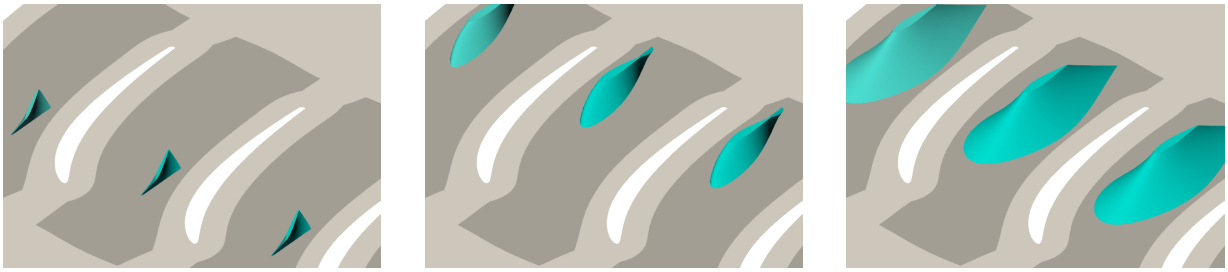

Figure 5.2: Example of various guide fins.

Part	Construction parameters		Optimisation parameters	
Hub	$\beta_{1,H}$ (°)	Metal angle at LE	$\Delta\beta_{1,H}$ (°)	Relative metal angle at LE with respect to the local camber
	$\beta_{2,H}$ (°)	Metal angle at TE	$\beta_{2,pc_\beta1}$ (-)	Metal angle at TE as a percentage of the metal angle at LE
	$x_{M,H}$ (%c_{GF})	Relative position of maximum of camber	$x_{M,H}$ (%c_{GF})	Relative position of maximum of camber
	$t_{M,H}$ (%c_{GF})	Relative maximum thickness	$t_{M,H}$ (%c_{GF})	Relative maximum thickness
	$c_{GF,H}$ (%c)	Chord	$\widetilde{c_{GF}}$ (-)	Percentage of authorised chord at hub
	$x_{bary,H}$ (%c)	Barycenter position (engine axis)	u (-)	LE position on authorised surface (streamwise direction)
	$y_{bary,H}$ (%c)	Barycenter position (azimuthal axis)	v (-)	LE position on authorised surface (pitchwise direction)
Tip	$\beta_{1,T}$ (°)	Metal angle at LE	$\Delta\beta_{1,T}$ (°)	Relative metal angle at LE with respect to the local camber
	$\beta_{2,T}$ (°)	Metal angle at TE	$\Delta\beta_{2,T}$ (°)	Relative metal angle at TE with respect to the local camber
	$x_{M,T}$ (%c_{GF})	Relative position of maximum of camber	$x_{M,T}$ (%c_{GF})	Relative position of maximum of camber
	$t_{M,T}$ (%c_{GF})	Relative maximum thickness	$t_{M,T,rel}$ (-)	Percentage of maximum thickness with respect to hub thickness
	$c_{GF,T}$ (%c)	Chord	$c_{GF,T,rel}$ (-)	Percentage of chord with respect to hub chord
	$x_{bary,T}$ (%c)	Barycenter position (engine axis)	λ_{sweep} (°)	Sweep angle (along the hub chord direction)
	$y_{bary,T}$ (%c)	Barycenter position (azimuthal axis)	λ_{lean} (°)	Lean angle (normal to the hub chord direction)
Height	H_{GF} (%c)	GF height	H_{GF} (%c)	GF height

Re-definition due to meshing constraint

Re-definition due to aerodynamic expertise

Table 5.1: Definitions of parameters sets defining guide fins. Parameters in white are common to both sets. $\%c$ / $\%c_{GF}$: percentage of stator chord / guide fin chord. LE : Leading Edge, TE : Trailing Edge, GF : Guide Fin. H refers to the Hub aerofoil, T to the Tip aerofoil.

5.1.1 Parametrisation of an aerodynamic shape

In order to ensure an aerodynamic shape, a guide fin is built using several aerofoils stacked at different spanwise locations, from hub to tip. So as to reduce the total number of parameters, it is chosen to build only one parametrised aerofoil, and to let the parameters values vary with the spanwise position. This parametrised aerofoil is built from a parametrised thickness law and a parametrised camber law. A thickness law of reference is built with the BEZIER-Parsec 3333 parametrisation described in (Salunke et al., 2014), in which geometrical parameters can be easily set and tuned. This parametrisation is based on a combination of splines of order 3, which notably guarantees continuity of curvature at the leading edge. In order to stay close to the simplest thickness laws, no inflexion point are permitted. From then, the parametrised thickness law is obtained by tuning a single parameter t_M*, representative of the maximum thickness value relative to the aerofoil chord. A circular trailing edge (TE) is added so that the dimensioned aerofoil has a constant trailing edge thickness, fixed to the smallest manufacturable value ($y_{TE,abs}$=0.5mm). The camber law is obtained from a spline of order 2 constrained by three parameters: the position of the maximum of camber (x_M) and the values of the metal angles at the leading edge (β_1) and trailing edge (β_2). Examples of thickness and camber laws obtained with this method are shown in Figure 5.3.

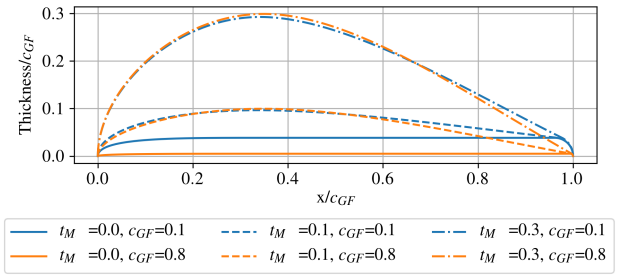

(a) Thickness laws for thin, medium and thick airfoils, for small and large chords.

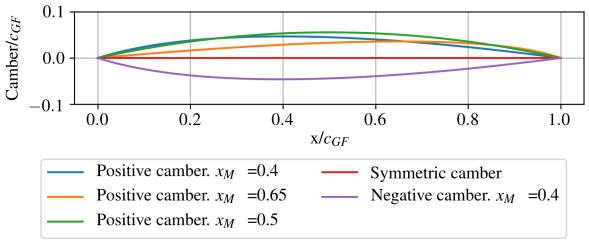

(b) Front-loaded, rear-loaded, symmetric and negative camber laws (without stagger angle).

Figure 5.3: Examples of thickness and camber laws. t_M is expressed in guide fin chord unit and c_{GF} in stator chord unit.

Providing a chord value (c_{GF}) and the barycentre position (x_{bary},y_{bary}) enable to scale and position the aerofoil. An aerofoil parametrised with 7 parameters is thus obtained (see Figure 5.4). A hub and a tip aerofoils are defined with 14 parameters. A linear evolution of the aerofoil parameters with the spanwise position is imposed to generate intermediate aerofoils. This process requires the guide fin height (H_{GF}). The resulting guide fin is therefore parametrised with 15 parameters, referred to as construction parameters. An example of hub, tip and intermediate aerofoils is shown in Figure 5.5.

*In order to bound the thickness parameter t_M with a physical value, the true thickness of the aerofoil is computed as $t_{M,true} = \frac{t_M \times c_{GF} + y_{TE,abs}}{c_{GF}}$. As such, $t_M = 0 \Rightarrow t_{M,true} \times c_{GF} = y_{TE,abs}$. Moreover, $t_M \times c_{GF} >> y_{TE,abs} \Rightarrow t_M \simeq t_{M,true}$. This is almost always true in this work, as $c_{GF} \geq 0.2c$ and $y_{TE,abs}$=0.04c.

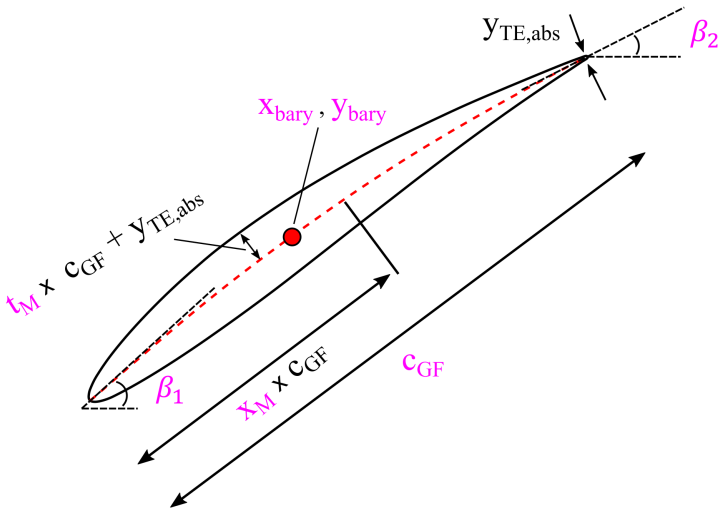

Figure 5.4: Example of aerofoil parametrised with the 7 construction parameters (in purple).

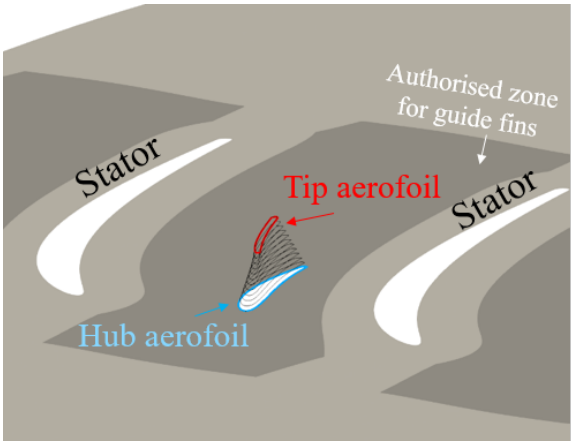

Figure 5.5: Stacking methodology.

5.1.2 Parametrisation with embedded constraints

These construction parameters are difficult to handle as such. Indeed, the hub and tip aerofoils should be consistent with one another, and take into account the geometry of the channel in which they will be placed. For that purpose, the set of construction parameters presented above is re-defined into a new set of optimisation parameters. In the following, quantities related to the hub aerofoil are indexed with the letter H. Quantities related to the tip aerofoil are indexed with the letter T.

Redefinition of the hub aerofoil parameters
The hub aerofoil must be placed within the authorised zone imposed by meshing constraints, in dark grey in Figure 5.5. Moreover, it should be aligned consistently with the local flow. $x_{bary,H}$, $y_{bary,H}$, $c_{GF,H}$, $\beta_{1,H}$, and $\beta_{2,H}$ are thus redefined to meet these constraint. $t_{M,H}$ and $x_{M,H}$ are not modified as they already refer to relevant aerodynamic parameters, independent of these constraints.

- **Replacing the barycentre position ($x_{bary,H}$,$y_{bary,H}$) with the LE position (u,v)**
  The authorised zone is parametrised with two parameters U and V as illustrated in

Figure 5.6a. These parameters roughly represent the streamwise and pitchwise directions at midspan. The position of the hub aerofoil leading edge in the (U,V) frame is denoted (u,v). The hub aerofoil is positioned with its relative leading edge position (u,v) instead of its barycentre position ($x_{bary,H}$, $y_{bary,H}$).

- **Replacing the hub chord $c_{GF,H}$ with the dimensionless chord $\widetilde{c_{GF}}$**
  To compute $c_{GF,H}$, an intermediate quantity L is computed. L is the value of the largest chord before intersecting one of the boundaries with the leading edge position imposed. Its computation results from an optimisation process which returns the hub aerofoil of largest chord still contained within the authorised zone. A minimal distance (d_{min}) to the boundaries is set to ease the meshing process. In this work, $d_{min} = 1\%c$, with c the stator chord. On top of that, a minimum value for the chord $c_{GF,min}$ is set by the user as an external constraint. In this work, $c_{GF,min}$ is set to 0.2c. The parameter $\widetilde{c_{GF}}$ is then introduced to compute the guide fin chord such that

$$c_{GF,H} = \widetilde{c_{GF}} \times (L - c_{GF,min}) + c_{GF,min} \tag{5.1}$$

  In this work, $\widetilde{c_{GF}}$ varies in [0,1], which ensures that $c_{GF,H} \geq c_{GF,min}$ and that the guide fin chord is contained within the authorised surface. Figure 5.6b illustrates the effect of $\widetilde{c_{GF}}$.

- **Replacing the LE metal angle $\beta_{1,H}$ with the relative LE angle $\Delta\beta_{1,H}$**
  The alignment and deflection of the hub aerofoil should be consistent with the flow at stake, which is driven by the stator camber. The metal angle $\beta_{1,H}$ of the hub aerofoil is thus re-defined with respect to the local camber of the stator using the relative LE angle $\Delta\beta_{1,H}$ such that

$$\beta_{1,H} \;=\; \beta_{local,LE} + \Delta\beta_{1,H} \tag{5.2}$$

  where $\beta_{local,LE}$ is the angle between the tangent to the stator camber line and the x-axis at the axial position of the LE of the hub aerofoil. The definition of this parameter is illustrated in Figure 5.7a.

- **Replacing the TE metal angle $\beta_{2,H}$ with the deflection parameter $\beta_{2,pc_\beta1}$**
  The metal angle $\beta_{2,H}$ is re-defined with respect to $\beta_{1,H}$ so that the hub aerofoil camber line deflects the flow towards the engine axis direction. This is equivalent to having $|\beta_{2,H}| \leq |\beta_{1,H}|$ (see Figure 5.8a). In addition, the hub aerofoil deflection must remain within a reasonable range, and is limited to 30°. The deflection parameter $\beta_{2,pc_\beta1}$ is thus introduced such that

$$\beta_{2,H} \;=\; min(\; \beta_{2,pc_\beta1} \times \beta_{1,H} \;, \beta_{1,H} - 30 \;) \tag{5.3}$$

  With this definition, $\beta_{2,pc_\beta1} \in [0,1]$ ensures $|\beta_{2,H}| \leq |\beta_{1,H}|$. The use of $\beta_{2,pc_\beta1}$ yields values of $\beta_{2,H}$ usually lower than the local stator camber. Therefore, it tends to create a local convergence of the section between the hub aerofoil pressure side and the stator suction side. The definition of this parameter is illustrated in Figure 5.8b.

Redefinition of the tip aerofoil parameters

The tip aerofoil should be built consistently with the hub aerofoil. Simple aerodynamic design rules are used to constrain the tip aerofoil geometry with respect to the hub aerofoil geometry. $x_{bary,T}$, $y_{bary,T}$, $c_{GF,T}$, $t_{M,T}$, $\beta_{1,T}$, and $\beta_{2,T}$ are thus redefined. As for the hub aerofoil, $x_{M,T}$ is not modified.

- **Replacing the barycentre position ($x_{bary,T}$,$y_{bary,T}$) with the sweep and lean angles (λ_{sweep},λ_{lean})**
  In order to couple the positions of the hub and tip aerofoils, a sweep and lean angle are introduced and replace the ($x_{bary,T}$,$y_{bary,T}$) parameters. These angles are used to position the mid-chord point of the tip aerofoil with respect to the mid-chord point of the hub aerofoil. Let us introduce d_{sweep} and d_{lean}, the distance between those points projected in the plane containing the hub aerofoil, respectively in directions along and normal to the hub chord line. These angles are then defined as

$$\lambda_{sweep} = arctan(d_{sweep}/H_{GF}) \tag{5.4}$$
$$\lambda_{lean} = arctan(d_{lean}/H_{GF}) \tag{5.5}$$

  A positive sweep angle corresponds to a tip aerofoil shifted towards downstream. A positive lean angle corresponds to a tip aerofoil shifted towards the pressure side of the stator. These quantities are illustrated in Figure 5.7b.

- **Replacing the maximum thickness and chord $t_{M,T}$ and $c_{GF,T}$ with the relative thickness and chord $t_{M,T,rel}$ and $c_{GF,T,rel}$**
  In the construction of conventional blades, the thickness and chord most often decrease along span. $t_{M,T,rel}$, and $c_{GF,T,rel}$ are thus introduced such that

$$t_{M,T} = t_{M,T,rel} \times t_{M,H} \tag{5.6}$$
$$c_{GF,T} = max(\ c_{GF,T,rel} \times c_{GF,H},\ c_{min,abs}\ ) \tag{5.7}$$

  Values of $t_{M,T,rel}$ in $[0,a]$ ensure $t_{M,T} \leq a \times t_{M,H}$. Values of $c_{GF,T,rel}$ in $[0,b]$ ensure $c_{min,abs} \leq c_{GF,T} \leq b \times c_{GF,H}$. In this work, $a = 1$ and $b = 1.1$.

- **Replacing the metal angles ($\beta_{1,T}$,$\beta_{2,T}$) with the relative angles ($\Delta\beta_{1,T}$,$\Delta\beta_{2,T}$)**
  $\Delta\beta_{1,T}$ and $\Delta\beta_{2,T}$ are defined similarly to $\Delta\beta_{1,H}$. They replace $\beta_{1,T}$ and $\beta_{2,T}$ and are used to align the tip aerofoil consistently with the stator camber line at hub.

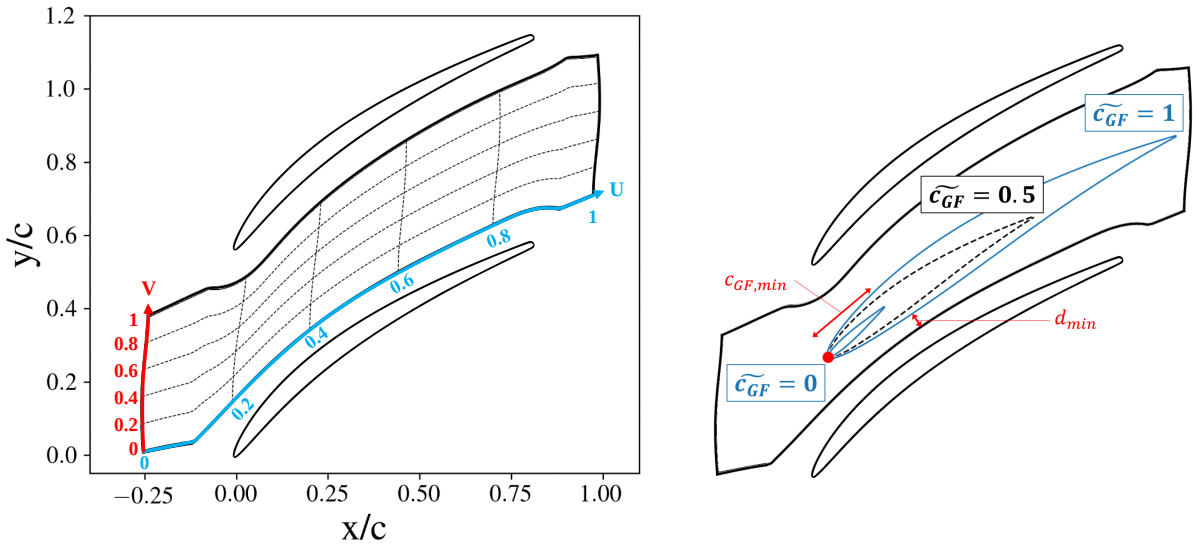

(a) Authorised surface parametrised by (U,V).

(b) Illustration of parameter $\widetilde{c_{GF}}$.

Figure 5.6: Illustration of the authorised surface (left) and chord (right) at hub.

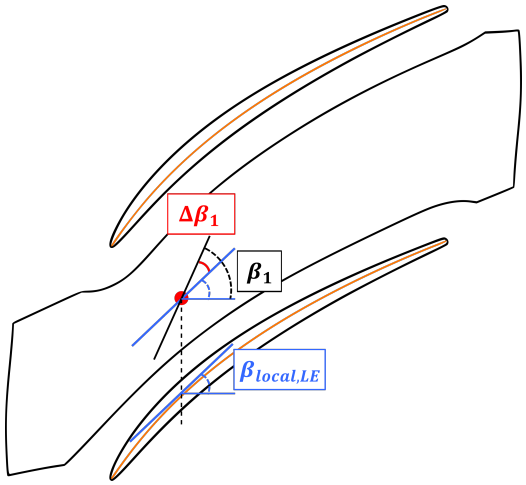

(a) Illustration of the parameter $\Delta\beta_1$.

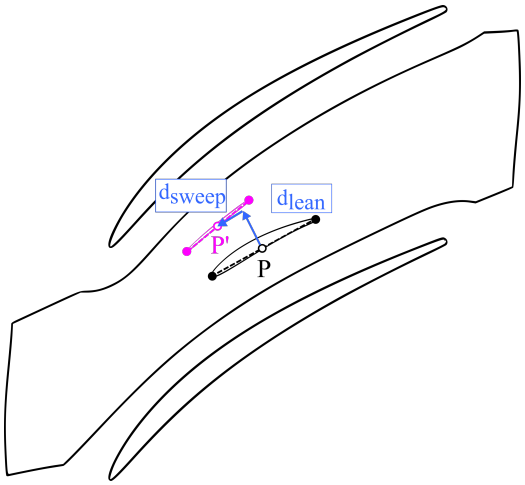

(b) Hub (black) and tip (purple) aerofoils. P and P' refer to mid-chord points.

Figure 5.7: Illustration of parameters $\Delta\beta_1$ (left), and d_{sweep} and d_{lean} (right).

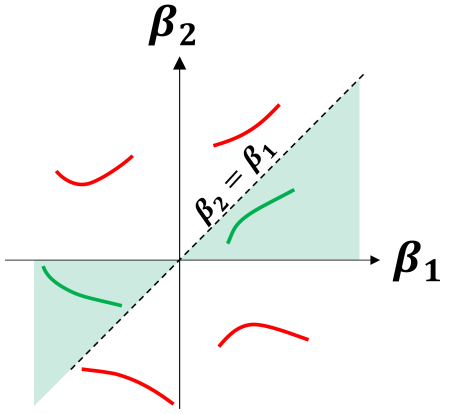

(a) Camber line aspect as a function of (β_1,β_2) values. Camber lines deflecting the flow towards the engine axis direction are represented in green.

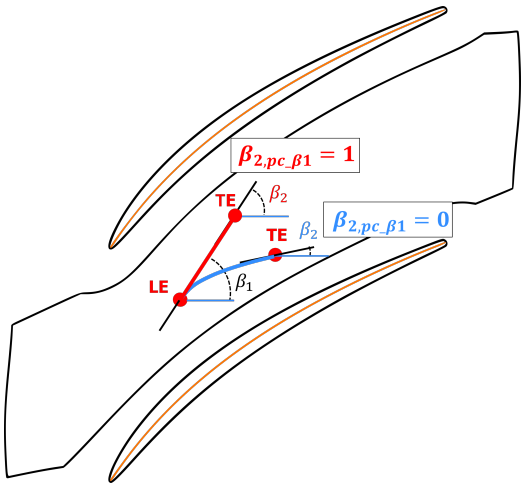

(b) Examples of camber lines obtained with $\beta_{2,pc_\beta1} = 1$ (in red) and $\beta_{2,pc_\beta1} = 0$ (in blue). In this latter case, the maximum deflection of 30° is reached and the resulting β_2 angle is non zero.

Figure 5.8: Illustration of the parameter $\beta_{2,pc_\beta1}$.

Optimisation parameters take into account some aerodynamic expertise and ensure a consistency between the hub and tip aerofoils, and between each aerofoil and the stator. They also include positioning constraints related to an authorised zone resulting from the meshing process. The definition of this zone is specified in Section 5.2.2. The definitions of the optimisation parameters are summarised in Table 5.1.

5.2 Hybrid meshing methodology

A mesh containing both the stator blade and the guide fin must be generated. In our approach, several guide fins of complex and various shapes must be tested with the same stator configuration. In order to save computational time and to uncouple the resolution of the two geometries,

the stator part is meshed separately from the guide fin part and is fixed, while the guide fin part is re-meshed for every guide fin. Figure 5.9 illustrates this methodology. The stator part is meshed using a conventional, reliable structured process which ensures a light, high quality mesh (Section 5.2.1). On the other hand, an unstructured mesh strategy is adopted for the guide fin part as it allows to mesh complex shapes (Section 5.2.2).

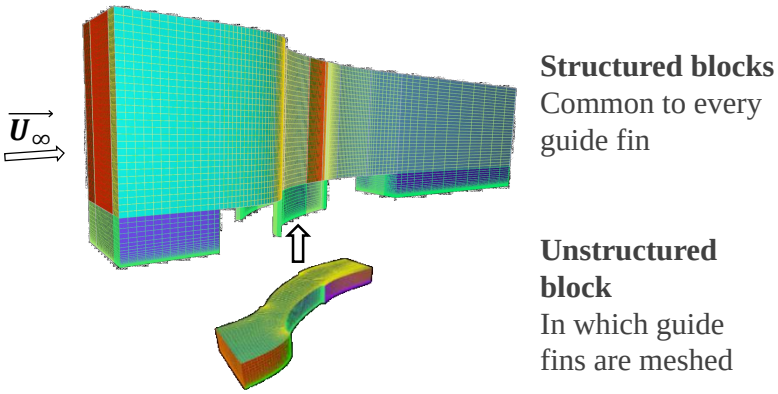

Figure 5.9: Illustration of the hybrid methodology.

5.2.1 Generation of the structured part

The initial structured mesh of the stator is obtained using the commercial meshing software AutogridV5 (Numeca). It is of O-4H type, contains $\simeq$ 1.1 10^6 cells, and is extended up to three stator chords upstream and downstream of the row to damp the influence of the inlet and outlet boundary conditions (see Figure 5.10). A maximum expansion ratio of 1.42, a maximum aspect ratio of 1032, a minimum skewness angle of 27° and a maximum value of y^+ of 4 in the leading edge region are reached.

Attention is paid to have an aspect ratio close to 1 in the region of the future unstructured block boundaries (near-hub, within the channel). Indeed, pyramids elements will grow from the rectangular faces of these boundaries, and their quality is enhanced with a square base. Moreover, the structured O-grid block surrounding the stator blade is not modified to ensure a systematic, high quality discretisation of the profile boundary layer, and to make the unstructured mesh generation more robust.

Blocks are then rearranged to centre the mesh on the channel, and to define one block of controlled dimensions (represented in red in Figure 5.11). This block will be replaced by an unstructured mesh containing the guide fin. It defines the authorised volume in which the guide fin can be placed. This way, the guide fin can not cross the periodic boundaries, and will be meshed independently of the stator.

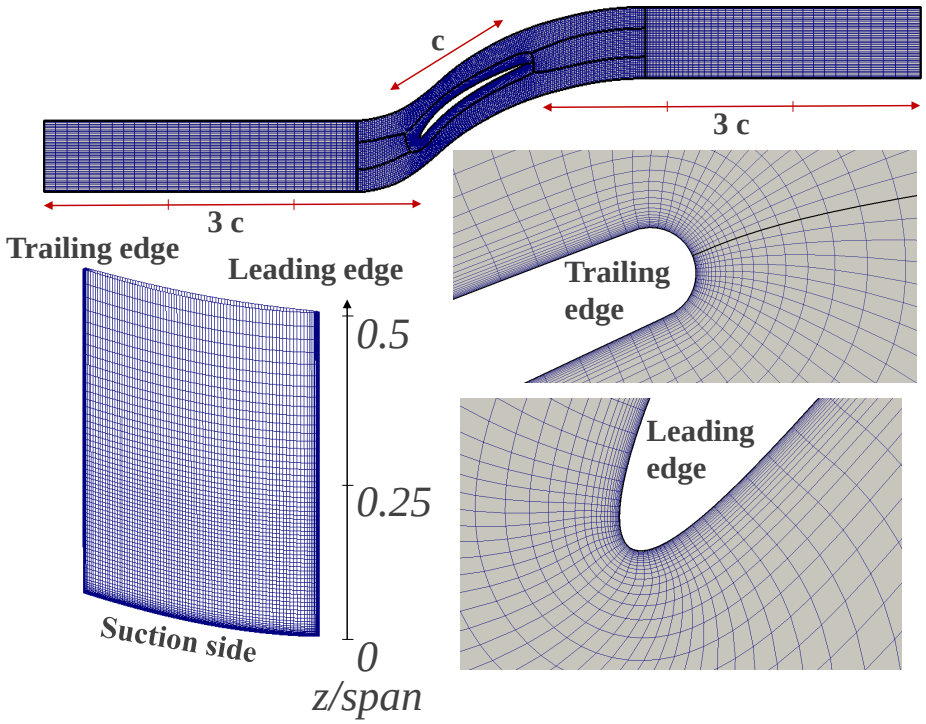

Figure 5.10: Illustration of the original structured mesh. *Black lines : blocks borders.*

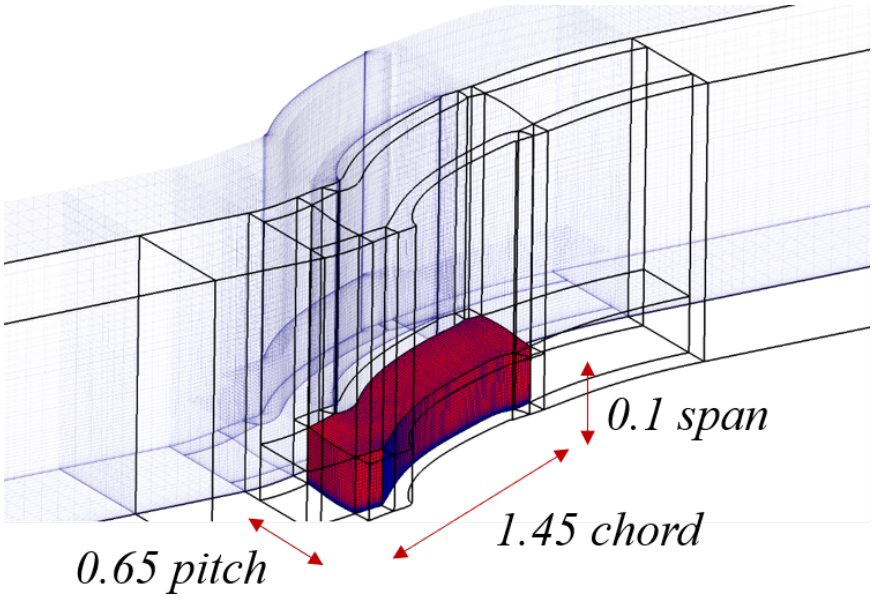

Figure 5.11: Unstructured block boundaries (in red). *Black lines : blocks borders. A second faded channel is added for visualisation purposes.*

5.2.2 Generation of the unstructured part

The unstructured mesh is obtained using the commercial meshing software ANSA (Beta, v19.1.4). The guide fin and the hub surface are first meshed with a mix of triangular and rectangular elements. A first set of volume elements (prisms) is then generated as a succession

of layers. These layers feature the same topology than the surface mesh, and grow from the hub and from the guide fin surface in the direction normal to the local surface (in green in Figure 5.12). These layers are necessary for the boundary layers to be properly discretised, and their effect is thoroughly investigated in next section. The points on the lateral boundaries of each layer automatically connect to the points of the structured-unstructured mesh interface, thus ensuring grid point coincidence. A second set of volume elements fills the remaining volume with tetrahedra for the inner part and pyramids for elements attached to the interface (in red in Figure 5.12). The growth rate is set, as in the structured mesh, to 1.2. This leads to an unstructured block containing typically 3.4×10^5 cells with a guide fin, and 1.7×10^5 cells without.

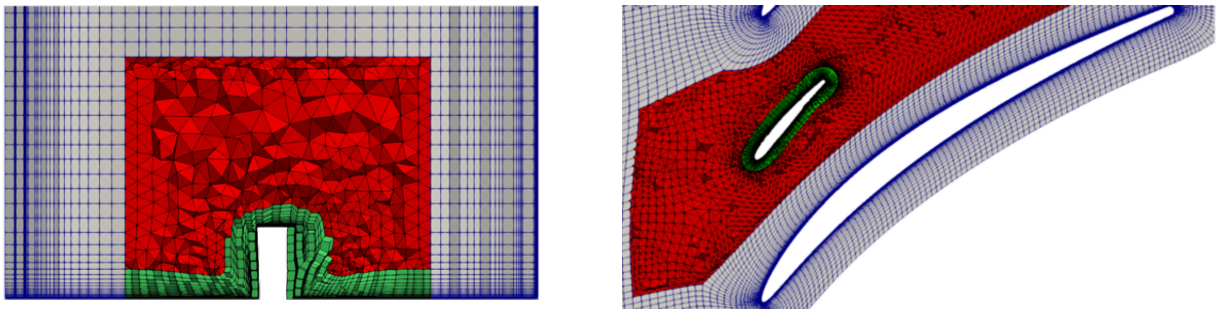

(a) View normal to the x-axis.

(b) Blade-to-blade view near the guide fin tip.

Figure 5.12: Portions of hybrid mesh with a guide fin. Grey elements : hexahedra (structured part). Green elements : prisms. Red elements : tetrahedra and pyramids. 24 layers are used for visualisation purposes.

5.2.3 Unstructured mesh refinement

The effect of the number of layers (N_{layers}) on the endwall losses is investigated. Figure 5.13a shows that the endwall losses are highly overpredicted for $N_{layers} = 0$, and are stabilised for values greater than 14, both at design incidence ($i = 0°$) and high incidence ($i = 4.9°$). The number of layers is thus fixed to 14.

A local refinement downstream of the guide fin might be of interest to better predict the effects of its wake. A refinement level is defined with a local growth rate (GR) and a local maximum length for the edges of the volume elements (l). A lower value of GR or of l increase the local resolution. Four levels of refinement are tested (see Table 5.2). Figure 5.14 illustrate the mesh resolution in the case of no wake refinement and with the most refined wake (refinement level 3). Figure 5.13b shows that the refinement level has a negligible effect on the endwall losses (below 0.25%), both at $i = 0°$ and $i = 4.9°$. Moreover, little effect is observed on the entire flow field. However, the number of cells increases from 3.4×10^5 cells (no wake refinement) to 4.8×10^5 cells (refinement level 3). Refining the wake would thus increase the computational time without affecting the prediction of the endwall losses. The wake region is thus not refined.

This section illustrates that the meshing process was undertaken carefully, during the structured process and the unstructured one, and shows that both parts must be meshed consistently with one another. The flexibility of unstructured grid is pointed out with the possibility to refine the mesh locally behind the guide fin, but this refinement is not proven necessary as a first step and will not be used in the optimisation process.

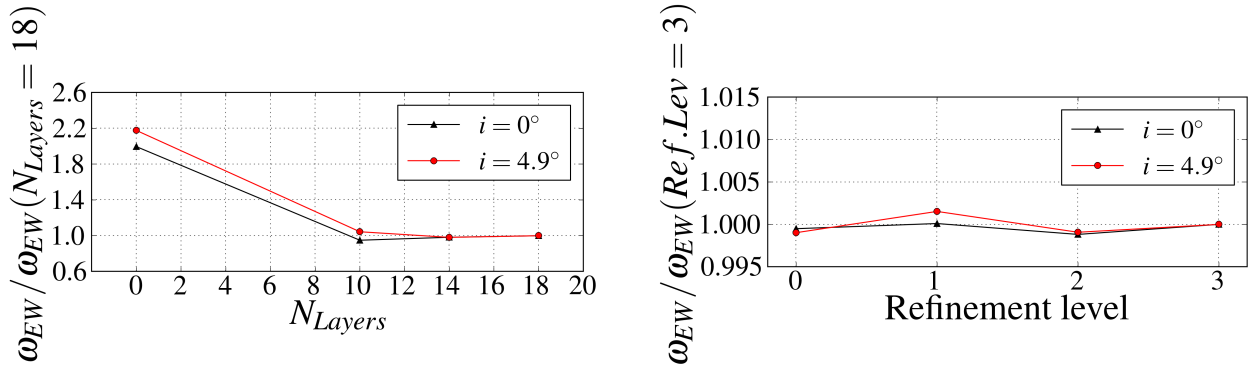

(a) Effect of N_{layers} on $\omega_{EW}/\omega_{EW}(N_{Layers} = 18)$.

(b) Effect of the refinement level on $\omega_{EW}/\omega_{EW}(Rev.Lev = 3)$.

Figure 5.13: Effect of the number of layers (left) and of the wake refinement level (right).

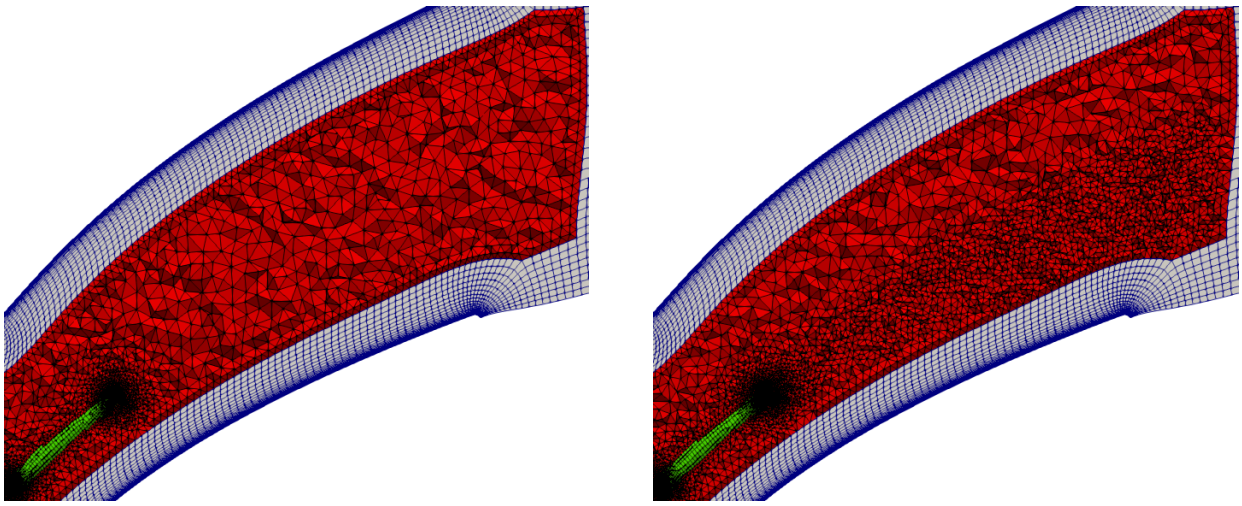

Figure 5.14: No wake refinement (left) vs refinement level 3 (right).

Refinement Level	0 (No wake refinement)	1	2	3
GR	1.2	1.2	1.2	1.1
l	1.4%c	1.2%c	1.0%c	1.0%c

Table 5.2: Wake refinement levels.

5.3 RANS computations

The RANS simulation of separated flows is complex and sensitive to the numerical environment. A linear grid of stator with an incompressible flow is a standard configuration, and most numerical parameters are thus set to conventional values (Section 5.3.1). However, RANS suffers from a specific artefact for corner separation predictions : the topological switch. The origin and consequences of this artefact are discussed (Section 5.3.2). Its sensitivity to the turbulence modelling is thoroughly investigated, and the turbulence model of $k\omega - BSL$

with the Quadratic Constitutive Relation is retained (Section 5.3.4). Finally, computations performed on hybrid meshes are fairly recent and still non conventional. Last results validate the use of hybrid meshes for corner separation prediction (Section 5.3.5).

5.3.1 Numerical set up

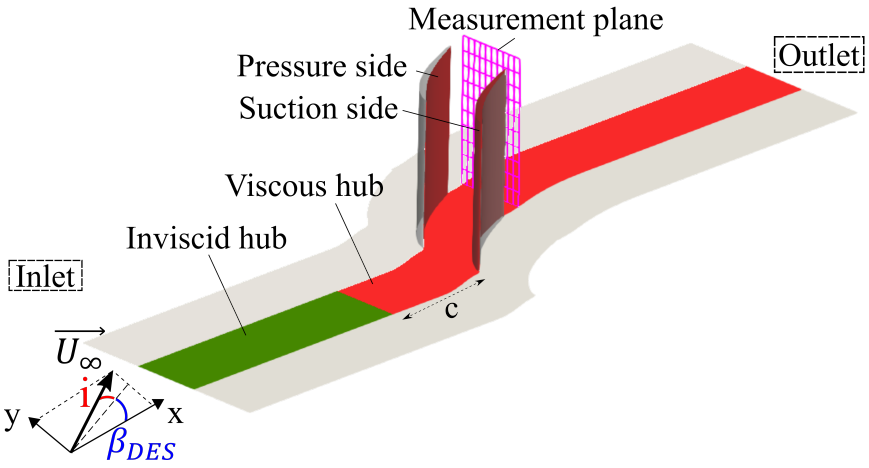

Figure 5.15: Computation domain. Inviscid (green) and no-slip (red) conditions.

CFD solver : RANS results are computed using the version 5.0.02 of the CFD solver elsA (ONERA).

Geometry : Computations are performed on the structured and hybrid meshes presented in Section 5.2. Only one stator channel is modelled, and the computational domain is shown in Figure 5.15.

Boundary conditions : A symmetry boundary condition is imposed at midspan. This enables to compute only half of the channel in the spanwise direction. The hub surface going from the inlet to 1c upstream of the stator LE is considered inviscid, and no-slip conditions are set on all other solid boundaries (see Figure 5.15). The starting position of the no-slip condition is set to retrieve the experimental boundary layer momentum thickness as explained below. The inlet velocity magnitude is set to the experimental value $U_\infty = 40\ m.s^{-1}$, angles are set by the incidence and the total enthalpy value is deduced from the inlet static temperature. The value of the turbulent kinetic energy is deduced from $k = \frac{3}{2}(Tu \times U_\infty)^2$ with $Tu = 2.4\%$. The arbitrary value of $\mu_t/\mu = 350$ sets the value of the second turbulent variable. A uniform static pressure is imposed at the outlet.

Flow modelling : The choice of a turbulence model is discussed in Section 5.3.4. The flow is considered fully turbulent as no laminar-turbulent transition models are available in elsA v5.0.02 when using hybrid meshes. A 2nd-order Roe spatial scheme is used with no limiter for variable reconstruction at cells interfaces. The temporal scheme is a Backward-Euler scheme with a local time step based on a local CFL number of 30.
The corner separation magnitude is highly sensitive to the inlet boundary layer. Dawkins et al. (2021) measured the boundary layer momentum thickness 0.25c upstream of the stator and

obtained an experimental value of $0.0030c \pm 6\%$. In this work, the length of the viscous hub upstream of the stator is tuned until reaching similar values at the same location. Values of $0.0028c$ at i=0° and of $0.0031c$ at i=4.9° are obtained with the final set up, thus ensuring consistent inflow conditions. Table 5.3 gathers the values of the RANS simulation parameters.

Name	**Value**
Free-stream velocity U_∞	40 $m.s^{-1}$
Inlet Mach number M	0.117
Chord-based Reynolds number Re_c	3.2×10^5
Inlet static Temperature $T_{S,\infty}$	288.15 K
Exit static Pressure $P_{S,out}$	101325 Pa
Dynamic viscosity μ_S	1.81×10^5 $kg.m^{-1}.s^{-1}$
Density ρ	1.22 $kg.m^{-3}$
Turbulent rate Tu	2.4%
Boundary layer momentum thickness $\theta(-c/4)/c$	$\in [0.0028, 0.0031]$

Table 5.3: RANS simulation parameters.

5.3.2 The topological switch

RANS computations have difficulties in predicting a smooth evolution of the corner separation as the inflow incidence increases. Notably, a saddle/focus pair of critical points can appear at the hub/blade junction, and rapidly moves away towards the centre of the channel. This appearance occurs for an incidence referred to as the *critical incidence* and denoted i_{crit}. At this incidence, the corner separation switches from a *single sided* topology to a *double sided* topology, causing a dramatic increase in losses and blockage. The effect of the topological switch on endwall losses and skin friction patterns is illustrated in Figure 5.16. In this work, this sudden behaviour is not retrieved experimentally. Moreover, a smooth motion of the saddle/focus pair is observed by Dawkins et al. (2021) on the same baseline. This topological switch is thus purely numerical.

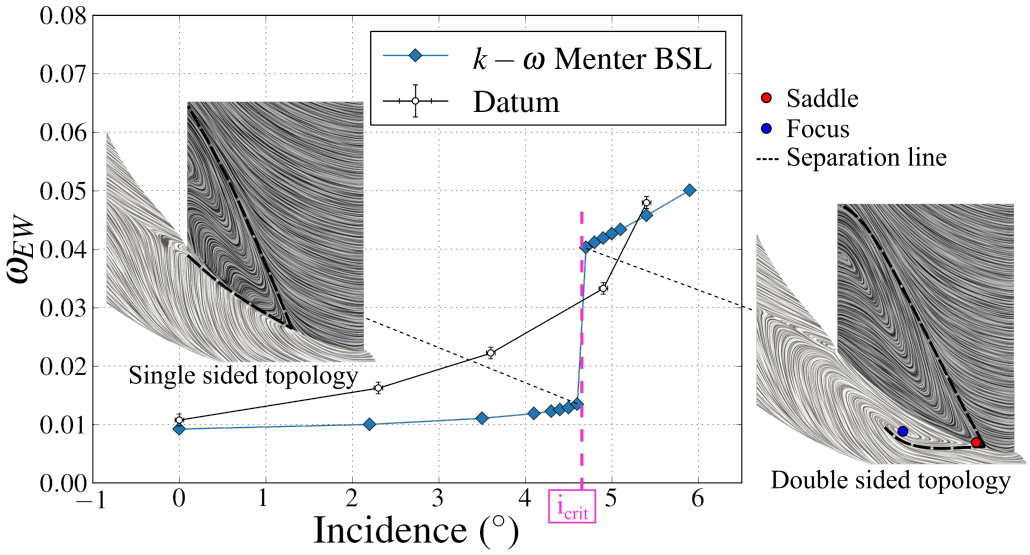

Figure 5.16: RANS predictions of the endwall losses and skin friction patterns using $k\omega - BSL$ turbulence model.

Such a defect can be explained by the anisotropy of the Reynolds stress tensor in the corner region (Gessner, 1973), not accounted for when using the Boussinesq hypothesis. Dawkins et al. (2021) showed that the flow anisotropy in the corner region increases with the incidence, together with total pressure losses. In this work, a guide fin aims at reducing the separation magnitude, which might help reducing the flow anisotropy. It is therefore assumed that best guide fins in terms of loss reduction are the best predicted ones. On the other hand, non-efficient guide fins are likely to feature a double sided topology and lead to large losses. With these assumptions, the topological switch could actually help sorting out efficient and non-efficient guide fins.

Later results prove this assumption right : efficient guide fins yield a single sided topology. In this case, the modelling of an efficient guide fin is not polluted by the topological switch, and the effect of two efficient guide fins on the flow can be compared. These results *a posteriori* justifies the use of RANS predictions for finding and comparing efficient guide fins.

5.3.3 Numerical convergence

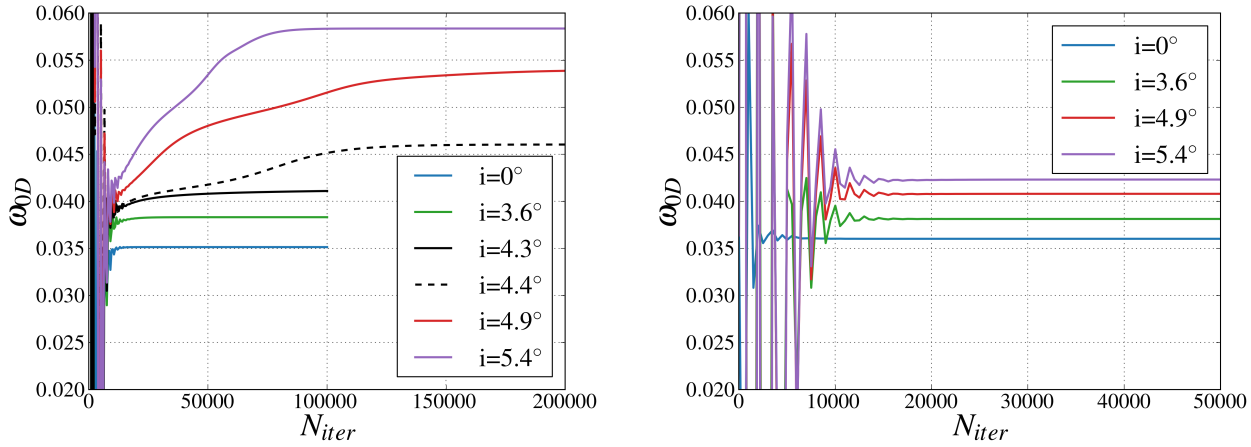

(a) Baseline (from uniform flow).

(b) Efficient guide fin (from baseline prediction).

Figure 5.17: Convergence of ω_{0D} for various incidences.

In this work, the mass averaged losses in the plane of measurement ω_{0D} is of primary importance. The evolution of ω_{0D} with the RANS iterations is investigated on the baseline configuration at various incidences (see Figure 5.17a). Results are obtained with the hybrid mesh described in Section 5.2.2 and the turbulence model $k\omega - QCR$ described in Section 5.3.4. In this configuration, the critical incidence is within [4.3°,4.4°]. The stabilisation of ω_{0D} appears to behave differently if the incidence is lower or greater than i_{crit}. If $i \leq 4.3°$, the stabilised value is rapidly reached. If $i \geq 4.4°$, the stabilisation is much slower. In the latter case, the stabilisation of ω_{0D} occurs for a much greater number of iterations than mass flow rate convergence or than conventionally accepted residuals decay. The computation is therefore considered converged when ω_{0D} is stabilised. For the baseline configuration, the number of iterations is set to 100 000 or 200 000 depending on the incidence to ensure this condition.

Numerous computations must be performed with guide fins, and the number of iterations must be limited to lower the computational cost. Here again, we rely on the idea that an efficient guide fin will improve the flow, and make the critical incidence artefact disappear. Figure 5.17b shows the evolution of ω_{0D} with an efficient guide fin. These computations are initialised with the converged baseline flow field of the corresponding incidence, with the same numerical set

up. The critical incidence is not triggered and the computations is rapidly stabilised. This methodology is retained for the optimisation process : the flow is initialised with the baseline flow of corresponding incidence, and 25 000 iterations are used. This yields a computational cost of $\simeq$ 100 CPU hours per prediction.

5.3.4 The choice of turbulent closure modelling

Selecting the proper turbulent closure model is a complex but essential step in RANS simulations. Different models can lead to very different results, especially when separations occur. The choice of a turbulent closure model relies on the comparison to experimental data. Several models are thus compared to the only *a priori* available data of the baseline configuration. Midspan characteristics, and more importantly, losses gradients in the corner separation region are compared. It is indeed assumed that the modification in the flow field induced by a guide fin is mainly characterised by loss redistribution in the channel as the flow is considered incompressible. The effect of the Quadratic Constitutive Relation on the best turbulence model is finally assessed.

Turbulence models In order to discriminate the influence of turbulence models, a conventional set up based on the structured mesh of reference without guide fins is used. Three well known turbulence models are compared : $Spalart - Allmaras$, $kl - Smith$, and the $k - \omega$ model of Menter denoted $k\omega - BSL$. $k\omega - BSL$ best retrieves the experimental wake for all tested incidences (i=0°, 2.3°, 3.6°, 4.9°). Cartographies of ω in the plane of measurement are mass-averaged in the azimuthal direction, and $k\omega - BSL$ also best retrieves the experimental gradients for the same incidences. Figure 5.18 shows this comparison for i=4.9°. Finally, Figure 5.19 compares the endwall loss predictions as the incidence increases. Every turbulence model features a critical incidence, even though its precise value depends on the model. No model seems particularly better than any other, even though $k\omega - BSL$ is the closest to the experimental endwall losses.

The turbulence model of $k\omega - BSL$ is thus selected. As an attempt to improve the predictions of this model, the effect of the Quadratic Constitutive Relation correction is now assessed.

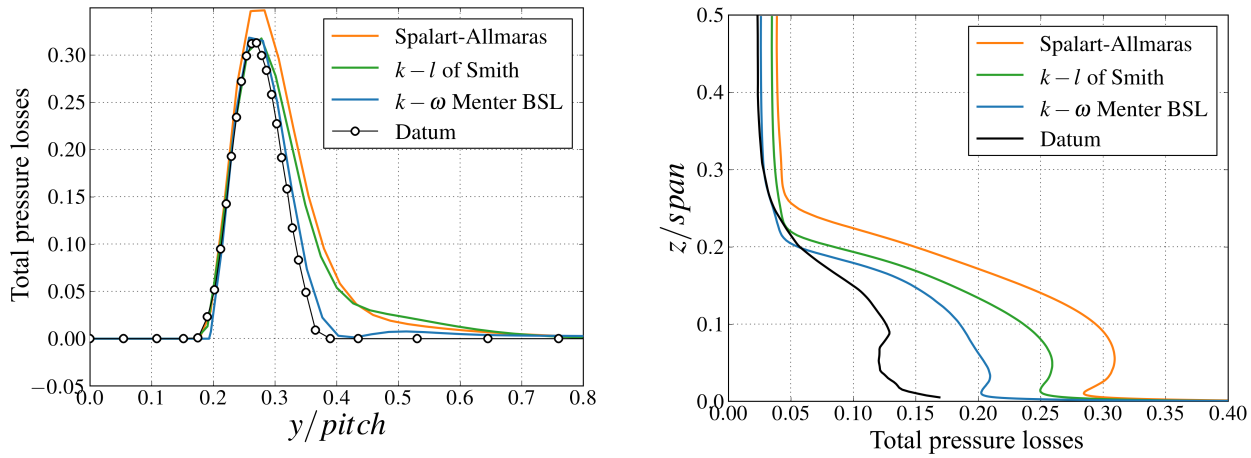

(a) Wake at midspan

(b) Radial profile

Figure 5.18: Effect of turbulence model on losses distribution at high incidence (i=4.9°).

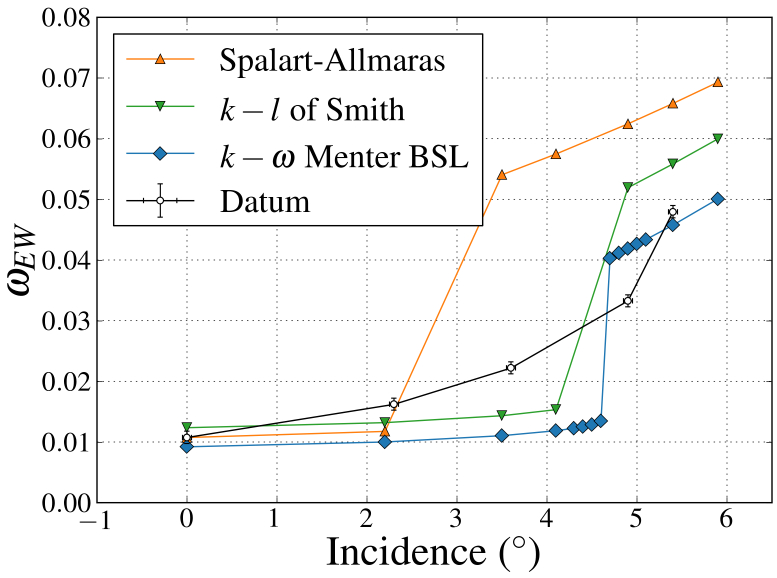

Figure 5.19: Effect of the turbulence model on endwall losses.

Quadratic Constitutive Relation correction The Quadratic Constitutive Relation (QCR) correction is interesting in this framework. It was originally proposed by Spalart (2000) to improve corner flow predictions. Let τ_{ij} be the Reynolds stress tensor computed with the Boussinesq hypothesis, μ_t the eddy viscosity, S_{ij} the strain rate tensor and O_{ij} the antisymmetric normalised rotation tensor. The non linear stress tensor with the QCR correction is then :

$$\tau_{ij}^{QCR} = \tau_{ij} - c_{nl1}[O_{ik}\tau_{jk} + O_{jk}\tau_{ik}] \tag{5.8}$$

with

$$S_{ij} = \frac{1}{2}(\frac{\partial u_i}{\partial x_j} - \frac{\partial u_j}{\partial x_i}) \tag{5.9}$$

$$\tau_{ij} = 2\mu_t S_{ij} \tag{5.10}$$

$$O_{ik} = \frac{\partial u_i/\partial x_k - \partial u_k/\partial x_i}{\sqrt{\sum_{n,m} \partial u_n/\partial x_m \partial u_n/\partial x_m}} \tag{5.11}$$

$$c_{nl1} = 0.3 \tag{5.12}$$

c_{nl1} is a constant calibrated by Spalart (2000). With this correction, the stress tensor depends on the normalised rotation tensor, which is the vorticity divided by the norm of the velocity-gradient tensor. This correction is thus expected to have an effect in regions where the fluid is highly rotational, such as in the corner region. Conversely, a negligible effect is expected in regions where the fluid deformation dominates the fluid rotation, such as in the midspan region.

The effect of the QCR correction is assessed on the $k\omega - BSL$ turbulence model, and Figure 5.20 compares their predictions on the endwall losses. The critical incidence is present in both cases. Its value is little affected and goes from 4.7° to 4.6°. However, the increase in losses is greatly lowered when using the QCR correction. Consistently with these results, the skin friction patterns show that the opening of the corner separation still occurs, but that the extension of the separated zone on the hub is much smaller with the QCR correction. Moreover,

Figure 5.21 shows that the losses gradient are more consistent with the experimental data with the QCR correction. However, it is worth noticing that the extension and magnitude of the corner separation is no longer over predicted, but under predicted. Finally, the wake at midspan is unaffected by the QCR correction as expected.

With the QCR correction, the critical incidence artefact is still present but its consequences are lowered. Moreover the losses gradient seem better predicted. The $k\omega - BSL$ turbulence model with the QCR correction, denoted $k\omega - QCR$, is thus selected.

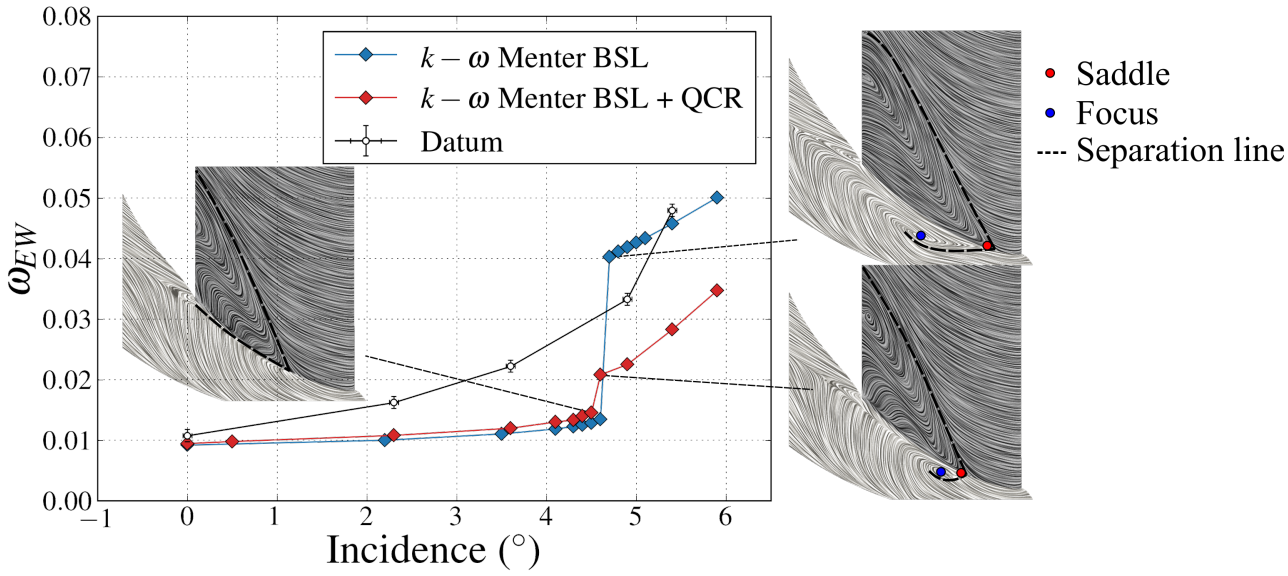

Figure 5.20: Effect of QCR correction on endwall losses.

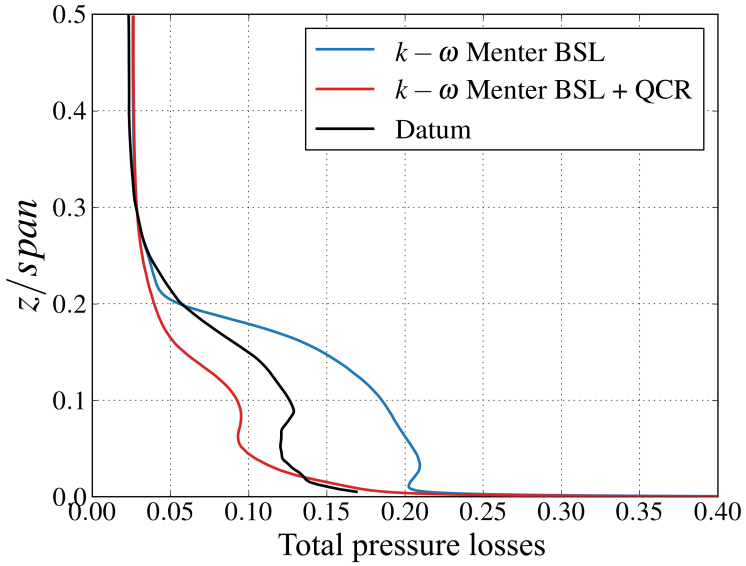

Figure 5.21: Radial profile (i=4.9°).

5.3.5 Validation of the hybrid methodology

The final numerical set up for evaluating guide fins involves the use of a hybrid mesh. In our case, the structured and unstructured parts are taken into account by the CFD solver elsA with dedicated algorithms for each part. The hybrid mesh is not converted to a full unstructured mesh before the computation, which lets a structured/unstructured interface within the computational domain.

Endwall losses obtained on the baseline configuration with the structured mesh and with two hybrid meshes are compared in Figure 5.22. Results are first compared with the hybrid mesh of reference defined in Section 5.2.2 (Tetrahedral). For incidences lower than 4°, the difference in endwall losses is below 0.1%. The critical incidence value is slightly affected, and goes from 4.6° to 4.4° when using the hybrid mesh. For incidences greater than 4.9°, the losses are slightly increased with a constant offset. Given the sensitivity to the numerical environment, these differences remain acceptable. The justifications for choosing the $k\omega - QCR$ model based on the structured mesh are thus considered valid on the hybrid mesh.

It might be of interest to understand the origins of these discrepancies. They can come from the hybrid junction itself, or from the modification of the cells topology in the unstructured zone. An intermediate hybrid mesh (Hexahedral) is thus created to uncouple these effects. From the structured mesh, the hexahedral elements of the red block (Figure 5.11) are converted into unstructured elements. Only the grid points connectivity is affected, leading to a hybrid mesh with the same exact cells topology and shape as the structured one. Figure 5.22 shows that the discrepancies are mainly due to the structured/unstructured interface, and not to the topology modification of the cells. This underlines a small drawback of the hybrid methodology used. However, it confirms that the tetrahedral unstructured mesh is of equivalent quality than the initial hexahedral mesh.

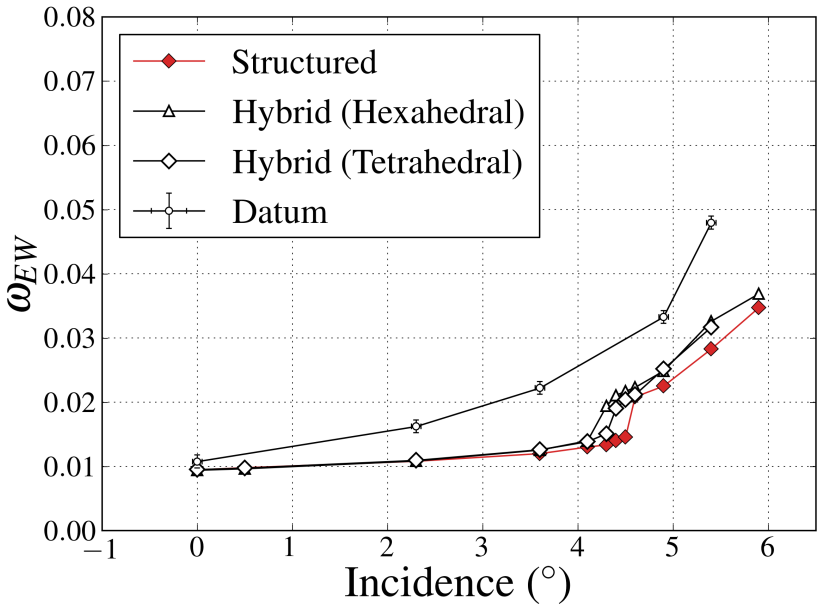

Figure 5.22: Effect of the mesh type on endwall losses. Structured mesh of reference, hybrid mesh of reference (Tetrahedral) and intermediate hybrid mesh (Hexahedral).

5.4 Conclusion

In this chapter, the numerical methodology implemented for evaluating guide fins of various shapes is presented. The guide fins parametrisation is first detailed. It enables to describe a large variety of shapes with a limited number of parameters (15), while taking into account aerodynamic and meshing constraints. An innovative hybrid meshing process is carefully implemented. It guarantees a robust, high quality meshing step fitted for automatically meshing complex guide fin shapes. The effect of RANS settings on the prediction of corner separation are thoroughly investigated, and notably the effect of the turbulence modelling. The final RANS set up relies on the $k\omega - BSL$ turbulence model with the QCR correction. The baseline is investigated with this set up, and RANS predictions tend to underestimate the endwall losses on the whole range of incidences tested. However, the wake at midspan and the radial loss profiles downstream of the stator blade are fairly retrieved. To conclude this analysis, a comparison between RANS predictions and experimental results at design (i=0°) and high (i=4.9°) incidences is proposed in Figure 5.23. The boundary layer developing on the endwall and the extension and shape of the corner separations are well predicted at both incidences. This numerical set up thus enables to predict the baseline flow with a satisfying precision. This set up will thus be used to assess the effect of guide fins through the optimisation process described in the next chapter.

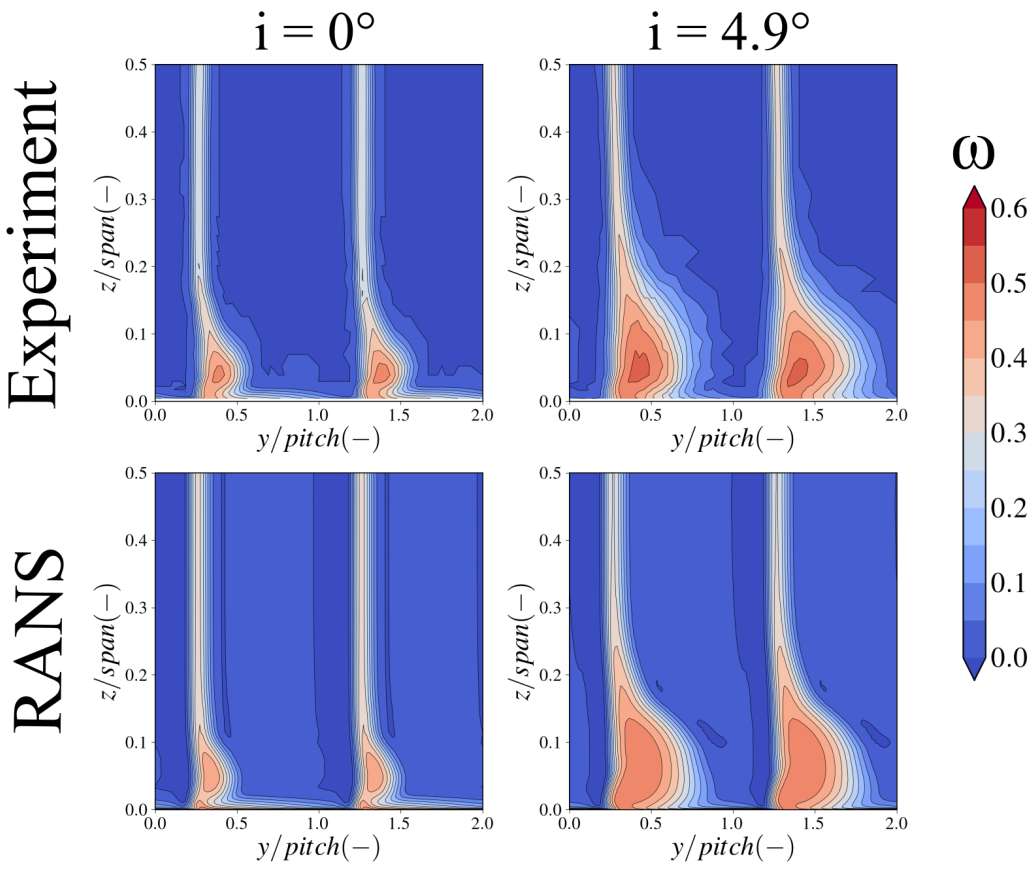

Figure 5.23: Total pressure losses at design (0°) and high (4.9°) incidences. Experiment vs RANS.

Chapter 6

Optimisation methodology

The previous chapter introduced a numerical methodology enabling to evaluate the effect of parametrised guide fins on the phenomenon of corner separation. In this chapter, this methodology is used to feed an optimisation process. Two objective functions characterising the effect of a guide fin on the corner separation are defined. The first objective of the optimisation process is to find guide fins that lower these objective functions i.e. efficiently reduce the corner separation. The second objective of this process is to model the relation between the input parameters and the objective functions with a low-fidelity model. Such a model would enable to explore the effect of the guide fin shapes with a negligible computational cost compared to RANS. In this framework, the number of input parameters is relatively large (15) and the physics at stake is complex. Moreover, the evaluation of a single guide fin in RANS is time-consuming. The optimisation methodology must be selected carefully to avoid irrational computational costs.

The iterative refinement of Kriging surrogate models is an optimisation methodology fitted to these two objectives. Mathematical properties of Kriging models are presented in Section 2.1. In this work, this method is initiated with RANS computations of a first sample of guide fins. This sample is called the Design Of Experiment (DOE). The corresponding results are used to define two objective functions, and a Kriging surrogate model is generated to interpolate the sample points with the objective functions values. The model can then promptly give an estimation of the objective functions for an unknown guide fin, as well as a measure of the uncertainty for this estimation. The Expected Hypervolume Improvement criterion (EHVI, described in Section 2.2.2) relies both on the value and uncertainty of this estimation. This criterion is used to define a new set of guide fins, whose evaluation should improve the knowledge and the precision of the model in the Pareto front region. Once evaluated, a second Kriging model is generated using all the available guide fins. The optimisation process eventually consists in refining iteratively the Kriging models until reaching a satisfactory approximation of the objective functions in the regions of local minima. This method efficiently explores the input space while generating a RANS database of efficient guide fins. In addition, this process yields a Kriging model reliable in the Pareto front region. Such a model can instantaneously approximate the RANS predictions of new guide fins, thus allowing a thorough analysis.

This chapter describes the implementation and the results obtained with this optimisation methodology. The objective functions are first defined (Section 6.1). The optimisation process is then carried out on the largest possible input space. A dedicated methodology is used to explore this complex space, characterised by a large subspace of non viable guide fins (without available RANS results). The convergence, results and limits of this process are detailed, which leads us to define a reduced input space (Section 6.2). A second optimisation process relying on this reduced input space is then presented. The convergence and results of this process are

detailed (Section 6.3). Finally, Section 6.4 summarises and compares the results obtained on these two input spaces.

6.1 Definition of the objective functions

The main objective of the guide fins is to improve the flow at off-design conditions. It is still necessary to monitor the losses at the design operating point to maintain a reasonable efficiency of the stator row. The effect of guide fins is thus monitored at two incidences, $i = 0°$ (design) and $i = 4.9°$ (off-design). In an adiabatic stator, the entropic losses are directly related to the total pressure losses (see the Appendix, Section A.5). To focus on losses related to corner separation, the endwall losses are used. The objective functions are thus defined as the loss reductions relative to the baseline configuration at the same operating point :

$$\Delta\omega_0 = \omega_{EW,i=0°,GF} - \omega_{EW,i=0°,BSL} \quad (6.1)$$

$$\Delta\omega_{4.9} = \omega_{EW,i=4.9°,GF} - \omega_{EW,i=4.9°,BSL} \quad (6.2)$$

$\Delta\omega_0$ and $\Delta\omega_{4.9}$ will abusively be called the *gain* at 0° and at 4.9°. A higher gain is equivalent to a better loss reduction, which corresponds to a lower value of the objective functions.

The performance of a stator row is also characterised with its deflection and diffusion. A selection of criteria characterising these quantities is detailed hereafter.

The deflection is usually quantified with the surface averaged value of the azimuthal exit angle β. The standard deviation of the exit radial profile of β is also interesting as it quantifies the non-uniformity of the exit flow field in the spanwise direction. A non-uniform distribution of angles can result in local over-loading of the rotor, leading potentially to flow separation and rotor stall.

The diffusion is naturally characterised with the static pressure rise coefficient $C_{p,s}$, which compares the integrated static pressure downstream and upstream of the stator row. The exit blockage coefficient can also be used, but it is strongly linked to $C_{p,s}$ in an incompressible flow (see Equation 1.14, proposed by Gbadebo et al. (2008)). Additionally, diffusion criteria could be used. Several criteria were implemented to anticipate separation at early design steps (see Section 1.3.1). Among the most well known criteria, only the Lei criterion (Lei et al., 2008) focuses on corner separation. This criterion attempts to anticipate the topological switch. Figure 6.1 shows the original results proposed by Lei et al. (2008), annotated with the RANS results of the current baseline. According to this criterion, all results should feature a single sided separation, while results at i=4.9° and 5.4° feature double sided separations. This criterion does not seem fitted to the current studied configuration. In this work, $C_{p,s}$ is therefore preferred to quantify the diffusion.

As a summary, the averaged azimuthal exit angle and standard deviation, $C_{p,s}$ and ω quantify the global performance of the stator at stake. However, in the context of incompressible flows, the losses are strongly linked to the blockage, itself related to the diffusion and deflection. It is therefore chosen to monitor only the losses in the optimisation process, and to verify *a posteriori* the influence of the guide fins on the other quantities.

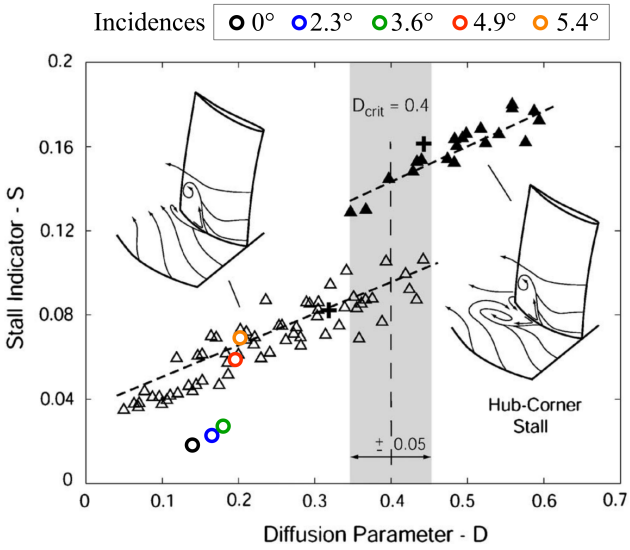

Figure 6.1: Correlation between diffusion factor and stall indicator. Reproduced from (Lei et al., 2008). Annotated with RANS computations on the current baseline.

6.2 Optimisation in the entire input space (15p)

This section presents the optimisation process performed on the largest input space allowed by the optimisation parameters. These parameters are defined in Chapter 5 and summarised in Table 5.1. The idea behind this optimisation is to explore a large input space without *a priori* assumptions on the shape of the efficient guide fins. The input space is firstly defined (Section 6.2.1), and the settings of the process thoroughly described (Section 6.2.2). The convergence of the optimisation process is then presented (Section 6.2.3). A refined surrogate model is obtained, and its predictability discussed (Section 6.2.4). These steps reveal the complexity of the input space, and a crude analysis of intermediate results is performed in order to define a reduced input space for a future, simpler optimisation procedure (Section 6.2.5).

6.2.1 Definition of the input space

A rectangular input space is defined with a given number of parameters and their continuous range of values. In this context, the 15 optimisation parameters are used. The bounds of several parameters intuitively derive from their mathematical definition. For instance, $\widetilde{c_{GF}}$ and $\beta_{2,pc_\beta 1}$ naturally vary within [0,1]. For the remaining parameters, larger ranges than the ones explored in conventional design processes are selected. The set of 15 optimisation parameters together with their range is summarised in Table 6.1 and defines the *initial rectangular input space*.

Unfortunately, and despite the definitions of dedicated optimisation parameters, most of the geometry generated at random in the initial rectangular space cannot be associated with a RANS prediction. Indeed, the CAD surface generation, the meshing process or the computation itself could fail in case of too complex geometries. In order to best explore the design space of *viable* guide fins (i.e. with an available RANS result), an original and specific strategy for handling such computational failures is used. A large database of guide fins is generated using a Monte Carlo methodology and only the guide fins with acceptable CAD surfaces are kept. Two criteria based on geometrical characteristics are implemented to define acceptable

surfaces. The first criterion detects ill-positioned tip aerofoils, and the second one detects surfaces with excessive angles at the leading edge and trailing edge (see Figure 6.2). For that purpose, new sweep and lean angles are computed. They are defined similarly as the guide fin sweep and lean angles, but are no longer related to the line joining the mid chord points. These angles are defined with respect to the lines joining the leading edges ($\lambda_{sweep,LE}$, $\lambda_{lean,LE}$) and the trailing edges ($\lambda_{sweep,TE}$, $\lambda_{lean,TE}$). The second criterion states that the maximum absolute value of these four angles cannot excess $\lambda_{tol} = 45°$. 6×10^5 guide fins are evaluated, and 9×10^4 are considered acceptable with these two criteria. The acceptable guide fins are referred to as *candidates*, and form the discrete candidate database that replaces the continuous initial rectangular input space. The main assumption in this process is that this database is representative of the set of all viable guide fins, which is reasonable. Indeed, the rate of accepted surfaces is about 15%. Even though meshing or computation failure might still occur, higher viability rates are expected from these steps. The CAD generation step is therefore likely to be the limiting one, and is bypassed with this strategy.

Parameter	$\Delta\beta_{1,H}$	$\beta_{2,pc_\beta1}$	$x_{M,H}$	$t_{M,H}$	$\widetilde{c_{GF}}$	u	v
Range	[-20°,10°]	[0,1]	[0.3,0.6]	[0,25%c_{GF}]	[0,1]	[0.1,0.92]	[0.03,0.97]
Parameter	$\Delta\beta_{1,T}$	$\Delta\beta_{2,T}$	$x_{M,T}$	$t_{M,T,rel}$	$c_{GF,T,rel}$	λ_{sweep}	λ_{lean}
Range	[-10°,10°]	[-10°,10°]	[0.3,0.6]	[0,1]	[0,1.1]	[-40°,40°]	[-40°,40°]
Parameter	H_{GF}						
Range	[0.8%c,20%c]						

Table 6.1: Parameters and ranges defining the initial rectangular input space.

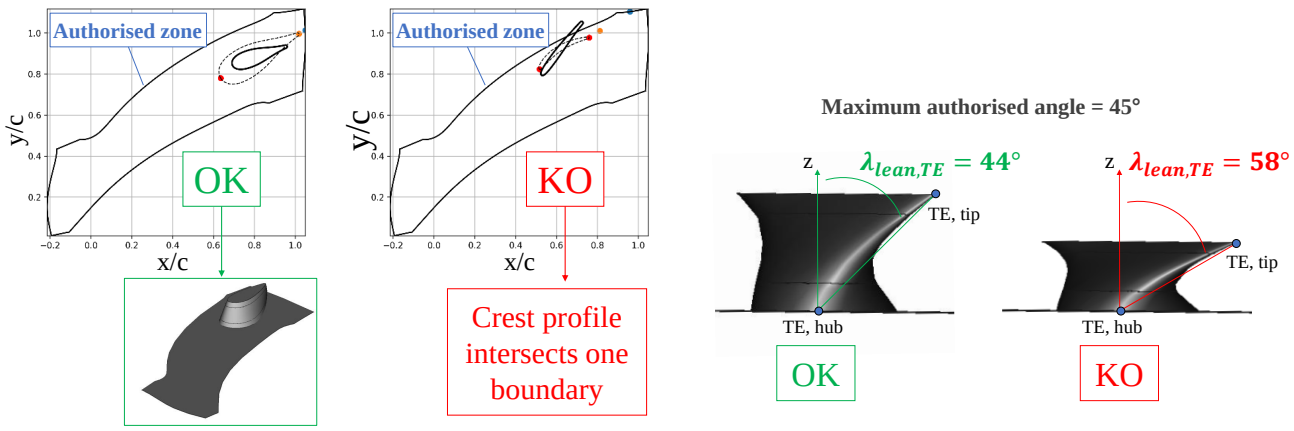

(a) Criterion on the tip aerofoil position. Solid line : tip aerofoil. Dashed line : hub aerofoil.

(b) Criterion on geometrical angles at LE and TE. In this example, the lean angle at the TE is the largest angle.

Figure 6.2: Illustrations of the geometrical criteria. LE=Leading Edge, TE=Trailing Edge.

The exploration of such a discrete database can be performed with an iterative refinement of Kriging surrogate models. However, a dedicated sampling methodology is required, and the surrogate models should be carefully exploited. Indeed, such models interpolate the values

of the objective functions on a continuous, rectangular input space. They can therefore be evaluated in regions of the input space corresponding to guide fins with non acceptable CAD surfaces.

6.2.2 Settings of the iterative process

The initial DOE is built by picking a small subset of candidate which spans as best as possible the entire candidate database. To achieve this, the "kernel herding" algorithm proposed by Chen et al. (2010) is used. It consists in minimising the distance between the empirical distribution defined on the DOE and the one on the entire candidate database. A DOE containing 150 guide fins is generated using this algorithm, 149 of which are viable. 10 iterations of refinement are then performed to complete the RANS database (see Table 6.2). Most refinements are performed using the EHVI criterion, described in Section 2.2.2. It is computed using guide fins of the candidate database only, and takes into account the two objective functions simultaneously. For the two last iterations, a manual selection of efficient guide fins is evaluated with RANS computations to assess the predictability of the refined surrogate model. The viability rate of each step is computed as the number of successful RANS evaluations over the total number of guide fins output by the refinement method. This viability rate is always greater than 69%, which indicates that the surrogate model is indeed refined with a large number of guide fins at each step. The final RANS database contains 526 viable guide fins. They are evaluated at two incidences (1052 RANS simulations), for a total numerical cost of about 10^5 CPU hours.

Step	**Refinement method**	N_{GF}**(viable / total)**	**Viability rate** (%)
DOE	Kernel Herding	149/150	99
Reft. 1	EHVI	13/15	87
Reft. 2	EHVI	14/14	100
Reft. 3	EHVI	20/20	100
Reft. 4	EHVI	40/50	80
Reft. 5	EHVI	112/150	75
Reft. 6	EHVI	23/30	77
Reft. 7	EHVI	25/30	83
Reft. 8	EHVI	31/45	69
Reft. 9	Manual selection	61/83	73
Reft. 10	Manual selection	36/52	69

Table 6.2: Exploration of the large input space (15p) : summary of the iterative refinements.

Figure 6.3 illustrates the evolution of the RANS database (red dots). The evolution of the predictions of the entire candidate database by the surrogate model are also indicated (black dots). This evolution illustrates that refining the surrogate model modifies its predictions on non-evaluated guide fins. The predictions of the guide fins selected by the EHVI criterion to refine the surrogate are indicated in green. Interestingly, these points are not necessarily selected among the best predicted guide fins. Indeed, the EHVI criterion relies on a balance between minimising the objective functions and minimising the surrogate uncertainty. The points selected far from the current pareto front are thus likely to be in regions of the candidate database with high uncertainty.

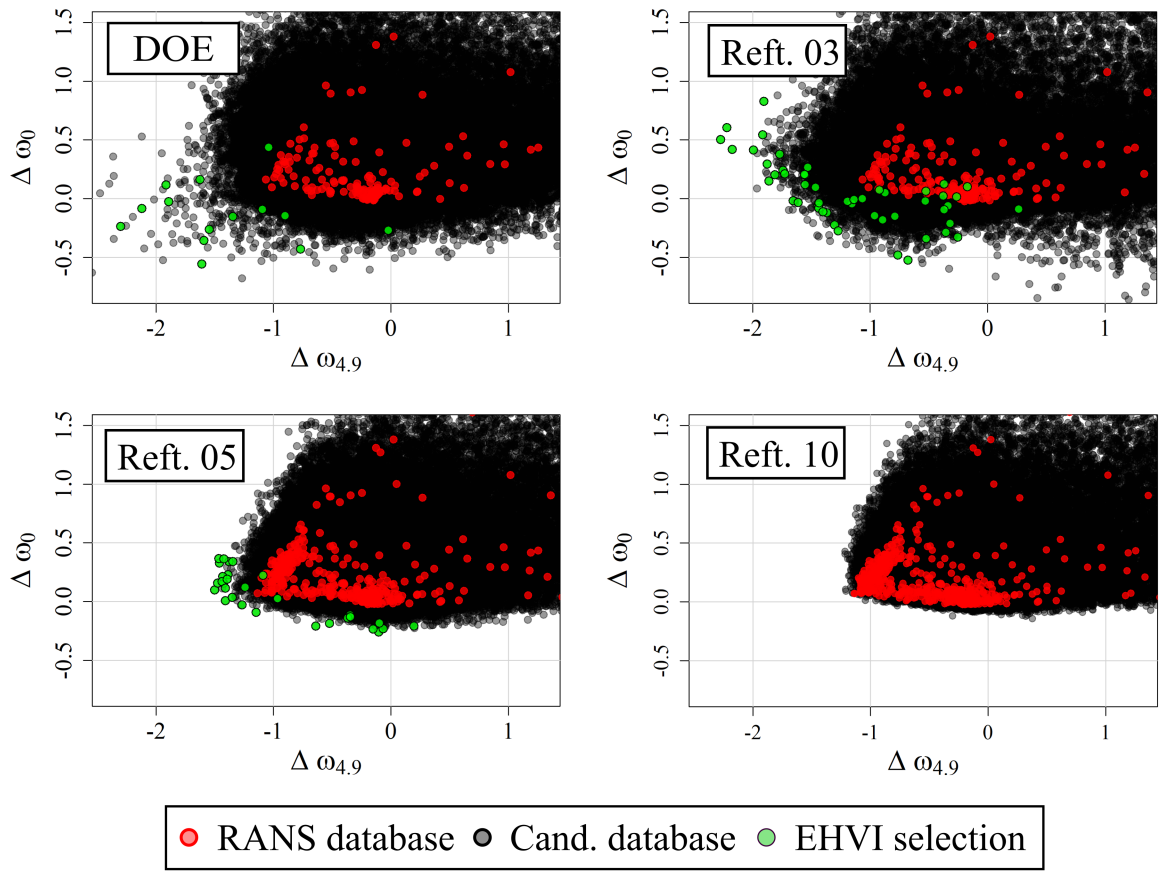

Figure 6.3: Evolution of the RANS database and candidate database predictions.

6.2.3 Convergence

For each refinement step, the set of best guide fins in the Pareto sense can be defined in several ways depending on the nature of the evaluations considered. A first set of interesting guide fins is defined as the best guide fins among the RANS database, and is called the *RANS Pareto front*. Two other sets are defined with the surrogate model. A conventional way to exploit the surrogate model is to perform an optimisation directly using its predictions. The widely used NSGA2 genetic algorithm is fitted to this bi-objective context with little expensive evaluations. However, this optimisation requires a continuous input space. In our specific case, the surrogate model is trained only on the discrete candidate database, but is mathematically defined on any subset of $\mathbb{R}^{15}$, and notably on the initial rectangular input space. The Pareto front found* on this rectangular space is called the *surrogate Pareto front*. Finally, the image of the discrete candidate database by the surrogate model provides a discrete set of predictions. The best guide fins among these predictions form the *candidate Pareto front*. This Pareto front is discrete and contains only guide fins of viable CAD surface.

Figure 6.4 illustrates the evolution of the three Pareto fronts at different refinement steps : the RANS Pareto front (blue diamond), the candidate Pareto front (purple diamond) and the surrogate Pareto front (purple line). The RANS database (in red) grows larger with the

*The NSGA2 algorithm is used through a routine of the software **R** (library mco). It is used with the following settings : popsize = 300, generations = 300, cprob = 0.7, cdist = 5, mprob = 0.2, mdist = 10. The optimisation is unconstrained and bounded by the initial rectangular input space bounds. The number of generation was increased until reaching repeatable Pareto fronts.

iterations, and the three Pareto fronts get closer to each other. The relative positions of the three Pareto fronts remain unchanged, and was expected. Indeed, the best elements on a subspace A can only be worse (or equal) than the best ones on a larger space including A. In our case, the RANS database is a restriction of the candidate database, which itself is a restriction of the initial rectangular input space. At the last iteration, the candidate and RANS Pareto fronts feature similar gains : the optimal gains computed by the refined surrogate model on the candidate database are realistic. On the contrary, the surrogate Pareto front features very different gains, that are considered unrealistic. These results are understandable as the surrogate model is trained on the candidate database only, but is explored by the genetic algorithm everywhere on the initial rectangular input space. The surrogate model can therefore predict minima on extrapolated results that actually correspond to guide fins with non acceptable CAD surfaces. As such, the refined surrogate model might be reliable on the candidate database, but not on the initial rectangular input space.

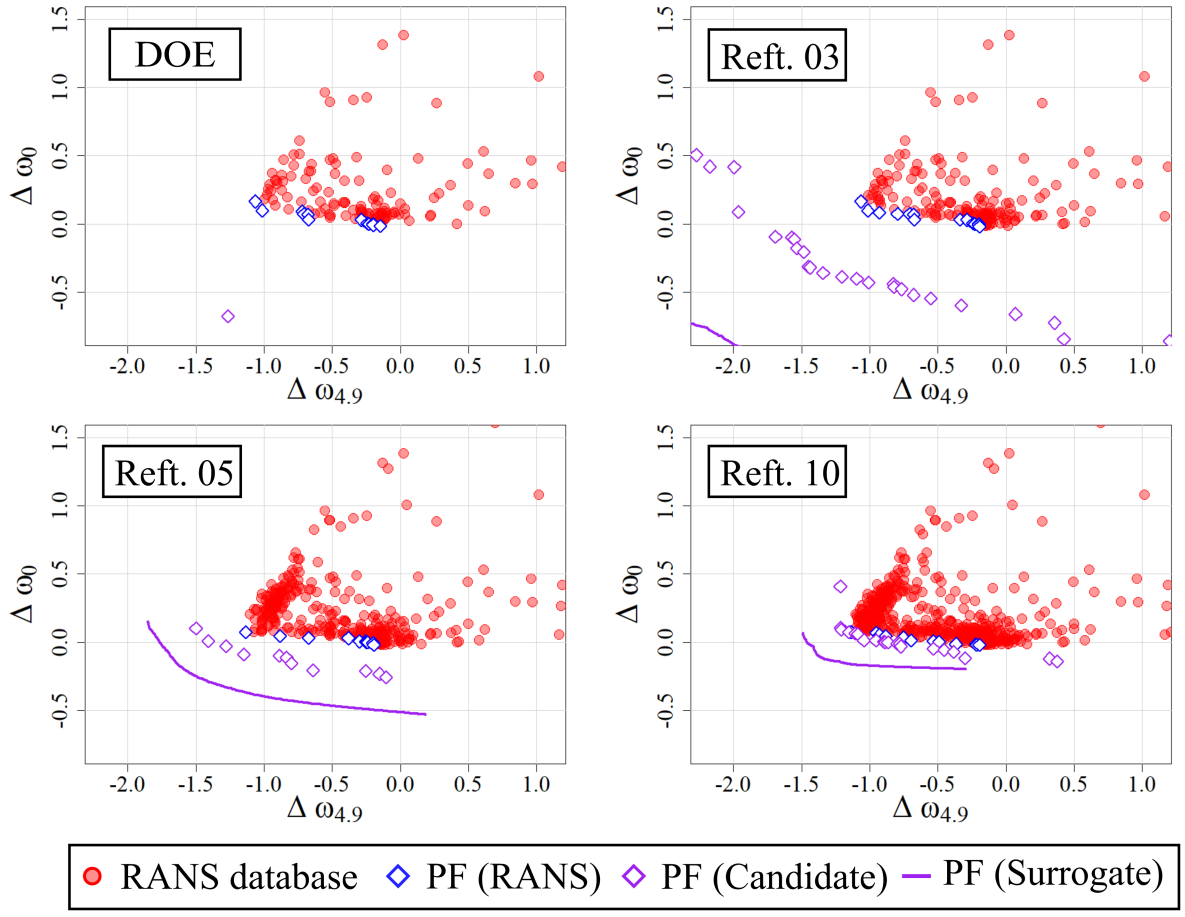

Figure 6.4: Evolution of the Pareto fronts.

The Hypervolume Indicator (HVI) is used to monitor the convergence of the Pareto fronts, and by extension the convergence of the optimisation process. The HVI is an indicator measuring the relative improvement of a given Pareto front (see Section 2.2.2). In our convention, the Pareto front is improved when the HVI increases. Figure 6.5a shows the evolution of the HVI for each Pareto front with the refinement steps. The HVI of the RANS Pareto front increases, showing that guide fins more efficient than the ones evaluated in the DOE are found. The relative positions of the Pareto fronts are retrieved, notably with a greater HVI for the candidate Pareto front than for the RANS Pareto front.

This specific optimisation process would be fully converged if the candidate and the RANS Pareto fronts merged and were insensitive to new refinements. This corresponds to HVI values converging towards the same asymptotic value. Figure 6.5a shows that the HVI values of the candidate and RANS Pareto front get closer with the refinement steps, but remain different. The first iterations are performed with the EHVI criterion until reaching the stagnation of the indicators (Reft. 7 and 8). To further improve the RANS database, several guide fins of the candidate Pareto front are evaluated (Reft. 9). This yields a drop in the surrogate HVI and a slight improvement of the RANS HVI. This operation is repeated (Reft. 10) but no further improvement is observed. Given the computational cost of a refinement step and the small improvement of the RANS HVI, the refinement process is stopped.

The Q2 criterion is also monitored and its evolution is illustrated in Figure 6.5b. This criterion gives an indication on the average predictability of the surrogate model on the initial rectangular input space for each objective function (see Section 2.1.1). The predictability is commonly considered very poor for Q2 values below 0.7, to give reasonable trends for values within $[0.7, 0.9]$, and excellent for values above 0.9. In our case, the Q2 criteria slightly decrease with the iterations, and globally stagnate at values close to 0.8. Let us underline that this criterion does not necessarily increase. Refining a region of the input space can reveal a more complex behaviour of the objective functions than the one predicted so far. The predictability can thus decrease with the refinement steps. This might be the reason for the decrease observed in this process. The value of 0.8 still indicates that the global trends are fairly predicted.

Even though the process is not fully converged, the objectives of the optimisation step are fulfilled : the RANS Pareto front is improved with very efficient guide fins, and a refined surrogate model is available. Given the intermediate values of the Q2 criteria, it is difficult to assess the average predictability of the surrogate model. The predictability is therefore quantified locally in the regions of efficient guide fins in Section 6.2.4.

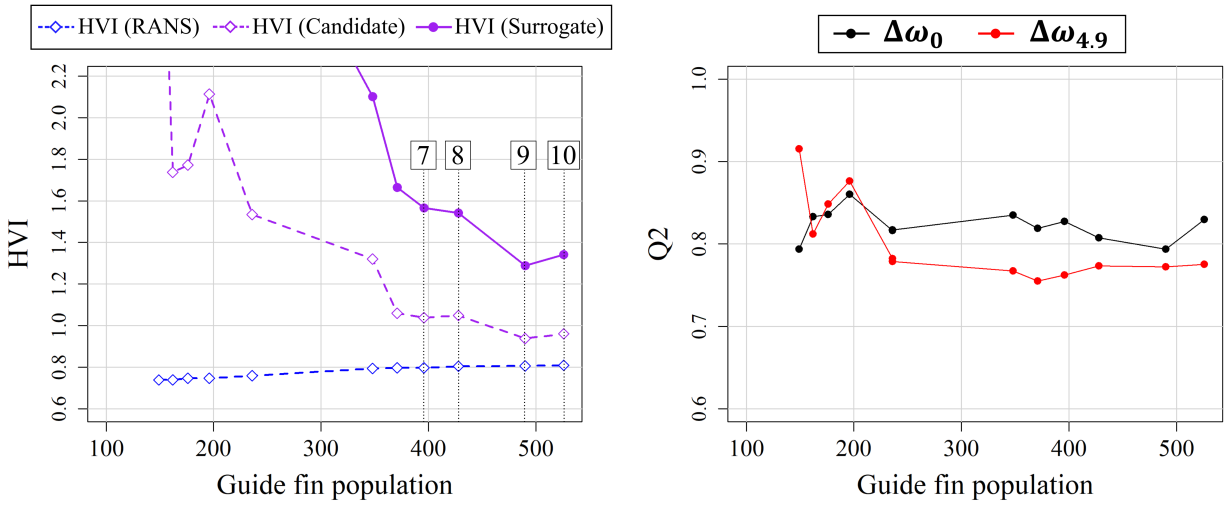

(a) HVI evolution for each Pareto front.

(b) Q2 evolution for each objective function.

Figure 6.5: Evolution of the HVI and Q2 criteria on the large input space.

6.2.4 Predictability in the Pareto front region

Two guide fins of the RANS database are selected in the region near the RANS Pareto front to evaluate the local predictability of the refined surrogate model. They are representative of two interesting types of geometries that will be further investigated, and are illustrated in Figure

6.6. They notably feature either a short chord and thin aerofoils or a long chord and thick aerofoils.

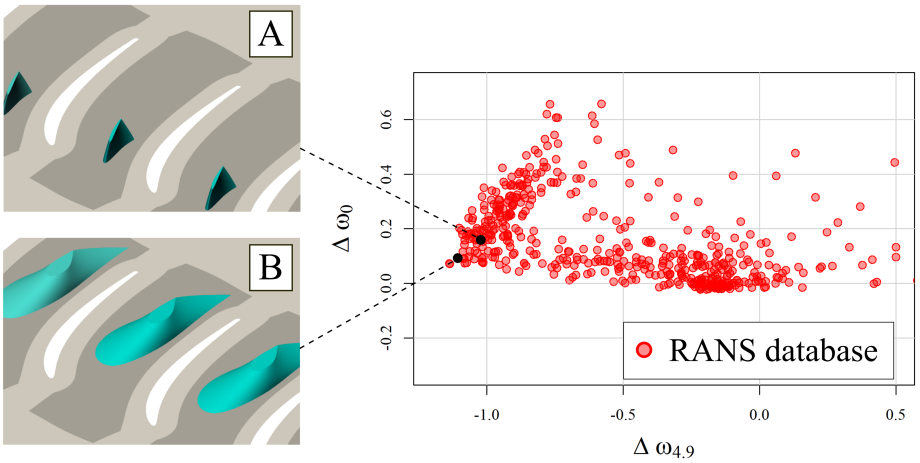

Figure 6.6: Shapes and positions in the RANS database of guide fins A and B.

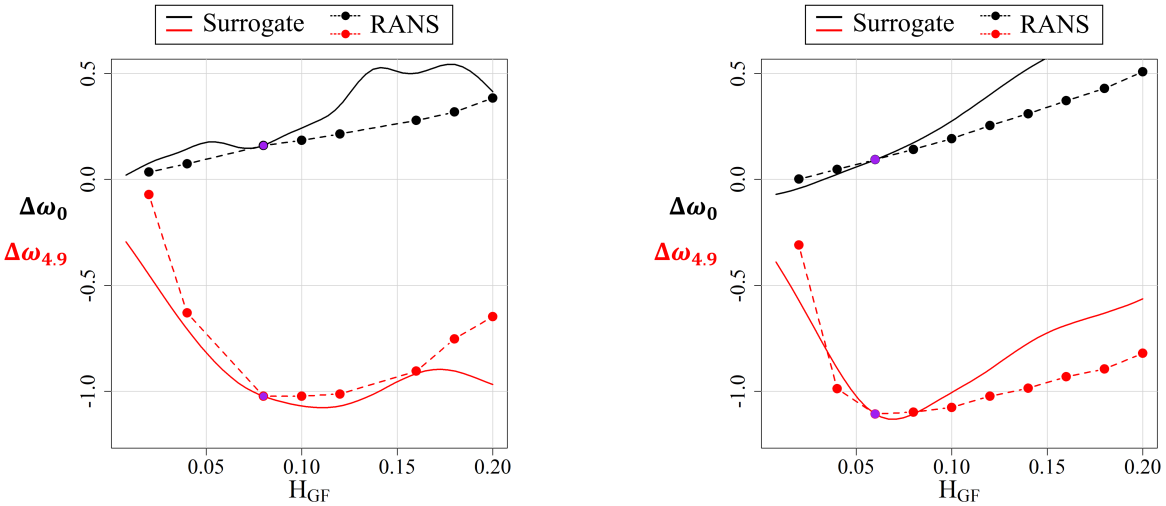

(a) Guide fin A.

(b) Guide fin B.

Figure 6.7: Surrogate predictions vs RANS computations. For each guide fin A and B, only H_{GF} varies from its minimum to its maximum value.

The height (H_{GF}) of guide fin A and B is varied, and the corresponding surrogate predictions are computed for both objective functions (solid lines, Figure 6.7). The surrogate is trained only with the guide fin with the height of reference (purple dot, Figure 6.7). The corresponding RANS computations are performed and compared to the predictions (dotted dashed lines, Figure 6.7).

For guide fin A, a chaotic evolution of the losses is predicted for $\Delta\omega_0$, far from the linear trend revealed with RANS computations. However, the levels and the trend are globally consistent with RANS results. On the other hand, the surrogate prediction of $\Delta\omega_{4.9}$ is excellent on a large range of values ($H_{GF} \in [0.04, 0.16]$). Notably, the behaviour near optimal values is well captured. The gradients close to the point of reference are also well predicted.

For guide fin B, the trends are very well predicted by the surrogate model for both objectives. Notably, the RANS optimum corresponds to the surrogate optimum for $\Delta\omega_{4.9}$, and the gradients

on the point of reference are correct for both objective functions. The main discrepancy can be seen for height greater than the reference, where losses are slightly over predicted.

As a summary, except for chaotic predictions, the surrogate model well predicts the effect of H_{GF} near these two efficient guide fins, which brings confidence in the surrogate predictions. Because of computational cost, no further investigations are carried out. The surrogate model is therefore considered reliable near evaluated guide fins, except for obviously unphysical predictions.

6.2.5 Definition of a reduced input space of interest

In this section, a basic analysis of intermediate results is performed to define a reduced input space. It will be used in a future, simpler optimisation process (Section 6.2.5) that focuses on efficient guide fins detected with the current process. This might enable to perform a fully converged optimisation, to find better guide fins, and to obtain a surrogate model reliable on the entire reduced input space.

To help define a region of interest, the concept of *depth* is introduced. For a given discrete sample in the space of the objective functions, a Pareto front is defined and is of depth 1. If this Pareto front is removed from the sample, a new Pareto front is defined, and is of depth 2. The depth is iteratively defined until every point is removed from the initial sample. The depth is therefore a measure of the distance to the Pareto front, as illustrated in Figure 6.8.

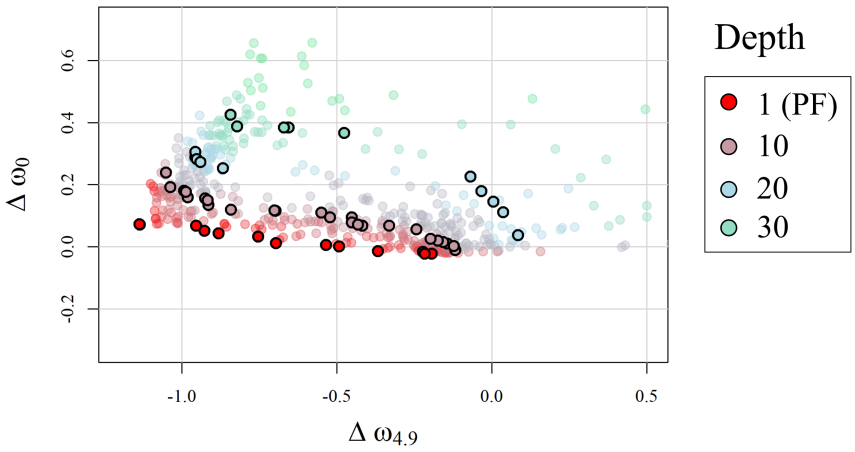

Figure 6.8: RANS database coloured by depth values. Depths 1, 10, 20, 30 are highlighted.

The selection of the most influential input parameters is performed on a subset of guide fins close to the RANS Pareto front. Guide fins of depth ≤ 10 (202 guide fins) are selected. These guide fins feature various chord values, and the parameter $\widetilde{c_{GF}}$ is replaced by the absolute chord value $c_{GF,H}$ to enhance its physical effect. Pearson coefficients are computed on this subset, between each parameter and with respect to each objective functions. Pearson coefficients quantify the linear trend between a distribution of parameters and an objective function if it exists (see Section 2.3). The sample considered is large enough for all coefficients to be statistically significant (see Section 2.3). Table 6.3 and 6.4 summarise the results.

Most parameters feature a negligible correlation with the objective functions. The gains seem to be mostly correlated with H_{GF}, u et $\Delta\beta_{1,H}$, which feature an absolute value of the correlation within $[0.33, 0.74]$. $\Delta\omega_0$ et $\Delta\omega_{4.9}$ are strongly correlated with one another, which is expected as the coefficients are computed on a subset close to the Pareto front region.

Parameter	$\Delta\omega_{4.9}$	$\Delta\beta_{1,H}$	$\beta_{2,pc_\beta1}$	$x_{M,H}$	$t_{M,H}$	$c_{GF,H}$	u	v
Pearson coefficient	-0.86	-0.33	-0.03	-0.13	-0.10	+0.28	-0.48	-0.01
Parameter	H_{GF}	$\Delta\beta_{1,T}$	$\Delta\beta_{2,T}$	$x_{M,T}$	$t_{M,T,rel}$	$c_{GF,T,rel}$	λ_{sweep}	λ_{lean}
Pearson coefficient	+0.74	+0.09	+0.19	-0.01	-0.06	+0.02	+0.09	-0.06

Table 6.3: Pearson coefficients with $\Delta\omega_0$.

Parameter	$\Delta\omega_0$	$\Delta\beta_{1,H}$	$\beta_{2,pc_\beta1}$	$x_{M,H}$	$t_{M,H}$	$c_{GF,H}$	u	v
Pearson coefficient	-0.86	+0.36	+0.04	+0.10	+0.13	-0.20	+0.57	+0.06
Parameter	H_{GF}	$\Delta\beta_{1,T}$	$\Delta\beta_{2,T}$	$x_{M,T}$	$t_{M,T,rel}$	$c_{GF,T,rel}$	λ_{sweep}	λ_{lean}
Pearson coefficient	-0.65	-0.09	-0.20	+0.04	+0.10	+0.01	-0.02	+0.01

Table 6.4: Pearson coefficients with $\Delta\omega_{4.9}$.

Further investigations (see Chapter 7.1) show that the efficient guide fins are either thin and short or thick and long. The chord and thickness parameters should therefore be included to cover the most efficient shapes. To limit the number of parameters, only the hub thickness ($t_{M,H}$) and hub chord ($c_{GF,H}$) are retained. Finally, to avoid restricting the guide fin positions to a specific azimuthal value, v is let free to vary.

The values of the six retained parameters ($\Delta\beta_{1,H}$, $t_{M,H}$, $c_{GF,H}$, u, v and H_{GF}) are plotted against $\Delta\omega_{4.9}$ for all guide fins of the subset (Figure 6.9). The guide fins of the Pareto front are represented with blue diamonds. Two clear correlations are indeed visible for H_{GF} and u. Moreover, the values of $t_{M,H}$ and $c_{GF,H}$ indeed indicate that the Pareto front is populated with two types of guide fins. Thin guide fins are also short, and thick guide fins are also long. This is consistent with the geometrical characteristics of guide fins A and B (Section 6.2.4), and will be further investigated in next chapter.

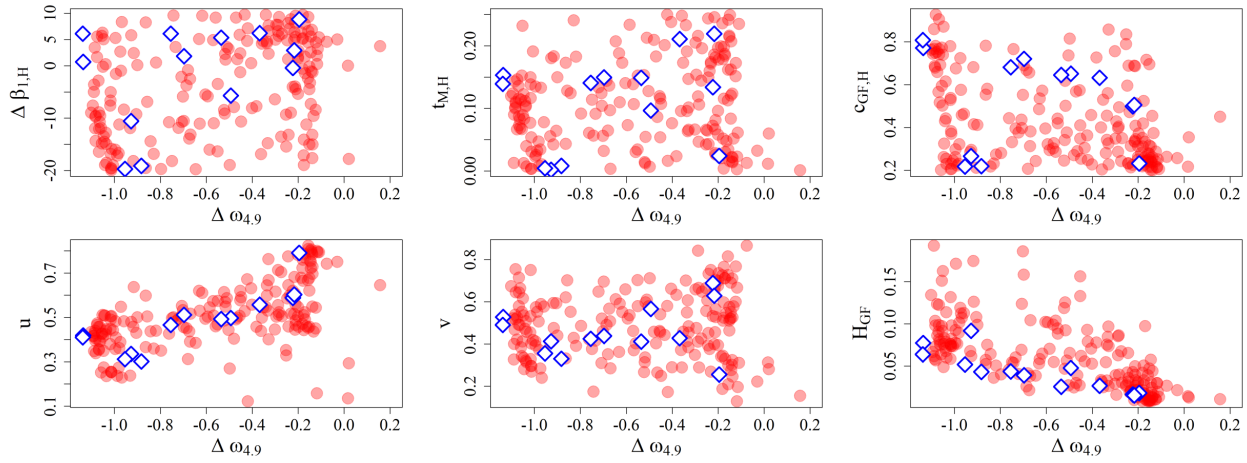

Figure 6.9: Guide fins used for computing Pearson coefficients (depth ≤ 10). The Pareto front is highlighted with blue diamonds.

The ranges of these 6 parameters are reduced to simplify the optimisation problem. They are inspired by the values of the parameters of the Pareto optimal guide fins. The 9 remaining parameters must be fixed to values that *a priori* least affect the shape of the future best guide fins. Table 6.5 summarises the ranges and values of the 15 parameters as they will be used in the reduced optimisation problem (Section 6.3).

Part	Parameter	Range	Comment
Hub	$\Delta\beta_{1,H}$	$\in [-20°, 10°]$	
	$\beta_{2,pc_\beta1}$	Such that $\Delta\beta_{2,H} = 0$	Guide the flow like the stator
	$x_{M,H}$	$= 0.45$	Mean value of previous range
	$t_{M,H}$	$\in [0, 0.25]$	
	$\widetilde{c_{GF}}$	$\in [0, 1]$	
	u	$\in [0.3, 0.8]$	
	v	$\in [0.25\ 0.75]$	
Tip	$\Delta\beta_{1,T}$	$= 0°$	Guide the flow like the stator
	$\Delta\beta_{2,T}$	$= 0°$	Guide the flow like the stator
	$x_{M,T}$	$= 0.45$	Mean value of previous range
	$t_{M,T,rel}$	$= 0$	Minimum value to reduce profile loss
	$c_{GF,T,rel}$	$= 1$	Simplify the stacking law, no geometrical sweep
	λ_{sweep}	$= 0$	Simplify the stacking law
	λ_{lean}	$= 0$	Simplify the stacking law
Height	H_{GF}	$\in [0.8\%c, 10\%c]$	

Table 6.5: Parameter ranges and values defining the reduced optimisation problem. Only 6 parameters vary (in blue).

6.3 Optimisation in a reduced input space (6p)

This section presents the optimisation process performed on the reduced input space described in Section 6.2.5. This reduced space is designed to focus on efficient guide fins revealed by the optimisation performed on the larger 15-parameter space, and aims at obtaining a surrogate model reliable on the entire reduced input space. The settings of the optimisation process are presented (Section 6.3.2). The convergence of the optimisation process is then described (Section 6.3.3). The last iteration assesses the predictability of the surrogate model near the Pareto front, and is thoroughly described (Section 6.3.4).

6.3.1 Definition of the input space

The bounds of the reduced input space are summarised in Table 6.5, Section 6.2.5. In this case, the input space is small enough to mainly contain viable guide fins. The iterative refinement of surrogate models is performed on the whole rectangular input space without discretisation.

6.3.2 Settings of the iterative process

In this optimisation process, 4 refinement criteria are used. Their characteristics are summarised hereafter, and further described in Section 2.2.2. The criteria are :

- Space filling : LHS sampling of the input space coupled to the maxProj algorithm. Aims at uniformly explore the input space.
- Global accuracy : Aims at increasing the average predictability of the surrogate models i.e. at increasing the Q2 criterion values.
- EHVI : Provides guide fin samples based on the EHVI criterion.
- Manual selection : Manual selection of guide fins among the predicted Pareto front of the current iteration step. Aims at evaluating the surrogate predictability and at verifying the convergence of the process.

Step	**Refinement method**	N_{GF}**(viable / total)**	**Viability rate** (%)
DOE	Space filling	55/60	92
Reft. 1	Global accuracy	15/20	75
Reft. 2	Global accuracy	12/20	60
Reft. 3	Global accuracy	28/40	70
Reft. 4	Global accuracy	20/30	67
Reft. 5	Global accuracy	30/50	60
Reft. 6	Global accuracy	31/50	62
Reft. 7	EHVI	62/80	78
Reft. 8	EHVI	40/80	50
Reft. 9	EHVI	28/50	56
Reft. 10	EHVI	7/20	35
Reft. 11	EHVI	43/80	54
Reft. 12	Manual selection	16/18	89
Reft. 13	Space filling	47/60	78
Reft. 14	EHVI	11/30	37
Reft. 15	EHVI	25/60	42
Reft. 16	EHVI	24/60	40
Reft. 17	Manual selection	13/21	62

Table 6.6: Exploration of the reduced input space (6p) : summary of the iterative refinements. The input space is enlarged from Reft. 13 (Gray rows).

The refinement steps are summarised in Table 6.6. The refinement criteria indicated for Reft. i corresponds to the criterion used on the surrogate of Reft. i-1 to obtain the RANS database and surrogate of Reft. i. The process is initiated with a DOE containing 55 guide fins. After 11 refinements, a manual selection of several guide fins of the Pareto front are evaluated with RANS computations to monitor the convergence of the process (Reft. 12). These guide fins appear to have the same values for the parameters $\Delta\beta_{1,H}$ ($-20°$), and v (0.25). These values correspond to the lower bound of the corresponding parameter range. The range of $\Delta\beta_{1,H}$ is increased from $[-20°, 10°]$ to $[-50°, 10°]$. The range of v is not modified. Refinements 13, 14, 15, 16 are then performed to explore this enlarged input space. The last iteration is Reft. 17 for computational budget reasons, and is used to evaluate the predictability of the surrogate model. A manual selection of guide fins on the predicted Pareto front is evaluated in RANS. Predictions and RANS results are compared in Section 6.3.4. The final RANS database contains 507 viable guide fins. They are evaluated at two incidences (1014 RANS computations), for a total numerical cost of about 10^5 CPU hours.

6.3.3 Convergence

In the 15p exploration, the implementation of a candidate database was necessary and a candidate Pareto front could be defined. In the exploration of the reduced space, no candidate database is used. Only two Pareto fronts are therefore used to monitor the exploration of the reduced space. The set of best guide fins in the Pareto sense among the RANS database defines the RANS Pareto front. The set of best guide fins predicted by the surrogate models is defined using the NSGA2 algorithm, with the same settings as described in 6.2.3, and is called the surrogate Pareto front.

Figure 6.10 shows the evolution of the RANS database at different refinement steps (red dots). The RANS and surrogate Pareto fronts are highlighted, with blue diamond and purple lines respectively. The surrogate models of Reft. 6 and 14 are refined using the EHVI criterion, which provides a new set of guide fins to evaluate. The predictions of this new set by the corresponding surrogate model are represented in green.

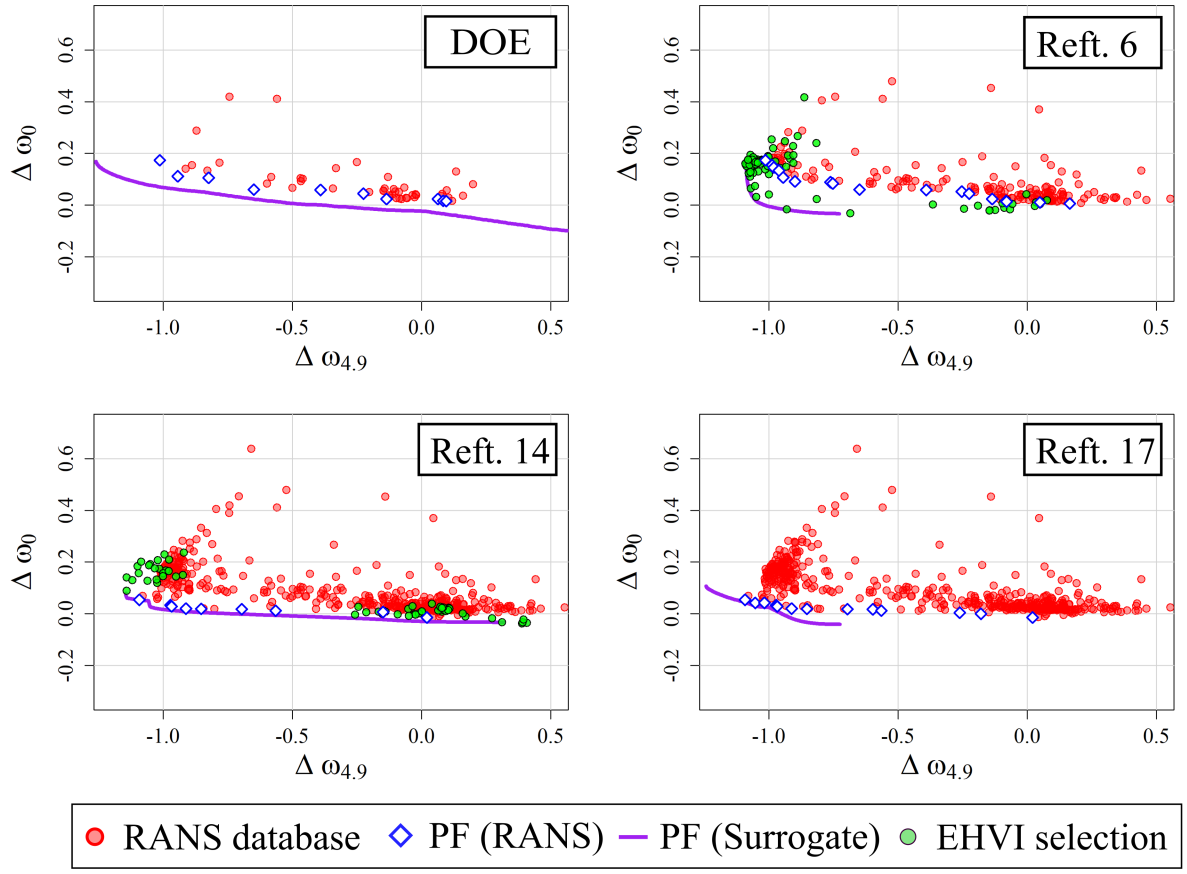

Figure 6.10: Evolution of the RANS database and Pareto fronts.

The Pareto fronts improvement are quantified using the HVI criterion, whose evolutions are presented in Figure 6.11a. The same reference point is used as for the 15-parameter exploration to make their values comparable : $(\Delta\omega_{0,ref}, \Delta\omega_{4.9,ref}) = (0.5, 0.5)$. The HVI evolution can be split in two parts, corresponding respectively to the exploration of the initial reduced space (Reft. ≤ 12) and to the exploration of the reduced space enlarged with new values of $\Delta\beta_{1,H}$ ($13 \leq$ Reft. ≤ 18). Within each part, the RANS and surrogate HVI converge towards each other, which is expected. At the end of both parts, a manual selection of guide fins of the surrogate Pareto front is evaluated in RANS. This yields an increase in the RANS HVI, which

is understandable, and more surprisingly, to an increase in the surrogate HVI. It is worth noticing that for numerous refinements (Reft ≥ 8), the RANS and surrogate HVI have close values. This indicates that the lowest values predicted by surrogate model remain at reasonable order of magnitudes.

The evolution of the surrogate predictability is also monitored using the Q2 criterion. Figure 6.11b shows that this criterion increases monotonously for both objective functions for Reft. ≥ 5. The final value reached is close to $Q2 = 0.9$ for both objectives functions. It is typically considered satisfying, and the surrogate model is therefore considered reliable on average over the entire reduced space.

In next section, the predictability in the Pareto front region is analysed.

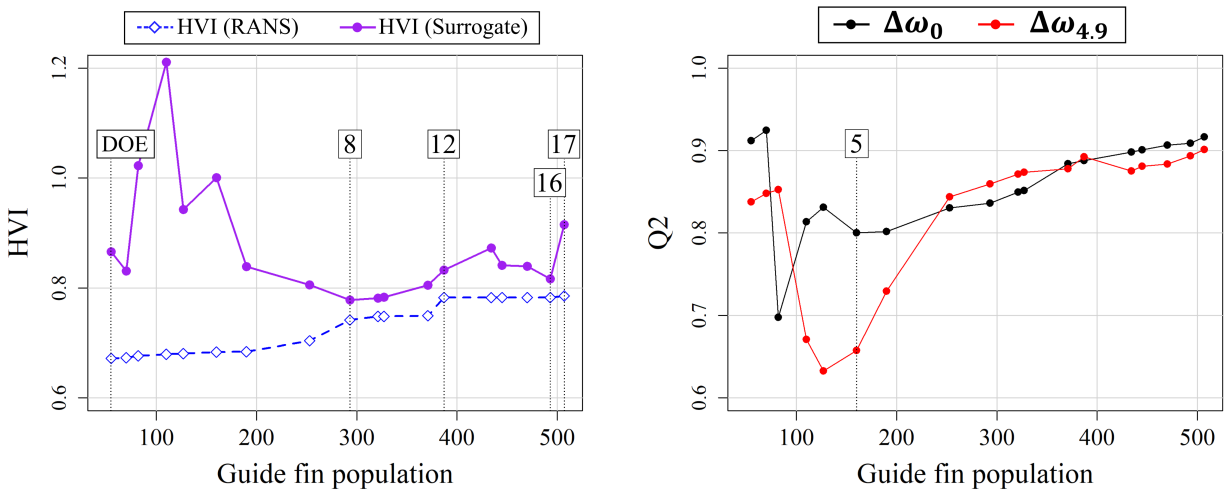

(a) HVI evolution for each Pareto front.

(b) Q2 evolution for each objective function.

Figure 6.11: Evolution of the HVI and Q2 criteria on the reduced input space (6p).

6.3.4 Predictability in the Pareto front region

In order to validate the surrogate predictions in the Pareto front region, a selection of guide fins of the surrogate Pareto front of Reft. 16 is evaluated in RANS (Figure 6.12). The maximum error in the $\Delta\omega_0$ predictions is of $\simeq 0.02\%$ total pressure loss, and is negligible. The maximum error in the $\Delta\omega_{4.9}$ predictions is of $\simeq 0.1\%$ total pressure loss, which remains low. Two particularly well predicted guide fins are encircled in Figure 6.12. The surrogate model is thus reliable on these guide fins. These RANS evaluations are then added to the RANS database, and constitute the last surrogate refinement (Reft. 17).

It is interesting to notice that incorporating these points changes the shape of the Pareto front. This can be seen by comparing the surrogate Pareto front at Reft. 16 (Figure 6.12, left) and 17 (Figure 6.10), and is consistent with the sudden increase of the surrogate HVI between Reft. 16 and 17 (Figure 6.11a). The new Pareto front predicts more efficient guide fins. However, the predictability of the evaluated points is not questioned, as they are included in the final RANS database, and similar guide fins should be predicted with a similar accuracy.

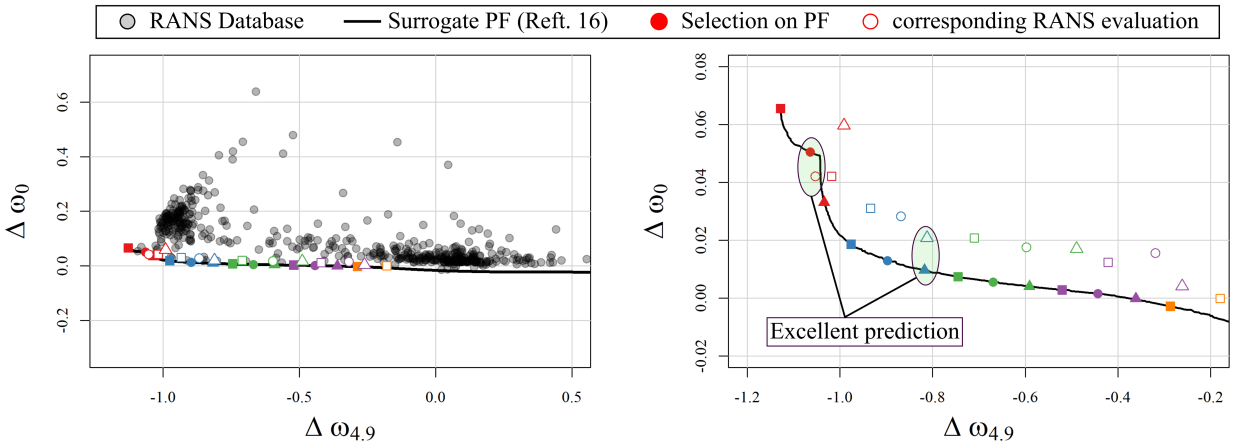

Figure 6.12: Predictability near Pareto Front : guide fins selection on the surrogate Pareto front at Reft. 16 vs RANS evaluations. Global view (left) and zoom in the evaluated region (right).

As a summary, 507 guide fins are evaluated in this optimisation process. The RANS pareto front is stabilised over the 5 last iterations, which justifies to stop the optimisation process. Unfortunately, the process cannot be strictly considered converged because of the sudden increase of the surrogate HVI at the last iteration. Still, the refined surrogate model is reliable on average and in the Pareto front region. It can thus be used instead of RANS to evaluate the effect of a new guide fins for a negligible numerical cost. The effect of the input parameters on the objective functions can therefore be thoroughly studied.

6.4 Summary

This section summarises the results of the two optimisation processes. The quantities relative to the entire input space are denoted with the “15p” prefix (15-parameter space), and those relative to the reduced space are denoted with the “6p” prefix (6-parameter space).

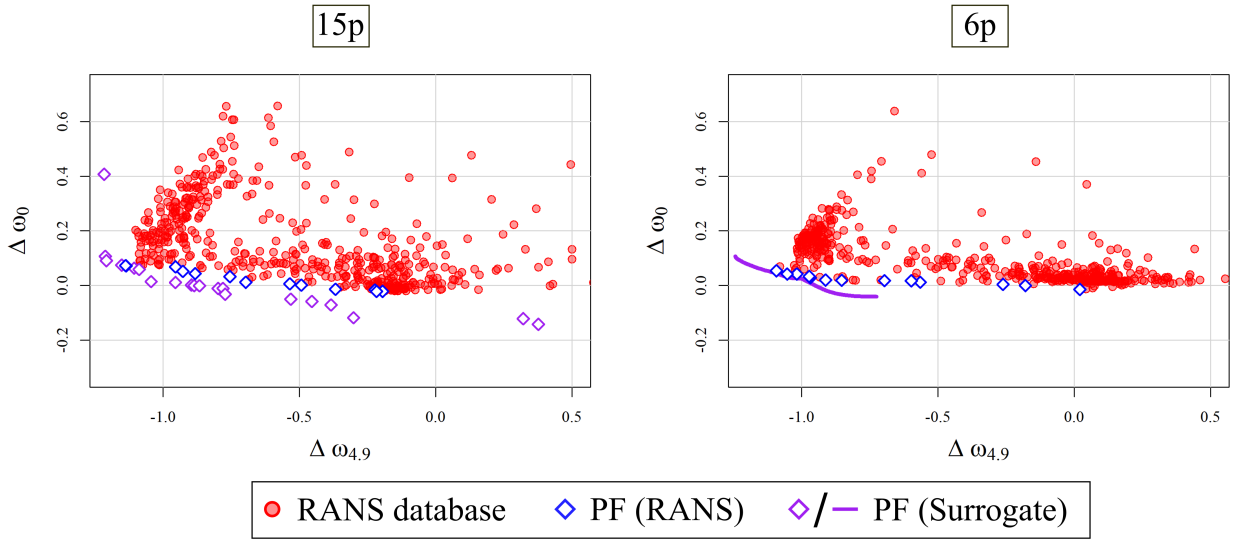

Figure 6.13: Comparison of 15p and 6p databases and Pareto fronts (PF).

Figure 6.13 compares the final RANS databases and Pareto fronts. The 15p database features a more scattered cloud of points than the 6p. Reducing the dimensions of the input

space therefore seems to focus on more interesting regions. Each database features two regions of dense points localised about $\Delta\omega_{4.9} \simeq 0$ and $\Delta\omega_{4.9} \simeq -1$. These regions are separated by a sparse zone about $\Delta\omega_{4.9} \simeq -0.5$. This behaviour is explained by the topological switch artefact described in Section 5.3.2. Indeed, a non efficient guide fin will not affect the topology of the corner separation, which remains double sided and induces a similar level of losses. However, as soon as a guide fin is efficient enough to induce a single sided corner separation, the losses suddenly (and artificially) drops. The two dense regions are thus interpreted as such : efficient guide fins with single sided separations ($\Delta\omega_{4.9} \simeq -1$) and non efficient guide fins with double sided separations ($\Delta\omega_{4.9} \simeq 0$). Rarely, guide fins might lead to double sided separations of lesser magnitude. These ones correspond to the sparse region about $\Delta\omega_{4.9} \simeq -0.5$. This artefact also explains the "flat" distribution of the RANS Pareto fronts : best guide fins spread across a larger range of $\Delta\omega_{4.9}$ than $\Delta\omega_0$. Finally, it is worth noticing that the losses at design incidence are globally lower in the 6p database. In the 6p exploration, the metal angles of the tip aerofoil are forced to follow exactly the local stator camber. The aerodynamic impact of the guide fin at design incidence is understandably low, as the deflection asked for is already achieved by the stator.

RANS characteristics	**15p**	**6p**
Number of guide fins	526	507
Best $\Delta\omega_0$ (corresponding $\Delta\omega_{4.9}$)	-0.02 (-0.20)	-0.01 (0.02)
Best $\Delta\omega_{4.9}$ (corresponding $\Delta\omega_0$)	-1.14 (0.07)	-1.09 (0.05)
HVI	0.809	0.785

Table 6.7: 15p vs 6p : characteristics of the RANS databases.

Surrogate characteristics	**15p**	**6p**
Nature of input space	Discrete candidate database	Continuous rectangular space
Best $\Delta\omega_0$ (corresponding $\Delta\omega_{4.9}$)	-0.14 (0.37)	-0.04 (-0.72)
Best $\Delta\omega_{4.9}$ (corresponding $\Delta\omega_0$)	-1.22 (0.41)	-1.24 (0.11)
HVI	1.34	0.915
Q2 ($\Delta\omega_0$,$\Delta\omega_{4.9}$)	(0.83,0.78)	(0.90,0.91)
Satisfying predictability	Near RANS evaluation	On the entire input space

Table 6.8: 15p vs 6p : characteristics of the surrogate models.

Table 6.7 summarises the characteristics of the RANS databases. Notably, the best gains on each objective functions and the RANS HVI are compared. It appears that similarly efficient guide fins are found in both databases. A slightly better compromise is found with the 15p database for lowering $\Delta\omega_0$. The close values of the HVI are consistent with the similar shapes of the RANS Pareto front observed in Figure 6.13.

Table 6.8 summarises the characteristics of the final refined surrogate models built with each database. The 15p surrogate model is trained and exploited on a discrete subset of the initial 15-parameter input space (see Section 6.2.1). The 6p surrogate model is defined on a continuous, rectangular 6-parameter space (see Section 6.3.1). The two Pareto fronts provided by the surrogate models contain equally efficient guide fins for $\Delta\omega_{4.9}$, while the 15p surrogate model contains more efficient guide fins on $\Delta\omega_0$. However, the 15p Pareto optimal guide fins are relatively far from the database, as pointed out by the high value of the surrogate HVI compared to the RANS HVI (Table 6.7). This reveals too optimistic predictions. More

generally, the predictability of the 15p surrogate model was validated only near the evaluated guide fins. Given the discrete nature of the input space and the intermediate values of the Q2 criteria, it is difficult to ensure a high level of predictability elsewhere. On the contrary, the 6p Pareto is close to the database, its predictability is excellent on average (Q2 criteria) and specifically in the Pareto front region (RANS evaluations, see Section 6.3.4).

Chapter 7

Characteristic shapes of efficient guide fins

In the previous chapter, two input spaces describing guide fins of various shapes are explored. A large number of guide fins reducing the endwall losses at high incidence are detected. In this chapter, the shapes of the guide fins that most reduce these losses are characterised.

The results of the 15-parameter (15p) analysis are first investigated. Geometrical criteria are defined to crudely gather guide fins in several families that are investigated separately. Two main families are revealed, and characterised with additional geometrical specificities. 6 parameters out of the 15 optimisation parameters appear to have a great influence on the losses at high incidence ($\Delta\omega_{4.9}$ objective function) and are thoroughly analysed (Section 7.1). The results of the 6-parameter (6p) analysis are then investigated. The same two main families are retrieved, but with different performances than in the 15p analysis. A third family of guide fins is highlighted (Section 7.2). These three families feature different geometrical specificities. They are likely to implement different physical mechanisms responsible for the loss reduction they induce. A representative guide fins of each family is therefore selected for further investigations (Section 7.3).

7.1 Analysis of the 15-parameter space results

In this section, a subset of efficient guide fins is extracted from the 15p RANS database and investigated. Two geometrical criteria are built to split this subset into 3 families of consistent geometries. Representative geometries of each family are illustrated and commented (Section 7.1.1). The two main families are then characterised with specific geometrical features and specific sensitivities to a restrained number of parameters (Section 7.1.2). The third family is then investigated and compared to the two main ones (Section 7.1.3). Finally, the geometrical specificities and the main sensitivities of the two main families are summarised (Section 7.1.4).

7.1.1 Investigation of the RANS database (15p)

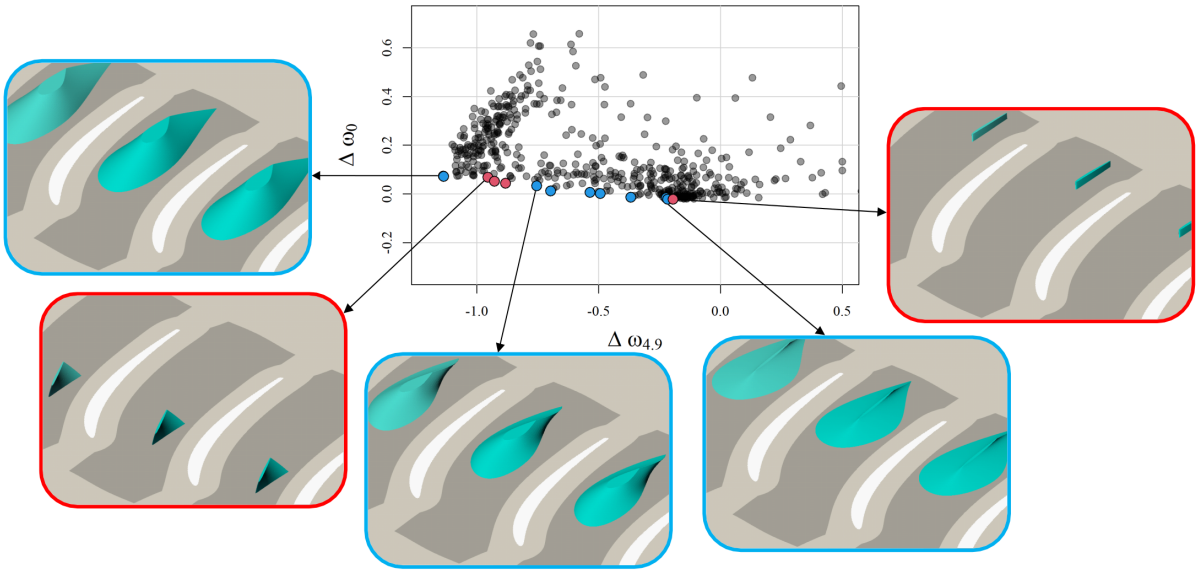

Figure 7.1: Characteristic shapes of RANS Pareto front (15p). RANS database (black) and intuitive repartition of Pareto optimal geometries into two groups (blue and red).

The optimisation process carried out on the 15-parameter space outputs a large database of guide fins of various shapes. This section attempts to gather the efficient guide fins with respect to geometrical similarities. Intuitively, the Pareto optimal guide fins are firstly investigated. It appears that the 13 Pareto optimal guide fins feature two characteristic shapes. 4 of them are thin and short, while the 9 remaining are rather thick and long as illustrated in Figure 7.1. In order to investigate if this trend is general among efficient guide fins, a larger sample is considered. The set containing the guide fins of depth ≤ 5 (81 guide fins) is considered. These guide fins are represented in Figure 7.2 with respect to their absolute hub chord $c_{GF,H}$ and absolute maximum thickness $t_{M,H,abs} = t_{M,H} \times c_{GF,H}$. Each guide fin is coloured with the endwall loss reduction at design incidence ($\Delta\omega_0$) and scaled proportionally to the endwall loss reduction at high incidence ($\Delta\omega_{4.9}$) to highlight their effects on the objective functions.

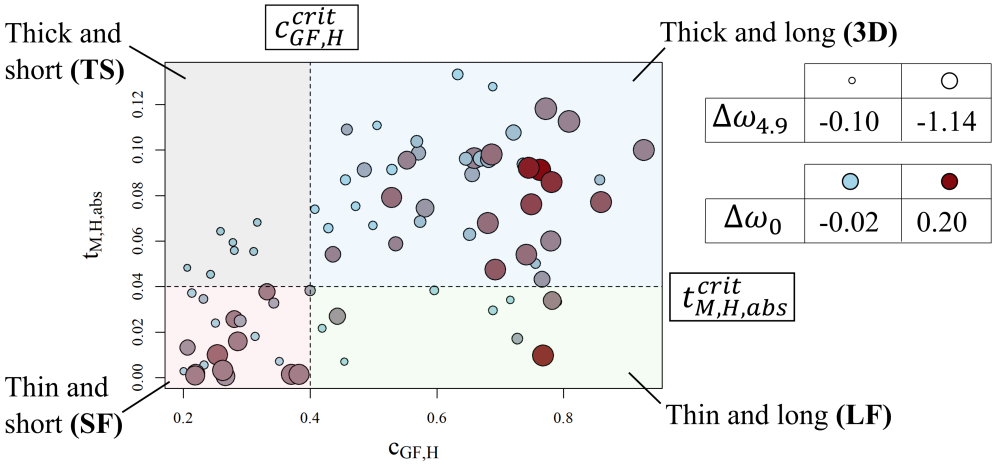

Figure 7.2: Hub chord vs absolute hub thickness of guide fins of depth ≤ 5. Coloured with $\Delta\omega_0$ and scaled with $-\Delta\omega_{4.9}$.

The following critical values are proposed to separate short and thin guide fins from thick and long ones :

$$t^{crit}_{M,H,abs} = 4\%c \quad (7.1)$$

$$c^{crit}_{GF,H} = 40\%c \quad (7.2)$$

As illustrated in Figure7.2, these critical values split the distribution into 4 families whose populations are summarised in Table 7.1. The majority of guide fins appear to belong to the family of thick and long guide fin (referred to as the 3D family), followed by the family of thin and short ones (referred to as the SF family). Moreover, these two families contain most of the guide fins that efficiently lower $\Delta\omega_{4.9}$(large circles). The third family is characterised with thin and long guide fins (referred to as the LF family). This family is little populated but contains several guide fins that efficiently lower $\Delta\omega_{4.9}$. The last family contains thick and short guide fins (referred to as TS family). It is little populated and only include guide fins with little impact on the losses. The TS family will therefore not be considered in the following.

The guide fins of depth ≤ 5 are therefore separated into 2 main families and one minor family according to geometrical criteria. The majority of these guide fins are either thin and short, or thick and long, which confirms the trends observed on the Pareto front. A third type of guide fins is also revealed with the thin and long family.

	$\mathbf{c_{GF,H} \leq 40\%c}$	$\mathbf{c_{GF,H} > 40\%c}$
$\mathbf{t_{M,H,abs} > 4\%c}$	7 (9%)	3D : 43 (53%)
$\mathbf{t_{M,H,abs} \leq 4\%c}$	SF : 21 (26%)	LF : 10 (12%)

Table 7.1: Number of guide fins in each family. Absolute number and percentage of the population investigated (depth ≤ 5).

Figure 7.3 shows representative geometries of these families in the objective function space. Each family spread over a large range of $\Delta\omega_{4.9}$ values, and is not restrained to a specific zone of the objective function space. The 3D family contains the guide fins that best lower $\Delta\omega_{4.9}$, but also the ones that most increase $\Delta\omega_0$. They are spread uniformly across the objective function ranges. The SF family contains guide fins that efficiently lower $\Delta\omega_{4.9}$ while keeping a reasonable level on $\Delta\omega_0$. They are gathered in two zones corresponding to $\Delta\omega_{4.9} \in [-0.4, -0.1]$ and $\Delta\omega_{4.9} \in [-1, -0.6]$. This is symptomatic of a binary behaviour of guide fins that either lower the losses at high incidence or merely affect the flow. This binary behaviour was already discussed on the whole RANS database in Section 6.4 and might be related to the topological switch. It indeed induces a sudden decrease in the losses when switching from the double sided to the single sided topology. A specific geometrical aspect of the SF guide fins might therefore monitor the topological switch.

It is worth noticing that the representative geometries of each family are consistent with the geometrical criteria used. Moreover, the represented geometries reveal two noticeable trends. Going from the bottom right to the top left of Figure 7.3, the height seems to increase and the hub aerofoil leading edge moves upstream. H_{GF} and u seem therefore strongly correlated to the objective functions. On top of that, other geometrical specificities might be suspected. 3D and LF guide fins seem to feature a shorter chord and smaller thickness at their tip than at their hub, resulting in a pyramidal shape. On the contrary, most SF guide fins seem relatively straight. In addition, guide fin SF-02 features an important twist and a noticeable converging section at hub. This local convergence is observed on other guides fins (SF-01 and SF-03) and might be a general characteristic of SF guide fins.

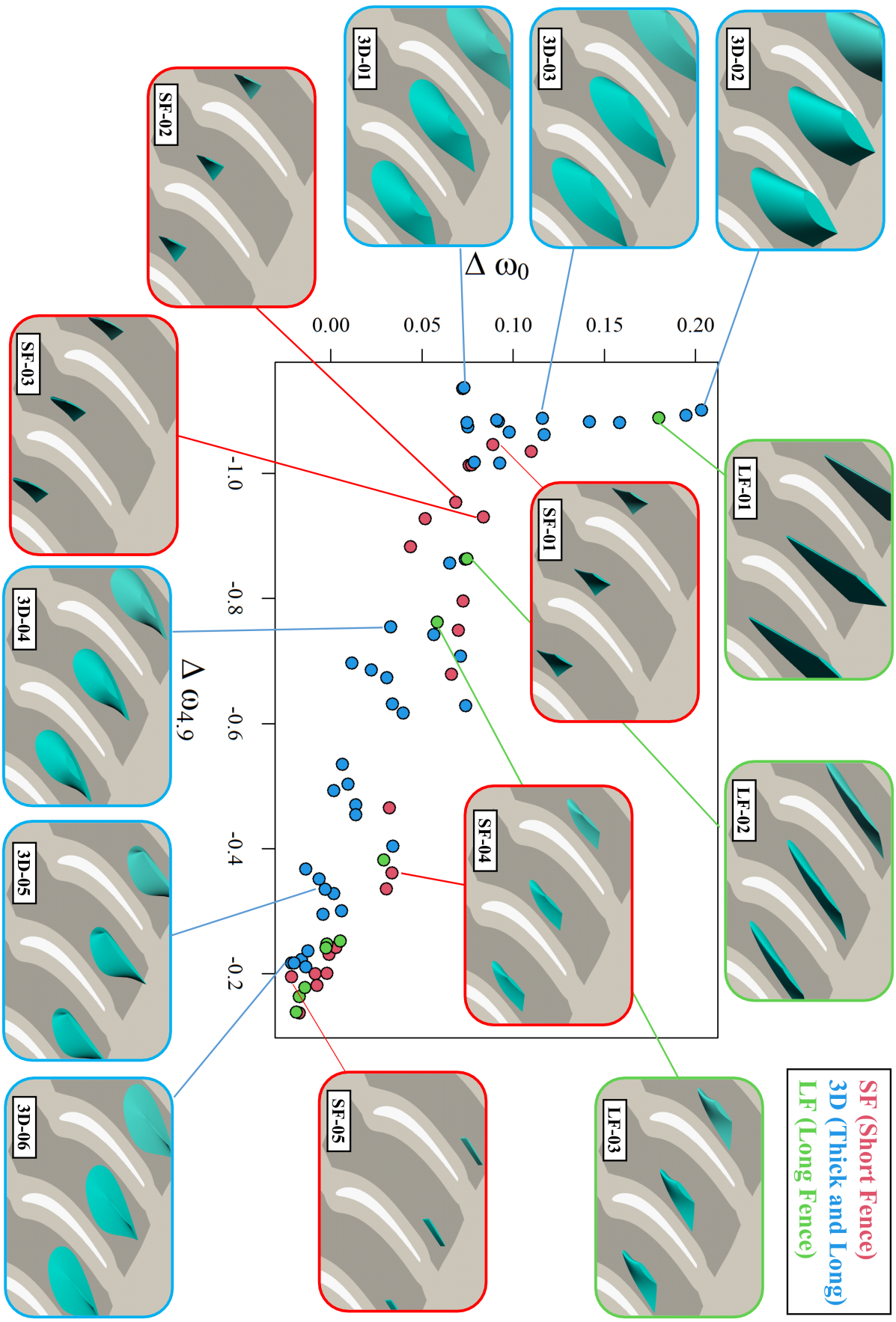

Figure 7.3: Performance and characteristic shapes of the SF, 3D and LF families (15p).

The characteristics of the two main families are thoroughly investigated in Section 7.1.2. The LF family will be investigated separately in Section 7.1.3.

7.1.2 Characterisation of the Short Fence (SF) and 3D families

Geometrical specificities of the 3D and SF families are first investigated. Among the 15 parameters, 6 main ones are defined and their effects on $\Delta\omega_{4.9}$ are investigated in a second step.

7.1.2.1 Geometrical specificities

Pyramidal shape

Two geometrical angles are introduced to characterise the trapezoidal shape of the guide fin in two directions :

$$\lambda_{chord} = \tan^{-1}\left(\frac{c_{GF,H} - c_{GF,T}}{2H_{GF}}\right) \tag{7.3}$$

$$\lambda_{thickness} = \tan^{-1}\left(\frac{t_{M,H,abs} - t_{M,T,abs}}{2H_{GF}}\right) \tag{7.4}$$

These angles are illustrated in Figure 7.4a. Values of (λ_{chord},$\lambda_{thickness}$) in $[45°, 90°]^2$ define a region of *straight* guide fins. Values of $\lambda_{chord} \leq 45°$ (respectively $\lambda_{thickness} \leq 45°$) refer to guide fins with highly trapezoidal shapes in the chordwise direction (respectively thicknesswise direction). A guide fin featuring a trapezoidal shape in at least one direction is called *pyramidal*. Let us underline that these angles rely only on the absolute thickness and chord of the tip and hub aerofoils. Notably, the stacking and camber laws are not taken into account. Figure 7.4b shows the guide fins of the families SF and 3D with respect to λ_{chord} and $\lambda_{thickness}$. Several geometries are shown to illustrate the evolution of the trapezoidal shapes in the chordwise and thicknesswise directions. It appears that these two families occupy different regions of the plot. Most of the 3D guide fins feature trapezoidal shapes in the chordwise direction ($\lambda_{chord} \leq 45°$). A large portion of this family also features a trapezoidal shape in the thicknesswise direction ($\lambda_{thickness} \leq 45°$). On the contrary, most SF guide fins are placed in the straight region.

As such, the pyramidal aspect is specific to the 3D family, while the straight aspect is specific to the SF family.

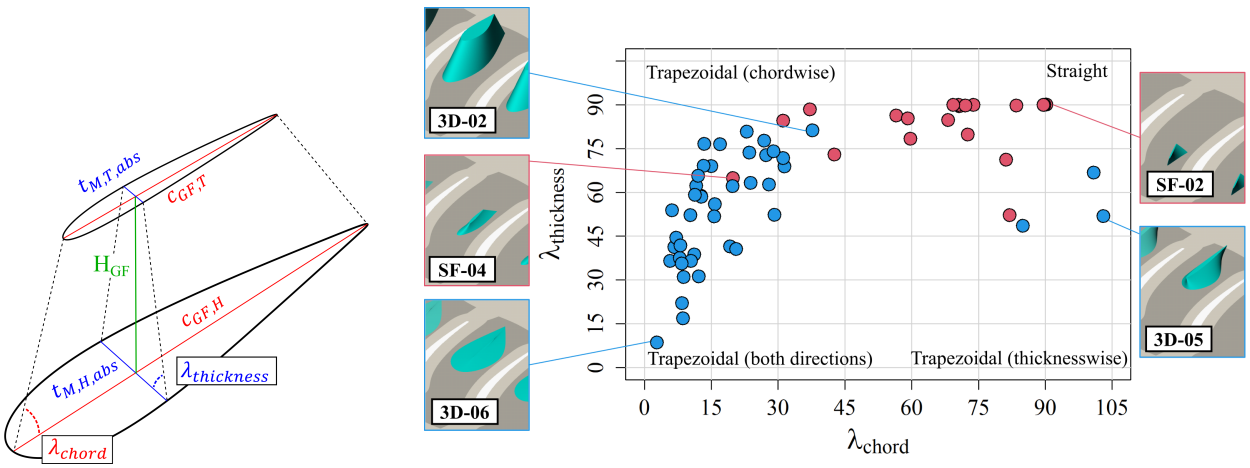

(a) Illustration of λ_{chord} and $\lambda_{thickness}$ parameters.

(b) Guide fins distribution with respect to their trapezoidal aspects. SF (red) and 3D (blue) families.

Figure 7.4: Pyramidal aspect of SF and 3D families.

Twist and local converging section at hub

The twist of the guide fins and the relative orientation of the hub aerofoils with the stator are investigated. The stagger angles of the hub and tip aerofoils are first computed (γ_H and γ_T respectively). On top of these angles, a local stagger angle relative to the stator is computed from the hub aerofoil positions ($\gamma_{local,H}$). These angles are illustrated in Figure 7.5a. Finally, the relative stagger angle and the twist are computed as :

$$(\Delta\gamma)_{conv} = \gamma_H - \gamma_{local,H} \tag{7.5}$$

$$(\Delta\gamma)_{twist} = \gamma_H - \gamma_T \tag{7.6}$$

As illustrated in Figure 7.5a, a negative value of $(\Delta\gamma)_{conv}$ corresponds to a hub aerofoil forming a local converging section between its pressure side and the suction side of the stator. On the contrary, a positive value corresponds to a local diverging section. A negative value of the twist indicates that the stagger angle increases along the span.

Figure 7.5b shows the guide fins of the families SF and 3D with respect to $(\Delta\gamma)_{conv}$ and $(\Delta\gamma)_{twist}$. They are scaled proportionally to $-\Delta\omega_{4.9}$. A correlation is observed between these two quantities. However, this correlation is not specific to the guide fins currently investigated (depth ≤ 5) and results from the guide fins parametrisation*. No correlation between these quantities and $\Delta\omega_{4.9}$ appears for the 3D guide fins. Moreover, the 3D guide fins occupy a large range of these parameters : $(\Delta\gamma)_{conv} \in [-12°, +10°]$, $(\Delta\gamma)_{twist} \in [-17°, +8°]$. On the contrary, SF guide fins feature a clear correlation between these quantities and $\Delta\omega_{4.9}$. SF guide fins that most lower the values of $\Delta\omega_{4.9}$ are located in a region of negative twist and of converging section at hub : $(\Delta\gamma)_{conv} \in [-18°, -4°]$, $(\Delta\gamma)_{twist} \in [-21°, -4°]$.

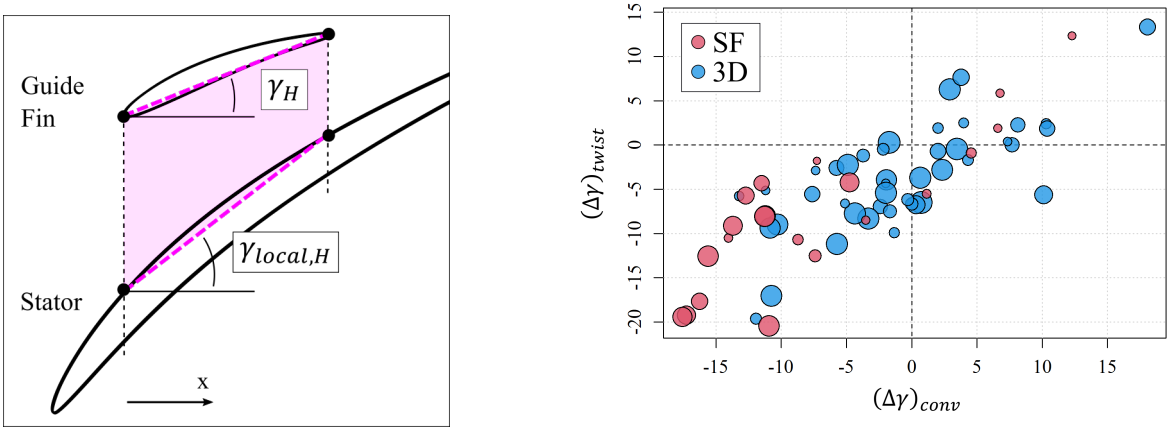

(a) Illustration of the local stagger angle.

(b) Relative stagger angle vs twist. Scaled proportionally to $-\Delta\omega_{4.9}$.

Figure 7.5: Investigation of local section convergence and twist.

As such, SF guide fins that efficiently lower $\Delta\omega_{4.9}$ values are characterised with high negative values of relative stagger angle and twist. On the other hand, 3D guide fins are characterised with little negative values of these parameters, which do not affect $\Delta\omega_{4.9}$ values.

*The correlation between $(\Delta\gamma)_{conv}$ and $(\Delta\gamma)_{twist}$ is observed on the entire database. These two quantities are actually monitored by the same parameter, $\Delta\beta_{1,H}$, as illustrated in the Appendix (Section C.2, Figure C.4.)

Aerofoil alignment with the flow

The distributions of the relative metal angles at the leading edge of the hub and tip aerofoils, $\Delta\beta_{1,H}$ and $\Delta\beta_{1,T}$, are investigated with respect to $\Delta\omega_{4.9}$. They are gathered in the Appendix (Section C.1, Figure C.2). For the 3D guide fins, the evolution of $\Delta\omega_{4.9}$ is insensitive to the values of these angles, even though they vary in large ranges ($\Delta\beta_{1,H} \in [-15°, +10°]$, $\Delta\beta_{1,T} \in [-10°, +10°]$). On the other hand, the SF guide fins that most lower the values of $\Delta\omega_{4.9}$ are characterised with negative values of these angles ($\Delta\beta_{1,H} \in [-20°, -10°]$, $\Delta\beta_{1,T} \in [-10°, 0°]$). These negative values can be related to the local flow physics. The transverse pressure gradient drives the flow close to the hub from the pressure side to the suction side of the stator (passage flow), which lowers the pitchwise flow angle. Negative values of $\Delta\beta_{1,H}$ correspond to metal angles more aligned with this flow. If the height of the guide fin is large enough, the tip aerofoil is no longer immersed in the passage flow. The local flow follows the local stator camber, and negative values of $\Delta\beta_{1,T}$ correspond to an overloading of the tip aerofoil. On the contrary, if the tip aerofoil is still immersed in the passage flow, the previous conclusion holds. Negative values of $\Delta\beta_{1,T}$ correspond to an attempt to align the aerofoil leading edge with the local flow.

As a summary, 3D guide fins do not exhibit specific trends regarding their leading edge angles. SF guide fins are characterised with low values of these angles, which might result either in an alignment with the locally skewed flow or to an overloading of the tip aerofoil.

7.1.2.2 Definition of main parameters

The shape of each guide fin results from the values of 15 parameters. The parameters whose variation most affect the objective functions value are selected, and referred to as the *main* parameters. For the sake of clarity, the distributions of each parameter with respect to the objective functions are gathered in the Appendix (Section C.1, Figures C.1 and C.2).

Pearson coefficients are computed to reveal the potential linear correlations between the parameters and the objective functions. $\widetilde{c_{GF}}$ is replaced with $c_{GF,H}$ to help revealing physical trends. These coefficients are computed with the RANS results available for each family, which correspond to 21 SF guide fins 43 3D guide fins. When using such little populated samples, the significance of the Pearson coefficients should be assessed (see Section 2.3). It appears that values of Pearson coefficient lower than 0.4 are not significantly different from 0 for both samples. Moreover, the distributions of each parameter with respect to each objective function are manually controlled. For both objective functions, the parameters whose coefficient value is lower than 0.48 do not feature any an intuitive linear trend. In this context, only parameters that feature at least one Pearson coefficient larger than 0.48 are considered. They are gathered in Table 7.2. $\Delta\omega_0$ et $\Delta\omega_{4.9}$ are strongly correlated with one another, as the coefficients are computed on a subset close to the Pareto front region. The trends obtained on $\Delta\omega_{4.9}$ are representative of the trends obtained on $\Delta\omega_0$ (with an opposite sign) and are therefore not shown. $\Delta\omega_{4.9}$ seems to be mostly correlated with H_{GF}, u, and $\Delta\beta_{1,H}$, with the same sign for both families. A strong correlation is also revealed with $c_{GF,H}$ for 3D guide fins, while SF guide fins seem insensitive to this parameter.

Parameter	$\Delta\omega_0$	H_{GF}	u	$c_{GF,H}$	$\Delta\beta_{1,H}$	$t_{M,H}$
Pearson coefficient (SF)	-0,94	-0,76	0,89	-0,09	0,77	0,48
Pearson coefficient (3D)	-0,87	-0,81	0,65	-0,58	0,50	0,47

Table 7.2: Pearson coefficients with $\Delta\omega_{4.9}$ for SF and 3D families. Only parameters with Pearson coefficient of absolute values greater than 0.48 on at least one objective function are considered.

In order to specifically focus on the sensitivity to $\Delta\omega_{4.9}$, the *efficient parameter ranges* are also computed. They are defined as the parameter ranges of guide fins that best lower $\Delta\omega_{4.9}$ values ($\Delta\omega_{4.9} \leq -0.8$). Six parameters feature particularly restrained ranges. They correspond to the five most correlated parameters shown in Table 7.2 and to the parameter v. The efficient parameter ranges are summarised in Table 7.3. They appear to be disjoint when comparing SF and 3D guide fins, and are therefore specific to each family.

Family	$\mathbf{\Delta\beta_{1,H}}$	$\mathbf{t_{M,H}}$	$\mathbf{c_{GF,H}}$	**u**	**v**	$\mathbf{H_{GF}}$
SF	[-20°,-10°]	[0%c,6%c]	[20%c,40%c]	[0.25,0.35]	[0.29,0.33]	[5%c,9%c]
3D	[-15°,+7°]	[7%c,15%c]	[50%c,90%c]	[0.35,0.45]	[0.4,0.7]	[6%c,11%c]

Table 7.3: Efficient parameter ranges of SF and 3D guide fins (15p).

Guide fins that efficiently lower the losses at high incidence feature values comprised within a specific reduced range for the 6 following parameters : H_{GF}, $\Delta\beta_{1,H}$, u, v, $t_{M,H}$ and $c_{GF,H}$. They are therefore considered as the main parameters. RANS results and predictions of the 15p surrogate model are used to detail their effect on $\Delta\omega_{4.9}$ in next section.

7.1.2.3 Analysis of main parameters effect on the losses at high incidence

RANS results and surrogate predictions are used to analyse the influence of the main parameters. Figure 7.6 to 7.10 compare the evolution of $\Delta\omega_{4.9}$ with a parameter of interest X for both families ($X \in [H_{GF}, \Delta\beta_{1,H}, u, v, t_{M,H}]$). RANS results are shown, and indicated with red dots. For each guide fin of the RANS database, the parameter X is varied on its whole range, and the predictions of the resulting guide fins are represented with a black line. Predictions obtained from little efficient guide fins ($\Delta\omega_{4.9}$ close to 0) are faded to focus on the guide fins that most efficiently lower the losses at high incidence. Optimal values of X minimising $\Delta\omega_{4.9}$ are denoted X^*.

- **Effect of H_{GF}**
  Figure 7.6 compares the evolution of $\Delta\omega_{4.9}$ with H_{GF} for both families. The trend observed on RANS results is similar on both families : $\Delta\omega_{4.9}$ decreases until reaching a critical value above which the height no longer improves the losses. This critical height is about $10\%c$ for SF guide fins, and $7\%c$ for 3D guide fins. The surrogate predictions show the existence of optimal values located in $[9\%c, 12\%c]$ for the SF family. As such, all the SF guide fins evaluated in RANS could be improved by increasing their height up to a value contained in these bounds. For the 3D family, the predictions reveal the existence of an optimal height common to most guide fins, $H^*_{GF} \simeq 7\%c$. The height can increase above this value without deteriorating too much $\Delta\omega_{4.9}$, consistently with the RANS trend. Finally, Figure C.1 (in the Appendix, Section C.1) shows a strong positive correlation between H_{GF} and $\Delta\omega_0$ on the whole range of variation and for both families.

A trend common to both family is revealed. $\Delta\omega_0$ increases with the height on the whole variation range. On the contrary, $\Delta\omega_{4.9}$ decreases with H_{GF} up to a critical value. Heights greater than this value seem to only bring additional losses on $\Delta\omega_0$ without improving $\Delta\omega_{4.9}$.

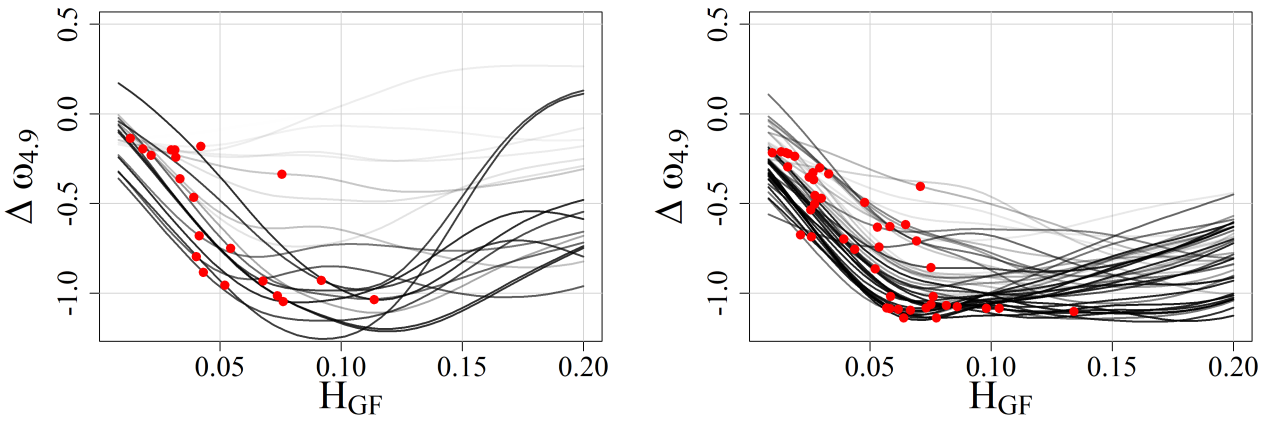

(a) SF family. (b) 3D family.

Figure 7.6: H_{GF} vs $\Delta\omega_{4.9}$. RANS database (red dots) and surrogate predictions (black faded lines).

- **Effect of $\Delta\beta_{1,H}$**
  Figure 7.7 compares the evolution of $\Delta\omega_{4.9}$ with $\Delta\beta_{1,H}$ for both families. RANS results show a positive correlation between $\Delta\beta_{1,H}$ and $\Delta\omega_{4.9}$ for both families. Moreover, the SF guide fins that best lower $\Delta\omega_{4.9}$ are located in the following specific range : $\Delta\beta_{1,H} \in [-20°, -10°]$. However, 3D guide fins are not characterised with a specific range. Finally, the surrogate predictions are insensitive to the $\Delta\beta_{1,H}$ values, and show little sensitivity to $\Delta\omega_{4.9}$.

The SF guide fins should feature a large negative value of $\Delta\beta_{1,H}$, indicating that the hub metal angle at the LE should be lower than the local stator camber. The 3D guide fins are little sensitive to $\Delta\beta_{1,H}$ and can vary on a large range without affecting $\Delta\omega_{4.9}$.

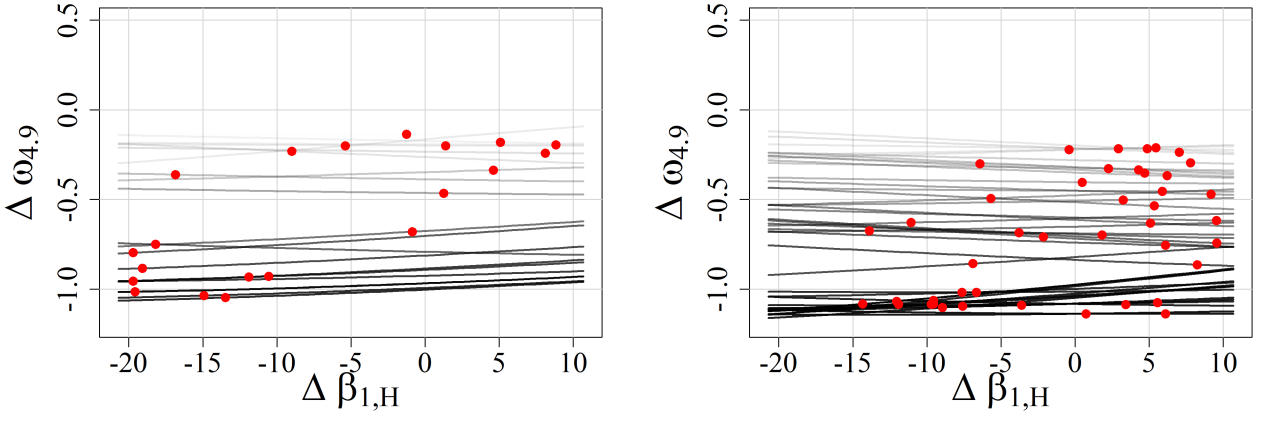

(a) SF family. (b) 3D family.

Figure 7.7: $\Delta\beta_{1,H}$ vs $\Delta\omega_{4.9}$. RANS database (red dots) and surrogate predictions (black faded lines).

- **Effect of u**
  Figure 7.8 compares the evolution of $\Delta\omega_{4.9}$ with u for both families. RANS results show a positive correlation between $\Delta\omega_{4.9}$ and u for both families. However, surrogate

predictions are highly non-linear and reveal the existence of optimal values. For SF guide fins, most of the predicted optimal values are in a restrained range corresponding to upstream positions, $u^* \in [0.25, 0.30]$. For 3D guide fins, the guide fins that best lower $\Delta\omega_{4.9}$ feature a common optimal value, $u^* \simeq 0.38$.

For both families, guide fins should be located upstream in the channel to lower the losses at high incidence. Guide fins from a given family have close optimal values, which shows a consistency within each family. The optimal values of the two families are different, and differentiate the families.

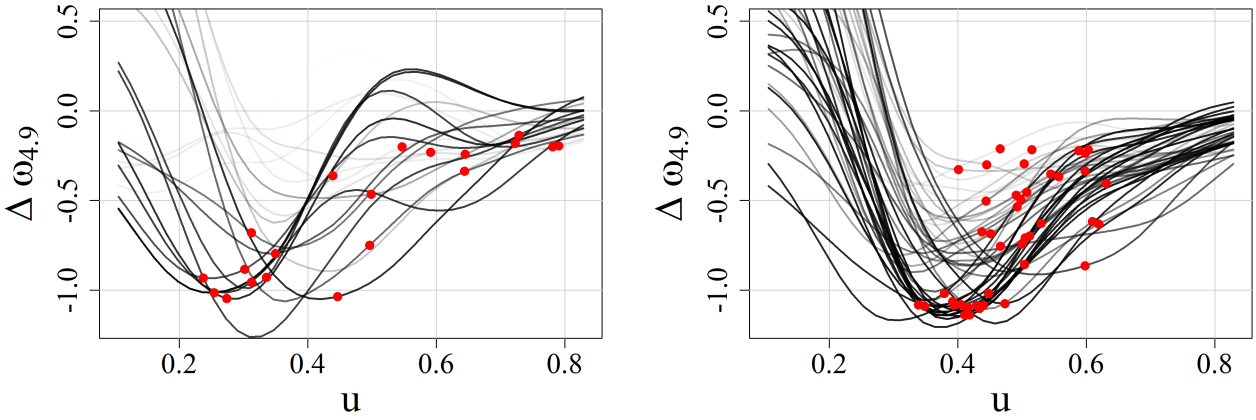

(a) SF family.

(b) 3D family.

Figure 7.8: u vs $\Delta\omega_{4.9}$. RANS database (red dots) and surrogate predictions (black faded lines).

- **Effect of v**
  Figure 7.9 compares the evolution of $\Delta\omega_{4.9}$ with v for both families. RANS results do not reveal any correlation between $\Delta\omega_{4.9}$ and v. However, the SF guide fins that best lower $\Delta\omega_{4.9}$ are located in a restrained range ($v \in [0.3, 0.4]$). On the other hand, 3D guide fins span across a large range of higher values ($v \in [0.4, 0.7]$). These higher values are consistent with the fact that 3D guide fins are thick, and cannot be physically placed too close to the stators. For the family SF, the surrogate predictions highlight the existence of a common optimal value at about $v^* \simeq 0.35$. However, v is of little influence on $\Delta\omega_{4.9}$ for the 3D guide fins that best lower $\Delta\omega_{4.9}$.

The SF guide fins should be positioned close to the stator suction side to lower $\Delta\omega_{4.9}$. The 3D guide fins that efficiently lower $\Delta\omega_{4.9}$ are positioned in the middle of the channel, with no major influence of their precise location.

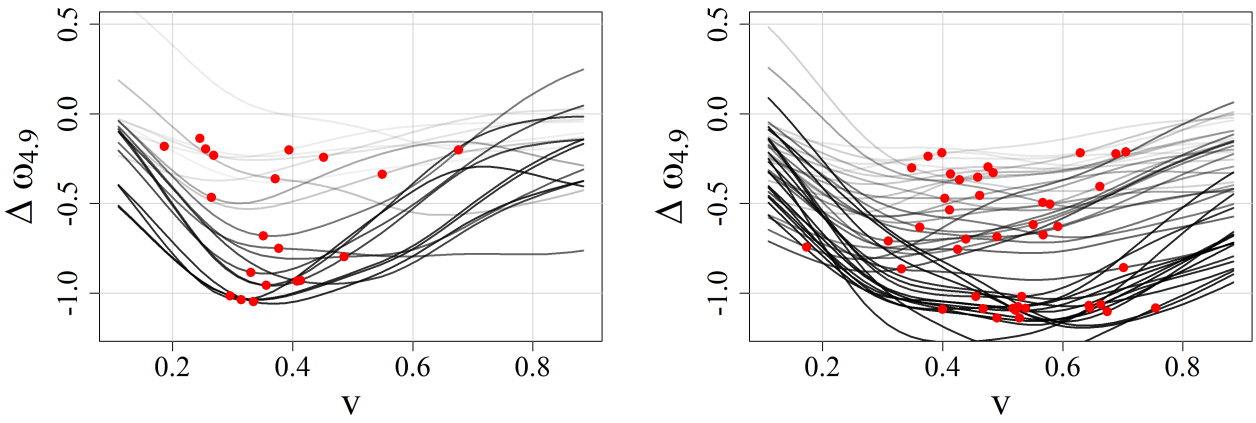

(a) SF family. (b) 3D family.

Figure 7.9: v vs $\Delta\omega_{4.9}$. RANS database (red dots) and surrogate predictions (black faded lines).

- **Effect of $t_{M,H}$**
  Figure 7.10 compares the evolution of $\Delta\omega_{4.9}$ with $t_{M,H}$ for both families. RANS results show that the best SF guide fins are thin ($t_{M,H} \leq 6\%c_{GF,H}$), which is consistent with the definition of the family. Predictions reveal a common optimal value for the best SF guide fins located at about $t^*_{M,H} \simeq 2.5\%c_{GF,H}$. The 3D family is characterised with large values of $t_{M,H}$ within $[7\%c_{GF,H}, 15\%c_{GF,H}]$, which is also consistent with the definition of the family. However, the surrogate predictions reveal little sensitivity to the precise value of the thickness.

SF guide fins must feature a thin aerofoil at hub to best lower $\Delta\omega_{4.9}$, while 3D guide fins only need to feature a sufficiently thick aerofoil at hub. The optimal thicknesses remain consistent with the family definitions.

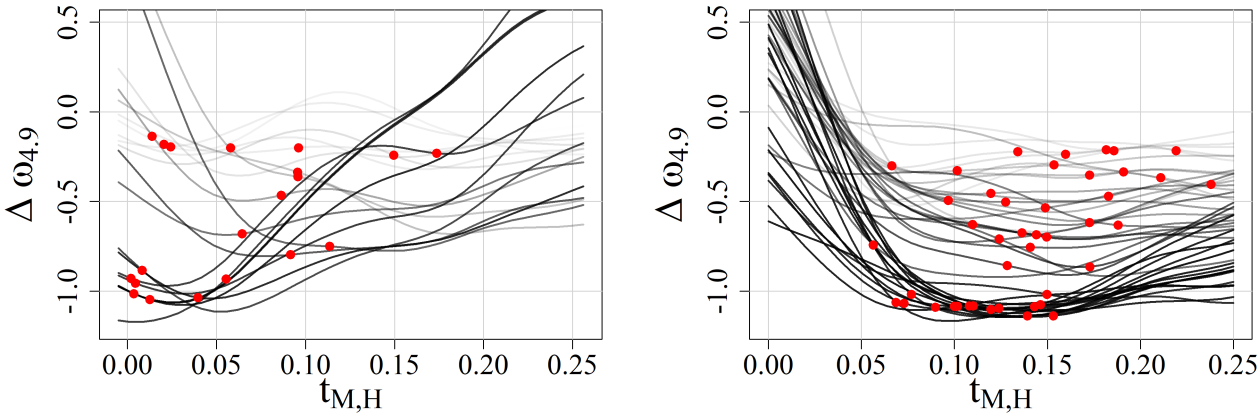

(a) SF family. (b) 3D family.

Figure 7.10: $t_{M,H}$ vs $\Delta\omega_{4.9}$. RANS database (red dots) and surrogate predictions (black faded lines).

- **Effect of $c_{GF,H}$**
  Figure 7.11 compares the evolution of $\Delta\omega_{4.9}$ with $c_{GF,H}$, for both families. No surrogate

predictions are available as $c_{GF,H}$ is not an optimisation parameter. For the SF family, RANS results show no correlations between these quantities. One can only conclude that for the SF guide fins, the chord value $c_{GF,H}$ has little influence on the losses as long as it remains within $[20\%c, 40\%c]$. For the 3D family, the chord parameter is negatively correlated with $\Delta\omega_{4.9}$. The lowest values of $\Delta\omega_{4.9}$ are reached only with chord values in the range $[65\%c, 95\%c]$. However, $\Delta\omega_0$ is greatly increased with $c_{GF,H}$ in this range.

For the SF family, the chord value $c_{GF,H}$ has little influence on the losses at both incidences as long as it remains within $[20\%c, 40\%c]$. For the 3D family, the chord parameter allows to significantly improve the losses at high incidence, but large values deteriorate the losses at design incidence.

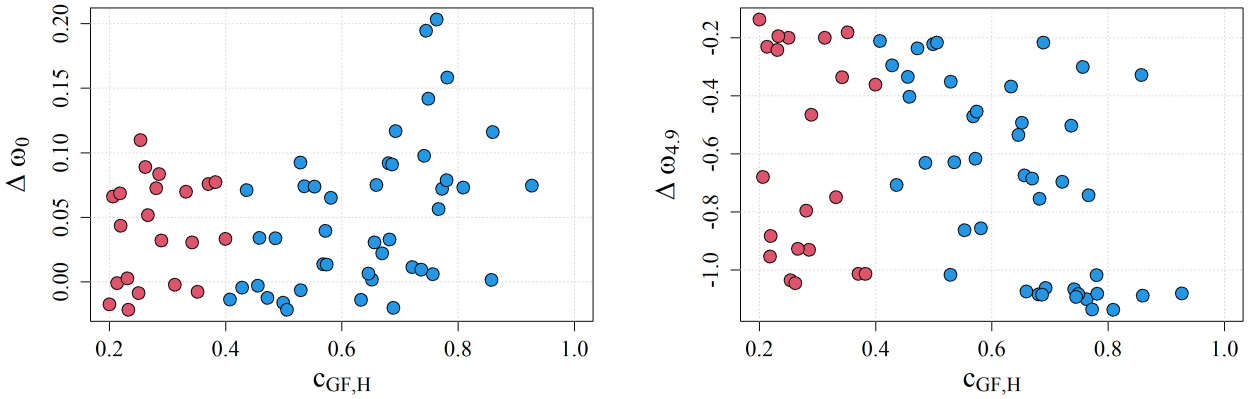

(a) $c_{GF,H}$ vs $\Delta\omega_0$.

(b) $c_{GF,H}$ vs $\Delta\omega_{4.9}$.

Figure 7.11: $c_{GF,H}$ vs $\Delta\omega_{4.9}$. RANS results : SF (red) and 3D (blue) guide fins.

7.1.3 Investigation of the Long Fence (LF) family

The sensitivities of the LF family are investigated and compared to the ones of the SF and 3D families. If specific trends are detected, the LF guide fins legitimately constitute a third family independent of the others. If not, these guide fins can be described as degenerated guide fins of the other families. The study focuses on LF guide fins with a significant impact on the losses ($\Delta\omega_{4.9} < -0.4$). Only 3 guide fins are retained, which is too few for a statistical investigation of RANS results. However, the surrogate predictions remain relevant.

The families are defined via the parameters $t_{M,H,abs}$ and $c_{GF,H}$. The effect of the corresponding optimisation parameters, $t_{M,H}$ and $\widetilde{c_{GF}}$, are therefore first investigated. Figure 7.12a shows the predictions of $\Delta\omega_{4.9}$ with the evolution of these parameters as well as the guide fins geometries. For the 3 guide fins, the chord values should be as large as possible to minimise $\Delta\omega_{4.9}$ ($\widetilde{c_{GF}}^* = 1$). However, they feature different values of optimal thickness. Guide fin LF-01 should remain rather thin, and guide fin LF-02 and LF-03 should thicken up to large values.

Figure 7.12b is an annotated version of Figure 7.2 in which guide fins LF-01, LF-02 and LF-03 are highlighted. Star elements are added, and represent the corresponding guide fins once modified with their optimal chord and thickness values. The optimised LF-01 guide fin remains in the same zone, and therefore still belong to the LF family. However, the optimised LF-02 and LF-03 guide fins move to the 3D family. Therefore, it is proposed to consider LF-02

and LF-03 as transient versions of two optimal guide fins of the 3D family. As such, they cannot be considered as representative guide fins of an independent, third family.

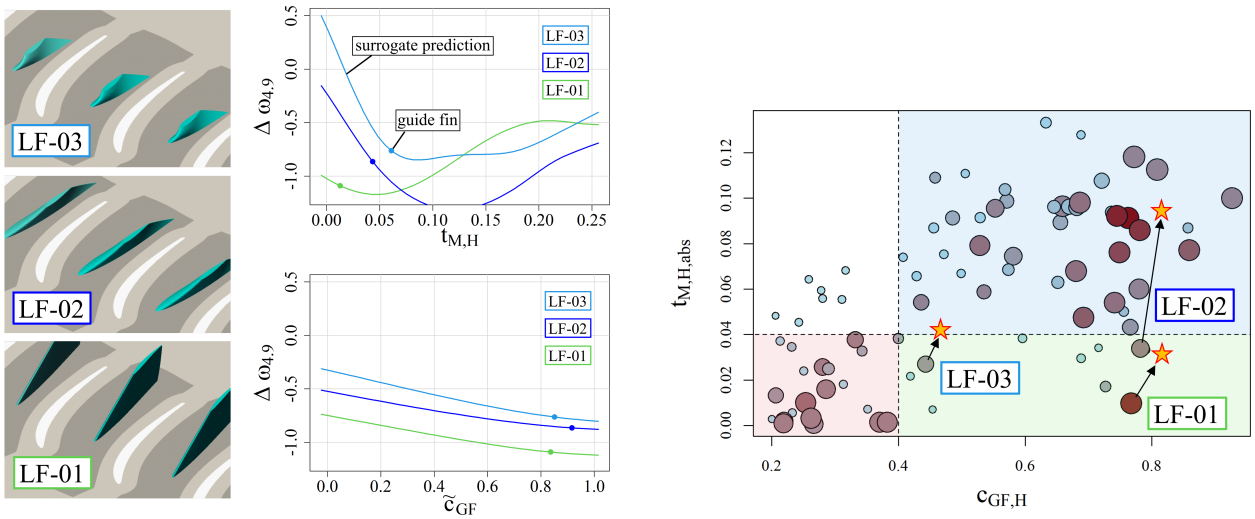

(a) Selected LF guide fins. Geometries and sensitivities to the thickness and chord parameters.

(b) Displacement of LF guide fins with optimised chords and thicknesses.

Figure 7.12: Limits of the LF family definition.

To support these results, the sensitivity to the other main parameters are investigated (Figure 7.13) :

- $\Delta\beta_{1,H}$: LF-01, LF-02 and LF-03 are found to be little sensitive to $\Delta\beta_{1,H}$, which is therefore not represented.

- u : Guide fin LF-01 features an optimal value of 0.42, different from the optimal values detected on the SF family ($u^*(SF) \in [0.25, 0.3]$) and on the 3D family ($u^*(3D) = 0.38$). On the contrary, guide fins LF-02 and LF-03 feature the same optimal value as for the 3D family.

- v : Guide fin LF-01 features an optimal value of $v^* \simeq 0.24$, different from the optimal value found for the SF ($v^*(SF) \in [0.3, 0.4]$) and 3D families ($v^*(3D) \in [0.4, 0.7]$). Guide fins LF-02 and LF-03 feature the same optimal value of $v^* \simeq 0.35$. They are little sensitive to v near the optimum, as noticed for guide fins of the 3D family.

- H_{GF} : Guide fin LF-01 features a large value of H_{GF}, greater than any other efficient guide fin investigated so far. An optimal value of $H_{GF} = 18\%c$ is noticeable. Guide fins LF-02 and LF-03 feature the same optimal value $H^*_{GF} \simeq 12\%c$, as well as similar gradients. Their optimal value is greater than the one detected for the 3D family ($H^*_{GF}(3D) \simeq 6\%c$). Similarly to the 3D family, H_{GF} seems to have little impact above the optimal value.

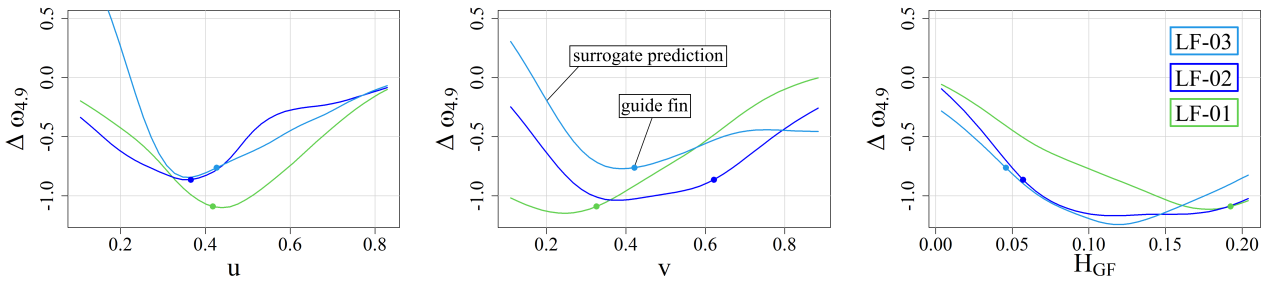

(a) (b) (c)

Figure 7.13: Sensitivities to the parameters u, v and H_{GF}.

Guide fins LF-02 and LF-03 behave consistently with one another in terms of sensitivity to 5 of the most influential parameters. In addition, some trends and optimal values detected around these guide fins are similar to the ones detected for the 3D family. Finally, optimised version of guide fins LF-02 and LF-03 with respect to $t_{M,H}$ and $\widetilde{c_{GF}}$ are placed within the 3D region in the ($t_{M,H,abs}$, $c_{GF,H}$) plot. On the contrary, guide fin LF-01 feature specific trends and optimal values, and its optimised version remains within the LF zone. As such, guide fins LF-02 and LF-03 are considered too similar to the guide fins of the 3D family to be representative of another family. They are therefore considered as exceptions ill-captured by the criteria defined with Equations (7.3) and (7.4). On the contrary, guide fin LF-01 seems to behave with specific trends, and might be the only guide fin representative of a third family captured in the optimisation process.

7.1.4 Summary

The 15p optimisation process outputs a large variety of guide fins. The 81 most efficient guide fins were extracted from the resulting database. Two main families containing most of these guide fins were defined, the Short Fence (SF) and 3D families. The definition of these families *a priori* only rely on the hub chord and hub thickness values. However, additional geometrical specificities among each family were noticed. These geometrical specificities are gathered in Table 7.4, and typical geometries of these families are presented in Figure 7.3. In addition 6 main parameters were defined, and their effects on $\Delta\omega_{4.9}$ was investigated. Specific trends and optimal ranges are revealed for each family. The trends related to the parameters differentiating the two families, ($t_{M,H}$, $\widetilde{c_{GF}}$) were expected to differ. However, specific trends were revealed on less intuitive parameters (H_{GF}, $\Delta\beta_{1,H}$, u, v). These trends are summarised in Table 7.5. As such, the SF and 3D guide fins are not only characterised with specific geometrical features but also with specific aerodynamic sensitivities, hence justifying the denomination of guide fins "families".

	SF family	3D family
Chord	Short at hub and tip ($c_{GF} \in [20\%c, 40\%c]$)	Long at hub ($c_{GF} \in [40\%c, 90\%c]$)
Thickness	Thin at hub and tip ($t_{M,H}, t_{M,T} \leq 4\%c$)	Thick at hub ($t_{M,H} \in [4\%c, 12\%c]$)
Hub LE position	Upstream and close to stator suction side	Upstream and about midpitch
Specificities	Local converging section at hub	Pyramidal aspect
	Negative twist	
	Alignement of hub LE angle with local flow	
	Overloading at tip LE	

Table 7.4: Geometrical specificities of SF and 3D families. LE refers to Leading Edge.

	SF family		3D family	
Parameter	**Optimal range**	**Sensitivity**	**Optimal range**	**Sensitivity**
H_{GF}	[9%c,12%c]	Strong	7%c	Strong
$\Delta\beta_{1,H}$	None	None	None	None
u	[0.25,0.3]	Strong	0.38	Strong
v	[0.3,0.4]	Intermediate	[0.4,0.7]	None
$t_{M,H}$	2.5%c	Intermediate	[7%c,14%c]	None
$c_{GF,H}$	None	None	None	Intermediate

Table 7.5: Sensitivity and optimal ranges of main parameters for SF and 3D families. In this Table, the sensitivity is a qualitative evaluation of the rise in $\Delta\omega_{4.9}$ values when leaving the optimal range. It is evaluated with the curvature of the predictions of $\Delta\omega_{4.9}$ in the optimal range, and with the RANS trends for $c_{GF,H}$.

7.2 Analysis of the 6-parameter space results

The 6-parameter input space was designed to precisely characterise the effect of 6 parameters of great influence on the loss reductions. These 6 parameters were identified with preliminary analysis carried out on the 15p design space (see Section 6.2.5) and correspond to the main parameters investigated in Section 7.1.2.2 : u, v, $\Delta\beta_{1,H}$, $\widetilde{c_{GF}}$, $t_{M,H}$ and H_{GF}. The 9 other parameters are fixed to values described in Table 6.5, and notably induce the following geometrical constraints :

- The metal angles are set so that they follow the local stator camber. Only the leading edge metal angle of the hub aerofoil varies.
- The chord of the tip aerofoil is equal to the chord of the hub aerofoil.
- The thickness of the tip aerofoil is fixed, and set to the minimum value.

Guide fins of the 6p RANS database are investigated similarly than in the 15p analysis. SF, 3D and LF guide fins are retrieved (Section 7.2.1). The guide fins corresponding to the SF and 3D guide fin families are investigated and compared to the ones detected previously

(Section 7.2.2 and 7.2.3). Few LF guide fins are detected, and are more efficient than in the 15p analysis. They appear to be related to the SF family and are investigated in Section 7.2.4.

7.2.1 Investigation of the RANS database (6p)

As for the 15p analysis, a subset containing the guide fins of depth ≤ 5 (72 guide fins) is investigated. The hub chord and absolute thickness are used to split this subset into four families with the same critical values (see Equations 7.1 and 7.2). The investigated guide fins are represented with respect to these parameters in Figure 7.14. Each guide fin is coloured with $\Delta\omega_0$ and scaled proportionally to $-\Delta\omega_{4.9}$. The majority of guide fins belong to the SF family. Both the LF and 3D families contain guide fins that efficiently lower the values of $\Delta\omega_{4.9}$. However, the corresponding 3D guide fins feature the largest values of $\Delta\omega_0$ (red dots). Similarly to the 15p analysis, the family characterised with thick aerofoils and short chords at hub (TS family) is little populated and contains only guide fins with little impact on the losses. The TS family is therefore not considered in the following. Table 7.6 summarises the number of guide fins in each family.

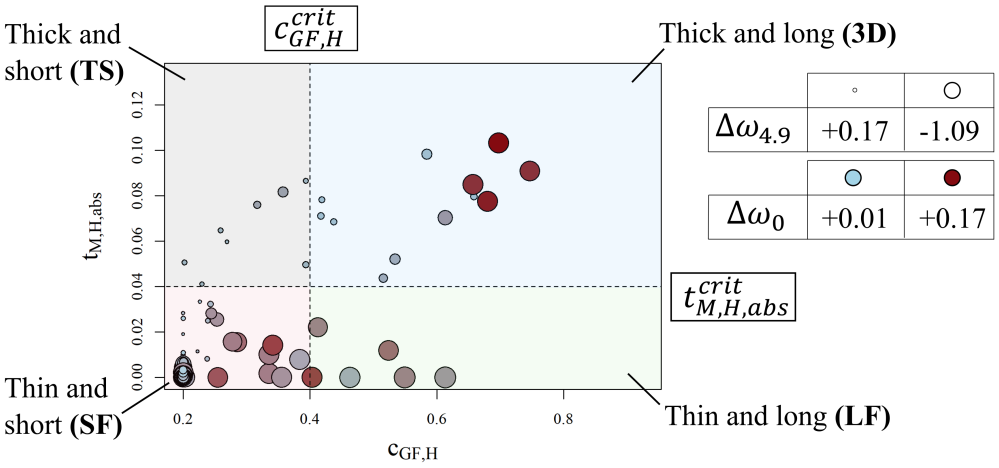

Figure 7.14: Hub chord vs absolute hub thickness of guide fins of depth ≤ 5. Coloured with $\Delta\omega_0$ and scaled proportionally to $-\Delta\omega_{4.9}$.

	$\mathbf{c_{GF,H} \leq 40\%c}$	$\mathbf{c_{GF,H} > 40\%c}$
$\mathbf{t_{M,H,abs} > 4\%c}$	8 (11%)	3D : 12 (17%)
$\mathbf{t_{M,H,abs} \leq 4\%c}$	SF : 46 (64%)	LF : 6 (8%)

Table 7.6: Number of guide fins in each family. Absolute number and percentage of the guide fin distribution (depth ≤ 5).

These SF, LF and 3D families are represented with respect to $\Delta\omega_0$ and $\Delta\omega_{4.9}$ in Figure 7.16. Representative geometries of each family are shown. SF and LF guide fins occupy the regions of lowest depth values. SF guide fins uniformly spread across a large range of $\Delta\omega_{4.9}$ values, thus offering a large choice of compromises between the two objective functions. LF guide fins are only located in regions of low values of $\Delta\omega_{4.9}$, and enable to reach the lowest values of that objective function. Finally, 3D guide fins are far less efficient than the other two families and occupy the region of greatest depth values ($4 \leq$ depth ≤ 5).

To help investigating these families, the distribution of their parameters with respect to $\Delta\omega_{4.9}$ is plotted in Figure 7.15. The parameter $\widetilde{c_{GF}}$ is replaced with the chord value of the hub aerofoil $c_{GF,H}$ to facilitate its physical interpretation. SF guide fins are represented in red, 3D guide fins in blue and LF guide fins in green. This figure will be used in Section 7.2.2, 7.2.3 and 7.2.4 to characterise these families. The distribution of these parameters with $\Delta\omega_0$ is shown in the Appendix (Section C.3, Figure C.5).

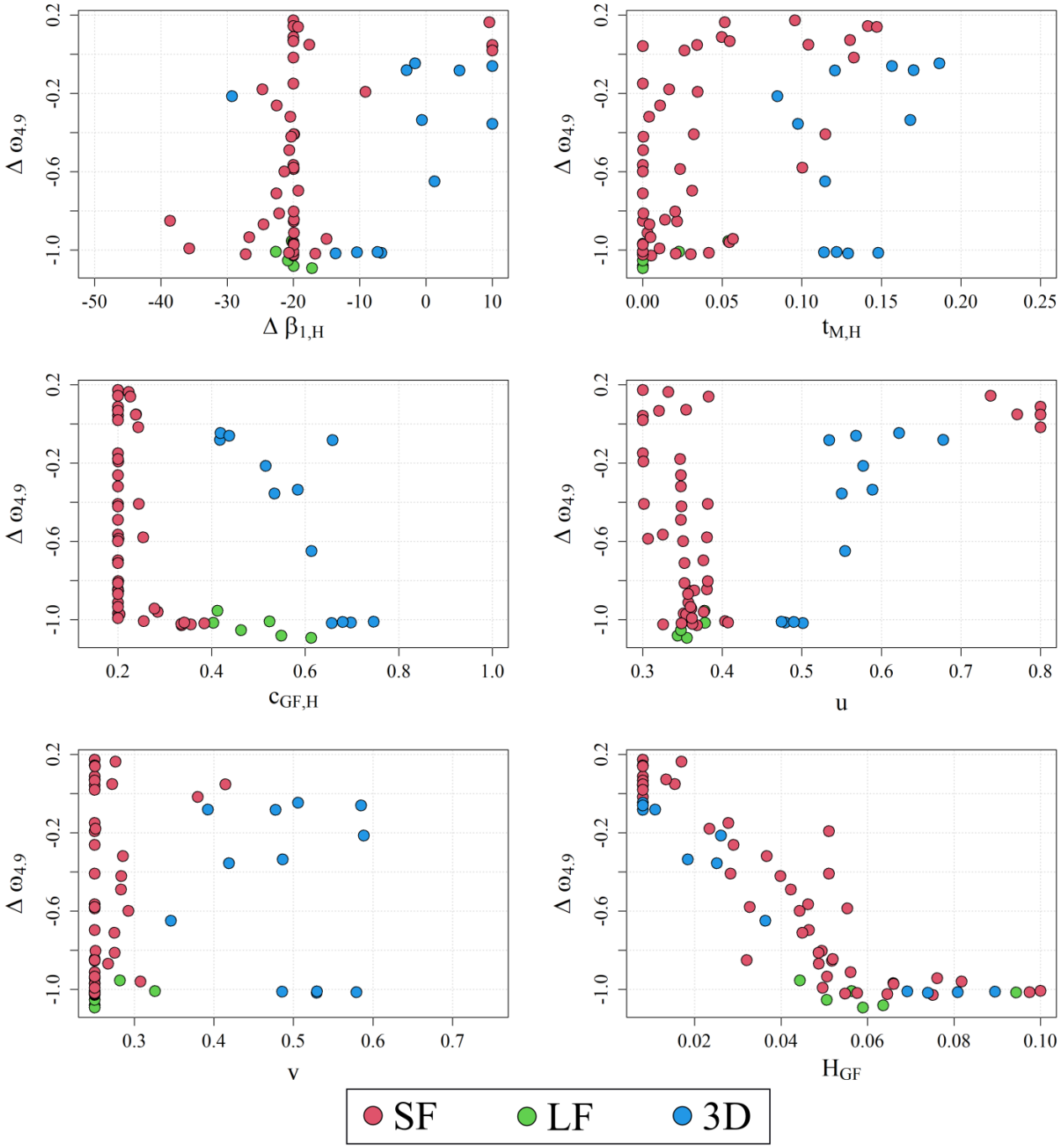

Figure 7.15: Parameter distributions of the 6p guide fins investigated against $\Delta\omega_{4.9}$.

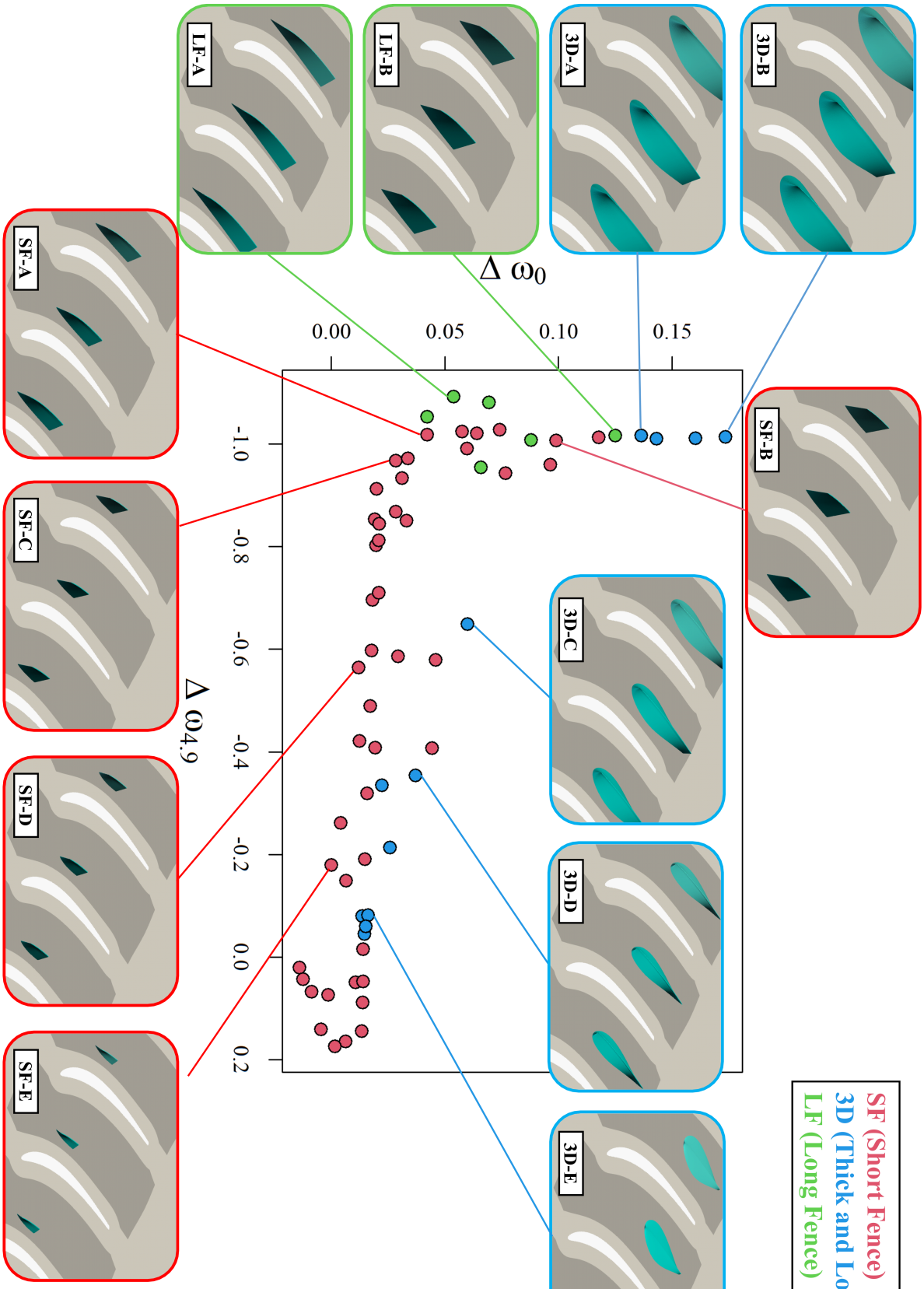

Figure 7.16: Performance and characteristic shapes of the SF, 3D and LF families (6p).

7.2.2 Investigation of the Short Fence (SF) family

The trends characterising the SF family are observed in Figure 7.15. $\Delta\beta_{1,H}$, $t_{M,H}$ and H_{GF} feature similar trends than the one observed in the 15p analysis (see Section 7.1.2.3) : $\Delta\omega_{4.9}$ is positively correlated with $\Delta\beta_{1,H}$ and $t_{M,H}$, and negatively with H_{GF}. However, the chord features a specific behaviour. It stays close to its minimal value down to $\Delta\omega_{4.9} = -0.9$, and tends to increase above this value. The other parameters are located within their corresponding efficient parameter range[†] without visible trends. The efficient parameter ranges computed for the SF guide fins of the 6p and 15p analyses are compared in Table 7.7. These ranges are consistent with one another and correspond to similar geometrical specificities. Let us recall that the variation range of $\Delta\beta_{1,H}$ is increased from $[-20°, +10°]$ to $[-50°, +10°]$ in the 6p exploration. As such, the efficient values of $\Delta\beta_{1,H}$ are among the lowest values authorised in each exploration.

SF	$\mathbf{\Delta\beta_{1,H}}$	$\mathbf{t_{M,H}}$	$\mathbf{c_{GF,H}}$	**u**	**v**	$\mathbf{H_{GF}}$
6p	[-39°,-17°]	[0%c,6%c]	[20%c,40%c]	[0.32,0.41]	[0.25,0.31]	[3,5%c,10%c]
15p	[-20°,-10°]	[0%c,6%c]	[20%c,40%c]	[0.25,0.35]	[0.29,0.33]	[5%c,9%c]

Table 7.7: Efficient parameter ranges of SF guide fins (6p vs 15p).

Similar efficient parameter ranges and similar trends are observed in the SF family when comparing 6p and 15p results, which therefore justifies the use of the same denomination. The 6p and 15p optimisation processes therefore investigated a unique SF family from two input spaces of different dimensions.

Figure 7.17 compares the SF guide fins resulting from these two optimisation process. RANS results are presented, as well as the best SF guide fins found on the 6p surrogate model (SF Pareto front). The SF Pareto front is obtained using the NSGA2 algorithm with restrained values of the chord parameter $\widetilde{c_{GF}}$ ($\widetilde{c_{GF}} \leq 0.35$.)[‡]. A population of 300 guide fins is used, and only 25 uniformly distributed guide fins are kept for visualisation purposes. In the region of low $\Delta\omega_{4.9}$ values ($\Delta\omega_{4.9} \leq -0.3$), the 6p guide fins are capable of lowering $\Delta\omega_{4.9}$ to the same extent as the 15p ones while inducing less losses on $\Delta\omega_0$. On the other hand, the 15p guide fins feature better guide fins on both objective functions in the region of low values of $\Delta\omega_0$. The 6p analyses thus provided better guide fins in the region of best compromise between the two objective functions. The SF Pareto front feature better guide fins than any other RANS result on both objective functions. It therefore provides the maximum gains reachable with a SF guide fin (see Table 7.8).

[†]As in the 15p analysis : parameter ranges of guide fins yielding $\Delta\omega_{4.9} \leq -0.8$.

[‡]The SF Pareto optimal guide fins feature a thickness of $t_{M,H} = 0$, and indeed correspond to SF guide fins.

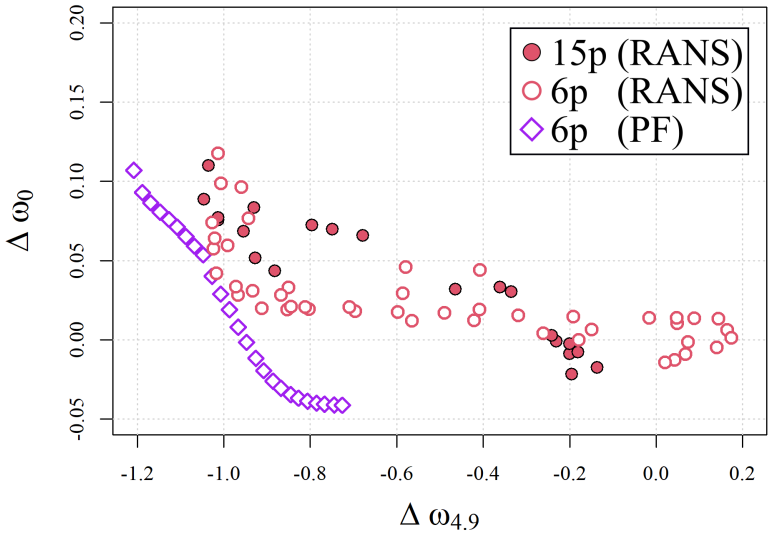

Figure 7.17: Performance of SF guide fins (6p vs 15p). PF : Surrogate Pareto Front.

Best $\Delta\omega_0$ (corresponding $\Delta\omega_{4.9}$)	Best $\Delta\omega_{4.9}$ (corresponding $\Delta\omega_0$)
-0.04 (-0.72)	-1.21 (0.11)

Table 7.8: Performance of best SF guide fins (6p, surrogate model).

7.2.3 Investigation of the 3D family

Figure 7.15 shows the parameters distribution of the 3D guide fins of the 6p analysis with respect to $\Delta\omega_{4.9}$. The trends observed on u, H_{GF} and $c_{GF,H}$ are similar to the ones observed in the 15p analysis : $\Delta\omega_{4.9}$ is positively correlated with u and H_{GF}, and negatively with $c_{GF,H}$. In the 6p analysis, $\Delta\omega_{4.9}$ appears to be positively correlated with $\Delta\beta_{1,H}$ while no trend was observed on that parameter in the 15p analysis. No particular trend is noticeable on the other parameters. The efficient parameter ranges characterising the 3D guide fins of the 6p and 15p analyses are compared in Table 7.9, and are consistent with one another. As such, the 3D guide fins of the 6p and 15p analyses correspond to the same, unique family.

3D	$\mathbf{\Delta\beta_{1,H}}$	$\mathbf{t_{M,H}}$	$\mathbf{c_{GF,H}}$	**u**	**v**	$\mathbf{H_{GF}}$
6p	[-14°,-7°]	[12%c,15%c]	[41%c,75%c]	[0.47,0.5]	[0.48,0.58]	[7%c,9%c]
15p	[-15°,+7°]	[7%c,15%c]	[50%c,90%c]	[0.35,0.45]	[0.4,0.7]	[6%c,11%c]

Table 7.9: Efficient parameter ranges of 3D guide fins (6p vs 15p). PF : Surrogate Pareto Front.

Figure 7.18 compares the 3D guide fins resulting from the 6p and 15p analyses. RANS results are shown, as well as the 3D Pareto front. The 3D Pareto front is obtained using the NSGA2 algorithm with restrained values of the thickness at hub ($t_{M,H} \geq 7\%c_{GF}$). The Pareto optimal guide fins feature a chord value of $\widetilde{c_{GF}} = 1$, and thus correspond to 3D guide fins. The 6p guide fins evaluated in RANS and with the surrogate model appear to be less efficient on both objective functions than in the 15p analysis. The maximum gains reachable with a 3D guide fins are therefore provided with the 15p analysis (see Table 7.10). The 6p input space therefore restrains the 3D guide fins to less efficient shapes. The tip chord is notably imposed to equal

the hub chord, thus preventing any potential trapezoidal aspect in the chordwise direction. This trapezoidal aspect was highlighted as a specificity of the 3D guide fins in the 15p analysis (see Section 7.1.2.1). Although difficult to confirm without further physical interpretations, the chordwise trapezoidal aspect is therefore suspected to play a major role in the loss reduction mechanisms implemented by the 3D family.

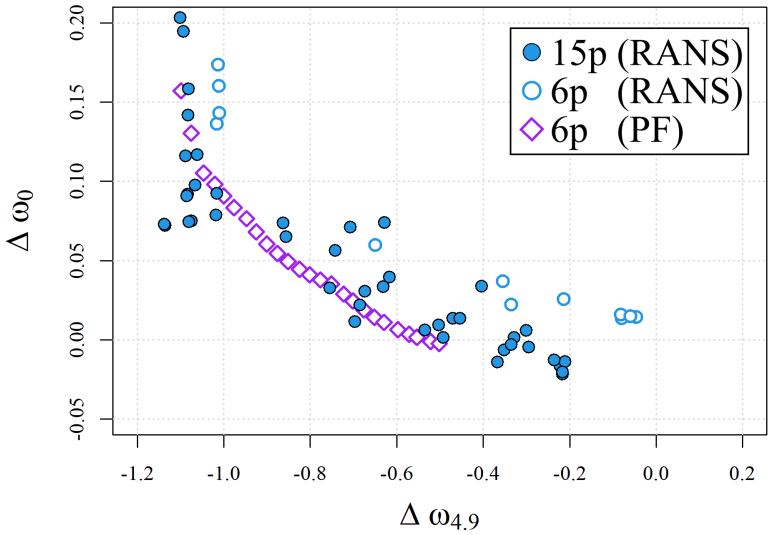

Figure 7.18: Performance of 3D guide fins (6p vs 15p). PF : Surrogate Pareto Front. PF : Surrogate Pareto Front.

Best $\Delta\omega_0$ (corresponding $\Delta\omega_{4.9}$)	Best $\Delta\omega_{4.9}$ (corresponding $\Delta\omega_0$)
-0.04 (-0.72)	-1.21 (0.11)

Table 7.10: Performance of best 3D guide fins (15p, RANS results).

7.2.4 Investigation of the Long Fence (LF) family

The LF guide fins are characterised with the same efficient parameter ranges than the SF family, except for the chord value that naturally differentiates them. The SF and LF guide fins could therefore be gathered in a unique set of guide fins characterised with a thin hub aerofoil. However, the evolution of the losses within this set is monitored with different parameters depending on the values of $\Delta\omega_{4.9}$. The lowest values of $\Delta\omega_0$ are obtained with SF guide fins of short heights. From these guide fins, increasing the height decreases the values of $\Delta\omega_{4.9}$ down to a limit value of $\Delta\omega_{4.9} = -0.9$ (see Figure 7.19a). Below this limit value, the height value little impacts $\Delta\omega_{4.9}$, but keeps increasing the values of $\Delta\omega_0$ (see Appendix, Section C.3, Figure C.5). To further lower $\Delta\omega_{4.9}$, the value of the chord must increase (see Figure 7.19b), thus switching to LF guide fins. The LF guide fins therefore correspond to an improvement of the best SF guide fins for lowering $\Delta\omega_{4.9}$.

Figure 7.20 compares the LF guide fins resulting from the 6p and 15p analyses. RANS results are shown, as well as the LF Pareto front. The LF Pareto front is obtained using the NSGA2 algorithm with restrained values of the chord parameter $\widetilde{c_{GF}}$ ($\widetilde{c_{GF}} \geq 0.65$). The Pareto optimal guide fins feature a thickness value of $t_{M,H} = 0$, and therefore correspond to LF guide fins. The Pareto optimal guide fins are better than any other LF guide fins for lowering $\Delta\omega_{4.9}$.

However the 6p surrogate model predicts that LF guide fins necessarily increase the losses at design incidence. LF guide fins reducing $\Delta\omega_0$ down to -0.02 are found in the 15p analysis. The best gains reachable with the LF guide fins are thus given by the 15p RANS database for $\Delta\omega_0$ and the 6p surrogate model for $\Delta\omega_{4.9}$ (see Table 7.11).

A beneficial effect of large chord values is therefore noticed for SF guide fins of sufficient heights. Such an increase in the chord values is likely to implement specific physical mechanisms. A representative guide fin of this family is selected in next section for further investigations.

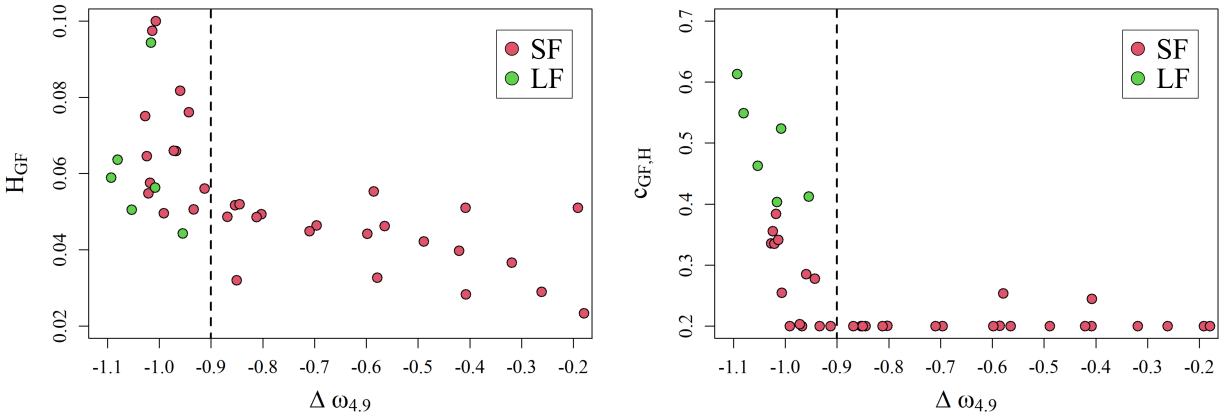

(a) $\Delta\omega_{4.9}$ vs H_{GF} (b) $\Delta\omega_{4.9}$ vs $c_{GF,H}$

Figure 7.19: Effects of H_{GF} and $c_{GF,H}$ depending on $\Delta\omega_{4.9}$ values.

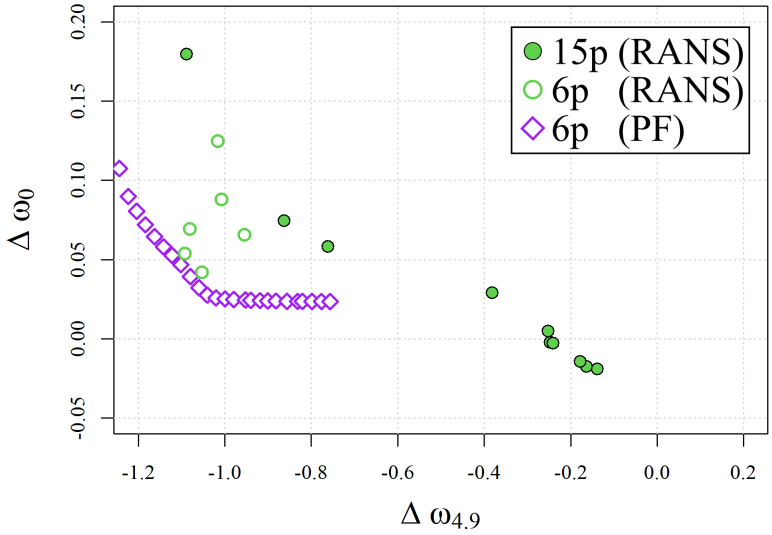

Figure 7.20: Performance of LF guide fins (6p vs 15p). PF : Surrogate Pareto Front.

Best $\Delta\omega_0$ (corresponding $\Delta\omega_{4.9}$)	Best $\Delta\omega_{4.9}$ (corresponding $\Delta\omega_0$)
-0.02 (-0.16)	-1.24 (0.11)

Table 7.11: Performance of best LF guide fins. 15p RANS results (grey) and 6p surrogate model (white).

7.2.5 Complementary analysis of the SF and LF Pareto fronts

The SF and LF Pareto front are plotted with the Pareto front computed on the whole input space (Surrogate Pareto front) in Figure 7.21. The latter appears to result from the best guide fins of the union of the SF and LF Pareto front, which explains its pointed shape. The evolution of the parameters along the SF and LF Pareto fronts are thoroughly studied in the Appendix (Section C.5). A unique type of guide fin can be defined within the LF Pareto front. Two subtypes of SF guide fins can be defined within the SF Pareto front, one of which corresponds to the LF type with a short chord. For both SF and LF guide fins, the performance of the Pareto optimal guide fins are monitored with different parameters depending on their position on the Pareto front. However, this analysis is out of the scope of the current investigation, and is only detailed in the Appendix.

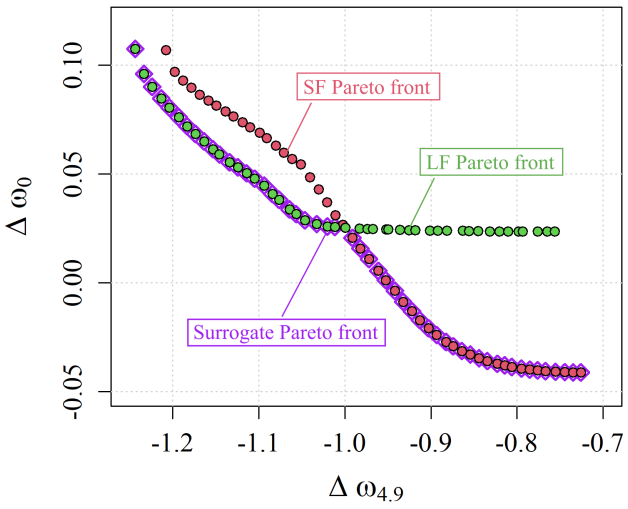

Figure 7.21: Comparison of SF, LF and surrogate Pareto fronts.

As a conclusion, the 6p exploration focuses on the same SF and 3D families than the one detected in the 15p exploration. For the SF family, better compromises between the objective functions are found and the SF Pareto front provides the maximum gains reachable with this family. On the contrary, the exploration of the 3D family is restrained to less efficient guide fins. The straight aspect imposed in the chordwise direction is suspected to be at the origin of this limitation. Finally, LF guide fins that efficiently lower the losses at high incidence are revealed. They are similar to SF guide fins except for the chord, and provides guide fins with a new type of geometry likely to implement interesting flow mechanisms.

7.3 Selection of representative guide fins of the three guide fin families

The analyses of the optimisation processes enabled to define and characterise three families of guide fins : SF (Short Fence), LF (Long Fence) and 3D (thick and long). Each family contains several guide fins that greatly lower the losses at high incidence. Given their geometrical differences, these guide fins are expected to implement different mechanisms yielding these loss reductions. In order to validate experimentally these gains and investigate these mechanisms,

a representative guide fin of each family is selected and will be thoroughly investigated in the next chapter.

The representative guide fins of each family are selected among the ones that most lower the endwall losses at high incidence while keeping a reasonable level of losses at design incidence ($\Delta\omega_0 \leq +0.10$, $\Delta\omega_{4.9} \leq -0.9$). Guide fins SF-03 is selected for the SF family. It was discovered in the early steps of this work and was intensively investigated. Guide fin 3D-01 is selected for the 3D family. It corresponds to the guide fin that features the lowest value of $\Delta\omega_{4.9}$ among all the guide fins evaluated in RANS. Guide fin LF-A is selected for the LF family. It corresponds to the best guide fin of the LF family for lowering the values of $\Delta\omega_{4.9}$. The geometrical characteristics of these guide fins are representative of their family. Notably, their parameter values are comprised within the efficient parameter ranges of their family.

These guide fins are represented in Figure 7.22. Table 7.23 gathers their characteristics. $\beta_{2,pc_\beta 1}$ and $\widetilde{c_{GF}}$ are replaced with $\Delta\beta_{2,H}$ and $c_{GF,H}$ to clarify their geometrical description. SF-03, 3D-01 and LF-A are also represented with respect to $\Delta\omega_0$ and $\Delta\omega_{4.9}$ among all the investigated guide fins in the Appendix (Section C.6, Figure C.7). Finally, to provide an extensive characterisation of these guide fins, the surrogate predictions near each guide fin is computed for the 6 main parameters. Results are gathered in the Appendix (Section C.6). For each guide fin, these predictions reveal consistent trends with the family they are representative of.



(a) Guide fin SF-03



(b) Guide fin LF-A

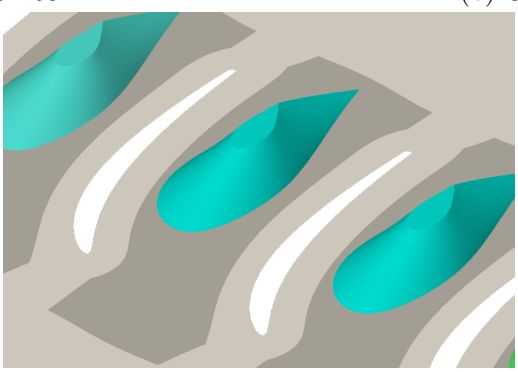

(c) Guide fin 3D-01

Figure 7.22: Representative guide fins of the SF, LF and 3D families.

	SF-03	LF-A	3D-01
$\Delta\omega_0$ (%)	0,08	0,05	0,07
$\Delta\omega_{4.9}$ (%)	-0,93	-1,09	-1,14
$\Delta\beta_{1,H}$ (°)	-11,9	-17,2	6,1
$\Delta\beta_{2,H}$ (°)	-16,4	0	-3,4
$x_{M,H}$ (%c_{GF})	51	45	42
$t_{M,H}$ (%c_{GF})	5,6	0,00	14,6
$c_{GF,H}$ (%c)	29	61	81
u (-)	0,24	0,36	0,41
v (-)	0,41	0,25	0,49
$\Delta\beta_{1,T}$ (°)	-4,8	0	3,3
$\Delta\beta_{2,T}$ (°)	-1,5	0	8,9
$x_{M,T}$ (%c_{GF})	0,42	0,45	0,33
$t_{M,T}$ (%c_{GF})	1,5	0	2,2
$c_{GF,T}$ (%c)	0,23	0,61	0,20
λ_{sweep} (°)	-10	0	11
λ_{lean} (°)	5	0	32
H_{GF} (%c)	6,8	5,9	6,4
λ_{chord} (°)	68	90	12
$\lambda_{thickness}$ (°)	84	90	58
$(\Delta\gamma)_H$ (°)	-14	-5	1
$(\Delta\gamma)_{twist}$ (°)	-9	-7	-6

Figure 7.23: Values of the objective functions, parameters and geometrical criteria associated to each representative guide fin. The main parameters are highlighted in green.

Chapter 8

Investigation of physical mechanisms reducing the corner separation

In the previous chapter, three families of guide fins are defined with respect to geometrical specificities and to similar sensitivities. A single representative guide fin is selected for each family. In this chapter, the effects of these representative guide fins on the corner separation are investigated.

The representative guide fins are investigated separately (Section 8.1, 8.2 and 8.3). For each one, the predictability of RANS results is first assessed on a large range of incidence. The experimental gains on both objective functions is notably investigated. The specific beneficial mechanisms implemented by the guide fin are then investigated. Finally, the flow modifications induced by the guide fin downstream of the stator row are quantitatively compared to the baseline flow. All the tested guide fins manage to considerably lower the losses, which validates the optimisation process implemented in this work. However, this process focused on the influence of the geometrical parameters of the guide fins. The stator configuration and the inlet conditions other than the incidence were fixed, although the stator deflection and the inlet boundary layer thickness are known to greatly affect the corner separation magnitude. A short numerical study is thus proposed in Section 8.4 to investigate the effect of the inlet boundary layer thickness on the guide fins performance. Finally, Section 8.5 gathers the main results of this chapter. The relevance of RANS predictions for controlling the phenomenon of corner separation is discussed. The beneficial mechanisms implemented by all guide fins are finally gathered in two families according to their action on the passage flow.

The investigation of the physical mechanisms notably relies on RANS and experimental cartographies downstream of the stator. For the sake of conciseness, only the relevant cartographies are used to highlight the beneficial mechanisms. Complementary RANS and experimental cartographies are gathered in the Appendix (see Section D.2). Various quantities of interest at different incidences are systematically compared to provide a thorough overview of the effect of each guide fin.

8.1 Investigation of the SF guide fin

The Short Fence (SF) guide fin is manufactured and evaluated experimentally at different incidences with the settings described in Chapter 4. Its geometry is recalled in Figure 8.1. Experimental results are first compared to RANS results to assess their predictability (Section 8.1.1). The physical mechanisms implemented by this guide fin are then investigated (Section

8.1.2). The effect of the guide fin is then quantitatively compared to the baseline with the investigation of radial profiles (Section 8.1.3). Finally, the specificities of these guide fins are summarised in Section 8.1.4.



Figure 8.1: Geometry of SF guide fin.

8.1.1 Validation of RANS predictions

The global effect of the SF guide fin is first investigated with the evolution of the endwall losses with the incidence. Figure 8.2 compares experimental and RANS results for the SF guide fin (red) and the baseline configuration (black). Experimentally, the SF guide fin reduces the endwall losses on the whole range of incidence, and notably at i=0° and i=4.9° (objective functions). The comparison between experimental and RANS results can be split in three regions depending on the incidence. For incidences lower than 2.3°, where the corner separation is small, the experimental trends with the guide fin are relatively well predicted. From 2.3° to 4.9°, the experimental losses strongly increase contrarily to the smooth increase predicted in RANS. Finally, above 4.9° the experimental losses of the guide fin increase slower, with a similar slope as predicted in RANS. Interestingly, up to 3.6° the experimental increase in losses with the guide fin is similar to the baseline one. Above 3.6°, the experimental losses with the guide fin increase much slower than in the baseline case, and the experimental gains rapidly increase up to -2.44% (see Table 8.1).

The experimental gains appear to be systematically underestimated with RANS. Let us first investigate the incidences lower than the baseline critical incidence $i_{crit} = 4.4°$. With the guide fin, the flow field features a single sided topology on the whole range of incidence. For incidences lower than the critical incidence, the baseline also features a single sided topology. As such, below the critical incidence ($i \in [0°, 4.3°]$) similar losses are predicted and the RANS gains are very small (below +0.1%). On the other hand, the experimental losses increase smoothly from the design incidence. The beneficial effect of the guide fin is therefore visible from the design incidence, which explains why the gains are under predicted below i_{crit}. For incidences greater than i_{crit}, the increase in losses is under predicted in the baseline configuration, which also yields an under prediction of the gains.

Incidence	0°	2,3°	3,6°	4,9°	5,4°
Gain (RANS)	0,10 %	0,07 %	0,01 %	-0,93 %	-1,61 %
Gain (Datum)	-0,13 %	-0,37 %	-0,35 %	-1,01 %	-2,44 %

Table 8.1: Gains with SF guide fin. RANS vs Experiment. Gains are measured with an uncertainty of ± 0.15%.

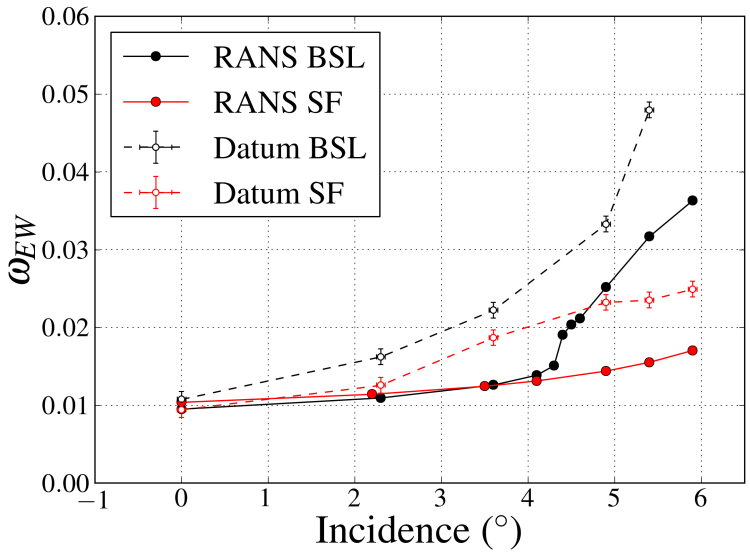

Figure 8.2: Evolution of the endwall losses on the measurement plane. Baseline vs SF guide fin. Black arrow : guide fin wake. Black rectangle : low loss region.

Figure 8.3 compares the RANS and experimental loss distribution with the SF guide fin in the measurement plane, 0.2c downstream of the stator trailing edge. Experimental measurements are performed across two adjacent channels, and reveal an excellent periodicity. The loss distribution is particularly well predicted at i=0°. Notably, the specific loss pattern (guide fin wake) pointed out by the black arrow is well retrieved. This confirms that the refinement levels in the experimental probe mesh and the numerical hybrid mesh are consistent with one another. For higher incidences, the loss level and corner separation shape are well retrieved. The region of maximum losses (core loss) is notably well retrieved. A low loss region near the hub (black rectangle) is also well captured. The corner separation extension is underestimated in both directions, consistently with the endwall losses underestimation revealed in Figure 8.2.

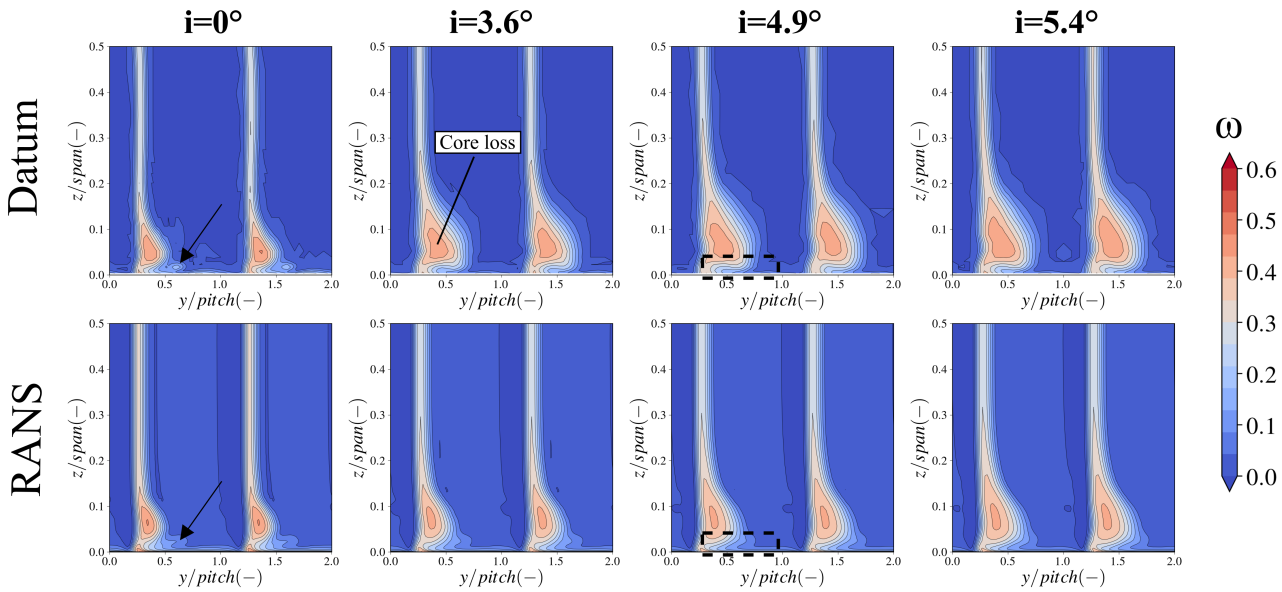

Figure 8.3: Total pressure losses with the SF guide fins at various incidences. RANS vs Experiment.

As such, this guide fin indeed lowers the endwall losses, which validates the chosen optimisa-

tion methodology. RANS predictions well retrieve specific loss patterns and corner separation shape, especially at 0° and 4.9°. The beneficial mechanisms implemented by the SF guide fin are now investigated.

8.1.2 Physical mechanisms

Topological analysis Adding the SF guide fin modifies the topology of the near-hub flow. Figure 8.4 compares the skin friction lines at hub with and without the SF guide fin at 4.9°. Critical points are added, and specific skin friction lines emerging from these points are highlighted (separating lines, in white). In the baseline configuration, a Saddle/Focus pair characteristic of a separation zone is observed. It is symptomatic of the double sided topology occurring at this incidence, and is located at an axial position of 0.19c downstream of the stator leading edge, close to the stator suction side. The SF guide fin is located close to this separation zone. The Saddle/Focus pair disappears, thus revealing a single sided topology. This explains the drop in endwall losses predicted in RANS at i=4.9° when adding the SF guide fin. Moreover, two new separating lines appear. They reveal that, locally, the passage flow reaching the stator suction side no longer originates from the stator pressure side, but from the guide fin pressure side. This occurs over a distance of about 0.37c.

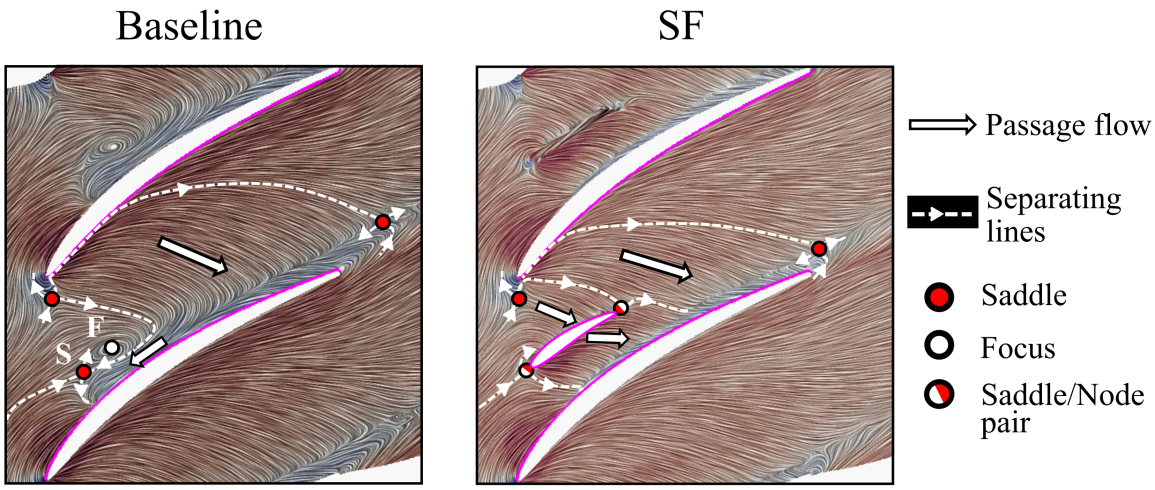

Figure 8.4: Topological organisation. Baseline vs SF guide fin (i=4.9°).

At the guide fin leading edge and trailing edge, a pair of Saddle/Node appears, and are represented with dots coloured in red and white. These pairs typically appear around sharp aerodynamic profiles (Duquesne et al., 2022), and their addition respects the index rule (see Equation 1.11). Figure 8.5 shows a zoom in these regions. The S_1/N_1 pair corresponds to the leading edge pair. The S_2/N_2 pair corresponds to the trailing edge pair. The zoom in the trailing edge region reveals additional pairs of critical points (S_3/F_3, S_4/F_4), which are symptomatic of a small separated region.

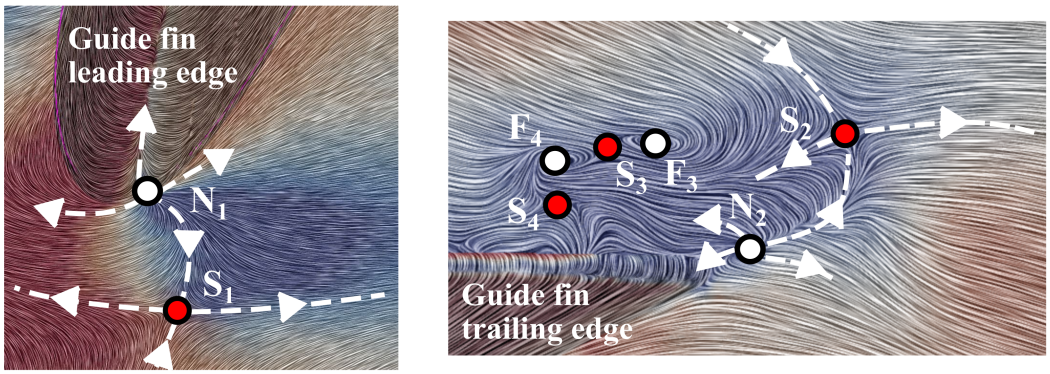

Figure 8.5: Topological organisation : zoom in guide fin leading edge and guide fin trailing edge regions (i=4.9°).

Effect of short fence The distribution of static pressure rise coefficient ($C_{p,s}$) at hub is presented in Figure 8.6a. The configuration with and without guide fins are compared. Without guide fin, a zone featuring little pressure gradients (pressure plateau) is visible and corresponds to the separated zone on the hub. Consistently with the skin friction line analysis, adding the guide fin removes the separation zone and this pressure plateau disappears. Transverse pressure gradients are also modified but do not disappear. Notably, two zones of transverse pressure gradients are visible on both sides of the guide fin and induce two passage flows. Figure 8.6b shows secondary streamlines obtained on axial slices. They represent the fluid motion with respect to the corresponding midspan flow and reveal two passage vortices.

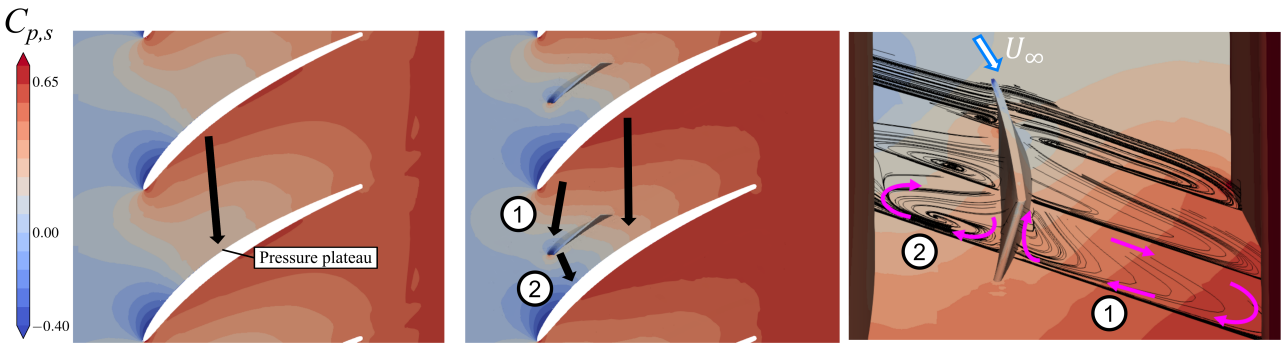

(a) Cps distribution at hub. SF guide fin vs Baseline (i=4.9°).

(b) Secondary streamlines : visualisation of passage vortices.

Figure 8.6: Illustration of the short fence effect.

The passage vortex 1 drives a portion of the near hub flow towards the guide fin suction side. This flow migrates radially along the guide fin and is deflected downstream, towards the stator pressure side (see Figure 8.7a). This deflection seems enhanced with the positive lean of the guide fin trailing edge. The SF guide fin therefore prevents this low momentum fluid to reach the stator suction side. The second passage vortex incorporates fluid with a strong axial component near the hub, and towards the stator suction side (see Figure 8.7b). Consequently, the passage flow that reaches the stator is energised and less prone to separate on the stator suction side. As such, this guide fin acts as a fence on a short axial extent, hence the denomination “Short Fence”.

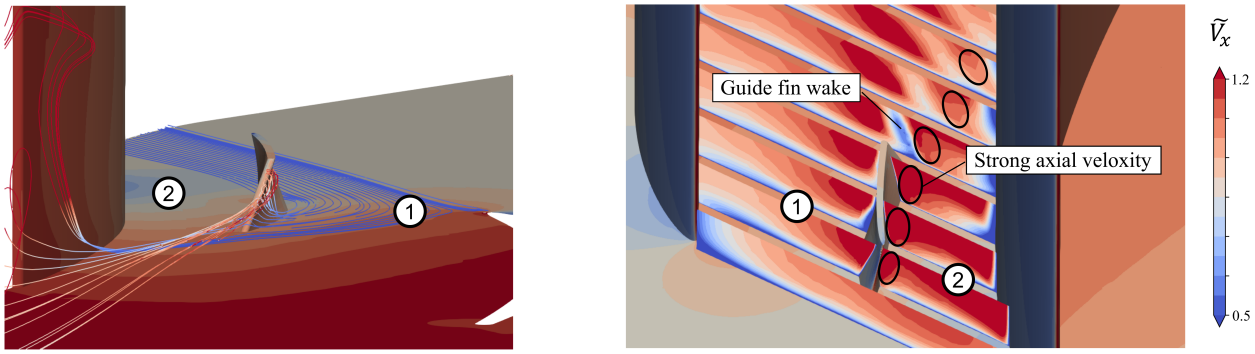

(a) Passage flow 1 : deflected. Colour : spanwise position.

(b) Passage flow 2 : accelerated in the axial direction. Colour : dimensionless axial velocity.

Figure 8.7: Beneficial effects of the fence mechanism.

Effect of tip vortex The guide fin features a depression on its suction side, characteristic of a positive incidence. This depression creates a tip vortex that develops along the tip aerofoil chord (see Figure 8.8). The beneficial effects implemented by the tip vortex are investigated in Figure 8.9. The secondary streamlines and the dimensionless axial velocity distribution ($\widetilde{V_x}$) are represented at different axial positions. The tip vortex is clearly visible on the secondary streamlines, and appears to rotate in the same direction than the passage vortices. The passage vortices are rapidly absorbed by the tip vortex, which becomes the main secondary flow pattern downstream of the guide fin. Two beneficial effects of this vortex are noticed. Firstly, the descending component of the tip vortex (black arrow) brings high momentum fluid in the near hub region. This high momentum fluid originates from the flow accelerated on the guide fin suction side and from the bulk flow. It is convected towards the stator suction side and reduces the low momentum flow accumulation in the corner region. Consistently, the descending component is associated to a low loss region (Figure 8.8, in blue). Secondly, the ascending component of the tip vortex (blue arrows) prevents of portion of the passage flow to reach the stator suction side by effect of radial migration. The tip vortex therefore also acts as an aerodynamic barrier limiting the azimuthal extension of the passage flow downstream of the guide fin.

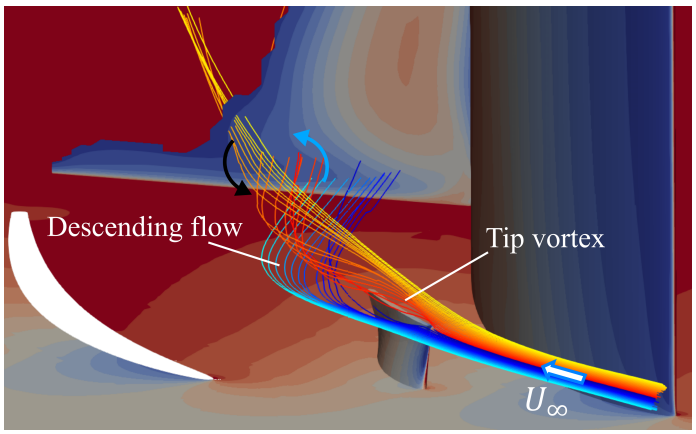

Figure 8.8: Illustration of the SF guide fin tip vortex.

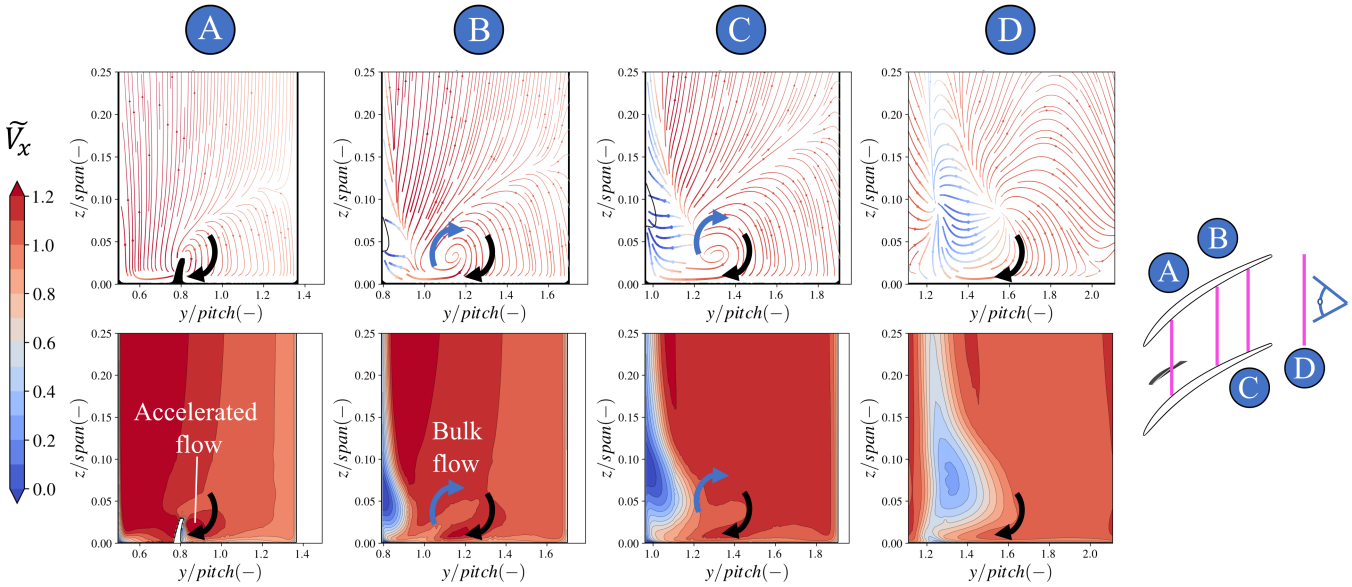

Figure 8.9: Secondary streamlines and dimensionless axial velocity distributions at different axial positions. Slice D : experimental measurement plane.

Experimental cartographies are used to characterise the flow modification induced by the guide fin (see Figure 8.10). The presence of the tip vortex is retrieved with the investigation of the pitchwise and spanwise angles, and indeed associated with a low loss region. On the other hand, the two passage vortices resulting from the effect of short fence are not visible, which is not surprising. The RANS analysis indeed predicts that they are absorbed by the tip vortex far upstream of the measurement plane.

- Pitchwise flow angle : the fluctuation of the pitchwise angle (β) with respect to its averaged midspan value (β_{MID}) is computed. The effect of the passage vortex is clearly observed, with a region of large negative values (over deflection due to passage flow) and a region of large positive values (under deflection due to transverse flow). These two regions reveal the presence of the passage vortex. Adding the guide fin reduces the spanwise extent of the under deflected region. However, the region of over deflected flow is enlarged, yielding a flow that crosses the stator wake.

- Spanwise flow angle : In the baseline configuration, the spanwise angle (ϕ) is mainly negative (in blue) which reveals a descending flow towards the hub. This is interpreted as the effect of the decreasing blockage of the corner separation as it is convected downstream of the stator row. Adding the SF guide fin reduces the intensity of this descending flow, consistently with the reduction of the corner separation blockage. A zone of positive angle is observed in the baseline configuration, and is much enhanced with the guide fin.

The modification of the pitchwise and spanwise angles (black arrows) are consistent with the presence of a tip vortex created by the SF guide fin. Consistently with RANS predictions, this vortex is associated with a zone of large axial velocity near the hub (black rectangle) that does not exist in the baseline configuration. The presence of this high velocity region corresponds to a region of low loss values. This correlation confirms that the vortex has a beneficial effect on the endwall losses by bringing high momentum fluid near the hub.

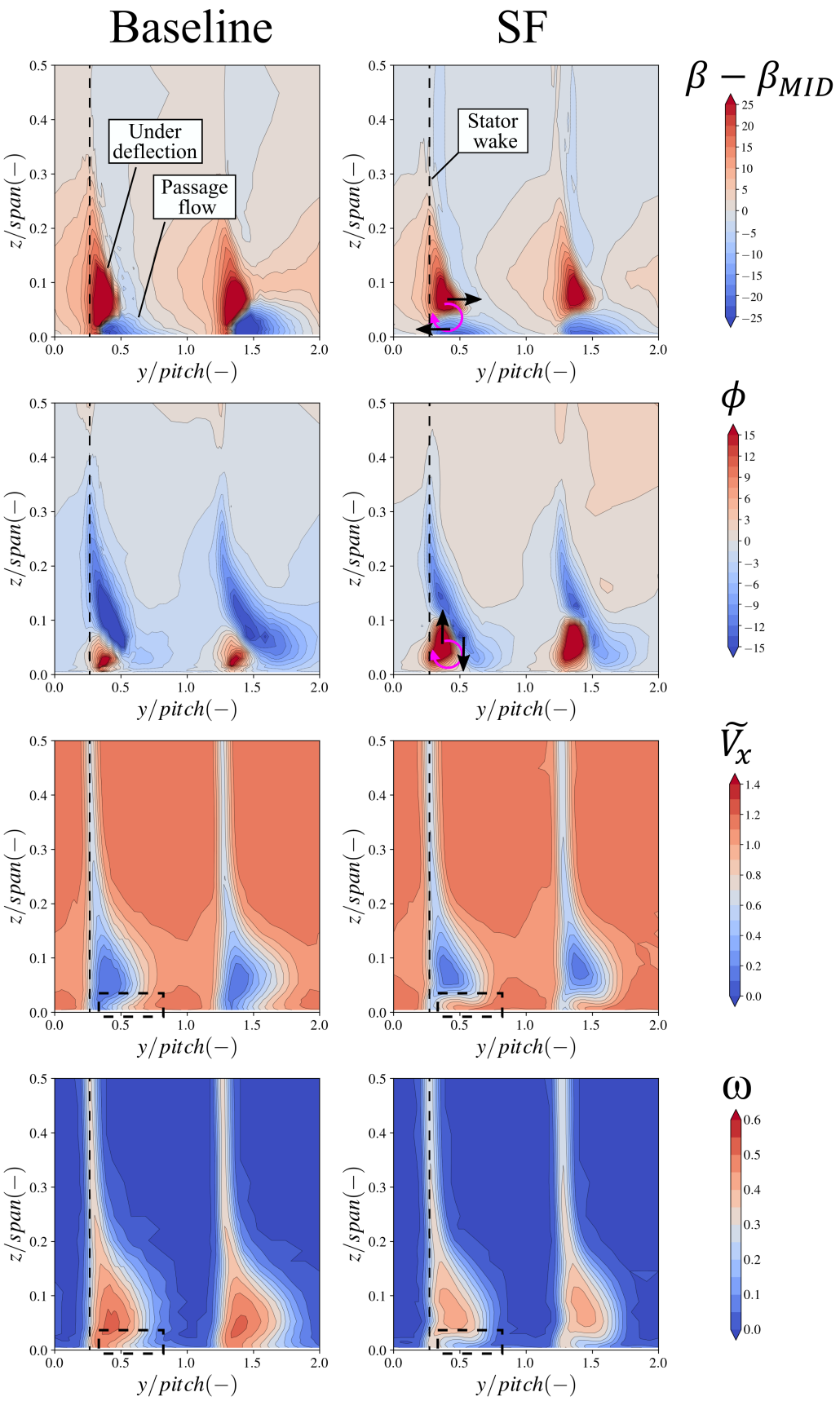

Figure 8.10: Validation of the presence and of the beneficial effect of the tip vortex (SF guide fin). Experimental data in the measurement plane.

8.1.3 Effect on downstream profiles

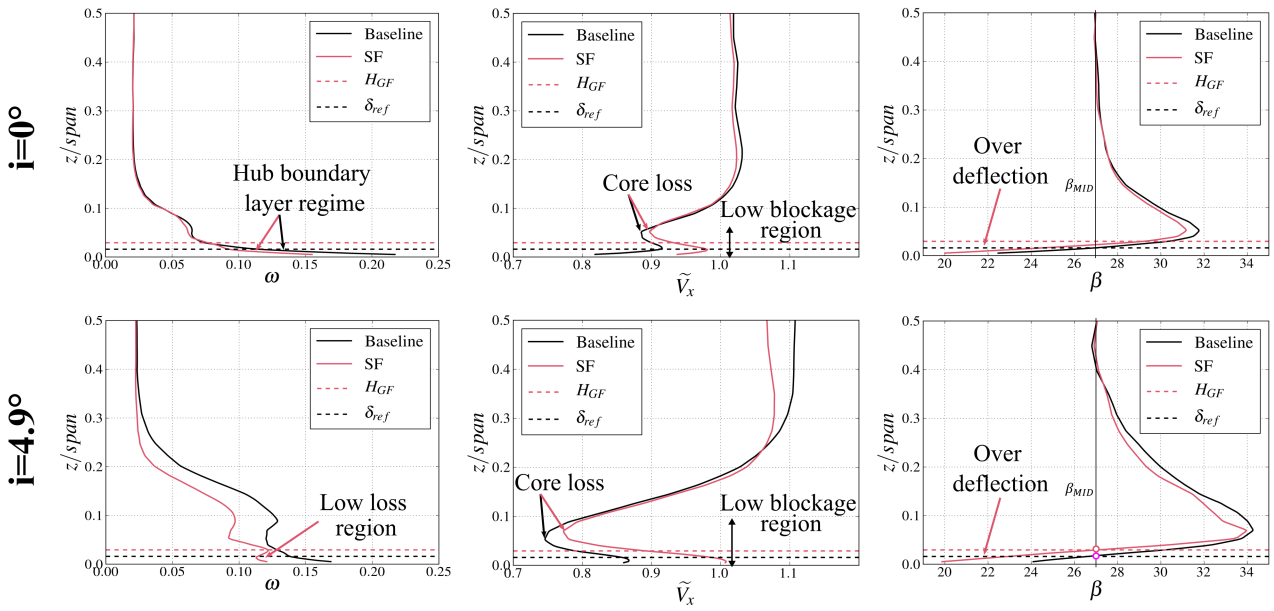

Figure 8.11: Experimental profiles in the measurement planes. SF guide fin (red) vs Baseline (black). H_{GF} : Guide fin height. δ_{ref} : inlet boundary layer thickness.

The effect of the SF guide fin is quantitatively compared to the baseline configuration through radial profiles (see Figure 8.11). They correspond to the experimental cartographies averaged in the pitchwise direction. The total pressure losses (ω) are mass averaged, while the dimensionless axial velocity ($\widetilde{V_x}$) and the pitchwise flow angle (β) are surface averaged. The guide fin height (H_{GF}) and the inlet boundary layer thickness (δ_{ref}) are added. When averaging in the azimuthal direction, the core loss may no longer correspond to the loss maximum. It is better localised with the zone of maximum blockage, which is evaluated with the dimensionless axial velocity.

Let us first investigate the profiles at design incidence ($i = 0°$). The evolution of the losses is little modified when adding the guide fin. A slight change in the loss gradient occurs when crossing the spanwise location corresponding to the inlet boundary layer thickness. In this region, the losses are dominated by the hub boundary layer : the baseline and the guide fin configurations behave similarly. The increase in axial velocity in the core loss region indicates a lower blockage when adding the guide fin. Let us underline that the gradient of $\widetilde{V_x}$ is consistent with the guide fin tip vortex mechanism : $\widetilde{V_x}$ locally increases when crossing the guide fin tip position towards the hub. This indicates that high momentum fluid is taken from above the guide fin tip (bulk flow) and brought below the guide fin tip (near hub region). As such, this increase in axial velocity probably results from both the tip vortex effect and the decrease in blockage. As for β, the over deflection is increased (-2°) with the guide fin, consistently with the rotational direction of the tip vortex.

At high incidence ($i = 4.9°$), values of losses are greatly lowered on a wide range of spanwise locations. Similar gradients are kept above the guide fin tip. However, the tip vortex induces a low loss region near the hub. This region appears to be confined between the hub and the guide fin tip, consistently with the tip vortex mechanism. Let us point out that this non monotonous evolution might yield extra losses when mixing out downstream of the row. A large decrease in blockage is revealed near the hub, mainly between the core loss and the hub. The axial velocity at midspan is consequently reduced. Despite the blockage reduction in the core loss region,

the under deflection is only little improved. Here again, this is consistent with the rotational direction of the tip vortex that drives the flow above the guide fin towards large values of β. Conversely, the over deflection below the guide fin tip is increased (-4°). Interestingly, the over deflection ($\beta < \beta_{MID}$) is driven by the guide fin tip position (tip vortex position) in the guide fin case, and by the boundary layer (passage flow) in the baseline case (see the purple and red dots).

8.1.4 Summary

The SF guide fins efficiently reduces the endwall losses on a large range of incidence. It acts as a local fence (hence the denomination Short Fence) that replaces the passage flow coming from the stator pressure side with a more energised passage flow. Moreover, the SF guide fin generates a tip vortex that brings high momentum fluid near the hub. This helps resisting the adverse pressure gradient and explains the reduction of the corner separation magnitude. However, this vortex slightly increases the over deflection at hub. Moreover, the high momentum fluid brought near the hub is likely to produce extra losses when mixing out with the hub boundary layer and stator wake. The effect of mixing downstream of the stator row is discussed for the SF, LF and 3D guide fins in the Appendix (Section D.1).

8.2 Investigation of the LF guide fin

The Long Fence (LF) guide fin is manufactured and evaluated experimentally at different incidences with the settings described in Chapter 4. Its geometry is recalled in Figure 8.12. Experimental results are first compared to RANS results to assess their predictability (Section 8.2.1). The physical mechanisms implemented by this guide fin are then investigated (Section 8.2.2). The effect of the guide fin is then quantitatively compared to the baseline with the investigation of radial profiles (Section 8.2.3). Finally, the specificities of this guide fins are summarised in Section 8.2.4.



Figure 8.12: Geometry of LF guide fin.

8.2.1 Validation of RANS predictions

The experimental and RANS evolutions of the endwall losses with and without the LF guide fin are presented in Figure 8.13. The experimental results are first investigated. Adding the guide fin efficiently reduces the increase in losses with the incidence. A slight increase in losses is observed at design incidence (+0.08%), and the guide fin starts having a beneficial effect from about 1.6° (given a linear interpolation of experimental results). A large beneficial effect

is observed at high incidences, notably at 5.4° with an experimental gain of -2.69%. RANS predictions are now investigated. The absolute values of the losses are under predicted in RANS, but the trend is well retrieved from 0° to 4.9°. Interestingly, above this incidence the experimental losses stagnate while they keep increasing in RANS. The experimental and RANS gains are summarised in Table 8.2. The gains at i=0° and 4.9° are particularly well retrieved, while RANS underestimates the gains at the other incidences. As explained with the SF guide fin (Section 8.1.1), this underestimation results from the sudden increase in the baseline losses caused by the topological switch.

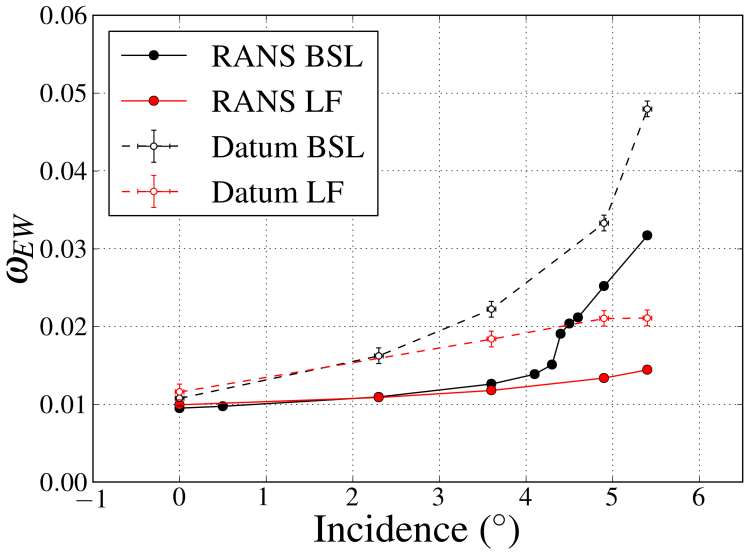

Figure 8.13: Evolution of the endwall losses on the measurement plane. Baseline vs LF guide fin.

Incidence	0°	3,6°	4,9°	5,4°
Gain (RANS)	0,05 %	-0,07 %	-1,09 %	-1,72 %
Gain (Datum)	0,08 %	-0,38 %	-1,23 %	-2,69 %

Table 8.2: Gains with LF guide fin. RANS vs Experiment. Gains are measured with an uncertainty of ± 0.15%.

The predicted and experimental cartographies of total pressure losses in the measurement plane are compared in Figure 8.14. With this guide fin, the experimental periodicity is excellent and the measurements are performed only downstream of the investigated blade, across one pitch ($y/pitch \in [0, 1]$). The results are duplicated to replicate the neighbouring channel ($y/pitch \in [1, 2]$). The size and intensity of the corner separation are underestimated with RANS results, but increase with the incidence in both cases, which is consistent with the endwall loss evolutions. The wake of the guide fin appears clearly in RANS in the zone denoted by the letter C. Interestingly, this wake is of greater intensity than with the SF guide fin. RANS results predict a region of low losses (region B) between the corner separation (region A) and the guide fin wake (region C). Experimentally, the region B is replaced with a high loss region, which makes it difficult to separate the guide fin wake and the corner separation. The presence of the wake is still noticeable through the S-shaped pattern indicated in purple. Finally, a low loss region is noticed near the hub (black rectangle at i=4.9°). However the pitchwise extension of this region is smaller in RANS.

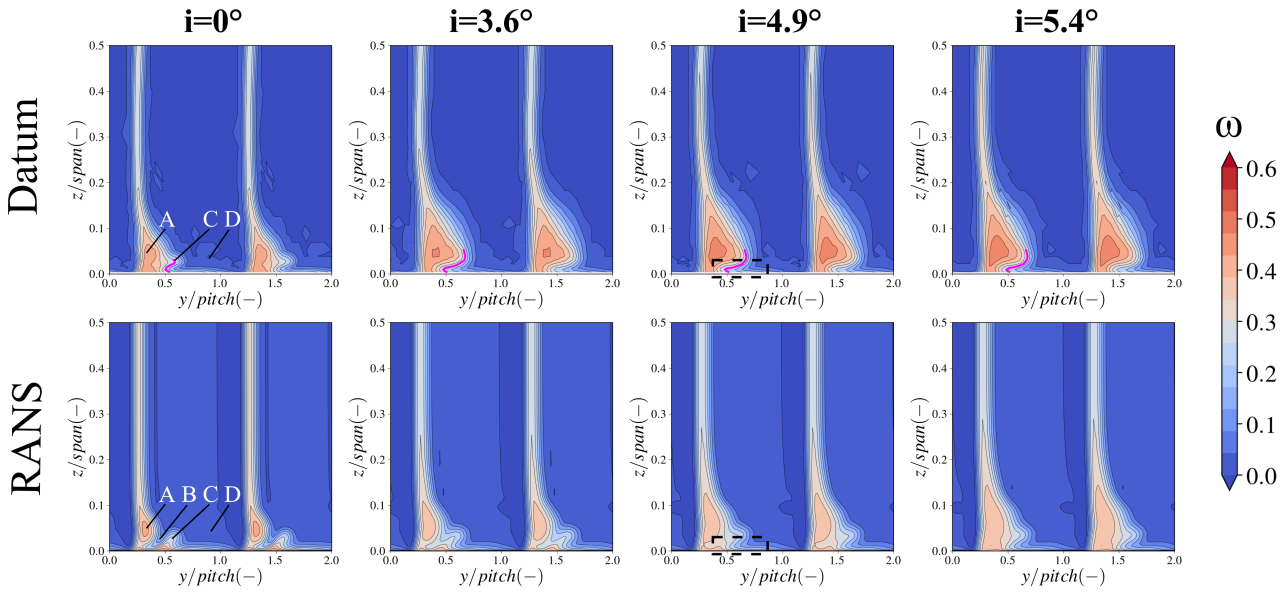

Figure 8.14: Total pressure losses with the LF guide fins at various incidences. RANS vs Experiment. A : Stator corner separation. B : Low loss region (RANS only). C : Guide fin corner separation. D : Bulk flow guided with low losses.

These results prove that the LF guide fin efficiently reduces the corner separation. RANS results are used in the following part to reveal its physical effects on the flow field and attempt to understand the discrepancy between RANS predictions and experimental results.

8.2.2 Physical mechanisms

Topological analysis The effect on the LF guide fin on the topological organisation is first investigated. Figure 8.15 compares the skin friction lines at hub with and without the LF guide fin. The separating lines are highlighted in white. The leading edge of the guide fin appears to be positioned in the baseline hub separation region, similarly than with the SF guide fin. However, the LF leading edge is particularly close to the Focus position. Indeed, it is characterised with a streamwise/pitchwise position of $(u, v) = (0.35, 0.25)$, and the Focus with $(u, v) = (0.38, 0.18)$. The optimal value for the guide fin leading edge seems to coincide with the location of the Focus point of the baseline configuration.

From this position, the LF guide fin splits the channel and induces two passage flows. Notably, the skin friction lines indicate that the passage flow occurring on the guide fin pressure side is progressively reoriented in the axial direction as it is convected downstream. The separating lines show that the entire passage flow coming from the stator pressure side is blocked by the guide fin and cannot reach the stator suction side, protecting the downstream portion of the stator over 0.65c. This organisation is different than with the SF guide fin whose chord is shorter, and which only blocks a portion of this flow (see Figure 8.4). However, a similar topological organisation than in the SF case is observed near the leading edge and the trailing edge (see Figure 8.5) : Saddle/Node pairs are created so that the index rule is respected.

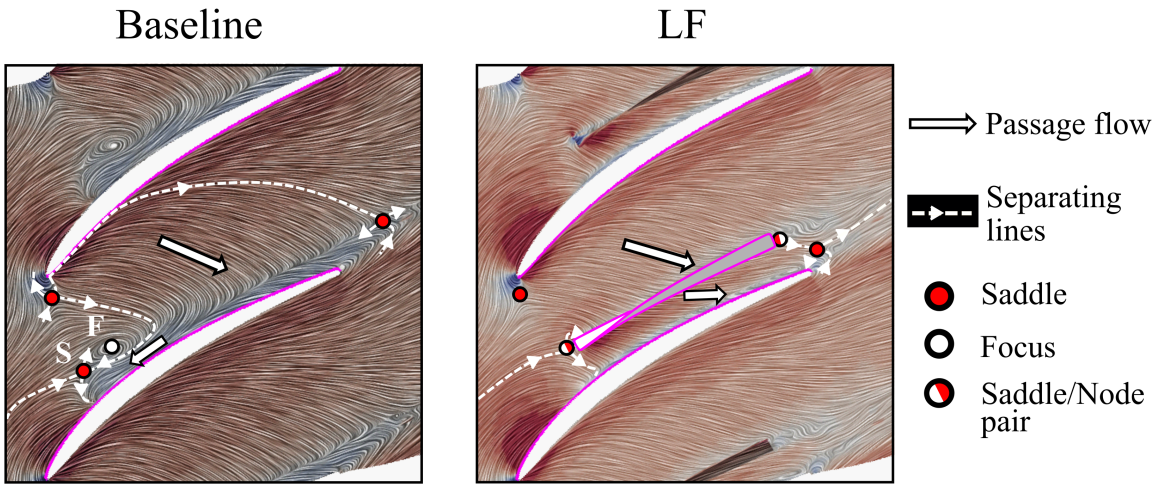

Figure 8.15: Topological organisation. Baseline vs LF guide fin (i=4.9°).

As a complementary analysis, the pressure distribution on the hub is investigated. It appears to be very similar to the midspan one, with particularly straight isobars from midspan towards the hub (see Figure 8.16). This guide fin therefore discards the pressure modifications induced by the secondary flows. Moreover, the beneficial effects implemented by the LF guide fin are not driven by specific pressure modifications.

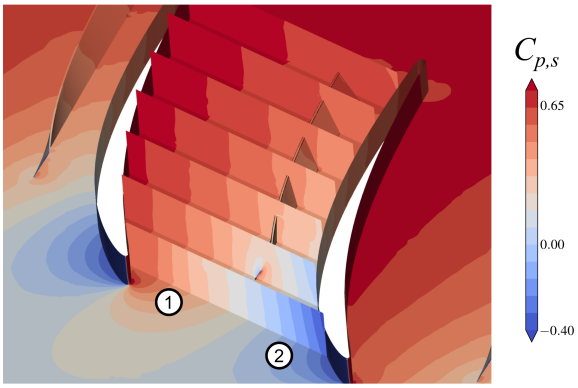

Figure 8.16: Pressure distribution near the hub.

Effect of long fence The LF guide fin implements two passage vortices, as illustrated in Figure 8.17. The LF guide fin therefore induces an effect of fence on a long distance, hence its denomination (Long Fence). The beneficial effect of the secondary passage vortex is illustrated in Figure 8.18a. Axial slices at different positions are computed and coloured with the dimensionless axial velocity field. High velocity fluid is indeed incorporated from the guide fin pressure side towards the stator suction side because of the passage vortex occurring in the secondary channel. This effect is enhanced with the increasing lean along the guide fin chord. The high velocity fluid is progressively incorporated under the corner separation and finally results in the low loss region observed in the measurement plane.

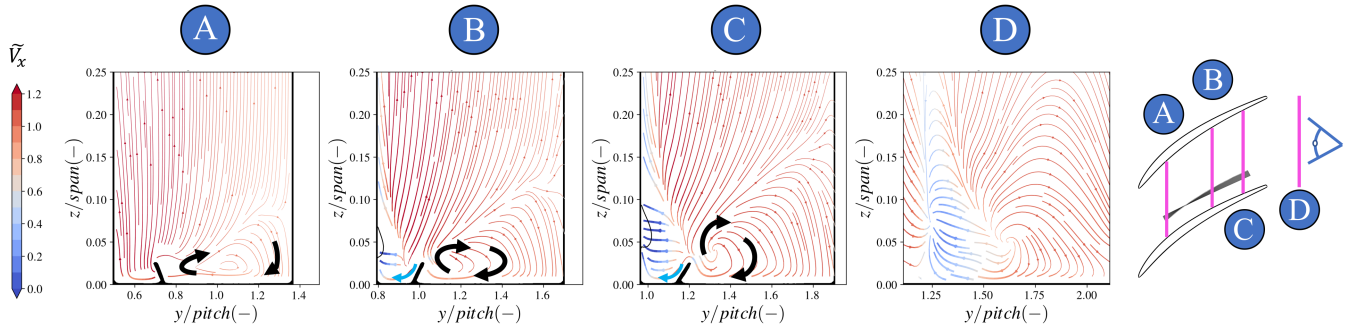

Figure 8.17: Secondary streamlines and dimensionless axial velocity distributions at different axial positions. Slice D : experimental measurement plane.

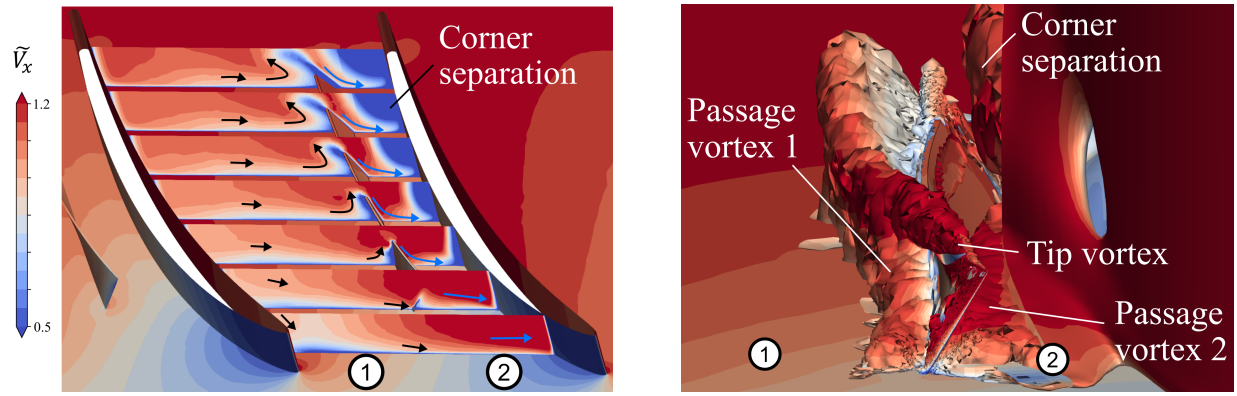

(a) Dimensionless axial velocity evolution along the axial direction.

(b) Merging of tip and passage vortices. Iso-contour of Q criterion ($Q = 150000s^{-2}$).

Figure 8.18: RANS predictability : experimental integrated losses and gains vs predictions for guide fins SF, LF and 3D.

This main passage vortex is due to the passage flow created between the stator pressure side and the guide fin suction side. The passage flow induces a corner separation when reaching the guide fin suction side. This corner separation is stronger than with the SF guide fin as more passage flow is collected. This corner separation induces a radial migration of the near hub flow, which is then deflected back towards the stator pressure side, thus creating the passage vortex. This deflection is particularly enhanced with the positive lean of the guide fin near its trailing edge.

However, contrarily to the SF guide fins, only a little pressure difference between the guide fin suction and pressure side is visible. It is only located near the guide fin leading edge. The tip and hub aerofoils indeed feature a positive incidence at their leading edge, but impose a small deflection along their chord. In particular the hub aerofoil is straight and induces no deflection passed its leading edge. As such, only a weak tip vortex is observed, and is rapidly absorbed by the main passage vortex (see Figure 8.18b).

The loss patterns observed in Figure 8.14 can thus be interpreted. From the stator suction side to the stator pressure side : stator corner separation (region A), high velocity flow incorporated near the hub in the secondary channel (region B), guide fin corner separation (region C), flow guided between the guide fin suction side and the stator pressure side (region D). However, this region of low loss progressively disappears when the incidence is increased. Figure 8.19 reveals the interaction between the low loss region and the guide fin corner separation at

two incidences. At design incidence, the over deflection of the near hub flow is small enough for these two regions not to interact. On the other hand, at high incidence (i=4.9°) the over deflection is stronger. The near hub flow coming from the main passage interacts with the high velocity fluid, which increases the losses in region B.

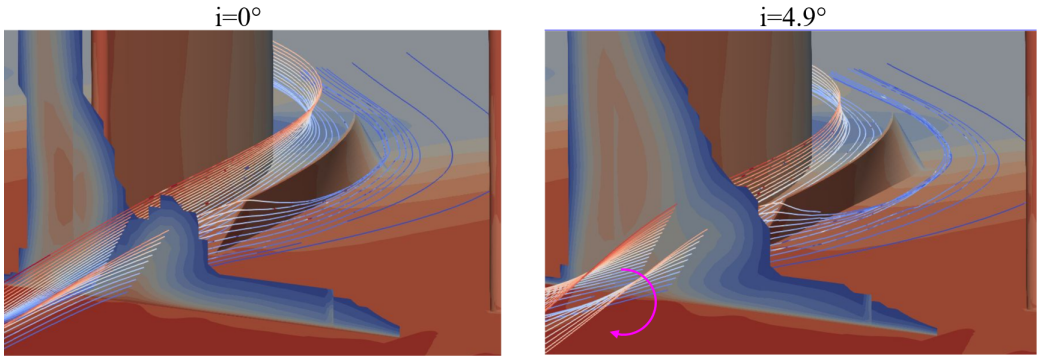

Figure 8.19: Streamlines seeded in low loss region and high loss pattern for i=0° and i=4.9°.

Comments on RANS predictability Contrarily to RANS results, experimental cartographies show that the region B is characterised with high losses at all incidences, including at design incidence. The study of the skin friction lines reveals the presence of separation zone near the LF leading edge (see Figure 8.20). This separation zone might be under predicted in RANS. Experimentally, this leading edge separation might be stronger and might increase the losses in the secondary passage.

Another difference between the experimental and the RANS results consists in the low loss region developing between the hub and the stator corner separation (black rectangle in Figure 8.14). In Figure 8.21, experimental and RANS cartographies of dimensionless axial velocity and pitchwise angle fluctuation are compared at high incidence (i=4.9°). The experimental blockage induced by the stator corner separation is under predicted in RANS. An acceleration of the flow is therefore visible experimentally in the midspan part and near the hub. The cartographies of angle fluctuations reveal that the over deflection and under deflection are underestimated in RANS. The passage vortex is therefore of greater intensity in the experiment. The stronger over deflection combined with the flow accelerated with the greater blockage explains the larger extent of the low loss region found near the hub.

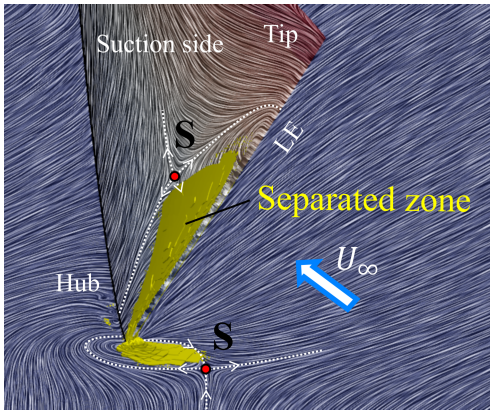

Figure 8.20: Zoom in guide fin leading edge. Skin friction and negative axial velocity region (in yellow) at design incidence i=0°.

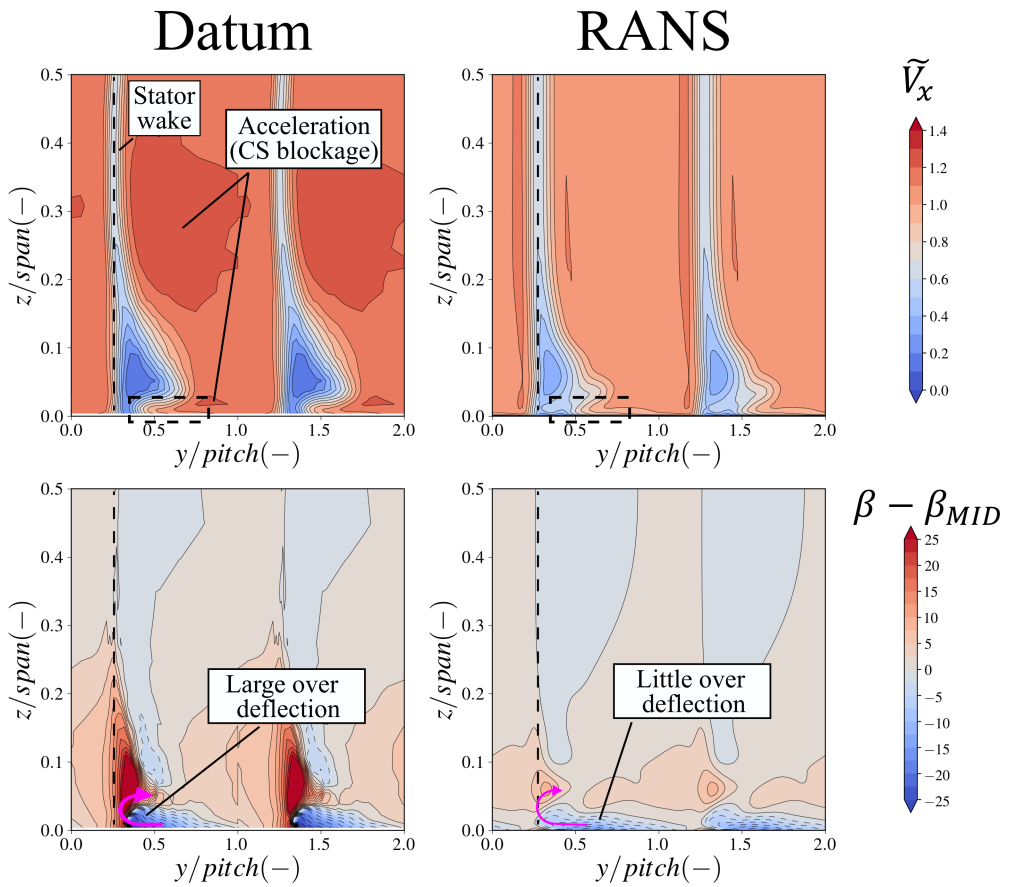

Figure 8.21: Comparison of experimental and RANS cartographies of $\widetilde{V_x}$ and $\beta - \beta_{MID}$. LF guide fins, i=4.9°. CS : Corner separation. Purple arrows : passage vortex.

8.2.3 Effect on downstream profiles

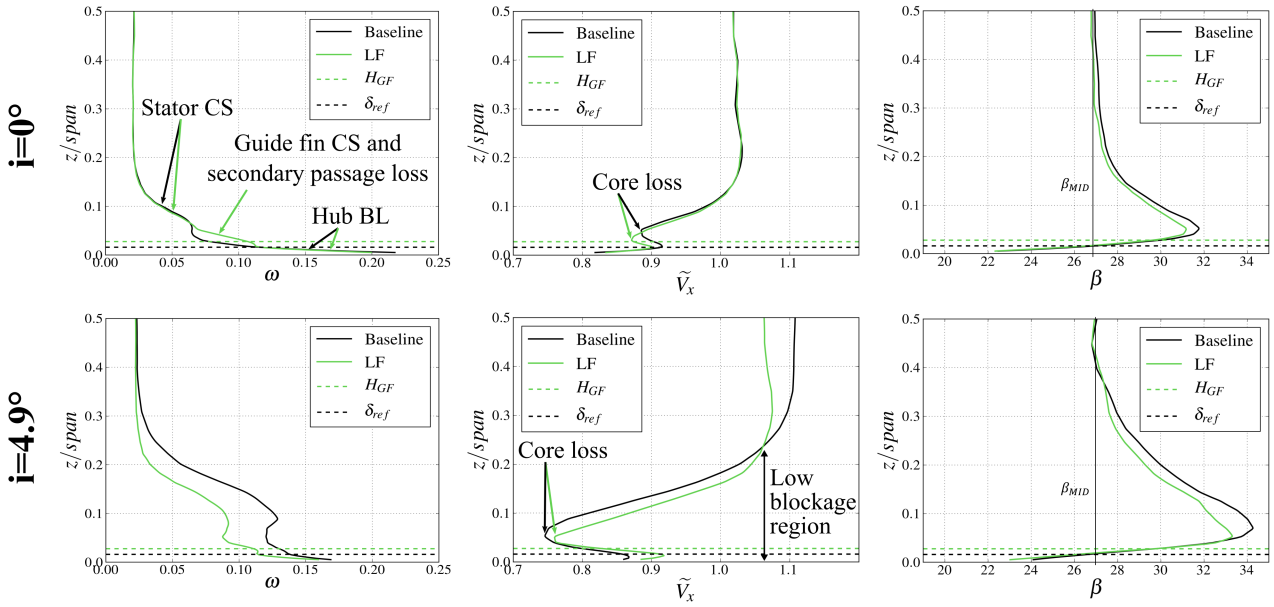

Figure 8.22: Experimental profiles in the measurement planes. LF guide fin vs Baseline. CS : Corner Separation. H_{GF} : Guide fin height. δ_{ref} : inlet boundary layer thickness.

As for the SF guide fin, the radial profiles of the total pressure losses (ω), the dimensionless axial velocity ($\widetilde{V_x}$) and the pitchwise flow angle (β) are compared to the baseline configuration. The guide fin height (H_{GF}) and the inlet boundary layer thickness (δ_{ref}) are added. Let us recall that the core loss is localised with the zone of maximum blockage when using radial profiles.

Let us first investigate the profiles at design incidence ($i = 0°$). The evolution of the losses reveals the region of high losses induced in the secondary channel and by interaction with the guide fin corner separation. This graph enables to clearly assess the influence of the hub boundary layer : the evolution of the losses is similar in both cases as soon as the inlet boundary layer thickness is reached. Consistently with the increase in losses, the axial velocity evolution indicates an increased blockage in the core loss region, but at a lower spanwise location. It occurs at a location corresponding to the guide fin height, consistently with the extra losses induced by the guide fin wake. Finally, the pitchwise angle evolution is little affected by the guide fin. A reduction by 1° of the maximum pitchwise angle is obtained.

At high incidence ($i = 4.9°$), values of losses are greatly lowered on a wide range of spanwise locations. Moreover, similar gradients are kept from midspan to the guide fin tip. No peak of losses is observed as with the SF guide fin, even though a small region of constant loss is observed above the hub boundary layer location. Consistently with the loss reduction, a decrease in blockage is observed. It induces a larger uniform distribution of axial velocity in the midspan region, with lower values. However, contrarily to the SF guide fin, the decrease in blockage mainly occurs in the region above the core loss (black arrow). Consequently, the pitchwise angle values are lowered in the same region.

8.2.4 Summary

The LF guide fins efficiently reduces the endwall losses at large incidences, but slightly increase the losses at design incidence. It acts as a fence on a long portion of the stator chord (hence the denomination Long Fence) by replacing the passage flow coming from the stator pressure side with a more energised passage flow. This beneficial effect is enhanced with the increasing lean developing along the guide fin chord. However, it necessarily induces a corner separation on the guide fin suction side, which yields extra losses. Moreover, RANS analysis predicts a pressure distribution particularly uniform in the spanwise direction. At high incidence, the study of the experimental profiles shows that this guide fin reduces the losses, dimensionless axial velocity and pitchwise angles in the near hub region. Moreover, the gradient of these quantities feature a similar shape than in the baseline case.

However, cartographies of losses reveal that specific loss patterns are only partially retrieved. Notably, RANS predicts a low loss region between the stator corner separation and the guide fin corner separation, that is not retrieved experimentally. A RANS analysis indicates that the guide fin leading edge is a sensible zone prone to separation. This separation may occur experimentally and may explain the discrepancy with experimental results. Unfortunately, no experimental data are available to confirm this assumption. If this is the case, it is worth questioning the interest of such a low value of the metal angle at the guide fin leading edge. Indeed, in the guide fin parametrisation (6p) the lean angle at the trailing edge is conditioned by the value of the metal angle at the hub leading edge ($\Delta\beta_{1,H}$). A positive lean is only possible with a negative value of $\Delta\beta_{1,H}$. Hypothetically, RANS might correctly predict the beneficial effect induced by the positive lean, but under predict the detrimental effect of the low metal angle at hub.

8.3 Investigation of the 3D guide fin

The 3D guide fin is manufactured and evaluated experimentally at different incidences with the settings described in Chapter 4. Its geometry is recalled in Figure 8.23. Experimental results are first compared to RANS results to assess their predictability (Section 8.3.1). The physical mechanisms implemented by this guide fin are then investigated (Section 8.3.2). The effect of the guide fin is then quantitatively compared to the baseline with the investigation of radial profiles (Section 8.3.3). Finally, the specificities of this guide fins are summarised in Section 8.3.4.

For the sake of clarity, the geometry of the 3D guide fin is recalled in Figure 8.23.

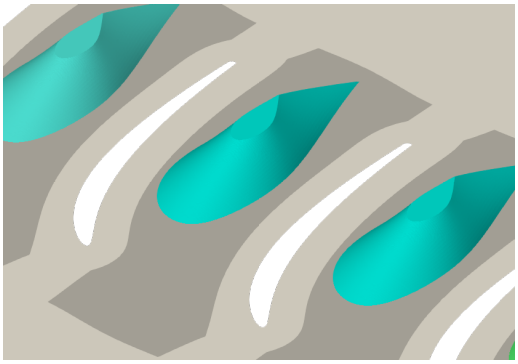

Figure 8.23: Geometry of 3D guide fin.

8.3.1 Validation of RANS predictions

The evolution of the endwall losses with the incidence is compared between the baseline and the 3D guide fin configurations (see Figure 8.24). This guide fin feature larger experimental gain than the SF and LF guide fins at every incidence. A gain of -1.60% is notably observed at $i = 4.9°$, bringing the endwall losses to a value found near $i = 2.6°$ in the baseline configuration. The experimental trend is particularly well retrieved in RANS. Moreover, the gains are systematically underestimated at all incidences (see Table 8.3).

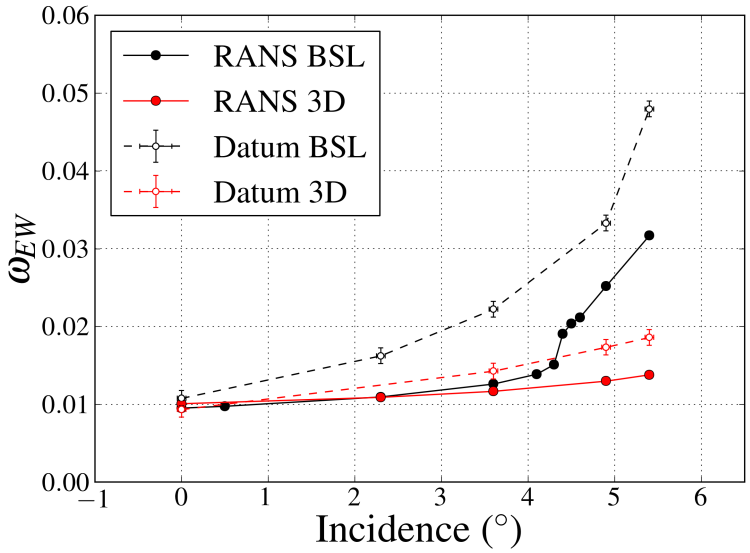

Figure 8.24: Evolution of the endwall losses on the measurement plane. Baseline vs 3D guide fin.

Incidence	0°	3,6°	4,9°	5,4°
Gain (RANS)	0,07 %	-0,08 %	-1,13 %	-1,78 %
Gain (Datum)	-0,14 %	-0,80 %	-1,60 %	-2,94 %

Table 8.3: Gains with 3D guide fin. RANS vs Experiment. Gains are measured with an uncertainty of ± 0.15%.

The predicted and experimental cartographies of total pressure losses are compared in Figure 8.25. The experimental periodicity is excellent and the measurements are performed only downstream of the investigated blade, across one pitch ($y/pitch \in [0, 1]$). The results are duplicated to replicate the neighbouring channel ($y/pitch \in [1, 2]$). The guide fin wake (black arrows) is well retrieved, and appears to be clearly separated from the corner separation at every incidence. The losses are slightly underestimated in the region between the guide fin wake and the corner separation, but the extension, shape and intensity of the loss patterns are very well retrieved.

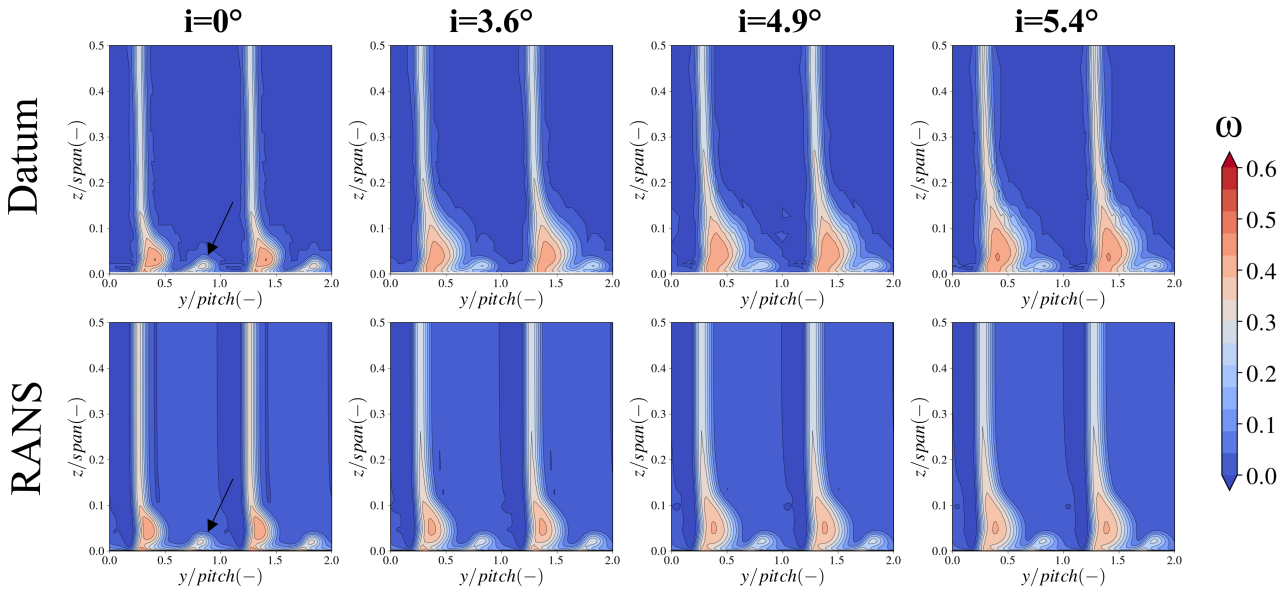

Figure 8.25: Total pressure losses with the 3D guide fins at various incidences. RANS vs Experiment. Black arrow : guide fin wake.

Among the three guide fins tested experimentally, the 3D guide fin best lowers the losses at every incidence. RANS predictions are excellent, and are used to analyse the physical mechanisms implemented by this guide fin.

8.3.2 Physical mechanisms

Topological analysis The topological organisation implemented by the guide fin 3D is investigated in Figure 8.26. The separating lines are highlighted in white (dotted lines). Adding the guide fin removes the Focus/Saddle pair symptomatic of the double sided separation. However, contrarily to the other guide fins, the 3D guide fin does not block the skin friction lines at this position and acts downstream of this position. Moreover, no Saddle/Node pairs appear at the guide fin leading edge and trailing edge. This is attributed to the pyramidal aspect of the guide fin that smoothly deflects the flow with no stagnation points.

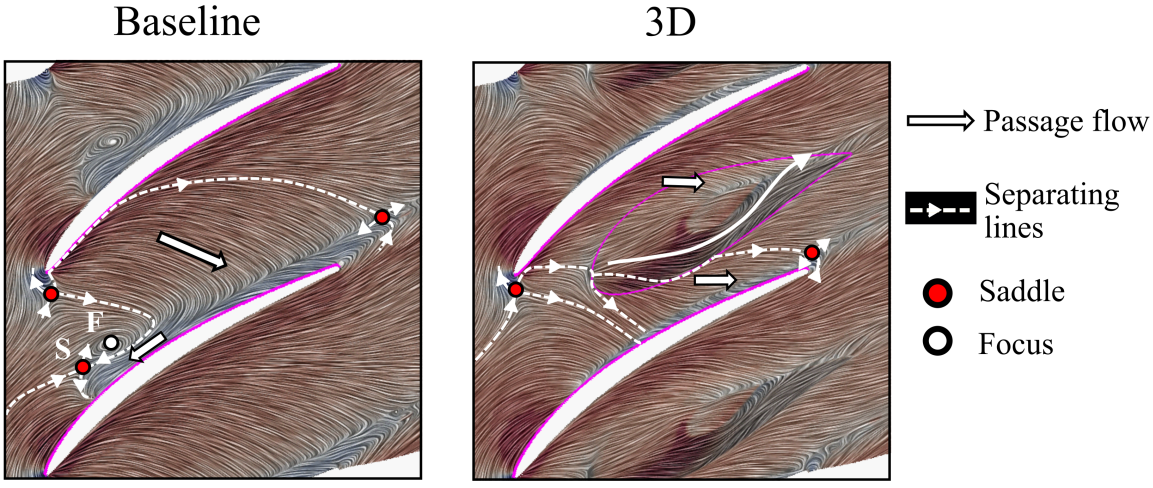

Figure 8.26: Topological organisation. Baseline vs 3D guide fin (i=4.9°).

Effect of fence To better visualise the fluid motion near the hub, streamlines seeded 1.5 mm away from the hub at the axial position the stator leading edge are generated (see Figure 8.27). The passage flow appears to be split in three regions. The guide fin blocks the portion 1 of the passage flow and deflects it back towards the stator pressure side. The 3D guide fin therefore acts as a fence. The portion 2 seems guided along the guide fin pressure side. The portion 3 reaches the stator suction side and joins the stator corner separation. This visualisation shows that the loss patterns observed downstream of the row are due to the passage flows of the portions 1 and 3. Notably, the loss pattern corresponding to the guide fin wake results from the corner separation occurring on the guide fin suction side. The portion 2 of the passage flow is investigated hereafter.

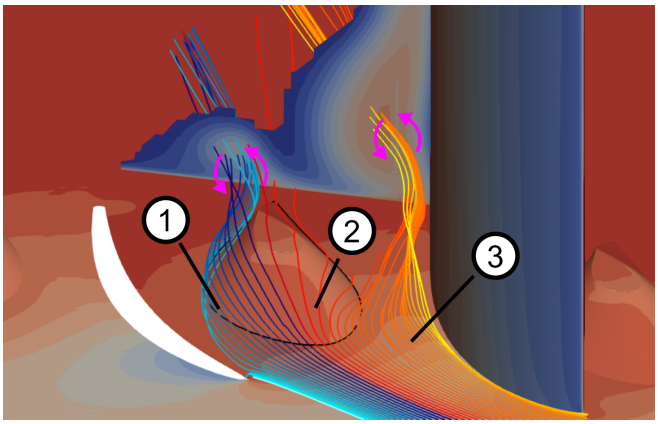

Figure 8.27: Effect of the guide fin 3D on near hub streamlines. Streamlines are seeded 1.5 mm away from the hub and coloured with their ID. The solid surfaces are coloured with $C_{p,s}$.

Guiding effect The portion 2 of the incoming passage flow is deflected along the pressure side of the 3D guide fin. This deflection creates a pressure drop by effect of positive incidence. Figure 8.28 shows the distribution of the pressure rise coefficient ($C_{p,s}$) on the hub. This pressure drop induces a favourable adverse pressure gradient, and a transverse gradient in the opposite direction than the one imposed by the stator. The first gradient tends to accelerate the flow in the axial direction and energises the boundary layer, while the second one reduces the local over deflection. These beneficial effects are combined with the increasing blockage induced by the guide fin, that globally accelerates the near hub flow. Downstream of this pressure drop, the guide fin blockage decreases and the boundary layer developing on the guide fin thickens. However, the flow remains attached and is guided far away from the stator suction side.

A beneficial effect of the pyramidal aspect is noticed. The apparent curvature of the leading edge is lowered, thus facilitating the flow deflection. Moreover, the increasing blockage accelerate the near hub flow and makes it less prone to separate. The pyramidal aspect therefore favours the implementation of the guiding effect.

The guiding effect and the effect of fence are retrieved experimentally. Figure 8.29 shows the distribution of total pressure (ω) and of pitchwise angle fluctuation about midspan ($\beta - \beta_{MID}$) at design and high incidences. β_{MID} corresponds to the average value of the pitchwise angle at midspan. The guide fin height is indicated (black dotted line) as well as the passage vortices (purple arrow). At both incidences, the guide fin wake is detached from the stator corner separation. It is associated to a vortex and extends on the whole guide fin height, thus confirming that it originates from a corner separation occurring on the guide fin suction side. The guided region (of low over deflection, denoted by 2) is visible, and splits the passage flow

in three distinct regions. This guide fins therefore creates two passage vortices and isolates the stator suction side from the passage flow portions 1 and 2, as predicted with the RANS.

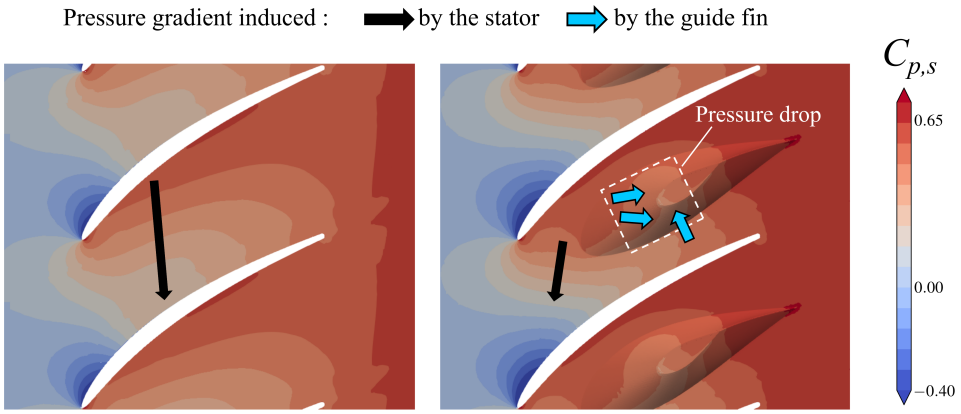

Figure 8.28: Illustration of beneficial gradients induced by guide fin 3D at i=4.9°. Baseline (left) vs 3D guide fin (right).

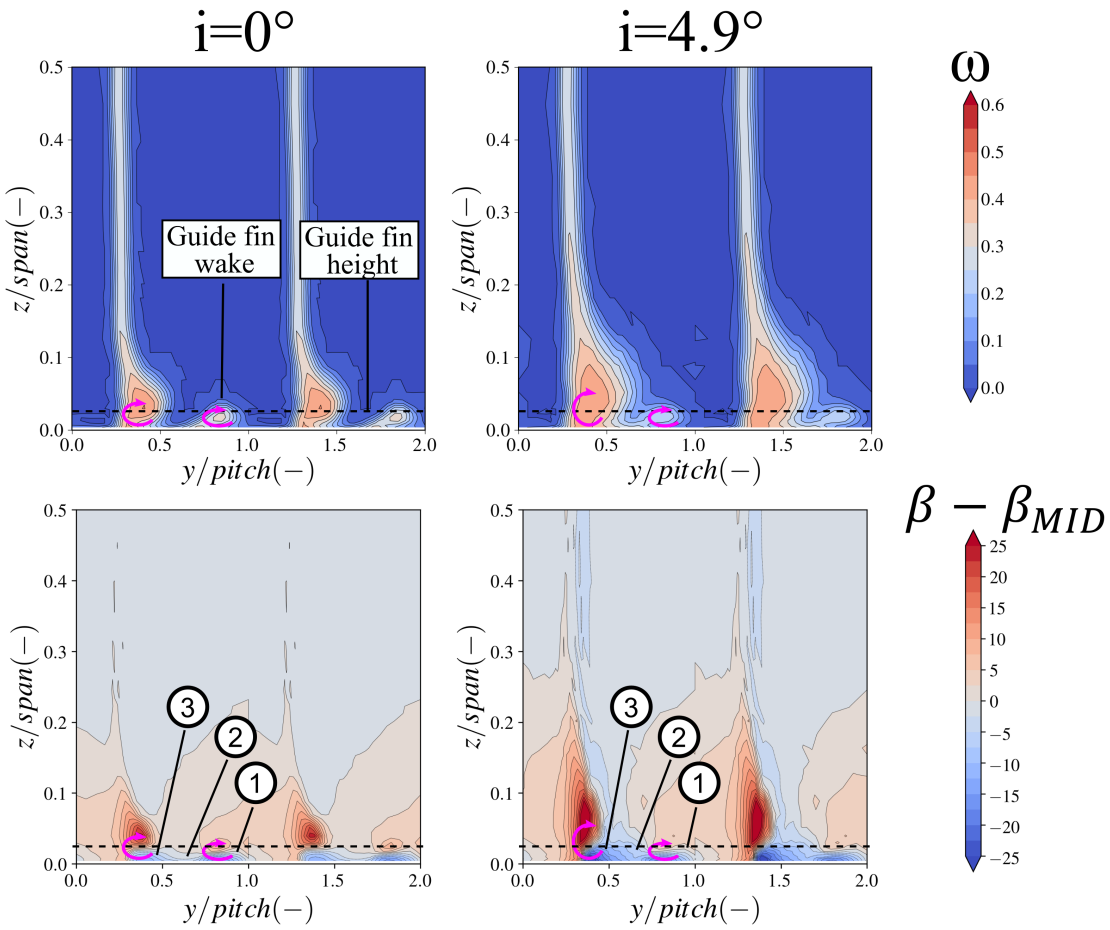

Figure 8.29: Experimental data : total pressure losses and pitchwise angle fluctuations at design and high incidences with guide fin 3D. Purple arrows : passage vortices. Black line : guide fin height.

8.3.3 Effect on downstream profiles

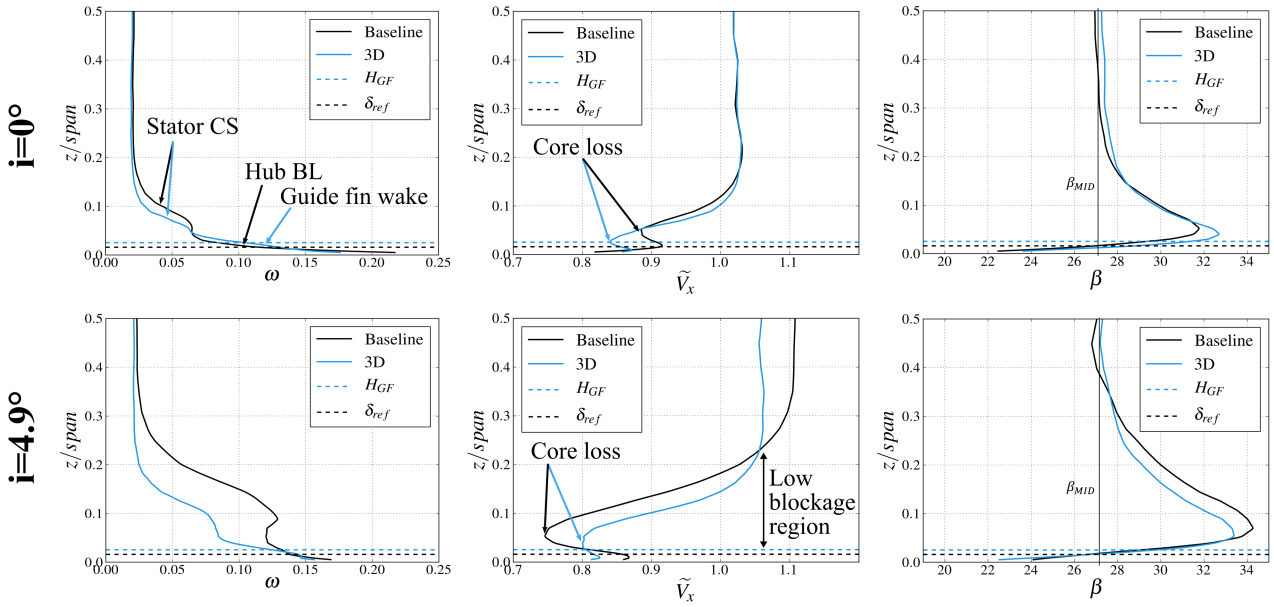

Figure 8.30: Experimental profiles in the measurement planes. 3D guide fin vs Baseline. CS : Corner Separation. BL : Boundary Layer. H_{GF} : Guide fin height. δ_{ref} : inlet boundary layer thickness.

The radial profiles obtained downstream of the 3D guide fin are compared to the baseline configuration in Figure 8.30. The experimental radial profiles of ω, $\widetilde{V_x}$ and β are evaluated. As for the SF and LF guide fin, the guide fin height (H_{GF}) and the inlet boundary layer thickness (δ_{ref}) are added, and the core loss is localised with the zone of maximum blockage.

At design incidence, the losses due to the stator corner separation are reduced and their radial evolution is smoothed out. However, the losses generated by guide fin wake exceed the losses generated with the boundary layer developing on the hub without guide fin. The evolution of $\widetilde{V_x}$ reveals a larger blockage near the hub. This blockage is induced by the guide fin wake. Consistently, the core loss position is lowered and is imposed by the guide fin tip position. Finally, adding the guide fin slightly increases the pitchwise flow angle (β), with a maximum increase of about 1° in the region of under deflection.

At high incidence, these behaviours are retrieved but are enhanced. The guide fin largely reduces the corner separation losses. It is worth noticing that the losses in the region below the guide fin height (guide fin wake) features a similar level of losses than at design incidence. The increase in losses between design and high incidence is therefore mainly due to the growth of the stator corner separation and not to the guide fin wake. At high incidence, a decrease in blockage is observed when adding the guide fin. In the midspan region, the extent of the region of uniform axial velocity is enlarged, with lower values. However, the decrease in blockage only occurs above the guide fin height (black arrow) which still reveal the blockage due to the guide fin wake. Consequently, the pitchwise angle values are reduced in this region. Interestingly, the maximum values of β remains similar between i=0° and i=4.9° when adding the guide, thus improving the robustness of β to the incidence.

8.3.4 Summary

This guide fin efficiently reduces the losses on a large range of incidence. It acts as a fence that prevents a portion of the passage flow to reach the stator suction side. More importantly, its three dimensional shape induces a depression on its pressure side, which locally reverse the transverse and adverse pressure gradients. This effect of incidence reduces the strength of the passage flow and helps evacuating the low momentum fluid downstream without reaching the stator suction side. This guide fin features several advantages, such as monotonous gradients of ω and $\widetilde{V_x}$ near the hub, a large region of uniform flow near midspan and maximum values of β robust to a variation of the incidence. However, a corner separation occurs on the guide fin suction side, inducing a zone of high loss and low momentum near the hub downstream of the stator.

8.4 Influence of the inlet boundary layer

The inlet boundary layer has a significant influence on the strength of the secondary flows and on the size on the corner separation (see Section 1.4.1). Indeed, the transverse pressure gradient is mostly set with the midspan behaviour, and is little affected by the boundary layer thickness. Increasing the boundary layer thickness therefore increases the amount of low momentum fluid driven by the same pressure gradients, thus causing stronger secondary flows and a larger corner separation. In this section, the sensitivity of the endwall losses to the boundary layer displacement thickness is evaluated on the baseline and guide fin configurations with RANS computations. The hub viscous boundary condition upstream of the stator leading is extended so that the inlet displacement thickness is doubled. Figure 8.31 gathers the endwall evolution with the incidence for the baseline and guide fins configuration for the initial boundary layer thickness (δ_{ref}) and the doubled boundary layer thickness ($2\delta_{ref}$).

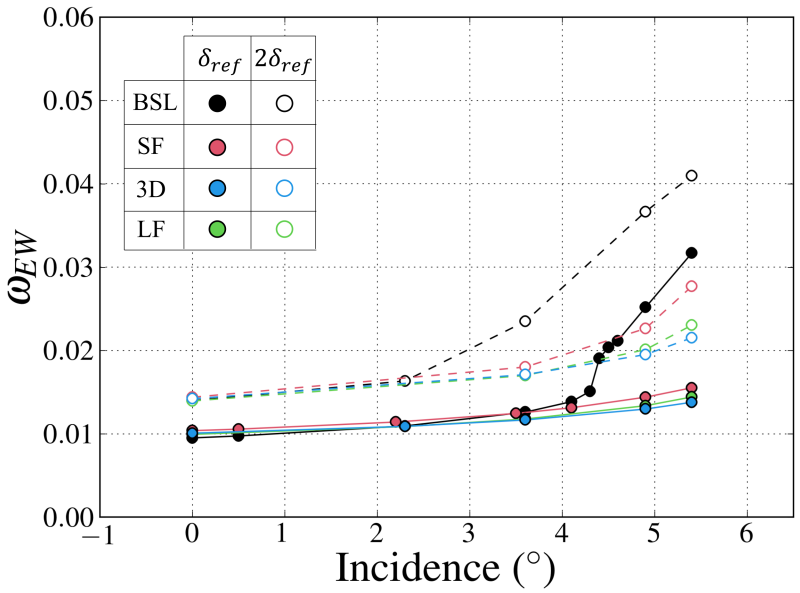

Figure 8.31: Evolution of the endwall losses when doubling the inlet boundary layer thickness. RANS results. BSL : Baseline configuration.

Incidence	SF	LF	3D
0	0.04%	0.00%	0.02%
4.9	-1.40%	-1.66%	-1.71%

Table 8.4: Gains with doubled inlet boundary layer thickness. RANS results.

Incidence	BSL	SF	LF	3D
0	0.46%	0.40%	0.40%	0.41%
4.9	1.24%	0.82%	0.67%	0.65%

Table 8.5: Variations in endwall losses when doubling the inlet boundary layer thickness. RANS results.

Let us first investigate the baseline configuration. Increasing the inlet boundary layer thickness greatly increases the endwall losses on the whole range of incidence. Notably, at design incidence the losses are increased from 0.94% (δ_{ref}) to 1.40% ($2\delta_{ref}$). Moreover, the corner separation features a single sided topology at i=2.3° and a double sided topology at i=3.6°. The critical incidence is thus comprised within [2.3°, 3.6°]. Increasing the inlet boundary layer thickness therefore lowers the critical incidence value, consistently with what is observed by Dawkins et al. (2021).

With the increased boundary layer thickness, adding any of the SF, LF or 3D guide fin still greatly lower the endwall losses. Notably, the design losses are similar to the baseline case and the gains at i=4.9°are increased (see Table 8.4). The relative efficiency of the guide fin is maintained, with the 3D guide fin being the most efficient, followed by the LF one and finally the SF guide fin. However, the SF guide fin appears less robust to the variation of the boundary layer thickness than the other ones (see relative loss increase, Table 8.5).

Finally, it is observed that the same beneficial mechanisms are implemented by each guide fin. Doubling the boundary layer thickness does not affect the topology of the flow in these configurations, thus explaining that the gains brought with the guide fins are conserved. However, $2\delta_{ref}$ roughly correspond to the height of the investigated guide fins. If the thickness of the inlet boundary layer is further increased, the mechanisms relying on the incorporation of high velocity fluid near the hub might be altered (effect of fence, effect of tip vortex). In this case, increasing the guide fin height might help recovering the beneficial effects of these mechanisms. The identification of the relation between the guide fin height and the inlet boundary layer thickness thus appears as an interesting perspective to this work.

8.5 Summary

In this last section, important results discussed on each guide fins are gathered. They allow to draw conclusions on two aspects : the use of RANS for designing a mean of control (methodological aspect) and the physical mechanisms that efficiently reduces the corner separation (design aspect).

8.5.1 Relevance of RANS in the guide fin design process

In this work, the ability of RANS to evaluate the corner separation phenomenon was an omnipresent question. In this chapter, experimental investigations bring material to evaluate the predictability of RANS in various corner separation configurations.

Reliability of the integrated losses predicted by RANS

The predictability of RANS predictions was discussed for each guide fin in their dedicated sections. The endwall losses and gains of all the configurations tested experimentally are gathered and compared with one another.

The predictions of gains are first evaluated (see Figure 8.32a). RANS computations predict that adding any of the tested guide fins increases the losses at design incidence to a small extent and brings a large gain at high incidence. At high incidence, large gains are indeed retrieved experimentally. Their absolute values is either correctly or under predicted with RANS, and the ranking of the high incidence gain is conserved (3D better than LF, itself better than SF). On the other hand, the guide fins SF and 3D feature an unexpected gain at design incidence. Interestingly, the increase in losses induced by the LF guide fin is well retrieved. The LF guide fin is therefore predicted to be the best one to lower the losses at design incidence, and is actually the worst. As such, the ranking of the gains is not preserved at design incidence. However, it is preserved at high incidence. On both incidence, the gains are either correctly or under predicted in RANS, which is sufficient enough for design perspectives.

The values of endwall losses are then used to evaluate the absolute predictability of RANS (see Figure 8.32b). This predictability is here measured as the distance between the experimental and RANS endwall losses at design and high incidences (dashed arrows). RANS computations systematically fail to predict the correct absolute values of endwall losses. However, the discrepancy between the experimental and RANS results is reduced when adding any of the tested guide fins.

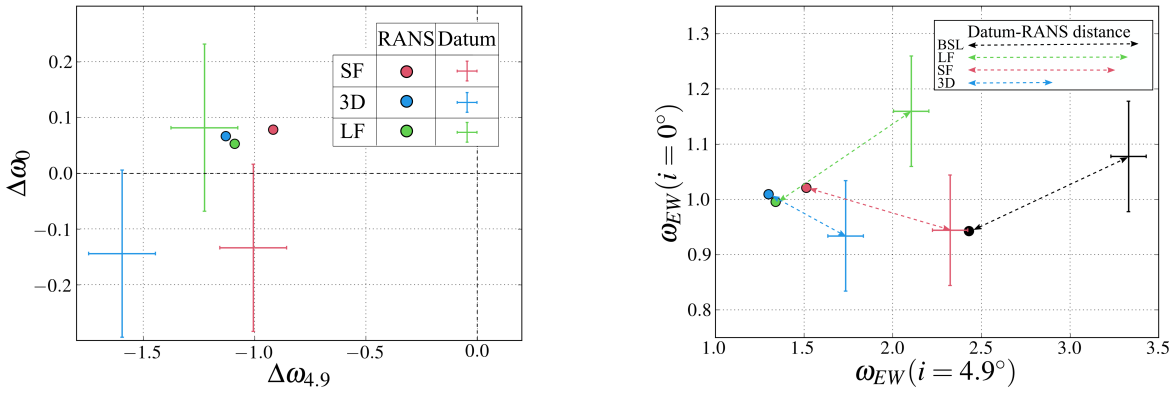

(a) Gains (objective functions).

(b) Integrated losses.

Figure 8.32: RANS predictability : experimental integrated losses and gains vs RANS predictions for guide fins SF, LF and 3D. BSL : Baseline configuration.

Validation of the hypothesis used in the design process

Because of the difficulties of RANS modelling to predict corner separation, the design process implemented in this work relied on the following hypothesis : RANS modelling is more reliable when the corner separation is smaller. An immediate consequence of this hypothesis is that a guide fin that reduces the corner separation according to RANS should reduce the corner separation experimentally. This hypothesis is now validated based on the four following aspects :

- The absolute predictability is improved when adding any of the tested guide fin.
- The evolution of the endwall losses with the incidence is better retrieved when adding a guide fin.

- The investigation of downstream cartographies revealed specific loss and deflection patterns well retrieved in RANS.
- The analysis of RANS flow field revealed plausible physical mechanisms explaining their beneficial effect.

Finally, it is noticed that the 3D guide fin best reduces the corner separation and is the one that features the best predictions on these aspects. The validation of this hypothesis justifies *a posteriori* the use of RANS in the design process implemented in this work.

Comments on the single sided and double sided topologies

The numerical artefact of the topological switch was clearly identified from the beginning of this work. In spite of this artefact, the numerical methodology implemented enabled to provide efficient guide fins and to interpret their effects on the flow.

However, the single sided topology makes the sensitivity analysis more complex. Indeed, the single sided topology artificially forces the flow field to remain in a low loss configuration of similar level regardless of the configuration at stake. This appears in Figure 8.31, by comparing the baseline losses before the critical incidence and the guide fin losses on the whole range of incidence. These similar values of losses are unrealistic as the three guide fins feature very different values of experimental gains at high incidences. The experimental variation of endwall losses are therefore under predicted when changing the guide fin. Consequently, the endwall loss variation predicted by RANS when varying a single parameter might as well be under predicted, and requires additional validations.

Finally, it is interesting to underline that the double sided topology is not in itself problematic. Experimentally, the separated region near the hub is characterised with several pairs of moving critical points (Dawkins et al., 2021). The stationary aspect of RANS computations produces a single Saddle/Focus pair at a specific location. Even though this is unrealistic, this pair of critical points highlights the flow field region to which corner separation is the most sensitive. In this work, the SF and LF guide fins are found to be positioned near the Saddle/Focus pair, and the corner separation magnitude is much influenced by this position (see Figure 8.33). As such, the double sided topology predicted in RANS indicates a region where a mean of control is likely to efficiently act on the corner separation.

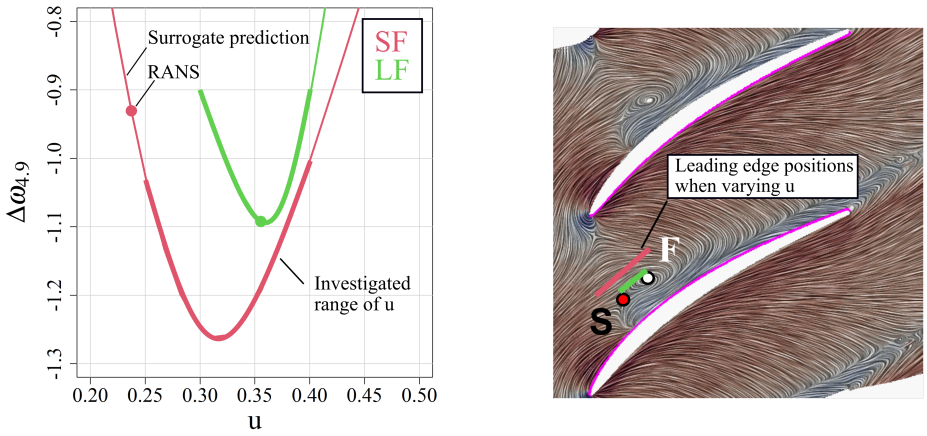

Figure 8.33: Left : Sensitivity of $\Delta\omega_{4.9}$ to the streamwise position of the guide fin leading edge (parameter u). Surrogate models and RANS predictions. Right : Positions corresponding to the investigated range of u, with respect to the Saddle/Focus pair observed on the baseline configuration at i=4.9°.

8.5.2 Beneficial mechanisms reducing corner separation

The investigations of the three guide fins revealed specific beneficial mechanisms, which are summarised hereafter.

SF guide fin The SF guide fin is positioned near the Saddle/Focus pair, is characterised with a short chord and features a pressure difference between its suction and pressure side. It is characterised with the following mechanisms :

- **Effect of fence :**
  - Guides the near hub flow along the guide fin suction side.
  - Ejects the near hub flow radially because of the passage vortex appearing on the guide fin suction side.
  - Energises the near hub flow because of the passage vortex appearing on the guide fin pressure side.
- **Effect of tip vortex :**
  - Limits the azimuthal extension of the passage vortex because of the induced radial migration (ascending component).
  - Energises the near hub flow by mixing effect (descending component).

The effect of tip vortex induces a stronger over deflection at hub. Moreover, the velocity gradients are increased near the hub, which induces additional losses by mixing effect.

LF guide fin The LF guide fin is positioned near the Saddle/Focus pair, is characterised with a long chord and yields a pressure distribution on the hub close to the midspan one. It is characterised with the same effect of fence than the SF guide fin, but acts on a longer distance. In this case, the passage flow coming from the stator pressure side is totally replaced with the energised fluid because of the passage vortex appearing on the guide fin pressure side. However, the LF guide fin increases the losses at design incidence with respect to the baseline case. This increase might be caused by a separation in the leading edge region, due to the low value of the hub leading edge metal angle.

3D guide fin The 3D guide fin features a thick and long hub aerofoil and is characterised with a strong pyramidal aspect. Its pressure side features a pressure drop located at mid pitch and in the downstream portion of the row (at an axial position of 0.53c). This guide fin is the best one output by the optimisation process and tested experimentally. It is characterised with the following mechanisms :

- **Effect of fence :**
  - Deflection of a portion of the passage flow with the guide fin suction side. Induces a passage vortex that does no interact with the stator corner separation.
- **Effect of three-dimensional shape :**
  - Acceleration of the near hub flow by effect of progressive blockage.

  - Near hub flow deflection facilitated by reduction of the guide fin apparent curvature.

- **Effect of local pressure drop :**
  - Reorientation of the flow in the axial direction by local cancellation of transverse and/or adverse pressure gradients.

However, the 3D guide fin induces two distinct zones of high losses that are convected downstream of the row (stator and guide fin corner separations). Moreover, it features a large solid blockage, which might be detrimental if envisioned in a context of transonic flows.

Note on guide fins and other passive means of control : In the light of the physical mechanisms implemented by these guide fins and of their geometrical characteristics, the SF, LF and 3D guide fins can be placed among existing families of mean of control. The SF guide fin acts as a Vortex Generator, the LF guide fin as a fence and the 3D guide fin is close to the 3D endwall contouring technique (see Section 1.4.4). However, they correspond to optimised geometries for the baseline configuration studied, while no generic and precise design rules are available for any of these means of control. Moreover, this work shows that these effects can be combined, notably with the SF guide fin (effect of fence and of vortex generator).

Finally, this chapter detailed elementary effects implemented by these mechanisms of fence, vortex generator and 3D contouring. All these elementary effects are beneficial for reducing the corner separation, and can be gathered into two means of action on the passage flow. These means of action consist in either energising the passage flow or guiding the passage flow towards downstream. Table 8.6 summarises these results, and highlights that the three guide fin investigated use both means of action. The reduction of the corner separation through these means of action is consistent with the commonly accepted origin of the corner separation : the accumulation of low momentum fluid in the corner region.

Mean of action	Elementary effect	Nature	Consequence	Guide fin
Guiding the passage flow	Local pressure drop	Aerodynamic	Favourable adverse/transverse gradient	3D
	Solid barrier	Solid	Increases passage flow deflection	SF, LF, 3D
Energising the passage flow	Passage vortex on guide fin pressure side	Aerodynamic	Brings high momentum fluid to the passage flow	SF
	Ascending component of tip vortex	Aerodynamic	Removes low moment fluid from the passage flow	SF, LF
	Descending component of tip vortex	Aerodynamic	Brings high momentum fluid to the passage flow	3D
	Solid blocage	Solid	Induces a thinner hub boundary layer	SF
	Radial migration induced by guide fin corner separation	Solid	Removes low moment fluid from the passage flow	SF, LF, 3D

Table 8.6: Elementary effects reducing the corner separation.

Chapter 9

Conclusion and Perspectives

The aim of this thesis was to assess the potential of a passive technological effect (guide fins) to reduce the detrimental effects caused by the phenomenon of corner separation. A numerical and experimental explorations are carried out for that purpose, and guide fins efficient at reducing corner separation are revealed and analysed. In this section, main results are first summarised and recommendations for future work are then discussed.

9.1 Conclusion

The effect of various guide fin shapes on corner separation are evaluated through a complex numerical chain and an experimental campaign. The numerical exploration relies on RANS computations performed with a hybrid meshing technique, using the QCR (Quadrative Constitutive Relation) correction. A parametrisation including aerodynamic constraints and based on 15 parameters is implemented to define guide fin shapes. The guide fin shapes are then optimised through an innovative coupling with Kriging surrogate models that are iteratively refined. Nearly 1000 guide fin geometries are evaluated at design and high incidences with this process. The resulting large RANS database contains numerous guide fins that efficiently reduce the corner separation magnitude.

Corner separation originates from near hub flow interactions, which are ill predicted with RANS modelling (with Boussinesq hypothesis) because of their highly anisotropic nature. This is believed to be the origin of the topological switch artefact. This artefact consists in the sudden apparition of a separated zone on the hub across a critical incidence, and induces a drastic increase in the endwall losses. The QCR correction successfully improves the prediction of the secondary flows and reduces the impact of the topological switch. This study shows that a) RANS successfully detects efficient guide fins in spite of this limitation, which legitimate the use of RANS within an optimisation process b) the topological switch is a fundamental limit of RANS for finely comparing efficient guide fins.

With these evaluations, guide fins that efficiently lower the high incidence total pressure losses with no degradation at design incidence are found. Three guide fin families of specific geometrical characteristics are defined : the Short Fence (thin aerofoil, short chord), Long Fence (thin aerofoil, long chord) and 3D families (strong pyramidal aspect, long chord). For all families, 6 principal parameters of particularly strong influence are detected :

- $\Delta\beta_{1,H}$: leading edge metal angle of the hub aerofoil (relative to the local stator camber)
- $t_{M,H}$: hub aerofoil thickness

- $c_{GF,H}$: hub aerofoil chord
- u: streamwise position of the hub leading edge
- v: pitchwise position of the hub leading edge
- H_{GF}: guide fin height

The efficient guide fins of each family are characterised with specific ranges of these parameters. The sensitivity of high incidence gains to these parameters is assessed with evaluations of the refined surrogate model. The gains obtained at high incidence are most sensitive to the hub leading edge streamwise position (u) and the guide fin height (H_{GF}).

A representative guide fin of each family is selected, manufactured and tested experimentally (SF-03, LF-A and 3D-01). Strong gains are measured, with a variation in endwall losses up to -0.14% at design incidence and -2.94% at near-stall incidence. These gains validate the optimisation methodology and the potential of the guide fin technology. The beneficial mechanisms implemented with these guide fins are then investigated through RANS results, and validated experimentally. Adding a guide fin necessarily splits the channel into two sub channels in the near hub region, and a passage flow develops in each sub channel. On the guide fin suction side, the passage flow is deflected back towards the stator pressure side. On the guide fin pressure side, the passage flow brings high momentum fluid from the bulk flow to the near hub region, towards the stator suction side. The LF-A guide fin uses this mechanism (effect of fence) to incorporate high velocity fluid on a long portion of the stator chord. The SF-03 and 3D-01 guide fins implement additional mechanisms. The SF-03 guide fin mixes high velocity fluid from the bulk flow to the passage flow (effect of tip vortex). The 3D-01 guide fin locally reduces the adverse and transverse pressure gradient (effect of local pressure drop), which helps guiding the passage flow towards downstream.

As a summary, all the elementary beneficial mechanisms implemented with these guide fins participate to reducing the corner separation magnitude through two means of actions : a) energising the passage flow that reaches the stator suction side and b) better guiding the passage flow.

The large gains and the explanations of the beneficial effects implemented with these guide fins reveal the potential of such a technology, whose efficiency should be assessed on more realistic configurations. Notably, the gains observed might be lower in a configuration where the corner separation is already optimised with conventional methods (stator with fillets, stator with lean, other 3D blading of the stator). Guide fins could thus be envisioned as a way to get a similar corner separation magnitude while releasing constraints on the stator design. A coupled design of the stator and the guide fin should thus be considered, and constitutes an interesting field of research to improve the performance of future stators.

9.2 Perspectives

The potential of the guide fins should now be assessed in more realistic flow conditions. Table 9.1 gathers the differences likely to impact the efficiency of the guide fin between the current academic configuration and a realistic stator in a modern compressor. Designing guide fins in such a different configuration is beyond the scope of the recommendations given in this manuscript. Intermediate configurations with partly academic, partly realistic conditions

should be investigated. This might be challenging experimentally, and complementary preliminary numerical investigations should be carried out. As an example, a RANS investigation of the effect of doubling the inlet boundary layer thickness was performed and shows encouraging results. The effect of compressibility is also evaluated with a similar investigation (see Figure 9.1). All guide fins efficient in incompressible flow condition (M=0.11) are efficient in intermediate compressible conditions (M=0.47), showing here again encouraging results.

This work proved that RANS modelling could bring fruitful information for designing efficient guide fins. However, high fidelity methods (LES, LES-LBM) would yield additional interesting results and should be considered for future studies. Firstly, these methods would remove the topological artefact, which notably under predicts the relative gain between two efficient guide fins. Using high fidelity methods would thus allow to compare more reliably the robustness of each guide fin to a modification of the characteristics gathered in Table 9.1. Secondly, the methodology of Design Of Experiment / Kriging surrogate model can now be implemented on a restricted number of influential parameters, on a new configuration. If the cost of the high fidelity method is not prohibitive (budget of the order of ten computations) this methodology will yield efficient guide fins, whose gains will be reliably predicted.

Finally, guide fins necessarily modifies the dynamic of the corner separation topology. Dawkins et al. (2021) highlights with experimental measurements that the separation at hub occurs on a region defined by the stochastic apparition of numerous pairs of critical points. The interaction between the guide fin and this region raises numerous questions : Is the apparition frequency of the critical pairs modified along the tip vortex path ? Can the sensitivity to the leading edge streamwise position be explained ? How is this region modified in the sub channel between the guide fin pressure side and stator suction side? These questions require a time resolved study of the hub/blade boundary layer interaction, which is challenging even for high fidelity methods. Experimental campaigns are therefore necessary to tackle this issue, and on a more general basis, to reveal the true mechanisms at the origin of the phenomenon of corner separation.

	Current configuration	Realistic configuration
Reynolds number	3.2×10^5	$\sim 1 \times 10^6$
Inlet BL : thickness	Thin	Thin to thick
Inlet BL : skewness	None	Skewed
Upstream wake	None	Periodic rotor wake
Flow compressibility	Incompressible flow (M=0.11)	Compressible flow (M>0.6)
Presence of shock waves	None	Possible
Stator geometry	No stacking law, one aerofoil	3D blading
Hub geometry	Planar	Annular

Table 9.1: Comparison between academic and realistic configurations. Characteristics likely to alter the guide fin efficiency. BL : Boundary Layer.

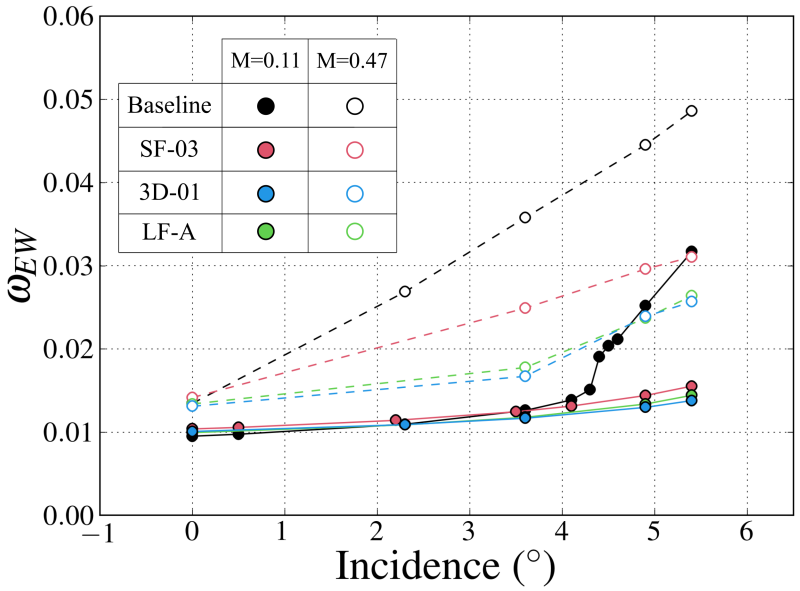

Figure 9.1: Evaluation of the baseline configuration and SF-03, LF-A and 3D-01 guide fins under compressible flow conditions. Evolution of the endwall total pressure losses (ω_{EW}) with the incidence. The inlet Mach number (M) varies between 0.11 and 0.47. The inlet Reynolds number is kept constant so that a similar boundary layer thickness develops on the hub and on the stator blades.

References

Ashrafpour, E. (2021). Document on ResearchGate profile : Difference between Simple Kriging and Ordinary Kriging.

Auchoybur, K. and Miller, R. (2018). The sensitivity of 3D separations in multi-stage compressors. Journal of the Global Power and Propulsion Society, 2:34C05T.

Bailie, S. T., Hile, G., and Puterbaugh, S. (2008). Initial characterization of three-dimensional flow separation in a compressor stator. In 44th AIAA/ASME/SAE/ASEE Joint Propulsion Conference & Exhibit, page 5064.

Barankiewicz, W. S. and Hathaway, M. D. (1998). Impact of Variable-Geometry Stator Hub Leakage in a Low Speed Axial Compressor. In ASME 1998 International Gas Turbine and Aeroengine Congress and Exhibition, Stockholm, Sweden.

Beselt, C., Eck, M., and Peitsch, D. (2014). Three-Dimensional Flow Field in Highly Loaded Compressor Cascade. Journal of Turbomachinery, 136(10):101007.

Beselt, C., Pardowitz, B., van Rennings, R., Sorge, R., Peitsch, D., Enghardt, L., Thiele, F., Ehrenfried, K., and Thamsen, P. U. (2013). Influence of the clearance size on rotating instability in an axial compressor stator. In Proceedings of the 10th European Conference on Turbomachinery Fluid Dynamics and Thermodynamics ETC, volume 10, pages 15–19.

Binois, M. and Picheny, V. (2019). GPareto: An R Package for Gaussian-Process-Based Multi-Objective Optimization and Analysis. Journal of Statistical Software, 89(8):1 – 30. Section: Articles.

Bolger, J. J. (1999). Three dimensional design of compressor blades. PhD Thesis, University of Cambridge.

Bordji, M. (2015). Analyse physique et simulations numériques avancées des écoulements de jonction sur les avions. PhD thesis, Université Pierre et Marie Curie.

Boudet, J., Lévêque, E., and Touil, H. (2022). Unsteady Lattice Boltzmann Simulations of Corner Separation in a Compressor Cascade. Journal of Turbomachinery, 144(1):011010.

Boussinesq, J. (1877). Essai sur la théorie des eaux courantes. Impr. nationale.

Box, G. E. P. and Wilson, K. B. (1951). On the Experimental Attainment of Optimum Conditions. Journal of the Royal Statistical Society. Series B (Methodological), 13(1):1–45. Publisher: [Royal Statistical Society, Wiley].

Brendel, T., Heutling, F., Eichmann, W., Ücker, M., and Uihlein, T. (2008). MTU Solutions Against Erosive Attack and Loss of EGT Margin in Turbo Engines—ERCoatnt. The Engine Yearbook 2008.

Chen, Y., Welling, M., and Smola, A. (2010). Super-Samples from Kernel Herding. pages 109–116, Catalina Island, CA. AUAI Press.

Chen, Y., Yang, L., and Zhong, J. (2019a). Control of secondary crossflow in a high-speed compressor cascade by endwall fences with varying locations. Proceedings of Global Power and Propulsion Society, page 8.

Chen, Y., Yang, L., and Zhong, J. (2019b). Numerical study on endwall fence with varying geometrical parameters in a highly-loaded compressor cascade. Aerospace Science and Technology, 94:105390.

Chima, R. V. (2002). Computational Modeling of Vortex Generators for Turbomachinery. In Volume 5: Turbo Expo 2002, Parts A and B, pages 1229–1238, Amsterdam, The Netherlands. ASMEDC.

Cho, J., Kim, K., Kim, J., and Jeong, E. (2011). Controlling the secondary flows near endwall boundary layer fences in a 90° turning duct using approximate optimization method. Journal of Mechanical Science and Technology, 25(8):2025–2034.

Coello Coello, C. A. and Reyes Sierra, M. (2004). A study of the parallelization of a coevolutionary multi-objective evolutionary algorithm. In Mexican international conference on artificial intelligence, pages 688–697. Springer.

Collette, Y. and Siarry, P. (2004). Multiobjective Optimization. Decision Engineering. Springer Berlin Heidelberg, Berlin, Heidelberg.

Courtiade, N. (2012). Experimental analysis of the unsteady flow and instabilities in a high-speed multistage compressor. PhD thesis, Ecole Centrale Lyon.

Cumpsty, N. A. (1989). Compressor aerodynamics. Longman Scientific & Technical.

Da Veiga, S. (2019). Optimisation - Formation Interne Safran.

Dawkins, I. (2021). The Unsteady Topology of Corner Separations. Thesis, University of Cambridge.

Dawkins, I., Taylor, J., Ottavy, X., and Miller, R. (2021). The Unsteady Topology of Corner Separations. Proceedings of ASME Turbo Expo 2021, page 17.

De Haller, P. (1953). Das verhalten von tragflügelgittern in axialverdichtern und im windkanal. Brennstoff-Wärme-Kraft (BWK), 5(333):24.

Deb, K., Pratap, A., Agarwal, S., and Meyarivan, T. (2002). A fast and elitist multiobjective genetic algorithm: NSGA-II. IEEE Transactions on Evolutionary Computation, 6(2):182–197.

Denton, J. D. and Xu, L. (1998). The exploitation of three-dimensional flow in turbomachinery design. Proceedings of the Institution of Mechanical Engineers, Part C: Journal of Mechanical Engineering Science, 213(2):125–137.

Dixon, S. (1998). Fluid Mechanics, Thermodynamics of Turbomachinery. Pergamon Press Ltd, 4th edition.

Dorfner, C., Hergt, A., Nicke, E., and Moenig, R. (2011). Advanced Nonaxisymmetric Endwall Contouring for Axial Compressors by Generating an Aerodynamic Separator—Part I: Principal Cascade Design and Compressor Application. Journal of Turbomachinery, 133(2).

Drela, M. (1985). Two-dimensional transonic aerodynamic design and analysis using the Euler equation. PhD thesis, Massachusetts Institute of Technology.

Duquesne, P., Chanéac, J., Mondin, G., and Dombard, J. (2022). Topology Rule-Based Methodology for Flow Separation Analysis in Turbomachinery. International Journal of Turbomachinery, Propulsion and Power, 7(3):21. Number: 3 Publisher: Multidisciplinary Digital Publishing Institute.

Délery, J. (2013). Three-dimensional separated flow topology: critical points, separation lines and vortical structures. Chapter 2. John Wiley & Sons.

Délery, J. M. (2001). Robert Legendre and Henri Werlé: Toward the Elucidation of Three-Dimensional Separation. Annual Review of Fluid Mechanics, 33(1):129–154.

Emmerich, M., Giannakoglou, K., and Naujoks, B. (2006). Single- and multiobjective evolutionary optimization assisted by Gaussian random field metamodels. IEEE Transactions on Evolutionary Computation, 10(4):421–439. Conference Name: IEEE Transactions on Evolutionary Computation.

Emmerich, M. T. M., Deutz, A. H., and Klinkenberg, J. W. (2011). Hypervolume-based expected improvement: Monotonicity properties and exact computation. In 2011 IEEE Congress of Evolutionary Computation (CEC), pages 2147–2154. ISSN: 1941-0026.

Encyclopedia2 (2022). https://encyclopedia2.thefreedictionary.com/boundary-layer+flow.

Flegg, G. C. (1974). From Geometry to Topology. London, english universities press edition.

Gallimore, S. J., Bolger, J. J., Cumpsty, N. A., Taylor, M. J., Wright, P. I., and Place, J. M. (2002). The use of sweep and dihedral in multistage axial flow compressor blading—Part I: University research and methods development. J. Turbomach., 124(4):521–532.

Gand, F., Deck, S., Brunet, V., and Sagaut, P. (2010). Flow dynamics past a simplified wing body junction. Physics of Fluids, 22(11):115111.

Gao, F., Ma, W., Sun, J., Boudet, J., Ottavy, X., Liu, Y., Lu, L., and Shao, L. (2017). Parameter study on numerical simulation of corner separation in LMFA-NACA65 linear compressor cascade. Chinese Journal of Aeronautics, 30(1):15–30.

Gao, F., Ma, W., Zambonini, G., Boudet, J., Ottavy, X., Lu, L., and Shao, L. (2015). Large-eddy simulation of 3-D corner separation in a linear compressor cascade. Physics of Fluids, 27(8):085105.

Gbadebo, S. (2003). Three-Dimensional Separations in Compressors. PhD thesis, University of Cambridge, UK.

Gbadebo, S. A., Cumpsty, N. A., and Hynes, T. P. (2005). Three-Dimensional Separations in Axial Compressors. Journal of Turbomachinery, 127(2):331–339.

Gbadebo, S. A., Cumpsty, N. A., and Hynes, T. P. (2008). Control of Three-Dimensional Separations in Axial Compressors by Tailored Boundary Layer Suction. Journal of Turbomachinery, 130(1):011004.

Gessner, F. B. (1973). The origin of secondary flow in turbulent flow along a corner. Journal of Fluid Mechanics, 58(1):1–25.

Godard, G. and Stanislas, M. (2006). Control of a decelerating boundary layer. Part 1: Optimization of passive vortex generators. Aerospace Science and Technology, 10(3):181–191.

Goodhand, M. N. and Miller, R. J. (2012). The Impact of Real Geometries on Three-Dimensional Separations in Compressors. Journal of Turbomachinery, 134(2):021007.

Gu, M. (2016). Robust uncertainty quantification and scalable computation for computer models with massive output. PhD Thesis, Duke University.

Gu, M., Wang, X., and Berger, J. O. (2018). Robust Gaussian stochastic process emulation. The Annals of Statistics, 46(6A):3038–3066. Publisher: JSTOR.

Hah, C. and Loellbach, J. (1999). Development of hub corner stall and its influence on the performance of axial compressor blade rows. Journal of Turbomachinery.

Hardy, R. L. (1971). Multiquadric equations of topography and other irregular surfaces. Journal of Geophysical Research (1896-1977), 76(8):1905–1915. _eprint: https://agupubs.onlinelibrary.wiley.com/doi/pdf/10.1029/JB076i008p01905.

Harvey, N. W. (2008). Some Effects of Non-Axisymmetric End Wall Profiling on Axial Flow Compressor Aerodynamics: Part I—Linear Cascade Investigation. In Volume 6: Turbomachinery, Parts A, B, and C, pages 543–555, Berlin, Germany. ASME.

Harvey, N. W. and Offord, T. P. (2008). Some Effects of Non-Axisymmetric End Wall Profiling on Axial Flow Compressor Aerodynamics: Part II—Multi-Stage HPC CFD Study. In Volume 6: Turbomachinery, Parts A, B, and C, pages 557–569, Berlin, Germany. ASME.

Helbert, C. (2020). Cours de statistiques appliquées aux sciences de l'ingénieur - Cursus ingénieur de l'Ecole Centrale de Lyon.

Hergt, A., Meyer, R., and Engel, K. (2006). Experimental Investigation of Flow Control in Compressor Cascades. In Volume 6: Turbomachinery, Parts A and B, pages 231–240, Barcelona, Spain. ASMEDC.

Hergt, A., Meyer, R., and Engel, K. (2013). Effects of Vortex Generator Application on the Performance of a Compressor Cascade. Journal of Turbomachinery, 135(2).

Hergt, A., Meyer, R., Liesner, K., and Nicke, E. (2011). A New Approach for Compressor Endwall Contouring. Proceedings of ASME Turbo Expo, (54679):177–186.

Hergt, A., Meyer, R., Mu¨ller, M. W., and Engel, K. (2008). Loss Reduction in Compressor Cascades by Means of Passive Flow Control. In Volume 6: Turbomachinery, Parts A, B, and C, pages 269–280, Berlin, Germany. ASMEDC.

Hergt, A., Steinert, W., Dorfner, C., Nicke, E., and Beversdorff, M. (2009). Experimental and numerical investigation of a novel compressor endwall design. 7th World Conference on Experimental Heat Transfer, Fluid Mechanics and Thermodynamics, page 10.

Horlock, J. and Lakshminarayana, B. (1973). Secondary flows: theory, experiment, and application in turbomachinery aerodynamics. Annual review of fluid mechanics, 5(1):247–280. Publisher: Annual Reviews 4139 El Camino Way, PO Box 10139, Palo Alto, CA 94303-0139, USA.

Jeong, S., Murayama, M., and Yamamoto, K. (2005). Efficient Optimization Design Method Using Kriging Model. Journal of Aircraft, 42(2):413–420. _eprint: https://doi.org/10.2514/1.6386.

Johnson, M. E., Moore, L. M., and Ylvisaker, D. (1990). Minimax and maximin distance designs. Journal of Statistical Planning and Inference, 26(2):131–148.

Jones, D. R. (2001). A Taxonomy of Global Optimization Methods Based on Response Surfaces. Journal of Global Optimization, 21(4):345–383.

Jones, D. R., Schonlau, M., and Welch, W. J. (1998). Efficient Global Optimization of Expensive Black-Box Functions. Journal of Global Optimization, 13(4):455–492.

Joseph, V. R., Gul, E., and Ba, S. (2015). Maximum projection designs for computer experiments. Biometrika, 102.

Joslyn, H. D. and Dring, R. P. (1985). Axial Compressor Stator Aerodynamics. Journal of Engineering for Gas Turbines and Power, 107(2):485.

Kang, S. and Hirsch, C. (1991). Three Dimensional Flow in a Linear Compressor Cascade at Design Conditions. In ASME 1991 International Gas Turbine and Aeroengine Congress and Exposition, Orlando, Florida, USA.

Kawai, T., Shinoki, S., and Adachi, T. (1989). Secondary flow control and loss reduction in a turbine cascade using endwall fences. JSME international journal. Ser. 2, Fluids engineering, heat transfer, power, combustion, thermophysical properties, 32(3):375–387. Publisher: The Japan Society of Mechanical Engineers.

Kleijnen, J. P. C. (2009). Kriging metamodeling in simulation: A review. European Journal of Operational Research, 192(3):707–716.

Kushner, H. J. (1964). A New Method of Locating the Maximum Point of an Arbitrary Multipeak Curve in the Presence of Noise. Journal of Basic Engineering, 86(1):97–106.

Lachmann, G. V. (1961). Boundary Layer And Flow Control Its principles and applications.

Lakshminarayana, B. and Horlock, J. H. (1967). Leakage and Secondary Flows in Compressor Cascades. Technical Report 3483, Ministry of Technology: Aeronautical research council reports and memoranda.

Langston, L. (2001). Secondary Flows in Axial Turbines—A Review. Annals of the New York Academy of Sciences, 934(1):11–26. _eprint: https://onlinelibrary.wiley.com/doi/pdf/10.1111/j.1749-6632.2001.tb05839.x.

Le Riche, R. (2014). Introduction to kriging. https://hal.archives-ouvertes.fr/cel-01081304.

Lei, V.-M., Spakovszky, Z. S., and Greitzer, E. M. (2008). A Criterion for Axial Compressor Hub-Corner Stall. Journal of Turbomachinery, 130(3):031006.

LeJambre, C. R., Zacharias, R. M., Biederman, B. P., Gleixner, A. J., and Yetka, C. J. (1995). Development and Application of a Multistage Navier-Stokes Flow Solver: Part II — Application to a High Pressure Compressor Design. In ASME 1995 International Gas Turbine and Aeroengine Congress and Exposition, Houston, Texas, USA. American Society of Mechanical Engineers.

Lieblein, S., Schwenk, F., and Broderick, R. (1953). Diffusion factor for estimating losses and limiting blade loadings in axial-compressor blade elements. NACA Technical Report.

Lifshits, M. A. (1995). Gaussian Random Functions. Springer Netherlands, Dordrecht.

Lin, J., Howard, F., Bushnell, D., and Selby, G. (1990). Investigation of several passive and active methods for turbulent flow separation control. In 21st fluid dynamics, plasma dynamics and lasers conference, page 1598.

Liou, T.-M., Chen, C.-C., and Tsai, T.-W. (2000). Heat transfer and fluid flow in a square duct with 12 different shaped vortex generators. J. Heat Transfer, 122(2):327–335.

Ma, S., Chu, W., Zhang, H., Li, X., and Kuang, H. (2019). A combined application of micro-vortex generator and boundary layer suction in a high-load compressor cascade. Chinese Journal of Aeronautics, 32(5):1171–1183.

Ma, W. (2012). Experimental Investigation of Corner Stall in a Linear Compressor Cascade. PhD thesis, Ecole Centrale Lyon.

MacKay, D. J. C. (1992). Information-Based Objective Functions for Active Data Selection. Neural Computation, 4(4):590–604. _eprint: https://direct.mit.edu/neco/article-pdf/4/4/590/812354/neco.1992.4.4.590.pdf.

Martin, J. D. and Simpson, T. W. (2005). Use of Kriging Models to Approximate Deterministic Computer Models. AIAA Journal, 43(4):853–863. _eprint: https://doi.org/10.2514/1.8650.

Martínez-Frutos, J. and Herrero-Pérez, D. (2016). Kriging-based infill sampling criterion for constraint handling in multi-objective optimization. Journal of Global Optimization, 64(1):97–115.

McCulloch, W. S. and Pitts, W. (1943). A logical calculus of the ideas immanent in nervous activity. The bulletin of mathematical biophysics, 5(4):115–133.

McDougall, N. M., Cumpsty, N., and Hynes, T. (1990). Stall inception in axial compressors. Journal of Turbomachinery.

McKay, M. D., Beckman, R. J., and Conover, W. J. (1979). Comparison of Three Methods for Selecting Values of Input Variables in the Analysis of Output from a Computer Code. Technometrics, 21(2):239–245. Publisher: Taylor & Francis _eprint: https://doi.org/10.1080/00401706.1979.10489755.

Meyer, R., Bechert, D., and Hage, W. (2003). Secondary flow control on compressor blades to improve the performance of axial turbomachines“. 5th European Conference on Turbomachinery.

Mockus, J., Tiesis, V., and Zilinskas, A. (1978). The application of Bayesian methods for seeking the extremum. Towards global optimization, 2(117-129):2.

Monier, J.-F. (2018). Analyse de la modélisation turbulente en écoulements tourbillonnaires. PhD thesis, Ecole Centrale Lyon.

Monier, J.-F., Poujol, N., Laurent, M., Gao, F., Boudet, J., Aubert, S., and Shao, L. (2018). LES Investigation of Boussinesq Constitutive Relation Validity in a Corner Separation Flow. In ASME Turbo Expo 2018: Turbomachinery Technical Conference and Exposition, Oslo, Norway.

Munkres, J. R. (2014). Topology. Pearson, Harlow, 2. ed., pearson new internat. ed edition.

Niederreiter, H. (1988). Low-discrepancy and low-dispersion sequences. Journal of Number Theory, 30(1):51–70.

Pearcey, H. (1961). Shock induced separation and its prevention. Boundary layer and flow control, 2:1170–1344. Publisher: Pergamon.

Picheny, V. (2015). Multiobjective optimization using Gaussian process emulators via stepwise uncertainty reduction. Statistics and Computing, 25(6):1265–1280.

Reutter, O., Rozanski, M., Hergt, A., and Nicke, E. (2017). Advanced Endwall Contouring for Loss Reduction and Outflow Homogenization for an Optimized Compressor Cascade. International Journal of Turbomachinery, Propulsion and Power, 2(1):1.

Salunke, N., Ahamad R. A., J., and Channiwala, S. (2014). Airfoil Parameterization Techniques: A Review. American Journal of Mechanical Engineering, 2(4):99–102.

Schlichting, H. and Kestin, J. (1961). Boundary layer theory, volume 121. Springer.

Schulz, H., Gallus, H., and Lakshminarayana, B. (1990). Three-dimensional separated flow field in the endwall region of an annular compressor cascade in the presence of rotor-stator interaction: Part 1—Quasi-Steady flow field and comparison with steady-state data. Journal of Turbomachinery.

Seo, S., Wallat, M., Graepel, T., and Obermayer, K. (2000). Gaussian Process Regression: Active Data Selection and Test Point Rejection. In Sommer, G., Krüger, N., and Perwass, C., editors, Mustererkennung 2000, pages 27–34, Berlin, Heidelberg. Springer Berlin Heidelberg.

Shimoyama, K., Sato, K., Jeong, S., and Obayashi, S. (2012). Comparison of the criteria for updating Kriging response surface models in multi-objective optimization. In 2012 IEEE Congress on Evolutionary Computation, pages 1–8. ISSN: 1941-0026.

Simpson, R. L. (1989). Turbulent boundary-layer separation. Annual Review of Fluid Mechanics, 21(1):205–232. Publisher: Annual Reviews 4139 El Camino Way, PO Box 10139, Palo Alto, CA 94303-0139, USA.

Sobol, I. M. (1967). On the distribution of points in a cube and the approximate evaluation of integrals. USSR Computational Mathematics and Mathematical Physics, 7(4):86–112.

Spalart, P. R. (2000). Strategies for turbulence modelling and simulations. International of Journal of Heat Fluid Flow, 21:252–263.

Srinivas, N., Krause, A., Kakade, S. M., and Seeger, M. (2012). Gaussian Process Optimization in the Bandit Setting: No Regret and Experimental Design. IEEE Transactions on Information Theory, 58(5):3250–3265. arXiv:0912.3995 [cs].

Steinhardt, E. (2003). Aero-Engine Design: A State of the Art-HP Compressors. VKI Lecture Series 2003, 6.

Sun, J., Ottavy, X., Liu, Y., and Lu, L. (2021). Corner separation control by optimizing blade end slots in a linear compressor cascade. Aerospace Science and Technology, 114:106737.

Svenson, J. (2011). Computer experiments: Multiobjective optimization and sensitivity analysis. PhD Thesis, The Ohio State University.

Taylor, J. V. (2019). Separated Flow Topology in Compressors. Journal of Turbomachinery, 141(9).

Taylor, J. V. and Miller, R. J. (2017). Competing Three-Dimensional Mechanisms in Compressor Flows. Journal of Turbomachinery, 139(2):021009.

Tinoco, E. N. (2006). DLR F6-FX2B Summary. In 3rd CFD Drag Prediction Workshop.

Tobak, M. and Peake, D. J. (1982). Topology of three-dimensional separated flows. Annual Review of Fluid Mechanics, 14:61–85.

Wagner, T., Emmerich, M., Deutz, A., and Ponweiser, W. (2011). On Expected-Improvement Criteria for Model-based Multi-objective Optimization. Schaefer, R., Cotta, C., Kołodziej, J., Rudolph, G. (eds) Parallel Problem Solving from Nature, PPSN XI. PPSN 2010. Lecture Notes in Computer Science, vol 6238. Springer, Berlin, Heidelberg, page 727.

Weber, A., Schreiber, H.-A., Fuchs, R., and Steinert, W. (2002). 3-D transonic flow in a compressor cascade with shock-induced corner stall. J. Turbomach., 124(3):358–366.

Wikipedia (2022). https://upload.wikimedia.org/wikipedia/commons/b/bc/Tfan-pw6000-kk-20050816.png.

Witte, R. S. and Witte, J. S. (2017). Statistics. John Wiley & Sons.

Zambonini, G. (2016). Unsteady dynamics of corner separation in a linear compressor cascade. Thèse, Ecole Centrale Lyon.

Zambonini, G., Ottavy, X., and Kriegseis, J. (2017). Corner Separation Dynamics in a Linear Compressor Cascade. Journal of Fluids Engineering, 139(6):061101.

Zheng, T., Qiang, X., and Teng, J. (2015). Effects of Vortex-Vortex Interaction in a Compressor Cascade With Vortex Generators. In ASME Turbo Expo 2015: Turbine Technical Conference and Exposition, Montreal, Quebec, Canada.

Zitzler, E. and Thiele, L. (1998). Multiobjective Optimization Using Evolutionary Algorithms - A Comparative Case Study. pages 292–301. Springer.

Appendix A

Axial compressors : basics of thermo-aerodynamics

An axial compressor is a thermodynamic machine, providing energy to a fluid thanks to a rotating part. In this section, orders of magnitude on modern engines architecture are provided. Several fundamental relations are then retrieved from both thermodynamic laws and fluid mechanics fundamental principles.

A.1 Orders of magnitude

Order of magnitudes vary depending on the gas turbine considered, as commercial aircraft, military aircraft and helicopters have very different needs and structures. The following orders of magnitude are relative to midrange commercial aircraft engines (**?**, **?**) :

	CFM 56	LEAP 1A
Application	A320 family	A320Neo family
Total flow rate	300 kg/s	
Max. climb pressure ratio	32	
Max. takeoff thrust	100 kN	115 kN
Max. climb thrus	26 kN	
Bypass ratio	5,3	11
Length	2,6 m	
Fan diameter	1,55 m	1,98 m
Dry Weight	2,4 tons	
Number of fan/low-pressure/high-pressure compressor stages	1+3+9	1+3+10
Number of low-pressure/high-pressure turbine stages	4+1	7+2

Table A.1: Order of magnitude : CFM 56, LEAP-1A.

A.2 Total and static quantities in compressible flows

Let us first consider a uniform flow defined by the state variables (P,T,ρ), denoting respectively the pressure, temperature and density, with no heat exchange and no mechanical work. The following equations are written with quantities per mass unit. The energy conservation yields

$$\Delta h + \Delta \frac{V^2}{2} = \Delta W_T + \Delta q = 0 \tag{A.1}$$

Where h is the enthalpy and W_T and q are the mechanical work and heat exchange respectively. We can then define the total enthalpy as $H = h + \frac{V^2}{2}$. This quantity remains constant even though irreversible processes may be present, and represents the total energy contained in the fluid. This quantity is also called *stagnation enthalpy* because it can be seen as the enthalpy value of the zero velocity system : $H = (h + \frac{V^2}{2})_{|V=0,S=cst} = h + \frac{V^2}{2}$.
During an evolution of the system, the conservation of the total enthalpy requires a re-balancing of the state variables P,T,ρ.
If the fluid is a perfect gas, $h = c_p T \Rightarrow H = c_p T + \frac{V^2}{2}$, with c_p the isobaric specific heat capacity of the fluid. Defining the total temperature as $T_t = \frac{H}{c_p}$, we obtain

$$T_t = T + \frac{V^2}{2c_p} \qquad \textit{Total temperature} \tag{A.2}$$

where T is the static temperature, resulting from the average kinetic energy at molecular level, and $\frac{V^2}{2c_p}$ is the dynamic temperature, resulting from the average kinetic energy of fluid particles at mesoscopic scale.
We can derive this expression to define the total density ρ_t and total Pressure P_t using the Laplace law, that assumes an isentropic transformation :

$$\frac{P_t}{P} = \left(\frac{\rho_t}{\rho}\right)^{\gamma} = \left(\frac{T_t}{T}\right)^{\frac{\gamma}{\gamma-1}} \tag{A.3}$$

It is important to notice that, contrarily to the total enthalpy and total temperature, the total density ρ_t and total Pressure P_t are defined assuming a reversible process : they are equal to the value of ρ and P in a fictitious state of a system brought back to a zero velocity state by a isentropic deceleration.
Introducing the Mach number $M = \frac{V}{a} = \frac{V}{\sqrt{\gamma R_{pg} T}}$ with a the velocity of acoustic waves in the fluid, we finally obtain

$$\frac{T_t}{T} = 1 + \frac{V^2}{2c_p} = 1 + \frac{\gamma - 1}{2} M^2 \tag{A.4}$$

$$\frac{P_t}{P} = \left[1 + \frac{V^2}{2c_p T}\right]^{\frac{\gamma}{\gamma-1}} = \left[1 + \frac{\gamma-1}{2} M^2\right]^{\frac{\gamma}{\gamma-1}} \tag{A.5}$$

$$\frac{\rho_t}{\rho} = \left[1 + \frac{V^2}{2c_p T}\right]^{\frac{1}{\gamma-1}} = \left[1 + \frac{\gamma-1}{2} M^2\right]^{\frac{1}{\gamma-1}} \tag{A.6}$$

Finally it is interesting to underline that there is no need to define a total and static entropy, the entropy being independent of the frame of reference, as it accounts only for heat transfer and production.

A.3 Euler equation

Rothalpy conservation along a streamline

Let us now consider the flow across a stage composed of a rotating part (rotor) and a fixed part (stator). The velocity component of the fluid in the relative frame $\mathbf{W}$ (rotor frame) and in the absolute frame $\mathbf{V}$ (stator frame) are linked by the entrainment velocity $\mathbf{U} = \mathbf{\Omega} \wedge \mathbf{R}$ where $\mathbf{R}$ is the radial component of the position vector and $\mathbf{\Omega}$ the angular velocity vector :

$$\mathbf{V} = \mathbf{W} + \mathbf{U} \quad \Leftrightarrow \quad \begin{cases} V_m = W_m \\ V_r = W_r \\ V_\theta = W_\theta + R\Omega \end{cases} \tag{A.7}$$

where the indices m, r ,θ denote respectively the engine axis direction, the radial component and the azimuthal component. The absolute angle $\alpha =< \mathbf{e_m}, \mathbf{V} >$ and the relative angle $\beta =< \mathbf{e_m}, \mathbf{W} >$ are key parameters as they allow to quantify the flow deviation, and are illustrated in Fig. A.1a.

The kinetic energy conservation equation for a fluid particle in the relative frame reads

$$\frac{D}{Dt}\left(h + \frac{W^2}{2} - \frac{U^2}{2}\right) = \frac{1}{\rho}\frac{\partial p}{\partial t} + T\frac{DS}{Dt} + \frac{1}{\rho}\mathbf{W} \cdot \mathbf{f} \tag{A.8}$$

where $\mathbf{f}$ denotes the resulting viscous forces acting on the fluid particle, T the temperature and S the entropy. We define the rothalpy I such that

$$I = h + \frac{W^2}{2} - \frac{U^2}{2} \qquad \textit{Rothalpy} \tag{A.9}$$

Using the first principle of the thermodynamics and the definition of entropy, $T\frac{DS}{Dt}$ can be expressed as $T\frac{DS}{Dt} = \frac{\phi_D + \lambda_C \Delta T}{\rho}$ where ϕ_D is the dissipated heat resulting from the fluid particle deformation and $\lambda_C \Delta T$ the heat gain transmitted by conduction. Equation (A.8) thus reads

$$\frac{DI}{Dt} = \frac{1}{\rho}\frac{\partial p}{\partial t} + \frac{\mathbf{W} \cdot \mathbf{f} + \phi_D}{\rho} + \frac{\lambda_C \Delta T}{\rho} \tag{A.10}$$

Under the assumptions of

- **Stationarity in the relative frame** : $\frac{\partial p}{\partial t} \simeq 0$
- Low heat transfer conduction : $\lambda_C \simeq 0$. This is acceptable for compressor stages.
- Balance between the viscous work $\mathbf{W} \cdot \mathbf{f} < 0$ and the deformation heat $\phi_D > 0$: $\mathbf{W} \cdot \mathbf{f} + \phi_D \simeq 0$. This is globally acceptable in compressor stages outside the boundary layers.

We obtain the rothalpy conservation in the relative frame along every streamline :

$$\frac{DI}{Dt} = 0 \qquad \Rightarrow \qquad I = \textit{constant} \quad \text{along a streamline} \tag{A.11}$$

In the specific case of an axial compressor, streamlines far from the solid boundaries tend to remain at the same radial position. For two fluid particle positions on the same streamline denoted by 1 and 2, this implies $U_1 \simeq U_2$ and the rothalpy conservation is then equivalent to the conservation of the total relative enthalpy :

$$H_1^R = h_1 + \frac{W_1^2}{2} = h_2 + \frac{W_2^2}{2} = H_2^R \quad \text{along a streamline} \tag{A.12}$$

Euler equation
The conservation of the rothalpy in the relative frame leads to a fundamental relationship in the absolute frame. Substituting $H = h + \frac{V^2}{2}$ and $W^2 = (\mathbf{V} - \mathbf{U})^2 = V^2 + U^2 - 2\mathbf{U} \cdot \mathbf{V}$ in equation (A.9) gives

$$I = H - \mathbf{U} \cdot \mathbf{V} = H - UV_\theta \tag{A.13}$$

Using the rothalpy conservation (A.11), $\Delta I = 0$ and we obtain the Euler equation, valid along a streamline :

$$\Delta H = \Delta(UV_\theta) \tag{A.14}$$

where H is the total absolute enthalpy, U the entrainment velocity and V_θ the azimuthal component of the velocity. It is worth underlining that for a stator $U = 0 \Rightarrow \Delta H = 0$: no work is provided to the fluid. For the rotor of an axial compressor, this becomes

$$\begin{aligned} \Delta H &= \Delta(UV_\theta) \\ &\simeq U\Delta(V_\theta) \\ &= -U\Delta(W_\theta) \\ &= R\Omega V_m(\tan\beta_1 - \tan\beta_2) \end{aligned} \tag{A.15}$$

with β_1, β_2 the upstream and downstream relative angle respectively. It is worth underlining that the total enthalpy gain provided by the rotor is linearly dependant on the radial position, the angular velocity of the shaft and the difference in the tangents of the relative angles.

A.4 Design coefficients

Definition and graphical interpretation

A compressor stage is designed to reach a given pressure ratio for a given rotating velocity and a given flow rate constituting the nominal operating conditions. In the early design steps, it is common to define the design coefficients

$$\phi = \frac{V_m}{U} \qquad \textit{Flow coefficient} \tag{A.16}$$

$$\psi = \frac{\Delta H}{U^2} \qquad \textit{Loading factor} \tag{A.17}$$

$$R = \frac{\Delta H^R_{Rotor}}{\Delta H_{Stage}} \qquad \textit{Reaction ratio} \tag{A.18}$$

The relationships between the flow coefficient and the loading coefficient can be easily illustrated on a dimensionless velocity triangle, dividing every quantity by the rotation velocity U as illustrated in Figure (A.1b). We recall that the Euler relationship (Equation A.15) gives $\Delta H = \Delta(UV_\theta) = U(V_{\theta_2} - V_{\theta_1})$ in an axial compressor as $U \simeq cst$ along a streamline.

The geometrical interpretation of the reaction ratio requires further manipulations. Along a streamline and in an axial compressor the total relative enthalpy is conserved and $h_1 + \frac{W_1^2}{2} =$

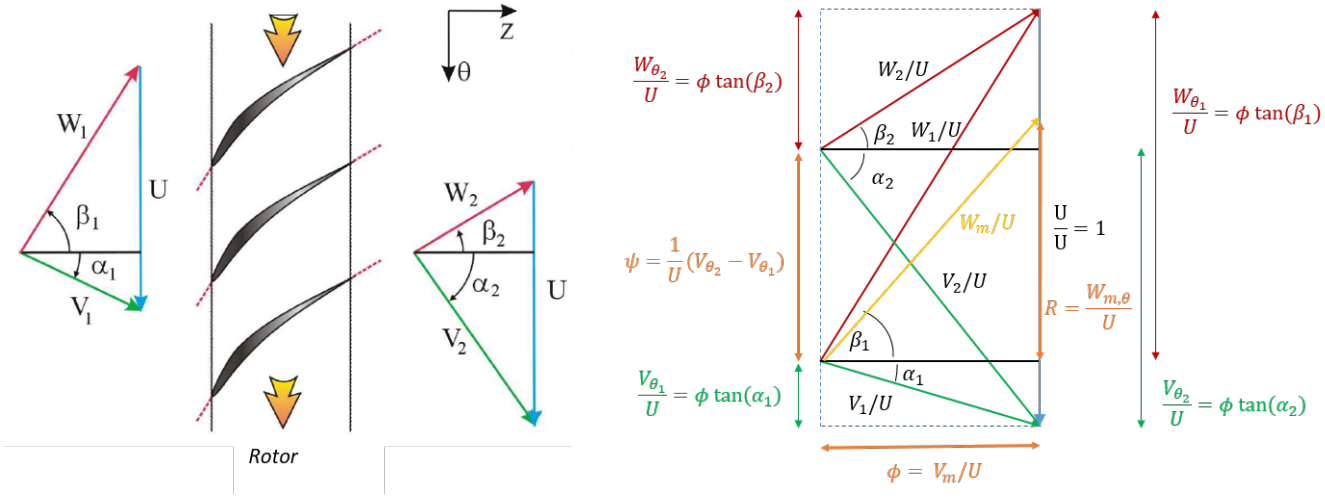

(a) Velocity triangles upstream and downstream of a rotor stage

(b) Dimensionless velocity triangles

Figure A.1: Design coefficients graphical interpretation

$h_2 + \frac{W_2^2}{2}$ yielding $\Delta H^R_{Rotor} = h_2 - h_1 = \frac{W_1^2 - W_2^2}{2}$. For normal stages, i.e. $V_3 = V_1$, $\Delta H_{Stage} = U(V_{\theta_2} - V_{\theta_1})$. This yields

$$\begin{aligned} R &= \frac{W_1^2 - W_2^2}{2U(V_{\theta_2} - V_{\theta_1})} \\ &= \frac{W_{1_\theta}^2 - W_{2_\theta}^2 + W_{1_m}^2 - W_{2_m}^2}{2U(V_{\theta_2} - V_{\theta_1})} \qquad \text{given that } W_{1_m} = W_{2_m} = V_m \\ &= \frac{(W_{1_\theta} + W_{2_\theta})(W_{1_\theta} - W_{2_\theta})}{2U(V_{\theta_2} - V_{\theta_1})} \qquad \text{and as } V_{\theta_2} - V_{\theta_1} = W_{\theta_1} - W_{\theta_2} \\ &= \frac{(W_{1_\theta} + W_{2_\theta})}{2U} \end{aligned}$$

If we define $\tan\,\beta_m = \frac{1}{2}(\tan\,\beta_1 + \tan\,\beta_2)$ and $\mathbf{W_m} = \frac{\mathbf{W_1 + W_2}}{2}$, the reaction ratio can be written as

$$R = \frac{W_{m,\theta}}{U} = \phi\,\tan\,\beta_m \tag{A.19}$$

Finally, the above equations and Fig. A.1b allow to get the following relationships

$$\psi = \frac{1}{U}(V_{\theta_2} - V_{\theta_1}) = \phi\,[\tan\beta_1 - \tan\beta_2] = \phi\,[\tan\alpha_2 - \tan\alpha_1] \tag{A.20}$$

$$1 = \psi + \phi\,[\tan\,\alpha_1 + tan\beta_2] \tag{A.21}$$

$$1 = \phi\,\tan\,\alpha_1 + \frac{\psi}{2} + R \tag{A.22}$$

Losses and efficiency

For an ideal fluid $TdS = 0$ implies that $dH = \frac{1}{\rho}dP$, that is for an incompressible fluid $\Delta H_{is} = \frac{1}{\rho}\Delta P$ where P denotes the total pressure.

Stage pressure rise thus reads

$$P_3 - P1 = \rho\Delta H + \Delta P^R_{Rotor} + \Delta P_{Stator} \tag{A.23}$$

with

$$\begin{array}{rcccl} \Delta P^R_{Rotor} & = & \frac{1}{2}\rho(W_2^2 - W_1^2) & = & -\frac{1}{2}\rho W_1^2\omega_R \\ \Delta P_{Stator} & = & \frac{1}{2}\rho(V_3^2 - V_2^2) & = & -\frac{1}{2}\rho V_2^2\omega_S \end{array}$$

where ω_R and ω_S are defined as the total pressure loss coefficients for the rotor blade and the stator blade respectively,

The isentropic efficiency of the compressor stage can thus be expressed :

$$\eta_{is} = \frac{\Delta H_{is}}{\Delta H} \tag{A.24}$$

$$= \frac{(P_3 - P_1) \ / \ \rho U^2}{\Delta H \ / \ U^2} \tag{A.25}$$

$$= 1 - \frac{1}{2\psi}\left[\frac{W_1^2}{U^2}\omega_R + \frac{V_2^2}{U^2}\omega_S\right] \tag{A.26}$$

Equation A.22 then yields

$$\eta_{is} = 1 - \frac{1}{2\psi}\left[\omega_R\left(\phi^2 + (R + \frac{\psi}{2})^2\right) + \omega_S\left(\phi^2 + (1 + \frac{\psi}{2} - R)^2\right)\right] \tag{A.27}$$

Usually, ω_R and ω_S are derived from empirical laws. Moreover, with a fixed value of ϕ and ψ, there is an optimal value of R maximising the isentropic efficiency. If $\omega_R = \omega_S$, then $R_{optimal} = 0.5$. With ϕ, ψ and R fixed, the velocity triangle is totally determined and the user can get the design angles α_1,α_2,β_1,β_2 allowing to reach the targeted parameters with minimum losses.

A.5 Relation between entropic losses and total pressure losses in an adiabatic stator row

In a stator, no mechanical work is exchanged between the flow and the structure, nor any heat as the configuration is assumed adiabatic (Equation A.31). Therefore, entropic losses are directly related to the total pressure loss coefficient $\omega = -C_{p,t}$ (Equation A.32). Indeed,

$$\Delta H = \Delta W_T + \Delta q \quad \text{Energy conservation} \tag{A.28}$$

$$\Delta H = \Delta(UV_\theta) = 0 \quad \text{Euler equation} \tag{A.29}$$

$$\Delta q = 0 \quad \text{Adiabatic assumption} \tag{A.30}$$

$$\Delta W_T = T_t dS + V dP_t \tag{A.31}$$

with H the total enthalpy, W_T the work exchanged, q the heat exchange, U the entrainment velocity, T_t the total temperature, S the entropy, V the volume, P_t the total pressure. With these assumptions, $\Delta W_T = 0$. Along a streamline, from a state 1 to 2, with quantities per mass unit and considering a constant density, this yields

$$\begin{aligned} \text{Entropic losses} = \int_1^2 -T_t ds &= \int_1^2 \frac{dP_t}{\rho} \\ &= \frac{P_{t,\infty} - P_{s,\infty}}{\rho} \quad C_{p,t} \\ &= -\frac{P_{t,\infty} - P_{s,\infty}}{\rho} \quad \omega \end{aligned} \tag{A.32}$$

Appendix B

Elements on Kriging modelling

B.1 Notion of Gaussian process

The notion of Gaussian process relies on a large mathematical background. Only fundamental notions necessary to illustrate the principle of Gaussian process are described in this section. A thorough mathematical approach can be found in (Lifshits, 1995).

Random variable (formal) A random variable is defined as a measurable mapping of a measurable space (Ω, F) endowed with a probability (unit) measure P taking values in $\mathbb{R}$.

Random variable (in practice) A random variable is an application which associates a value of $\mathbb{R}$ to each event ω of a sample space Ω, each ω being characterised with a probability to be realised.
Remark : in this section, continuous random variables are considered. Given a sample space Ω and a probability density function f, the probability of the random variable X to take a value within $[a, b] \in \Omega$ reads :

$$P(X \in [a, b]) = \int_b^a f(x)dx \tag{B.1}$$

Expected value If it exists, the expected value of a random function X is defined as :

$$\mathbb{E}[X] = \int_\Omega X(\omega)dP(\omega) = \int_\Omega X(\omega)f(\omega)d\omega \tag{B.2}$$

Variance If it exists, the variance of a random function X is defined as :

$$Var(X) = \mathbb{E}[(X - \mathbb{E}[X])^2] \tag{B.3}$$

Covariance For two random variables X and Y with finite variances, the covariance of X and Y is defined such that :

$$Cov(X, Y) = \mathbb{E}[(X - \mathbb{E}[X])(Y - \mathbb{E}[Y])] \tag{B.4}$$

Covariance matrix Let us consider a collection of n random variables $\mathbf{X} = (X_1; ...; X_n)$. The covariance matrix of this collection is defined as

$$K = (Cov(X_i, X_j))_{1 \leq i,j \leq n} \tag{B.5}$$

Gaussian random variable : Let X be a square-integrable random variable. X is a Gaussian random variable with parameters m and $\sigma > 0$ if its probability density distribution is :

$$f(x) = \frac{1}{\sqrt{2\pi\sigma^2}} e^{\frac{-(x-m)^2}{2\sigma^2}} \tag{B.6}$$

Remark : A Gaussian random variable X is therefore entirely defined with a mean ($m = \mathbb{E}[X]$) and a standard deviation ($\sigma = \sqrt{Var(X)}$).
Random vector : A random vector is a vector of random variables defined on the same sample space Ω.
Gaussian random vector : X is a Gaussian random vector of $\mathbb{R}^n$ if any linear combination of its components $\Sigma_{j=1}^{n} a_j X_j$ ($\forall (a_j) \in \mathbb{R}^n$) is a Gaussian random variable.

Remarks :

- if $\mathbf{X} = (X_1; ...; X_n)$ is a Gaussian random vector, it is entirely defined with a mean vector $\mathbf{m} \in \mathbb{R}^n$ with $m_j = \mathbb{E}[X_j]$ and a positive definite covariance matrix C with elements $c_{ij} = Cov(X_i, X_j)$. The probability density of $\mathbf{X}$ is given by :

$$f_{\mathbf{X}}(\mathbf{x}) = \left(\frac{1}{2\pi}\right)^{n/2} \left(\frac{1}{det(C)}\right)^{1/2} exp\left(-\frac{(\mathbf{x}-\mathbf{m})C(\mathbf{x}-\mathbf{m})^\intercal}{2}\right) \tag{B.7}$$

- If $\mathbf{X} = (X_1; ...; X_n)$ is a Gaussian random vector, each X_i is a Gaussian random variable.
- Let $\mathbf{X} = (X_1; ...; X_n)$ be a random vector. If each X_i is a Gaussian random variable, $\mathbf{X}$ is a Gaussian random vector.

Stochastic process : A stochastic process $X = (X_t)_{t \in T}$ is a collection of random variables defined on the same sample space Ω, and indexed by a set T.

Remark : T can be a discrete set or a continuous set. If T is a discrete set, a Stochastic process corresponds to a random vector.

Gaussian process : A stochastic process is a Gaussian process if any $(X_{t_1}, X_{t_2}, ..., X_{t_n})$ is a Gaussian random vector, $\forall n \in \mathbb{N}, \forall (t_1, t_2, ..., t_n) \in$ T.

A such, a Gaussian process can be seen as a stochastic process for which any discretisation yields a Gaussian random vector. Given that a Gaussian random vector is entirely defined with a mean vector and a covariance matrix, a Gaussian process can be entirely defined with

- A mean value function $m(t) = \mathbb{E}(X_t)\ \forall t \in T$
- A covariance function $k(t, \tilde{t}) = Cov(X_t, X_{\tilde{t}})\ \forall t, \tilde{t} \in T$

Indeed, the mean vector of any Gaussian vector extracted from the Gaussian process is therefore given by $\mathbf{m} = (m(t_1); ...; m(t_n))$, and its covariance matrix by $K_n = (k(t_i, t_j))_{1 \leq i,j \leq n}$.

As such, a user can define a mean value function and a covariance function to describe the stochastic evolutions of a system. Historically, the concept of Gaussian process was applied to describe the Brownian motion of small particles submitted to thermal forces. In this case,

X can be seen as the probability for a particle to be located at an axial position x $\in \mathbb{R}$ at an instant t $\in \mathbb{R}^+$. The Brownian motion can be replicated with a Gaussian process of mean value constant equal to 0 and a covariance function of $K = Cov(X_{t_i}, X_{t_j}) = min(t_i, t_j)$. Three realisations of the Brownian motion are illustrated in Figure B.1. $X_{t=0}$ corresponds to a Dirac function (degenerated Gaussian) : the initial position of the particle is imposed. For $t > 0$, the probability of the particle to be located at a position x is given by X_t, a Gaussian random variable of mean 0, variance $min(t, t) = t$, and standard deviation $\sigma = \sqrt{t}$. These paths correctly reproduce the observed Brownian motion, thus showing an example of a physical process well modelled with a Gaussian process.

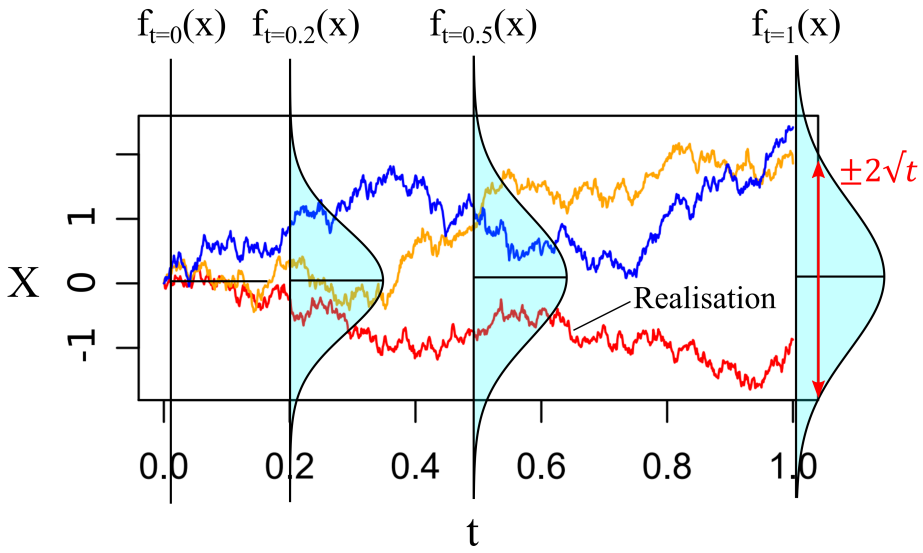

Figure B.1: Realisations of a Gaussian process replicating the Brownian motion and evolution of the probability density function f as a function of the time t. Adapted from Helbert (2020).

Gaussian processes can be tuned to model various physical phenomena with different constraints through the definition of their mean function and covariance functions. Notably, the covariance function can be adjusted to describe trajectories more or less dependant of their past positions (regularity of the covariance function). Moreover, the Gaussian process can be conditioned to specific observations, thus imposing the stochastic realisations to cross specific locations (conditioned Gaussian process).

B.2 Parameters of Kriging modelling

Kriging modelling consists in modelling the relation between a set of parameters and a response function as a Gaussian process. As illustrated in the previous section, Gaussian processes can be tuned though the definition of their mean function and covariance function. Formally, this reads :

$$Y(t) = m + Z(t) \tag{B.8}$$

with $Y(t)$ the realisation of the Gaussian process modelling the response function, m its mean function, $Z(t)$ a Gaussian process with zero mean, variance σ and a correlation structure r_θ such that its covariance function reads $k(t, \tilde{t}) = \sigma \times r_\theta(t - \tilde{t})$. In this formulation, θ is called

the *range* and can be interpreted as a correlation length of the successive values of a given realisation.

It is proposed to illustrate the effect of the correlation structure on the Kriging predictions. Among the most famous correlation structures, the Exponential, Matern 3/2 and Gaussian are selected. They are defined such that :

$$\textbf{Exponential} \;:\; r_\theta(t-\tilde{t}) = exp\left(-\frac{|t-\tilde{t}|}{\theta}\right) \tag{B.9}$$

$$\textbf{Matern 3/2} \;:\; r_\theta(t-\tilde{t}) = \left(1+\frac{\sqrt{3}|t-\tilde{t}|}{\theta}\right) exp\left(-\frac{\sqrt{3}|t-\tilde{t}|}{\theta}\right) \tag{B.10}$$

$$\textbf{Gaussian} \;:\; r_\theta(t-\tilde{t}) = exp\left(-\frac{(t-\tilde{t})^2}{\theta^2}\right) \tag{B.11}$$

These three functions are plotted in Figure B.2 with $\theta = 1/3$. For the exponential function, the correlation between two Gaussian variables rapidly drops when the distance between these variables $(t-\tilde{t})$ increases. As a consequence, the realisations are little dependant of their past positions and feature irregular paths. When these realisations are conditioned with an observation set, their paths is rapidly independent of the values of the observation points. This results in a large envelope of possible realisations and hence a large uncertainty in the Kriging modelling. With the Matern 3/2 and Gaussian correlation structure, the correlation between two parameter values remains significant on a larger scale. Consequently, the corresponding realisations feature smoother evolutions, and the Kriging modelling is much influenced by the observation data. In this specific example, the Gaussian correlation structure is the one that best fits the test function (sin). However, such a dependence to the observation data might be unwanted depending on the quantity modelled.

In this work, the correlation function used is Matern 5/2 (more regular than Matern 3/2), defined as :

$$\textbf{Matern 5/2} \;:\; r_\theta(t-\tilde{t}) = \left(1+\frac{\sqrt{5}|t-\tilde{t}|}{\theta}\times\frac{5|t-\tilde{t}|^2}{3\theta^2}\right) exp\left(-\frac{\sqrt{5}|t-\tilde{t}|}{\theta}\right) \tag{B.12}$$

In this work, the Ordinary Kriging formulation is used : the mean function m and the variance parameter σ are assumed constant and are estimated from the observation set. The θ parameter is also estimated. These parameters are estimated by numerical optimisation with the rgasp function from the RobustGaSP library (Software **R**).

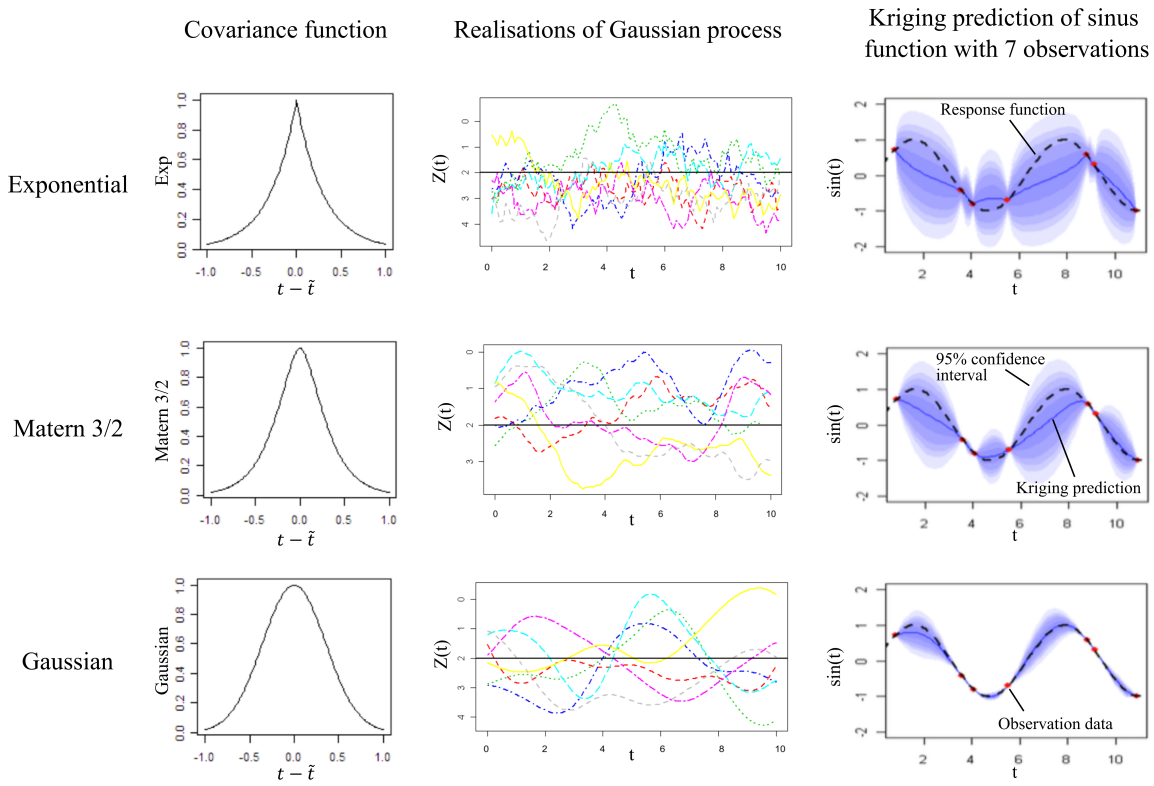

Figure B.2: Effect of the covariance function of the realisations of the Gaussian process, unconditioned and conditioned. Adapted from Helbert (2020) and Da Veiga (2019).

Remarks :

- A formal introduction to Kriging modelling and additional information on commonly used correlation structures can be found in (Gu et al., 2018).
- In this chapter, the notion of Gaussian process and Kriging parameters are illustrated with simple mono-parameter examples. The same notion exists with several parameters. The Gaussian random variable becomes multi-variate, the Gaussian process is called a Gaussian random field, the mean value is replaced by a mean vector value. The same three correlation function exists, but are adapted to take into account each dimension (the θ parameter is then replaced by a vector).
- Several formulations of Kriging modelling exists : Simple Kriging (constant mean function, constant variance σ, known and input by the user), Ordinary Kriging (constant mean function, constant variance σ, estimated from the observation set) and Universal Kriging (mean function with a trend, constant variance σ, estimated from the observation set). For more details, see (Le Riche, 2014) and (Ashrafpour, 2021).
- The Kriging formulation is natively interpolating. This is useful to replicate deterministic response functions. To help describing stochastic response functions, a white noise $\epsilon(t)$ can be added in Equation B.8 (effect of nugget). See Gu (2016).

Appendix C

Characteristic shapes of efficient guide fins : complementary results

C.1 Distribution of parameters with respect to $\Delta\omega_0$ and $\Delta\omega_{4.9}$ (15p analysis).

In Section 7.1, 74 guide fins of depth ≤ 5 are selected based on two geometrical criteria. Their geometrical specificities and the effect of a restrained number of parameters on the objective functions are analysed. In this section, the distribution of all parameters are shown with respect to both objective functions. SF, 3D and LF families are coloured respectively in red, blue and green.

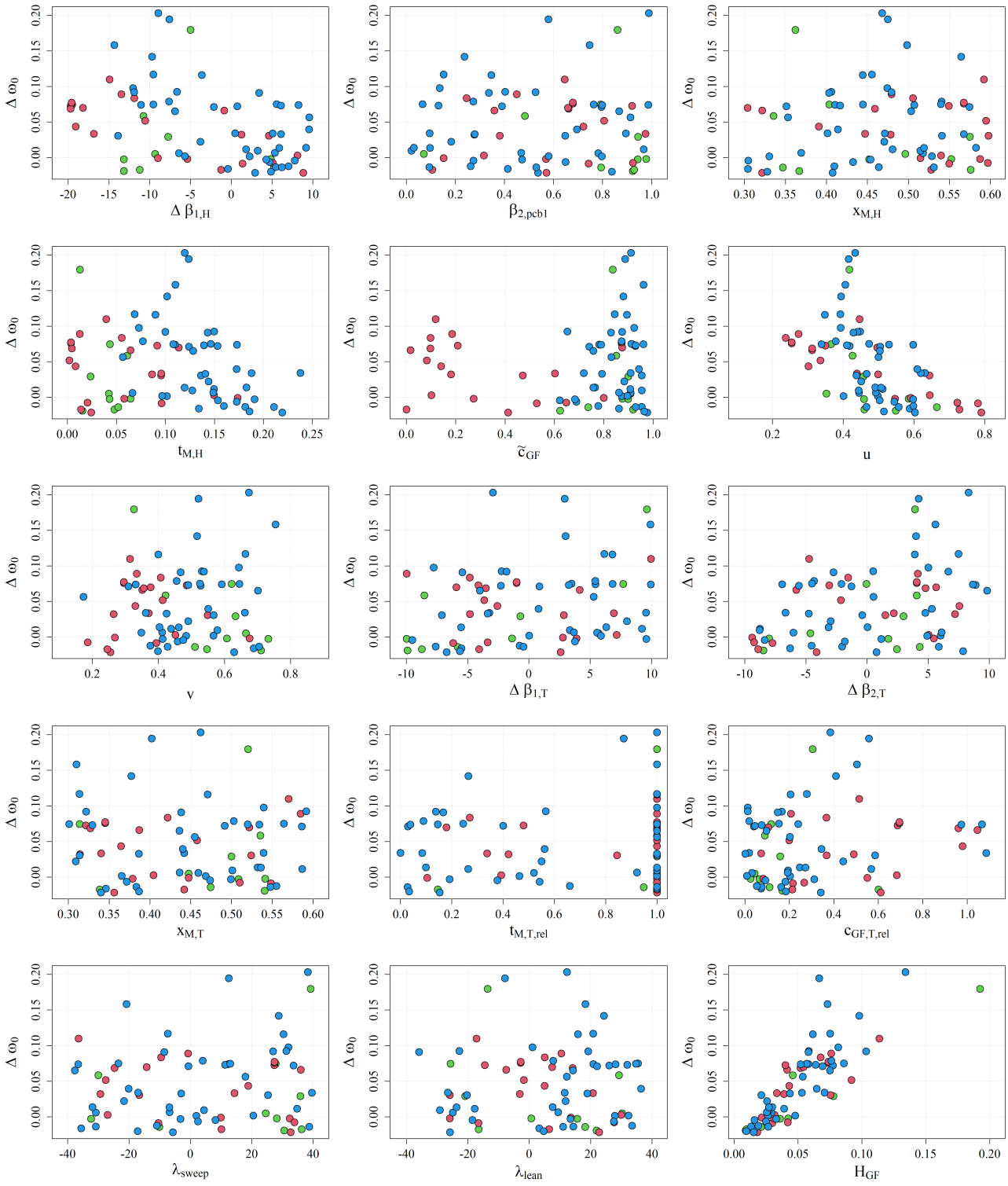

Figure C.1: Distribution of the optimisation parameters against $\Delta\omega_0$. SF (red), 3D (blue) and LF (green) families.

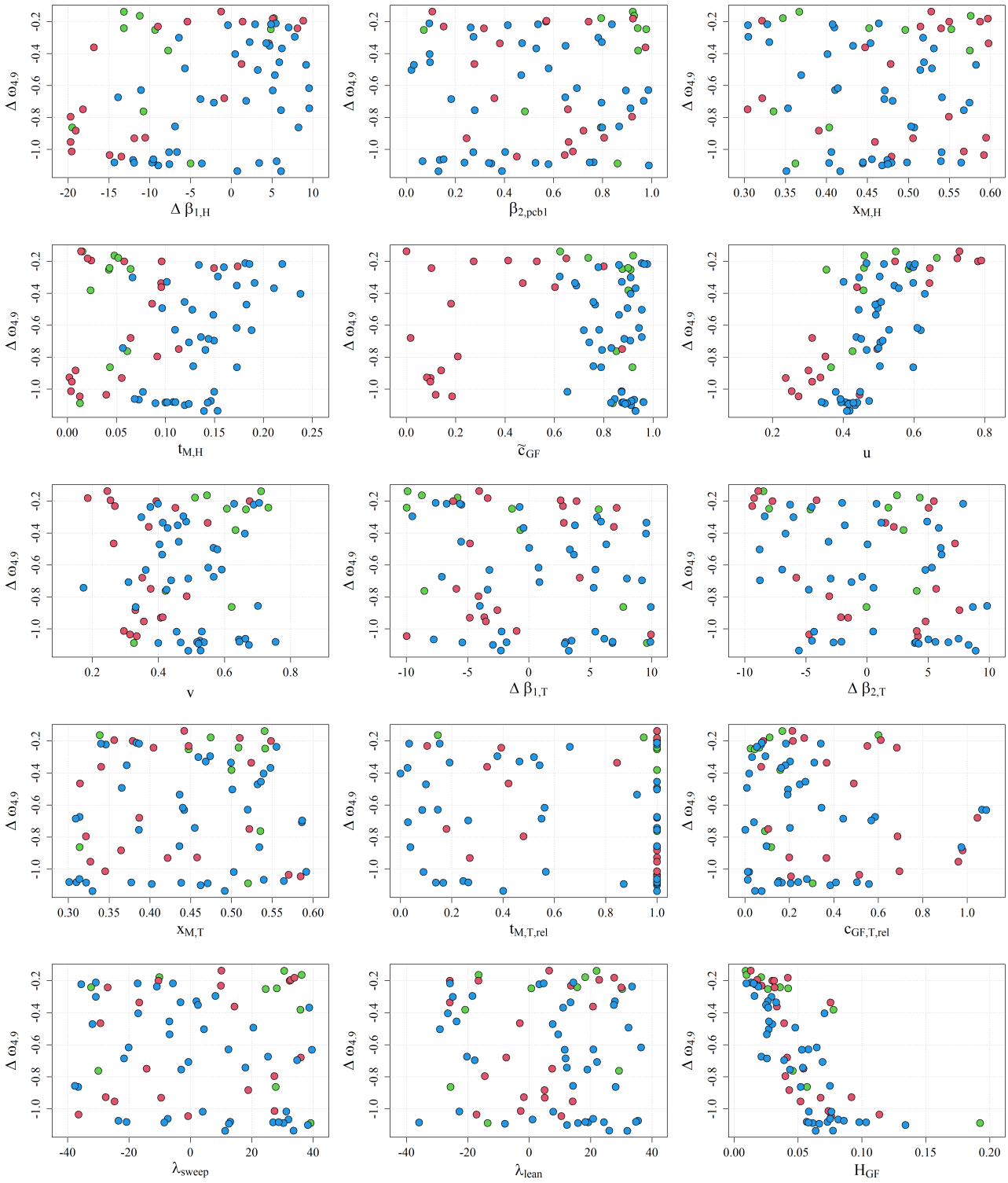

Figure C.2: Distribution of the optimisation parameters against $\Delta\omega_{4.9}$. SF (red), 3D (blue) and LF (green) families.

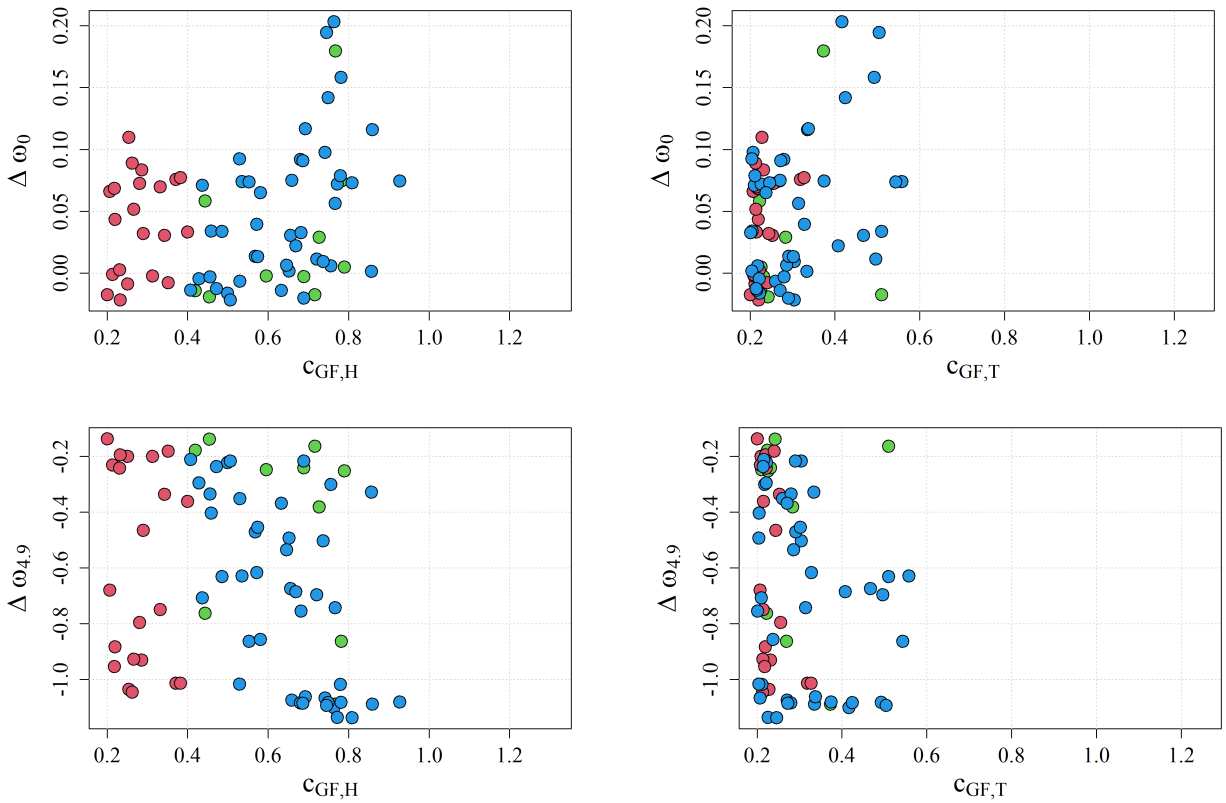

Figure C.3: Distribution of the hub chord $c_{GF,H}$ values against $\Delta\omega_0$ and $\Delta\omega_{4.9}$. $c_{GF,H}$ is expressed in stator chord unit. SF (red), 3D (blue) and LF (green) families.

C.2 Relation between relative stagger angle, twist and $\Delta\beta_{1,H}$

The relative stagger angle and the twist (defined in Section 7.1.2.1) are computed for all guide fins of the 15p RANS database (see Figure C.4). A correlation between these two quantities appears. These two quantities characterise the shapes of the guide fins once they are generated, and are not imposed in the guide fin construction. They appear to be strongly correlated with the input parameter $\Delta\beta_{1,H}$, which is imposed in the exploration process. The value of $\Delta\beta_{1,H}$ therefore constrains the authorised values of the relative stagger angle and of the twist.

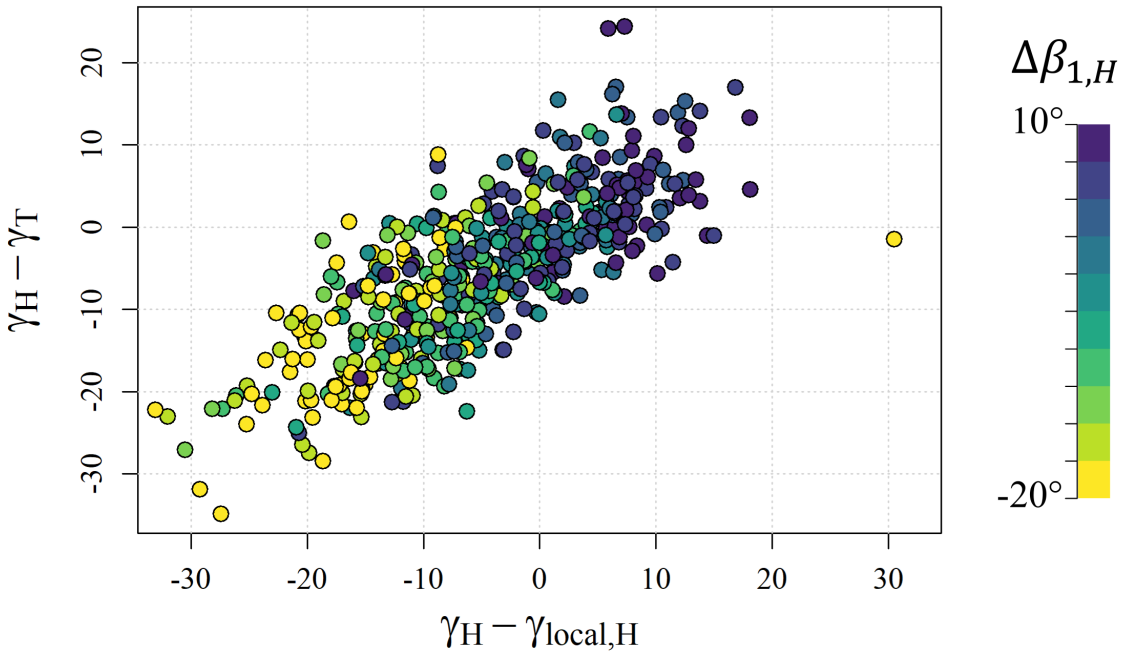

Figure C.4: Relative stagger angle vs twist for all guide fins of the 15p RANS database. Coloured with $\Delta\beta_{1,H}$.

C.3 Efficient 6-parameter guide fins : evolution of $\Delta\omega_0$ and $\Delta\omega_{4.9}$ with all parameters.

In Section 7.2, 64 guide fins of depth ≤ 5 are selected among the 6p RANS database. The distribution of their parameters was shown against $\Delta\omega_{4.9}$ only. In this section, the distribution of their parameters is presented against $\Delta\omega_0$. Their distribution against $\Delta\omega_{4.9}$ is recalled for comparison purposes.

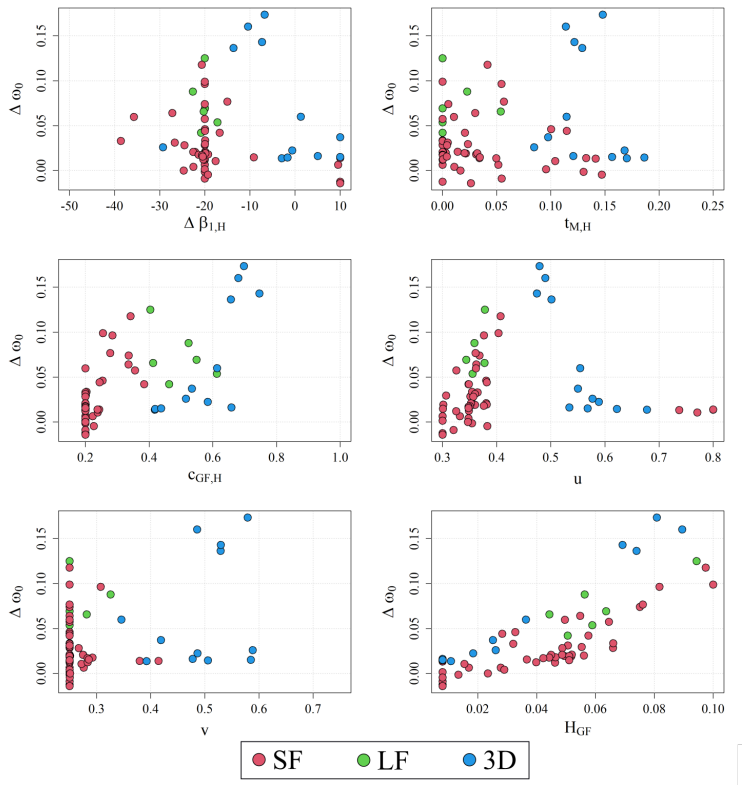

Figure C.5: Distribution of all optimisation parameters against $\Delta\omega_0$. SF (red), 3D (blue) and LF (green) families.

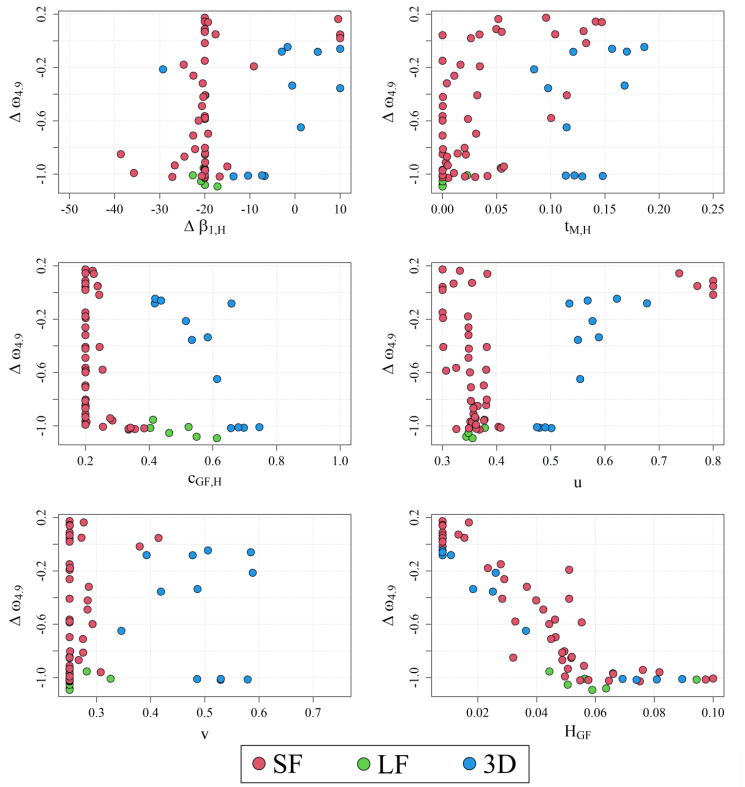

Figure C.6: Distribution of all optimisation parameters against $\Delta\omega_{4,9}$. SF (red), 3D (blue) and LF (green) families.

C.4 Comparison of 15p and 6p families

All the guide fins investigated in the 15p (Section 7.1.1) and 6p (Section 7.2.1) analyses are represented with respect to $\Delta\omega_0$ and $\Delta\omega_{4.9}$ in Figure C.7. The representative guide fins selected for each family (SF-03, 3D-01 and LF-A, see Section 7.3) are indicated in this Figure.

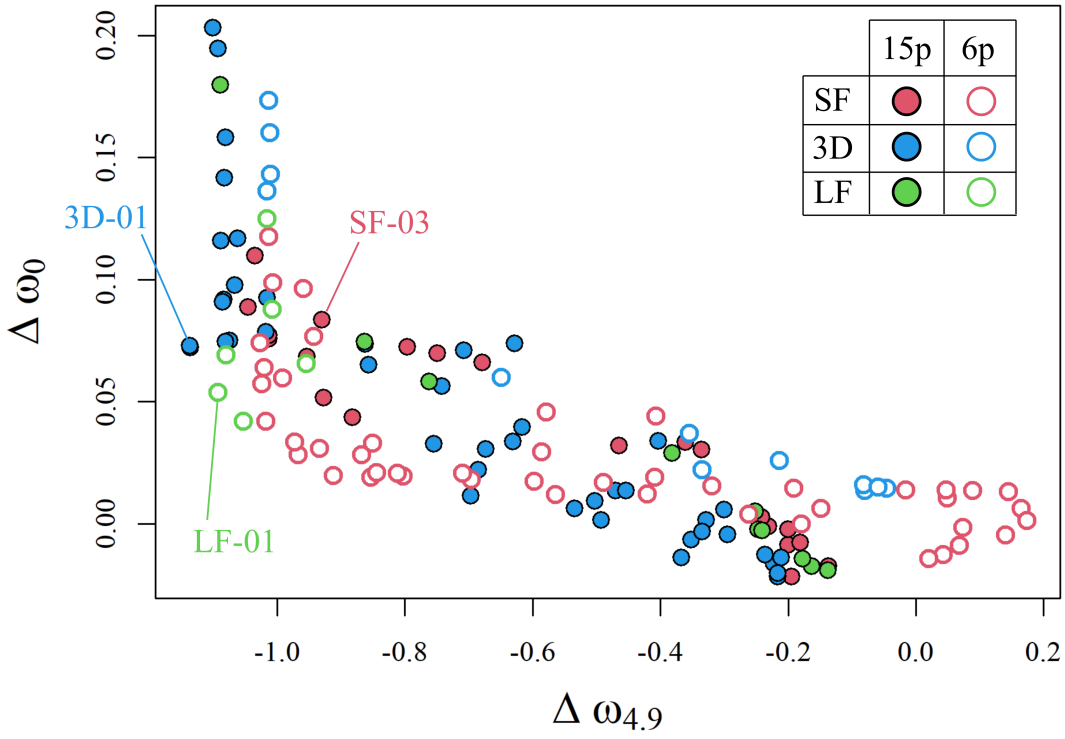

Figure C.7: Comparison of 15p and 6p guide fins of each family in the objective function space.

C.5 Investigation of the SF and LF Pareto front (6p analysis)

The SF (Section 7.2.2) and LF (Section 7.2.4) Pareto fronts are plotted with the Pareto front computed on the whole input space (Surrogate Pareto front) in Figure C.8a. The latter appears to be the union of the SF and LF Pareto front, which explains its pointed shape.

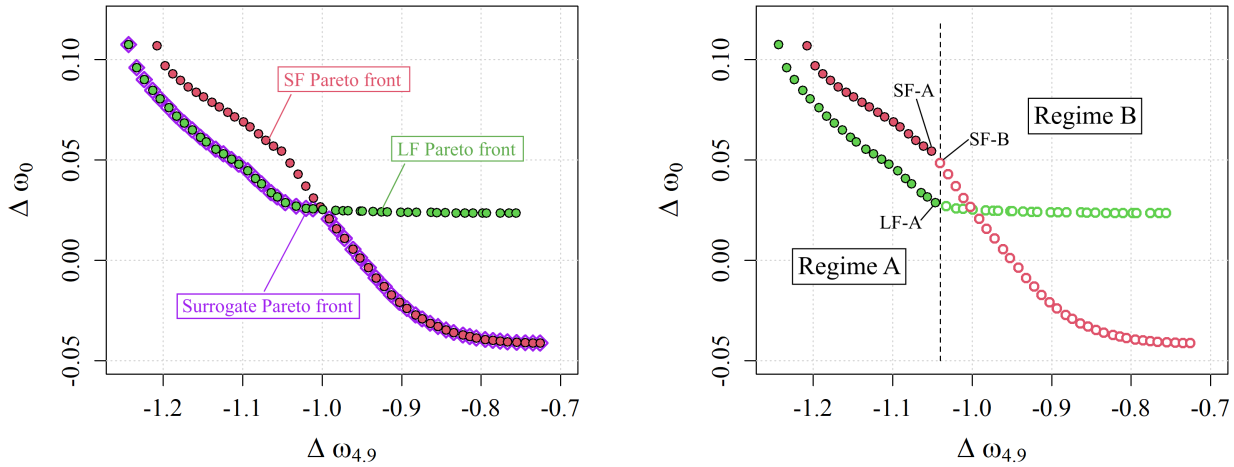

(a) Comparison of SF, LF and surrogate Pareto fronts.

(b) Illustration of regimes A and B.

Figure C.8: Investigation of SF (red) and LF (green) Pareto fronts.

Figure C.8b shows the SF and LF Pareto fronts with a different legend. Indeed, the investigation of the parameters evolution within the SF and LF Pareto fronts reveals the existence of two regimes, denoted regime A (dots) and regime B (circles). The distribution of parameters for the SF and LF Pareto front are shown in Figure C.9. For all guide fins of these Pareto fronts, a unique value of the thickness ($t_{M,H} = 0$) and of the azimuthal position ($v = 0.25$) is found. These parameters are therefore not represented. Two regimes can be noticed for values lower and greater than $\Delta\omega_{4.9} = -1.04$. For $\Delta\omega_{4.9} \leq -1.04$ (regime A), $\Delta\beta_{1,H}$ and H_{GF} are the main parameters that vary. On the contrary, for $\Delta\omega_{4.9} \geq -1.04$ (regime B), $\Delta\beta_{1,H}$ and H_{GF} are constant and u is the main parameter that varies. $\widetilde{c_{GF}}$ is also constant for LF guide fins, while it rapidly drops from 0.35 to 0 for SF guide fins. As such, the evolution along each Pareto front is monitored by $\Delta\beta_{1,H}$ and H_{GF} in the regime A, and mainly by u in the regime B.

The values of the LF guide fin parameters evolve continuously across the two regimes. On the contrary, a sudden change of the H_{GF} values is observed for the SF guide fins when switching from regime A to regime B. The SF guide fins of the regime A are similar to the LF guide fins of the same regime, except for the chord value. On the contrary, SF and LF guide fins of the regime B differ by their trend on the parameter u, their value of H_{GF}, and their chord value.

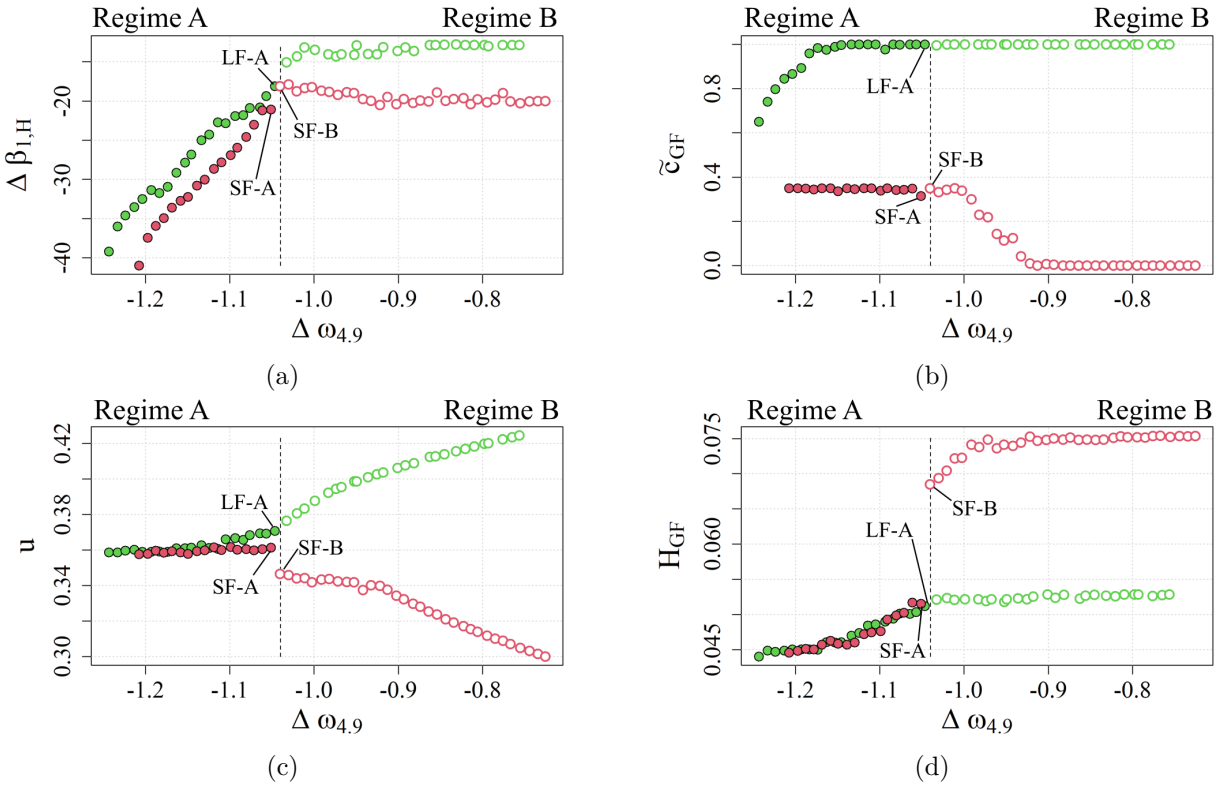

Figure C.9: Parameter evolution along the SF (red) and LF (green) Pareto fronts.

Cartographies of the objective functions evolution with $\Delta\beta_{1,H}$ and H_{GF} are computed to investigate the regime A (Figure C.10). The variation ranges of $\Delta\beta_{1,H}$ and H_{GF} are uniformly discretised with 100 points. The 6p surrogate model is used to evaluate guide fins with the same parameters as SF-A except for $\Delta\beta_{1,H}$ and H_{GF} that vary. The guide fins of the SF Pareto front in the regime A correspond to these predictions, as they only differ from SF-A by their values of $\Delta\beta_{1,H}$ and H_{GF}. They indeed feature constant values of u and $\widetilde{c_{GF}}$ on that regime. They are consequently added to the cartographies, and SF-A is marked with a red cross. A local minimum of $\Delta\omega_{4.9}$ is observed. The SF guide fins follow the steepest descent towards this minimum, which involves coupled values of $\Delta\beta_{1,H}$ and H_{GF}. This explains the simultaneous evolution of these two parameters along the Pareto front in the regime A (see Figure C.9a and C.9d, red dots). Conversely, this path corresponds to an ascending gradient of $\Delta\omega_0$. It appears that SF-A is located in a region with flat gradients with no preferred directions for reducing $\Delta\omega_0$. $\Delta\beta_{1,H}$ and H_{GF} are therefore not the most relevant parameters to further lower $\Delta\omega_0$, which explains the switch to regime B.

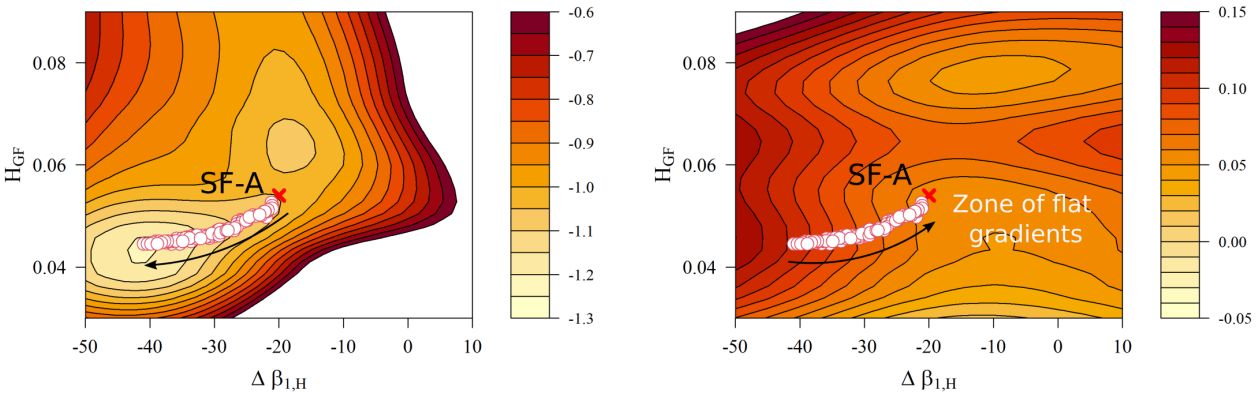

(a) $\Delta\omega_{4.9}$ (b) $\Delta\omega_0$

Figure C.10: Objective functions evolution with ($\Delta\beta_{1,H}$,H_{GF}) around SF-A.

Cartographies of the objective functions evolution with u and H_{GF} are then computed to investigate the switch to regime B (Figure C.11). The same methodology is used and predictions are obtained with SF-A parameters, except for u and H_{GF} that vary. Guide fin SF-A and SF-B are represented with a red and white cross respectively. A local minimum of $\Delta\omega_0$ is observed in regions of large values of H_{GF} and small values of u. The values of u and H_{GF} describing SF-A result from the minimisation of $\Delta\omega_0$ in the regime A. From SF-A, a large modification of these values is required to reach the new minimum of $\Delta\omega_0$. Such a modification might have little impact on $\Delta\omega_{4.9}$ as SF-A is located in a region of flat gradient of $\Delta\omega_{4.9}$. SF-B appears to be the next best compromise to lower $\Delta\omega_0$ while keeping $\Delta\omega_{4.9}$ to a similar level as SF-A. As such, the simultaneous change in H_{GF} and u between SF-A and SF-B results from the mismatch between the minimum region of $\Delta\omega_0$ in the ($\Delta\beta_{1,H}$, H_{GF}) parameter subspace and the minimum region of $\Delta\omega_0$ in the (u, H_{GF}) parameter subspace.

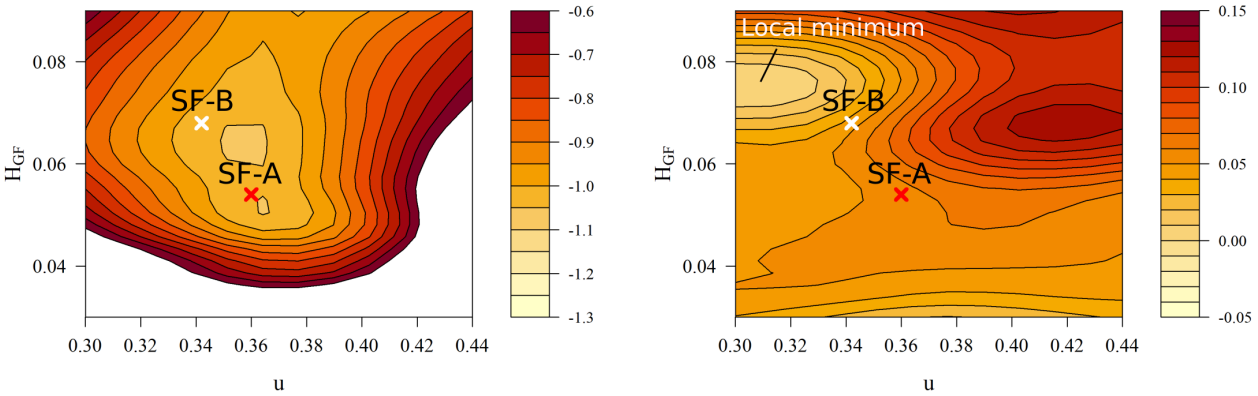

(a) $\Delta\omega_{4.9}$ (b) $\Delta\omega_0$

Figure C.11: Objective functions evolution with (u,H_{GF}) around SF-A.

Contrarily to SF guide fins, the LF guide fins show a continuous evolution of the parameters across the regime A and B (green dots and circles, Figure C.9). The cartographies of the objective functions evolution with u and H_{GF} are therefore computed around LF-A (Figure C.12). Similar gradient as for the SF guide fins are found for $\Delta\omega_{4.9}$, but the evolution of $\Delta\omega_0$ greatly differs. Starting from LF-A, a zone of slightly descending gradient is observed in the direction of constant height and increasing values of u. As such, the next best compromise to

lower $\Delta\omega_0$ (LF-B) is located close to LF-A, thus explaining the continuity in the evolution of the parameters across the regime A and B.

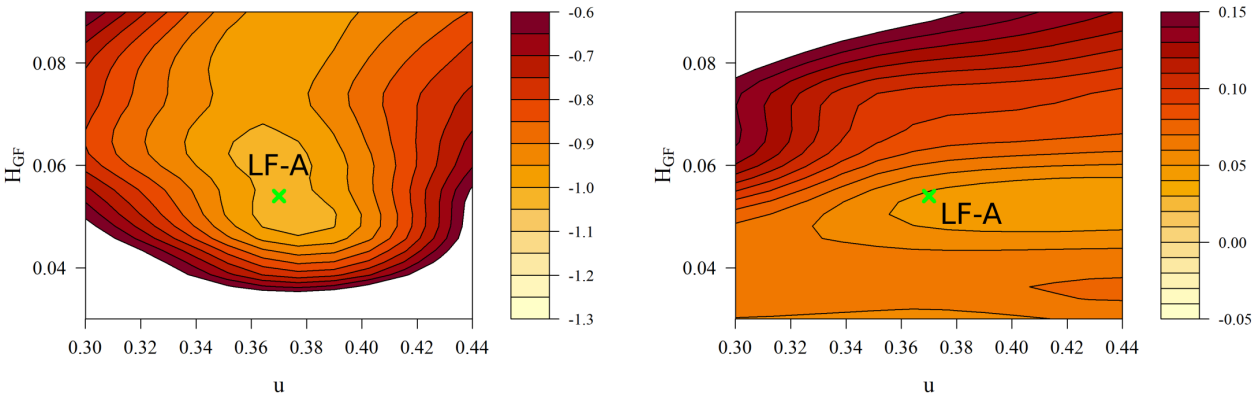

(a) $\Delta\omega_{4.9}$ (b) $\Delta\omega_0$

Figure C.12: Objective functions evolution with (u,H_{GF}) around LF-A.

As a summary, the Pareto front found on the whole surrogate model results from the intersection of two sub-Pareto fronts corresponding to Pareto optimal SF and LF guide fins. The SF and LF Pareto front are characterised with two regimes. In the regime minimising $\Delta\omega_{4.9}$, the SF and LF guide fins are similar and differ only by their chord value. The evolution along each Pareto front is monitored with a coupled evolution of $\Delta\beta_{1,H}$ and H_{GF}. In the regime minimising $\Delta\omega_0$, SF and LF guide fins behave differently. SF guide fins feature a larger value of H_{GF} than in the previous regime, which remains constant. On the contrary, LF guide fins feature the same value of H_{GF} than in the previous regime. For each, the evolution towards lower values of $\Delta\omega_0$ is mainly monitored with the evolution of u in this regime.

C.6 Surrogate predictions of SF-03, LF-01, 3D-01

For each of the SF, LF and 3D family, one representative guide fin is selected (see Section 7.3). Their geometry is recalled in Figure C.13. In order to evaluate the sensitivity of these guide fins to the main parameters ($\Delta\beta_{1,H}$, $t_{M,H}$, $\widetilde{c_{GF}}$, u, v, H_{GF}), the predictions of the surrogate model around these guide fins are computed. Predictions of $\Delta\omega_0$ values are gathered in Figure C.14 and predictions of $\Delta\omega_{4.9}$ values in Figure C.15.

The sensitivity to each parameter is qualitatively evaluated. A guide fin is said to be insensitive to a given parameter if this parameter induces less than a 0.1% variation in the gain when varied across its whole range. Table C.1 and C.2 summarise the sensitivity to the main parameters for each guide fin.

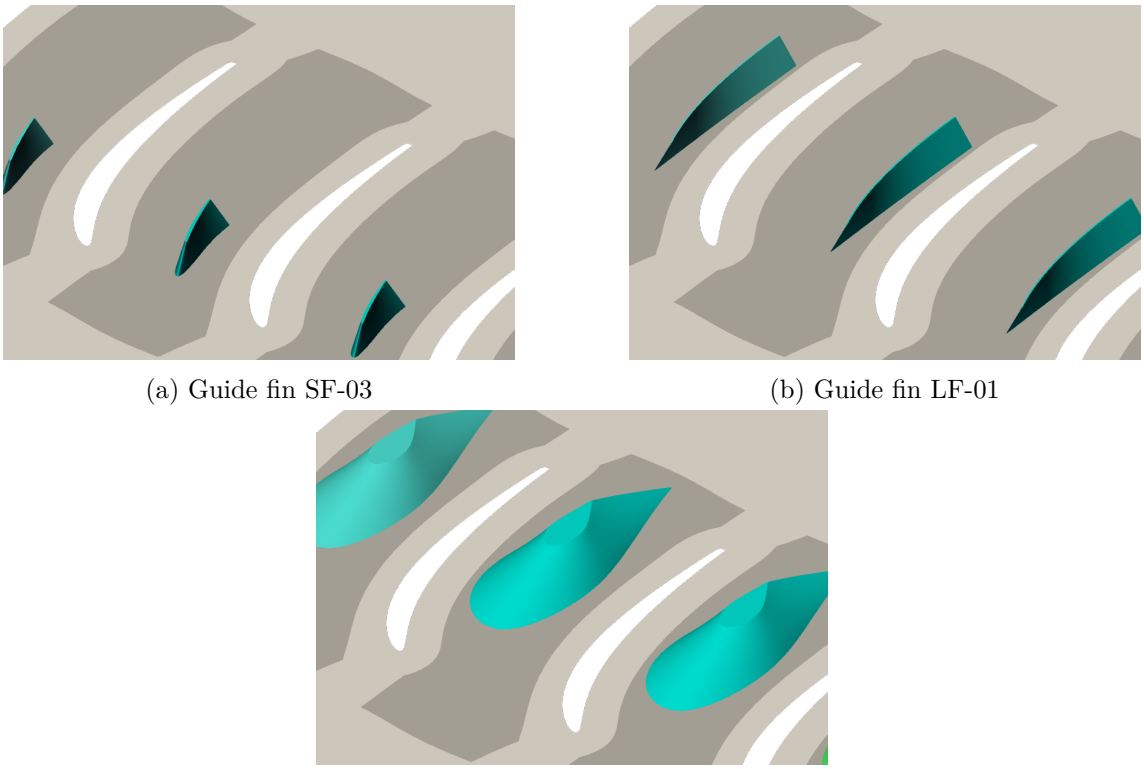

(a) Guide fin SF-03

(b) Guide fin LF-01

(c) Guide fin 3D-01

Figure C.13: Representative guide fins of the SF, LF and 3D families.

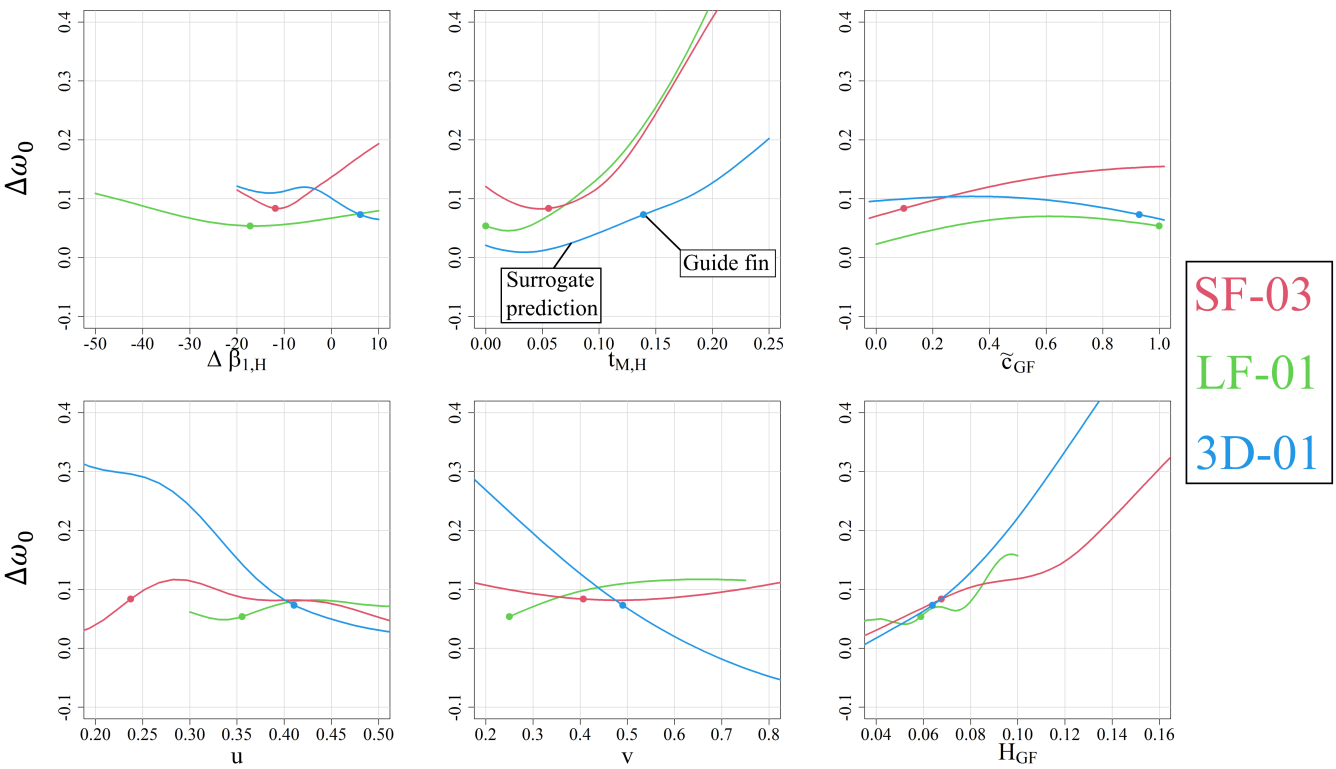

Figure C.14: Surrogate predictions near guide fins SF-03, LF-01, 3D-01. Main parameter values vs $\Delta\omega_0$.

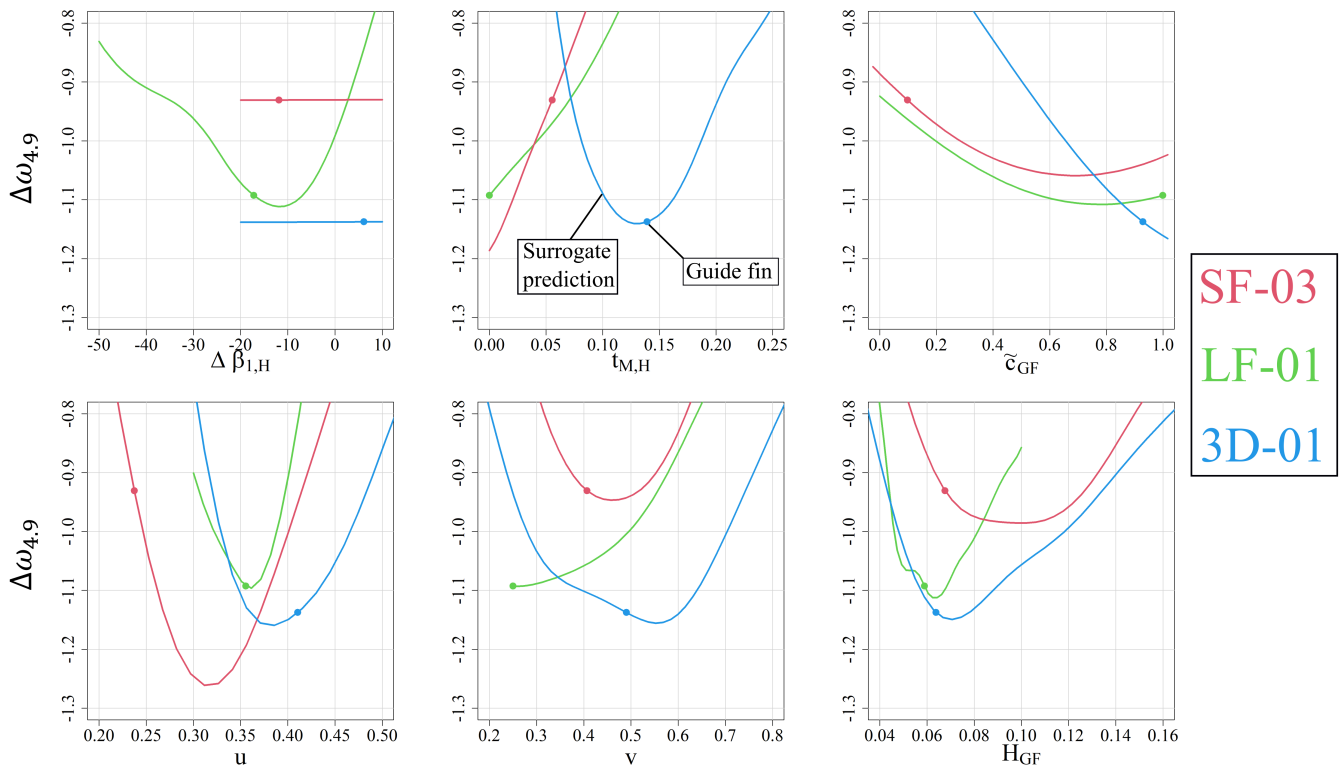

Figure C.15: Surrogate predictions near guide fins SF-03, LF-01, 3D-01. Main parameter values vs $\Delta\omega_{4.9}$.

Family	$\Delta\beta_{1,H}$	$t_{M,H}$	$\widetilde{c_{GF}}$	u	v	H_{GF}
SF		✗				✗
LF		✗				✗
3D		✗		✗	✗	✗

Table C.1: Parameters yielding more than a 0.1% variation in $\Delta\omega_0$ across their range.

Family	$\Delta\beta_{1,H}$	$t_{M,H}$	$\widetilde{c_{GF}}$	u	v	H_{GF}
SF		✗	✗	✗	✗	✗
LF	✗	✗	✗	✗	✗	✗
3D		✗	✗	✗	✗	✗

Table C.2: Parameters yielding more than a 0.1% variation in $\Delta\omega_{4.9}$ across their range.

Appendix D

Investigation of physical mechanisms : complementary results

D.1 Axial evolution of total pressure losses : effect of mixing

In this section, a short RANS analysis of the evolution of the integrated losses along the x-axis is carried out. In particular, the evolution of the losses downstream of the measurement plane is investigated. Let us underline that the integrated losses are used in this section, and not the endwall losses. Figure D.1 gathers this evolution for the baseline case and for the SF, LF and 3D guide fin configurations. These four configurations feature the same behaviour upstream of the channel, and up to about 0.2c after the stator leading edge. From then, the effect of the guide fins becomes noticeable and the losses are lowered accordingly to their efficiency (3D better than LF, better than SF). From the measurement plane (purple line) to the end of the RANS domain, the losses increase and reach an asymptotic behaviour. In this portion, the fluid is simply convected downstream, and this increase in losses is attributed to the mixing effect. It is interesting to notice that :

- The mixing effect conserves the ranking observed in the measurement plane.
- After a propagation over 2.6c, the baseline configuration features higher mixing losses (+1.3%) than with the guide fins (+0.8% to +0.9%)
- The 3D and LF guide fins feature a similar loss increase due to the mixing effect (+0.8%). The SF guide features a slightly greater increase (+0.9%).

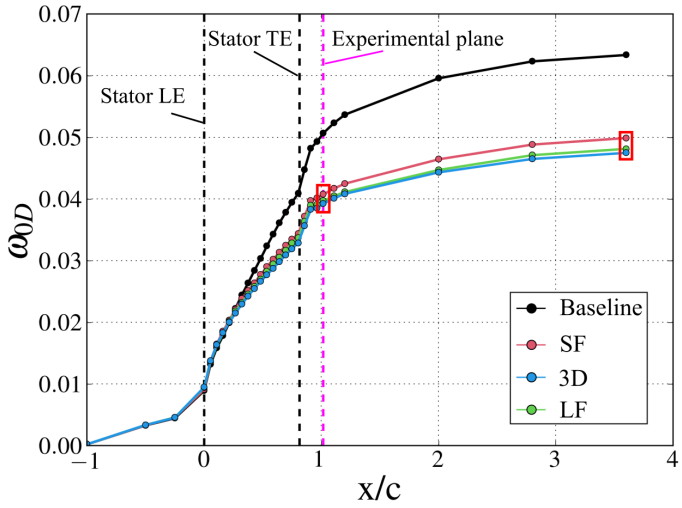

Figure D.1: Axial evolution of mass averaged total pressure losses in the measurement plane. Baseline configuration vs SF, LF and 3D guide fins. RANS results.

Let us underline that the mesh used for this study was progressively coarsen from the measurement plane to the outlet boundary condition. This results in an artificial reduction of the gradients of the convected quantities, and was used on purpose to damp the effect of the outlet boundary condition on the stator row. In this study, the mixing effect is therefore probably artificially enhanced. However, the portion of the mesh downstream of the measurement plane is common to every configuration, which enables to compare them.

D.2 Cartographies

This section gathers experimental cartographies and their prediction with RANS for the incidences i=0°, 3.6°, 4.9°, 5.4°. Cartographies of total pressure losses (ω), dimensionless axial velocity ($\widetilde{V_x}$), pitchwise flow angle fluctuation ($\beta - \beta_{MID}$) and spanwise flow angle ϕ are presented. They allow to a) compare the effect of the different guide fins on the flow by comparison to the baseline b) visualise the effect of the incidence on the four configurations c) assess the RANS predictability. Each figure contains results at the same incidence. Experimental results are followed by RANS predictions. The incidences are presented in the increasing order.

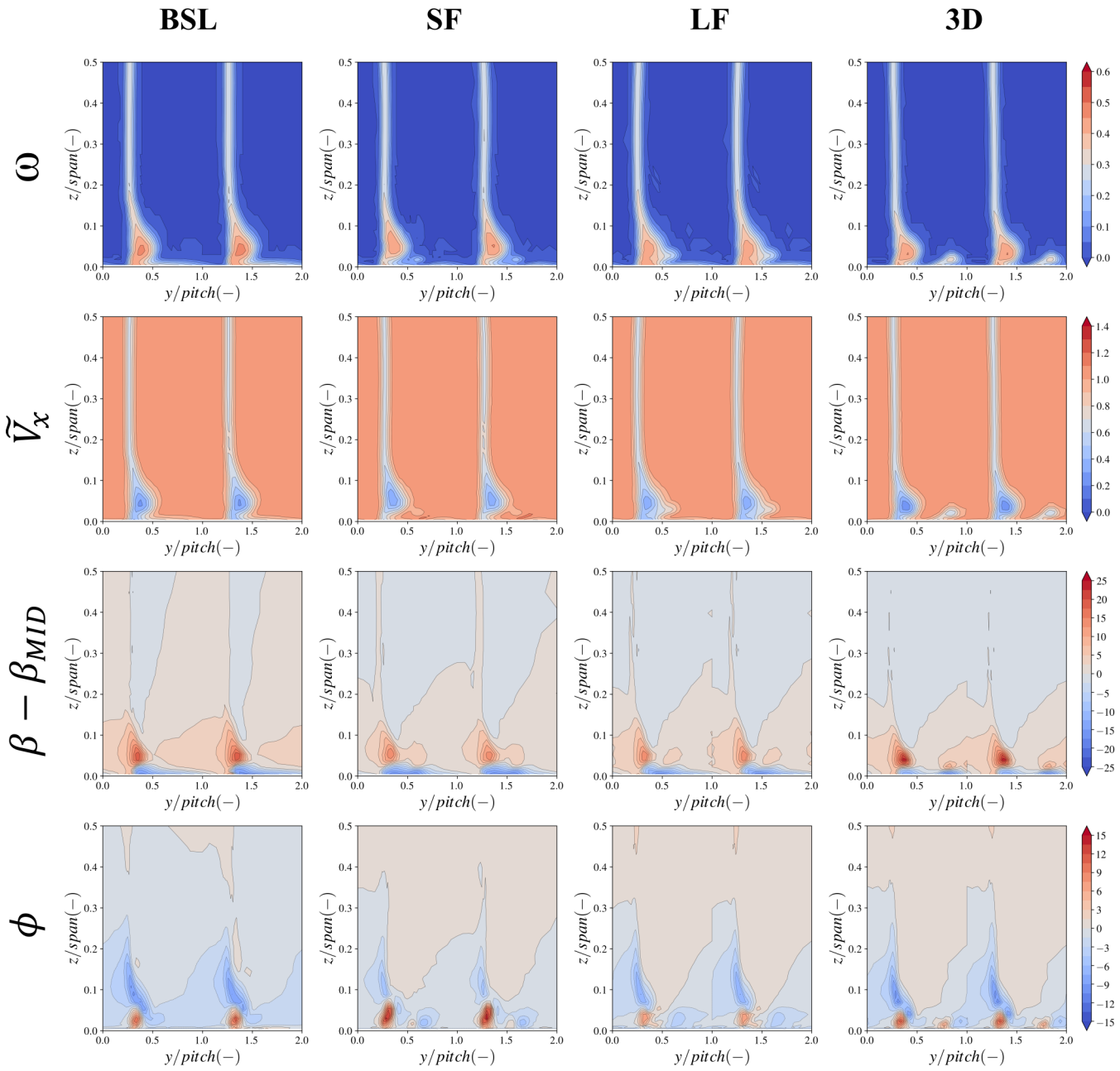

Figure D.2: **Experimental measurement at i=0°.**
Baseline configuration vs SF, LF and 3D guide fins.

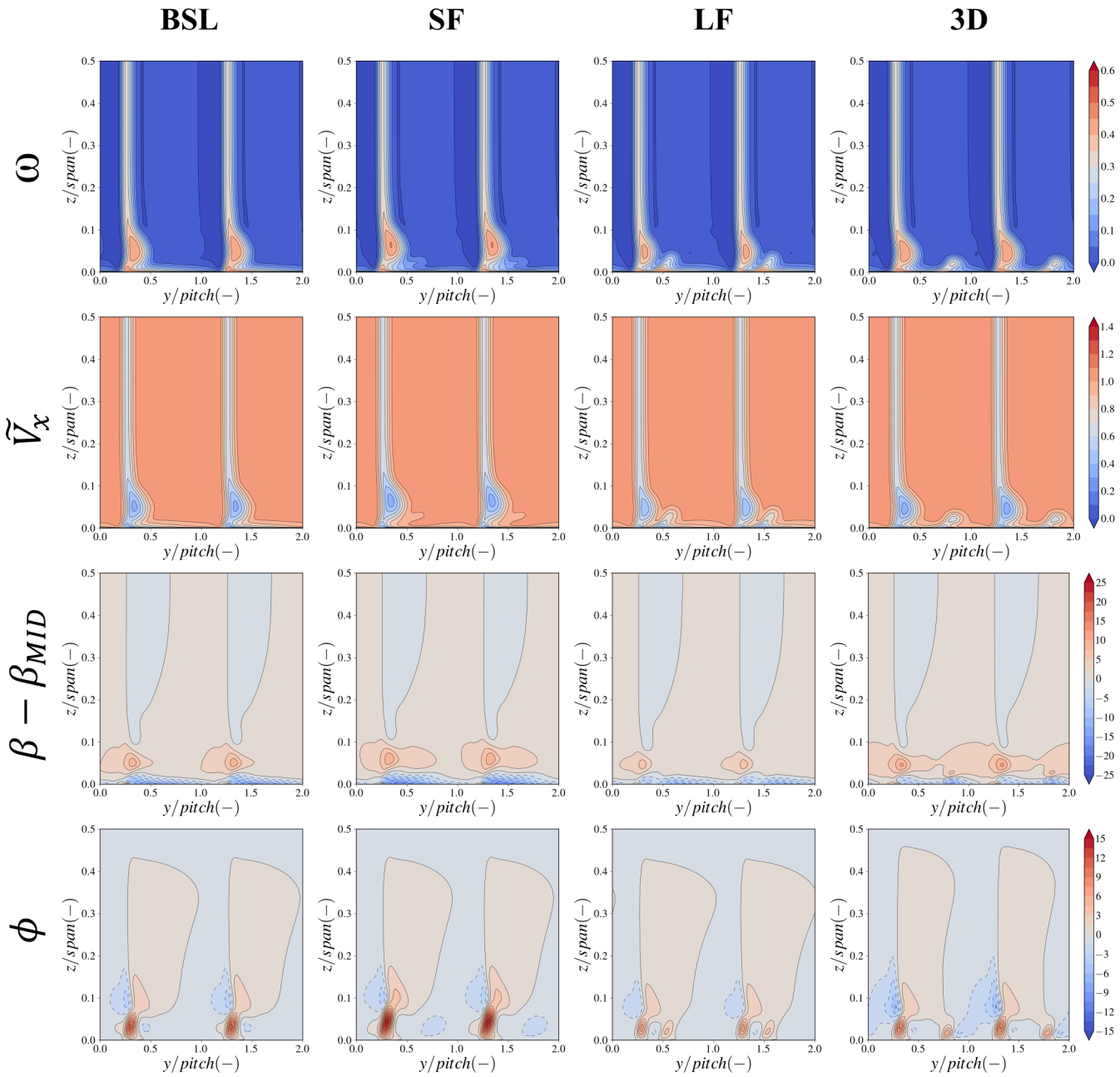

Figure D.3: **RANS in measurement plane at i=0°.**
Baseline configuration vs SF, LF and 3D guide fins.

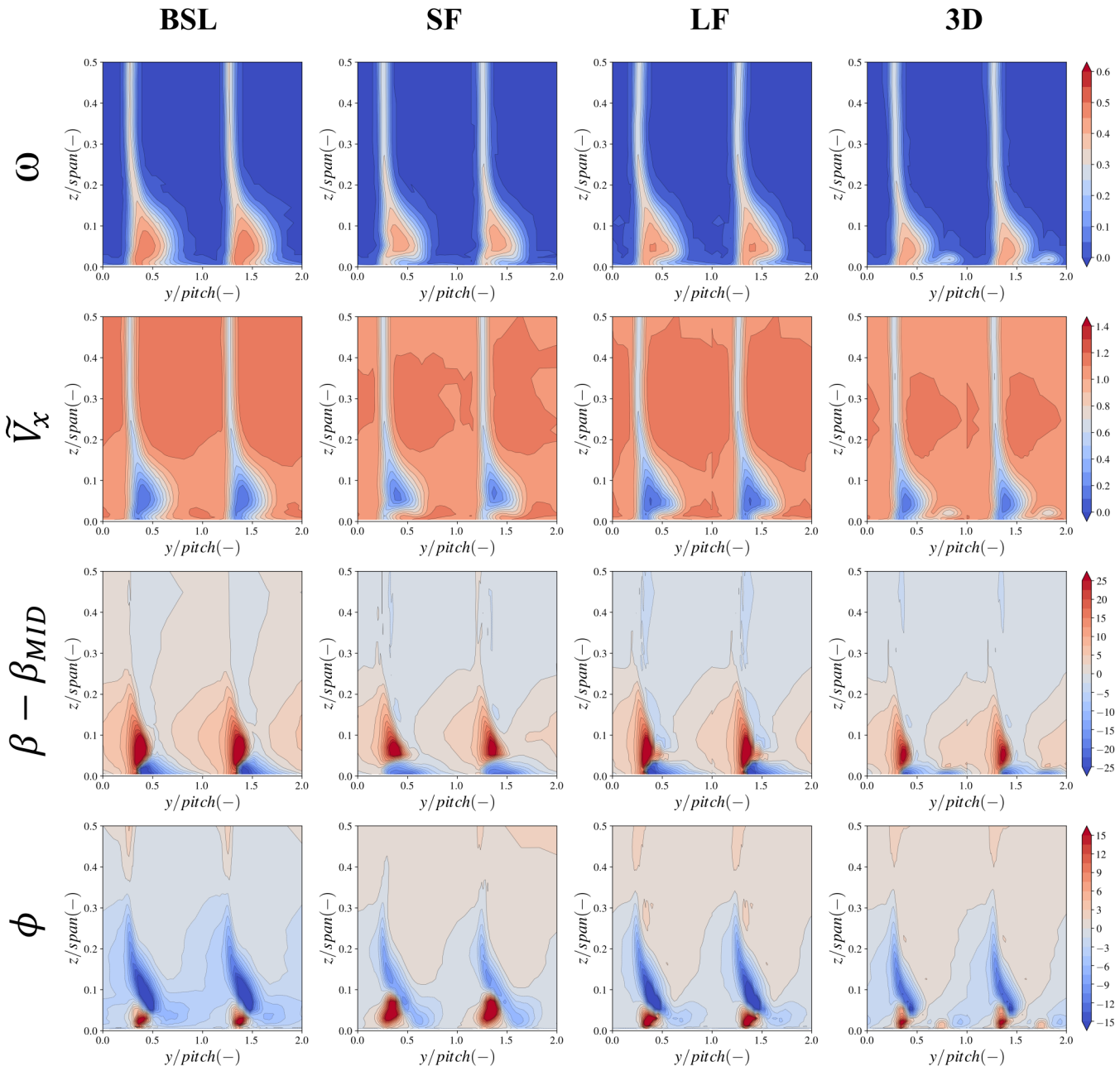

Figure D.4: **Experimental measurement at i=3.6°.**
Baseline configuration vs SF, LF and 3D guide fins.

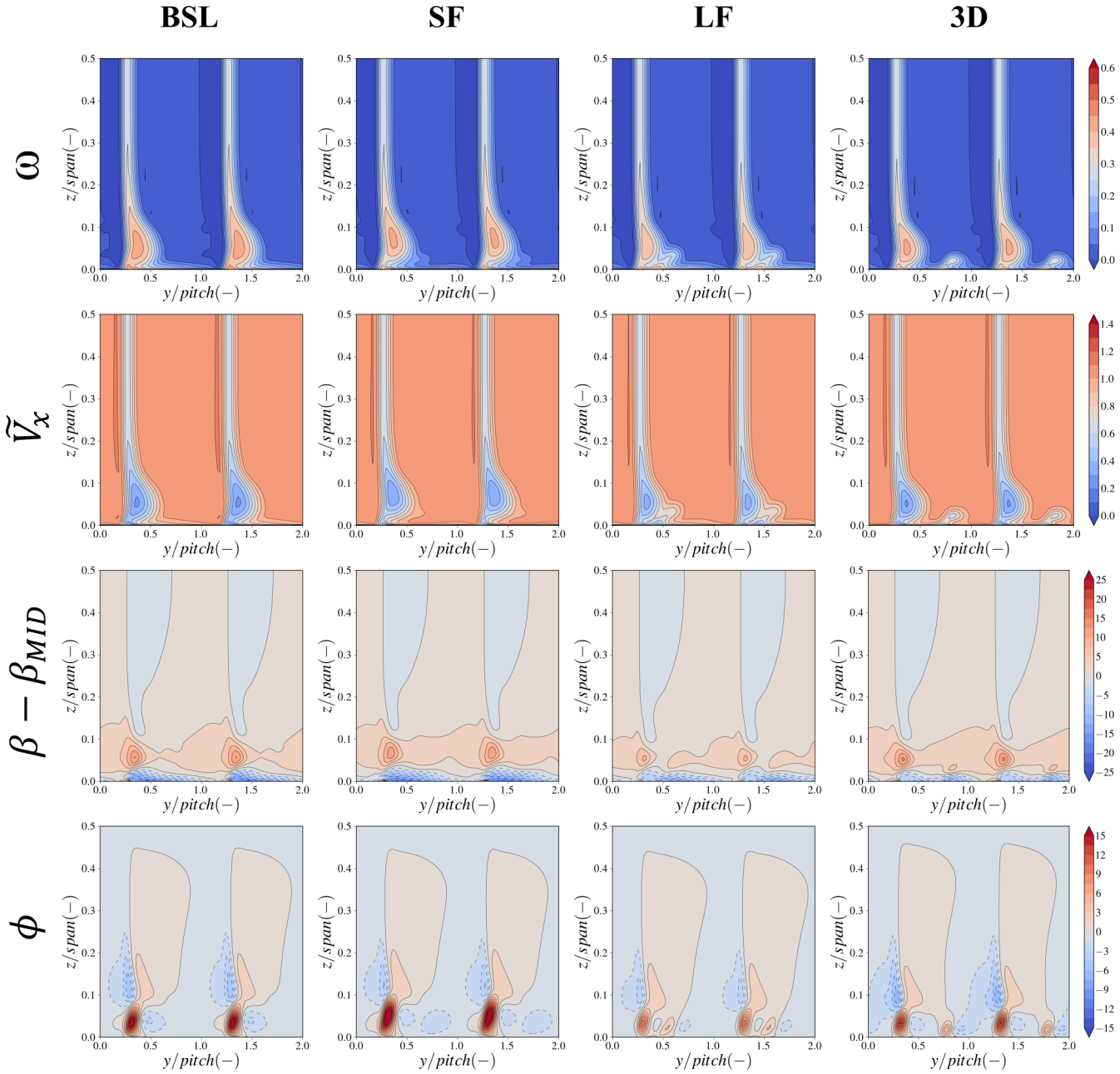

Figure D.5: **RANS in measurement plane at i=3.6°.**
Baseline configuration vs SF, LF and 3D guide fins.

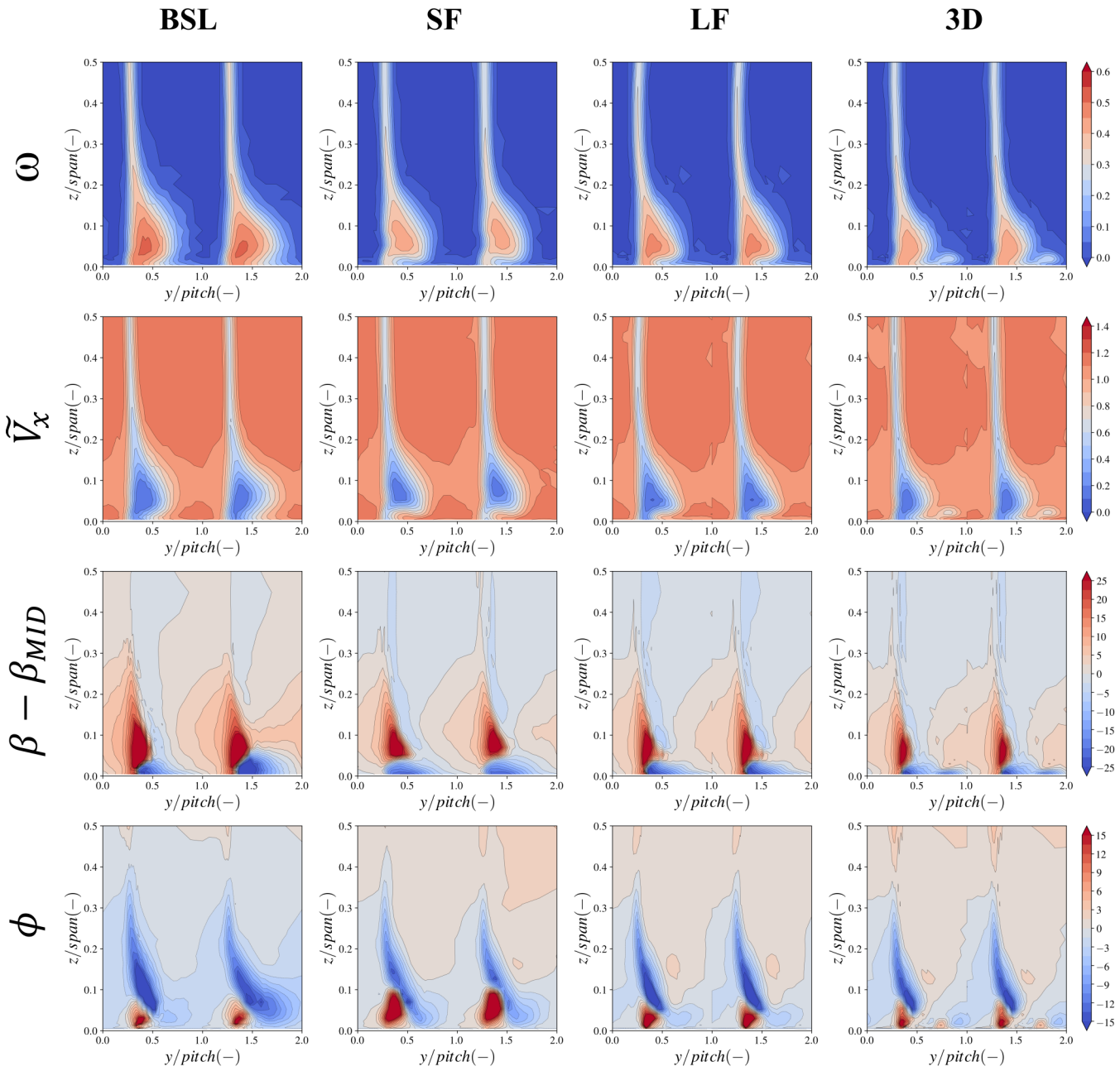

Figure D.6: **Experimental measurement at i=4.9°.**
Baseline configuration vs SF, LF and 3D guide fins.

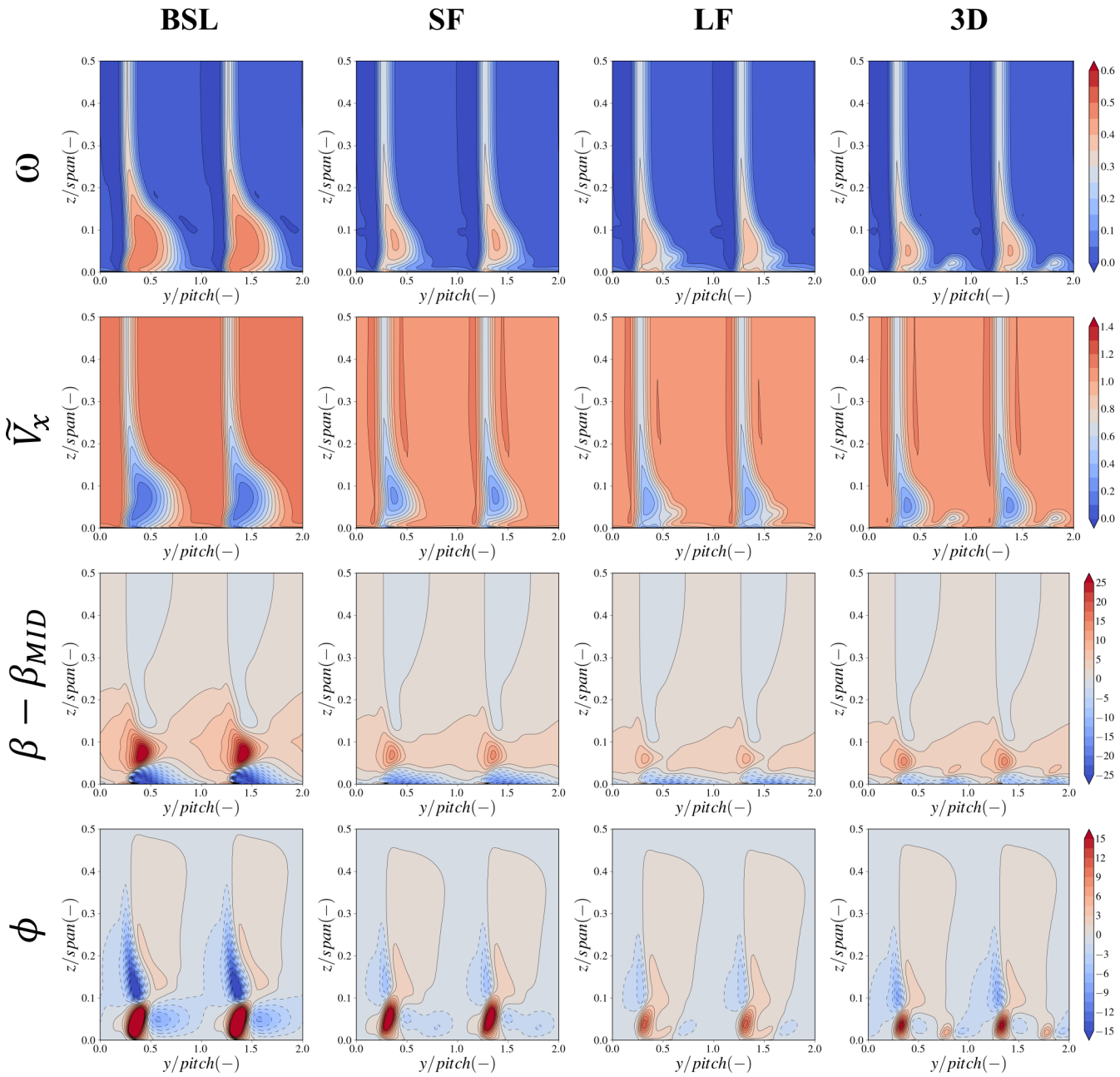

Figure D.7: **RANS in measurement plane at i=4.9°.**
Baseline configuration vs SF, LF and 3D guide fins.

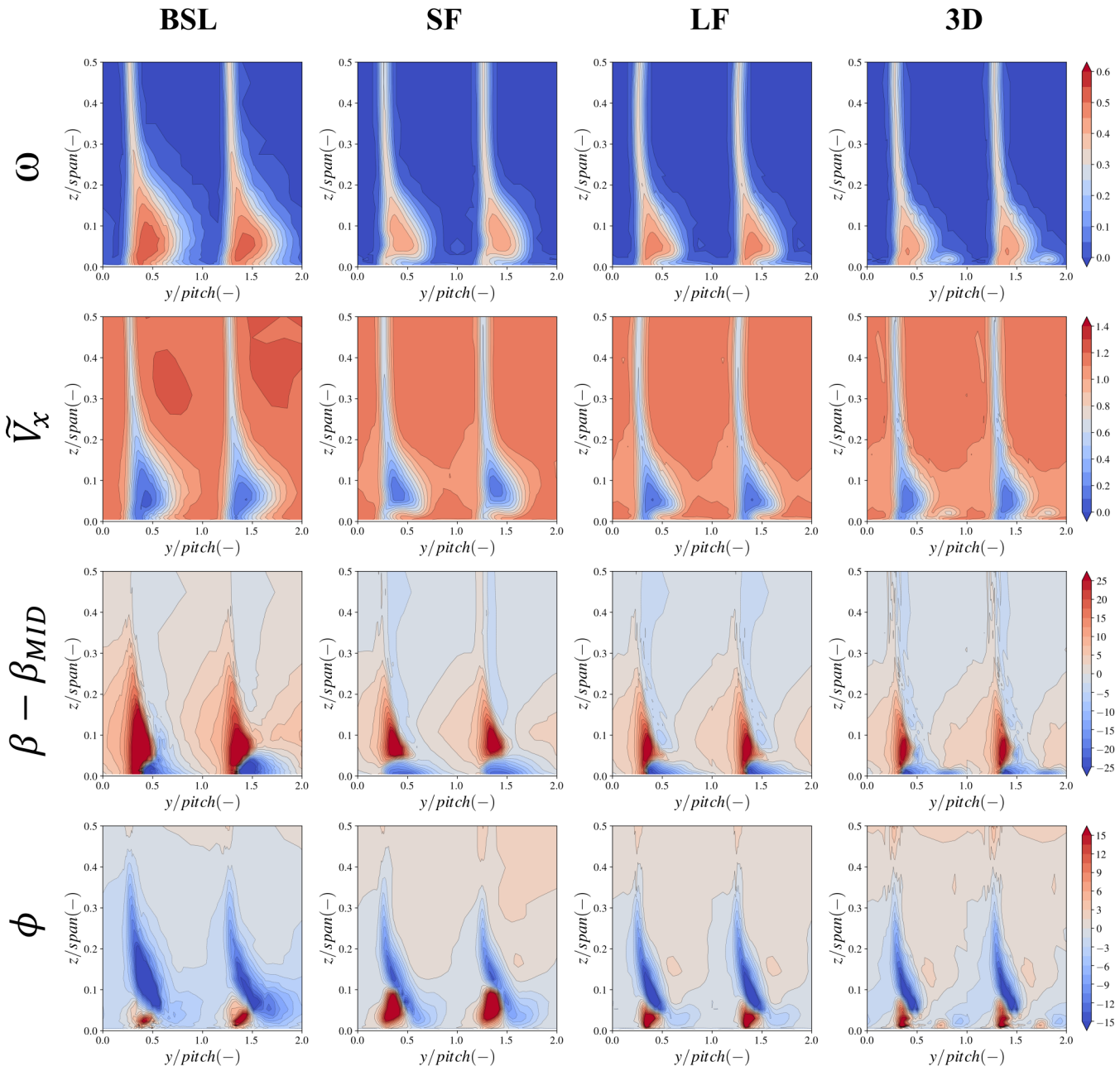

Figure D.8: **Experimental measurement at i=5.4°.**
Baseline configuration vs SF, LF and 3D guide fins.

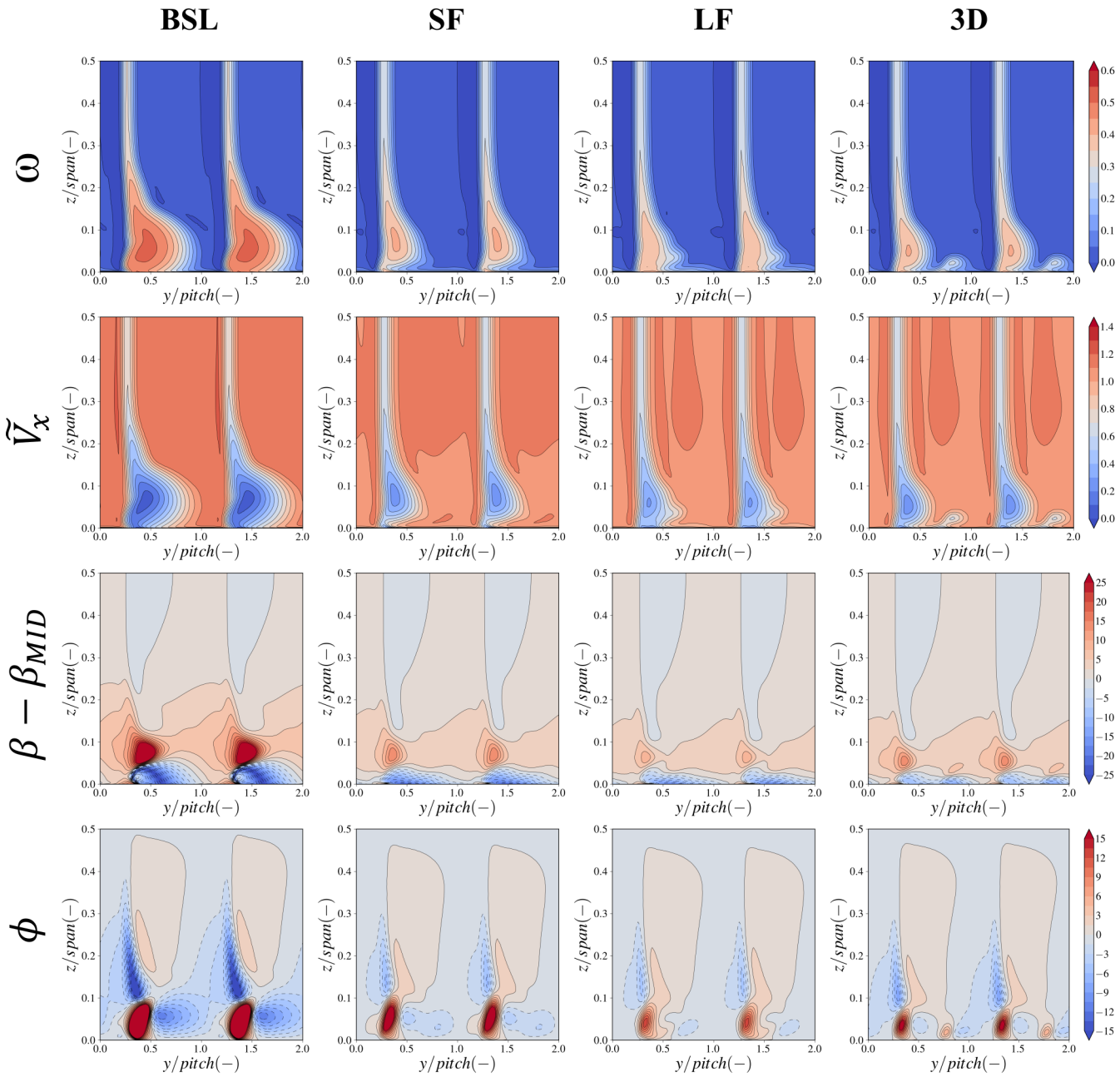

Figure D.9: **RANS in measurement plane at i=5.4°.**
Baseline configuration vs SF, LF and 3D guide fins.

dernière page de la thèse

AUTORISATION DE SOUTENANCE

Vu les dispositions de l'arrêté du 25 mai 2016 modifié par l'arrêté du 26 août 2022,

Vu la demande du directeur de thèse

Monsieur X. OTTAVY

et les rapports de

M. A. KALFAS
Professeur - Aristotle university of thessaloniki - School of Engineering - GR-54124 Thessaloniki Grèce

et de

M. A. DAZIN
Professeur - Laboratoire de Mécanique des Fluides de Lille - Kampé de Fériet
CNRS UMR 9014 - bd Louis XIV - 59046 Lille cedex

Monsieur MONDIN Gabriel

est autorisé à soutenir une thèse pour l'obtention du grade de **DOCTEUR**

Ecole doctorale Mécanique, Energétique, Génie civil, Acoustique

Fait à Ecully, le 24 octobre 2022

Pour le directeur de l'Ecole centrale de Lyon
Le directeur des Formations

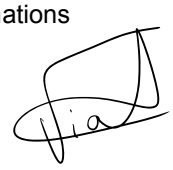

Grégory VIAL